LEIBNIZ INSTITUTE FOR
TROPOSPHERIC RESEARCH

Biennial Report

Zwei-Jahresbericht

2008 / 2009

Leibniz Institute for Tropospheric Research

Biennial Report

Zwei-Jahresbericht

2008 / 2009

LEIBNIZ INSTITUTE FOR
TROPOSPHERIC RESEARCH

Imprint

Published by
Leibniz Institute for Tropospheric Research (IfT)
Leibniz-Institut für Troposphärenforschung e.V. Leipzig (IfT)

Member of the Leibniz Association (WGL)

Postal address: Permoserstr. 15
04318 Leipzig
Germany

Phone: ++49 - 341-235-2321
Fax: ++49 - 341-235-2361
E-mail: katja.broedner@tropos.de
Internet: http://www.tropos.de

Editors
Katja Schmieder, Katja Brödner; Konstanze Kunze, Kerstin Müller, Claudia Peter, Heike Scherf

Editorial Board
Jost Heintzenberg, Hartmut Herrmann, Andreas Macke, Eberhard Renner

Table of contents

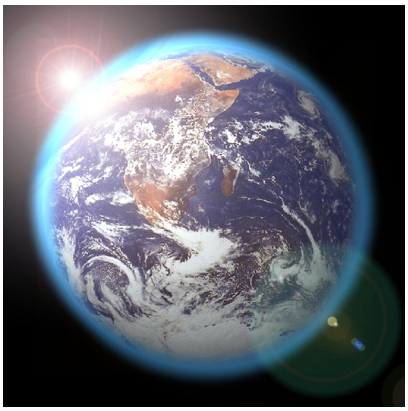

Introduction / Einleitung

Overview / Übersicht

Introduction

In the “Research Park Leipzig/Permoserstraße” close to the Helmholtz Centre for Environmental Research, other research establishments and related businesses you find the Leibniz Institute for Tropospheric Research (IfT). Its name identifies the IfT as a member of the Leibniz Association. The IfT was founded for the investigation of physical and chemical processes in the polluted troposphere.

Fig. / Abb. 1: *IfT main building. / IfT Hauptgebäude.*

A well-defined and globally unique research profile of IfT emerged, with a focus on aerosols, i.e. small airborne particles and droplets. Despite their minute absolute amount, aerosol particles and cloud droplets are essential parts of the atmosphere because they control the budgets of energy, water and trace substances of the Earth System. Human activities can change these highly disperse systems and thus feed back on human beings. This may happen via health effects caused by inhaled particles and fog droplets and through regional and global climate change.

Despite these strong connections between human beings, aerosols, and clouds, important physico-chemical processes of aerosol and cloud formation and the relationships with climate and health are poorly understood. This limitation is mainly due to difficulties with analyzing the very small samples and with the complex behavior of tropospheric multiphase systems, in which individual processes seldom can clearly be distinguished. In climate research this limitation is reflected in much larger uncertainties in predicted anthropogenic aerosol and cloud effects in comparison to numbers published by the Intergovernmental Panel on Climate Change for additional greenhouse gases.

Rapid advances in our understanding of tropospheric multiphase processes and an application of this process understanding to the prediction of the consequences of human impacts can only be expected from concerted approaches from several directions. Consequently, the Leibniz

Einleitung

Auf dem Gelände des „Wissenschaftsparks Leipzig/Permoserstraße“ in Nachbarschaft zum Helmholtz-Zentrum für Umweltforschung, anderen Forschungseinrichtungen und verwandten Firmen, befindet sich seit 1992 das Leibniz-Institut für Troposphärenforschung e. V. Sein Name weist es als Mitglied der Wissenschaftsgemeinschaft Gottfried Wilhelm Leibniz aus. Gegründet wurde es zur Erforschung physikalischer und chemischer Prozesse in der belasteten Troposphäre.

Fig. / Abb. 2: *IfT cloud laboratory. / IfT Wolkenlabor.*

Es hat sich ein klares und weltweit einzigartiges Forschungsprofil herausgebildet, in dessen Mittelpunkt Aerosole, also kleinste luftgetragene Partikel, und Wolken stehen. Trotz geringster absoluter Mengen sind diese Partikel wesentliche Bestandteile der Atmosphäre, weil sie den Energie-, Wasser- und Spurenstoffhaushalt des Erdsystems beeinflussen. Menschliche Aktivitäten können die Eigenschaften dieser hochdispersen Systeme verändern und direkt sowie indirekt auf den Menschen zurück wirken. Das kann sowohl über die gesundheitlichen Wirkungen eingeatmeter Partikel und Nebeltröpfchen als auch über regionale und globale Klimaänderungen geschehen.

Trotz dieser wichtigen Beziehungen zwischen Mensch auf der einen und Aerosol/Wolken auf der anderen Seite sind die physiko-chemischen Prozesse von Aerosol- und Wolkenbildung und die Wechselwirkungen mit Gesundheit und Klima noch wenig verstanden. Dies liegt vor allem an Schwierigkeiten bei der Analyse der beteiligten kleinsten Stoffmengen und an dem komplexen Verhalten troposphärischer Mehrphasensysteme, deren Einzelprozesse in der Atmosphäre nicht klar getrennt beobachtet werden können. In der gegenwärtigen Klimadiskussion zum globalen Wandel spiegelt sich diese Kenntnislage in den sehr viel größeren Unsicherheiten in allen zu Aerosol- und Wolkenwirkung veröffentlichten Zahlen im Verhältnis zu Treibhauseffekten der Gase wider.

Institute for Tropospheric Research conducts field studies in several polluted regions parallel to the development of analytical methods for aerosol and cloud research.

These tools are not only applied in field experiments but also in extensive laboratory investigations, which form a second major activity. A third and equally important approach consists of the formulation and application of numerical models that reach from process models to regional simulations of the formation, transformation and effects of tropospheric multiphase systems. The process models in particular derive their parameters from laboratory experiments.

Field experiments

Field experiments elucidate the atmospheric life cycle and related processes of aerosol particles and cloud droplets. This task is vastly more difficult than comparable trace gas studies, in which only one number has to be known for each substance at each point in time and space. Particle and droplet diameters in the nano and micrometer size range over more than six orders of magnitude in atmospheric aerosols and clouds, all of which play an important role in certain processes. All atmospheric condensable substances can be found in the aerosol and a large number of them

Fig. / Abb. 3: *Laser beams transmitted at IfT by Polly (2-channel lidar), two Polly XT (6-channel lidars), and the EARLINET lidar (9-channel lidar). / Laserstrahlen über dem IFT von Polly (2-Kanal-Lidar), zwei Polly XT (6-Kanal-Lidar) und dem EARLINET-Lidar (9-Kanal-Lidar).*

Fig. / Abb. 4: *IfT research station Melpitz near Leipzig. / IfT-Forschungsstation Melpitz bei Leipzig.*

Rasche Zuwächse beim Verständnis troposphärischer Mehrphasenprozesse und eine Anwendung dieses Prozessverständnisses auf die Vorhersage der Folgen menschlicher Eingriffe lassen sich nur durch ein konzertiertes Vorgehen in mehreren Richtungen erwarten. Das Leibniz-Institut für Troposphärenforschung betreibt daher neben Feldstudien in belasteten Regionen auch die Entwicklung eigener physikalischer und chemisch-analytischer Verfahren zur Untersuchung von Aerosolen und Wolken. Diese Verfahren werden auch in ausgedehnten Laboruntersuchungen eingesetzt, der zweiten Hauptarbeitsrichtung des Instituts. Ein dritter, gleichermaßen wichtiger Arbeitsansatz ist die Formulierung und Anwendung numerischer Modelle von der Prozessbeschreibung bis zur Beschreibung der regionalen Bildung, Umwandlung und Wirkung troposphärischer Mehrphasensysteme auf der Basis eigens durchgeführter komplexer Laborexperimente.

Feldexperimente

Die Feldexperimente des Instituts dienen der Aufklärung des atmosphärischen Kreislaufs der Aerosolpartikel und Wolkentropfen und der damit verbundenen Prozesse. Die Komplexität des Systems wird dabei unter anderem dadurch bestimmt, dass in der Atmosphäre Partikel und Tropfen auftreten, deren Größe sich im Nano- und Mikrometerbereich um mehr als sechs Zehnerpotenzen unterscheiden kann, die dem entsprechend auch unterschiedlichen Umwandlungsprozessen unterliegen. Außerdem kann man im Aerosol alle kondensationsfähigen Stoffe des Erdsystems finden, von denen eine große Zahl das Klima und die Biosphäre und deren Wirkung beeinflussen. Als Folge dieser Vielfalt und der mengenbedingten analytischen Schwierigkeiten sind wesentliche globale Aerosol- und Wolkeneigenschaften noch wenig bekannt.

Diese Unsicherheit beginnt schon bei den Partikelquellen, die Forschungsgegenstand am Leibniz-Institut für Troposphärenforschung sind.

Fig. / Abb. 5: *Arterial road in Leipzig. / Hauptverkehrsader in Leipzig.*

contribute to climate and biospheric effects. Essential properties of aerosol particles and cloud droplets of this multidimensional system are not well established on a global scale yet.

The uncertainty and thus the research efforts of the Leibniz Institute for Tropospheric Research start with particle sources. The combustion of fossil and contemporary fuels is one of the most prominent aerosol sources. However, these sources are still poorly characterized in terms of climate-relevant aerosol parameters. According to long-term urban and rural measurements of the institute emissions of particles and their precursor gases are subject to strong physical and chemical transformations that need to be followed with high-resolution sensors in order to identify the underlying processes.

Not even the largest highly polluted regions in the plumes of North America, Europe, Africa, the Indian subcontinent, Amazonia, and Eastern Asia are sufficiently characterized in terms of aerosol burdens and ensuing climate effects. The institute focuses thus its participation in international field campaigns and dedicated long-term studies in Asia. In recent years, the study of climate-relevant aspects of mineral dust near its most important

Fig. / Abb. 6: *View from the Campus of Peking University on a heavily polluted day. / Blick vom Gelände der Peking Universität an einem stark verschmutzten Tag.*

Die Verbrennung fossiler und nachwachsender Brennstoffe zur Energieerzeugung und im Verkehr sind wichtigste Aerosolquellen. Wie sich aus Messungen des Instituts an vielen urbanen Messstellen und kontinentalen Hintergrundstationen ergab, unterliegen die Emissionen von Partikeln und deren Vorläufern enormen physikalischen und chemischen Umwandlungen, die mit hoher zeitlicher Auflösung verfolgt werden müssen, um die beteiligten Prozesse aufzuklären.

Selbst die am höchsten verunreinigten Regionen über Nordamerika, Europa, Afrika, dem indischen Subkontinent, dem Amazonasgebiet und Ostasien sind noch bei weitem nicht hinreichend bezüglich ihrer Aerosolbelastungen und den daraus resultierenden Klimawirkungen charakterisiert. Auf diese Regionen konzentrieren sich daher in internationaler Zusammenarbeit die Feldexperimente des Instituts. Das Institut beteiligt

Fig. / Abb. 7: *Monitoring station Leipzig-Eisenbahnstrasse (red building). / Messstation Leipzig-Eisenbahnstrasse (rotes Gebäude).*

sich deshalb an internationalen Messkampagnen und Langzeitmessungen insbesondere in Asien. Seit einigen Jahren nehmen Untersuchungen zum Mineralstaub und dessen Wirkung auf den Strahlungshaushalt und Wolkenbildung im Quellgebiet der Sahara aber auch im Fernfeld über dem Nordatlantik wachsenden Raum ein. Durch Nutzung eines kommerziellen Verkehrsflugzeuges der Lufthansa werden auch Aerosolverteilungen in der belasteten oberen Troposphäre auf regelmäßig beflogenen interkontinentalen Routen vermessen.

Auf kleineren Skalen werden Untersuchungen zur Partikelbildung und Wechselwirkung zwischen Aerosolpartikeln und Wolken und der Einfluss turbulenter Mischungsprozesse auf die Wolkenentwicklung mit Hilfe der hubschraubergetragenen Messplattform ACTOS durchgeführt. Zusätzlich werden an Bergstationen Studien durchgeführt, die sich dem Verständnis von Einzelprozessen, wie der Partikelneubildung, der physiko-chemischen Veränderung des Aerosols beim Wolkendurchgang und dem Einfluss von Aerosolen auf die Entwicklung von Wolken widmen.

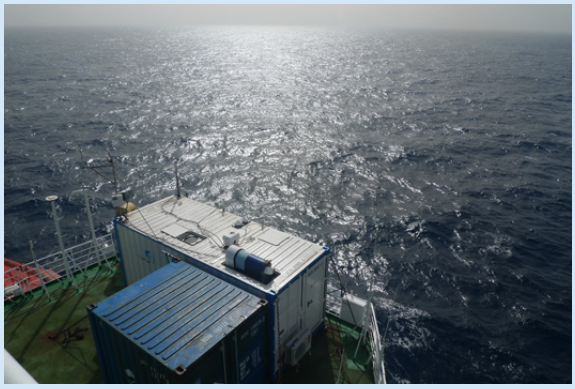

Fig. / Abb. 8: *Container based OCEANET Atmospheric Observatory on its first mission onboard Research Vessel Polarstern in the North and South Atlantic. / Containerbasiertes OCEANET Atmosphärenobservatorium auf der ersten Mission an Bord des Forschungsschiffes Polarstern im Nord- und Südatlantik.*

Saharan source and in the far field over the Atlantic have gained more weight in the institute's research. By means of a commercial aircraft operated by Lufthansa on intercontinental routes, aerosol measurements are conducted even in the polluted upper troposphere in the framework of the CARIBIC project.

On smaller scales, investigations concerning new particle formation, the interactions between aerosol particles and clouds, and the influences of turbulent mixing processes on cloud development are carried out with help of the helicopter-borne measurement platform ACTOS. In addition, process studies are conducted at suitable locations such as mountain observatories to study particle nucleation, particle processing through clouds and the influence of anthropogenic aerosols on the optical properties of clouds.

In the framework of the WGL-PAKT-project OCEANET ship-based measurements of aerosol, cloud and radiation properties of the marine troposphere are carried out in various climate regions of the northern and southern hemisphere. IfT is one of the leading institutions of the European aerosol networks for lidar (EARLINET) and in-

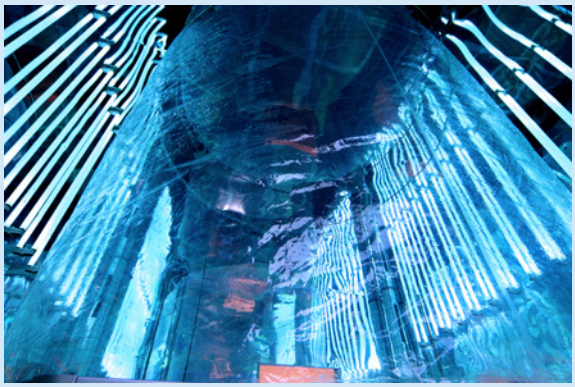

Fig. / Abb. 9: *The IfT aerosol chamber (LEAK) with UV lamps. / Die IfT Aerosolkammer (LEAK) mit UV-LAMPEN.*

Im Rahmen des WGL-PAKT-Projektes OCEANET werden schiffsgetragene Messungen der Aerosol-, Wolken- und Strahlungseigenschaften der maritimen Troposphäre in verschiedenen Klimazonen der Nord- und Südhemisphäre durchgeführt. Das IfT ist maßgeblich an den Europäischen Aerosol-Netzwerken für Lidarmessungen (EARLINET) und in-situ Messungen (EUSAAR) beteiligt und koordiniert ein europaweites Projekt zur Unterstützung von weltraumgestützten Aerosolmessungen mit dem CALIPSO-Lidar der NASA. Das IfT betreibt weiterhin das Weltkalibrierzentrum der WMO für physikalische Aerosolmessungen zur Qualitätssicherung von in-situ Messungen an nationalen und internationalen Messstationen.

Laborexperimente

In der Atmosphärenforschung werden kontinuierlich physikalisch-chemische Modelle zur Beschreibung der wesentlichen Prozesse ent-

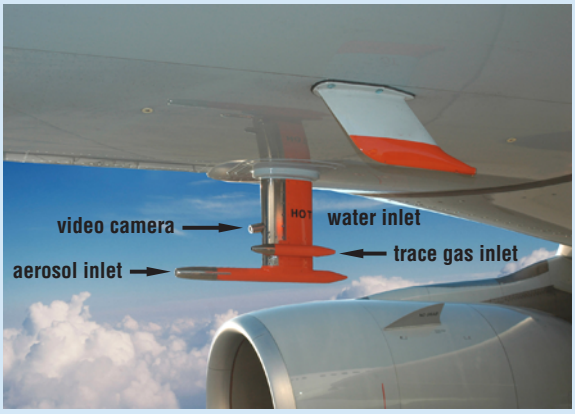

Fig. / Abb. 10: *CARIBIC inlet system at the lower fuselage of a Lufthansa Airbus A340-600. In CARIBIC regular measurements of trace gases and aerosol particles are carried out in the free troposphere since 1997 using commercial aircraft. / CARIBIC-Einlasssystem an der Rumpfunterseite eines Lufthansa-Airbus A340-600. In CARIBIC werden mit Hilfe eines kommerziellen Flugzeugs seit 1997 regelmäßige Messungen von Spurengasen und Aerosolpartikeln in der freien Troposphäre durchgeführt.*

wickelt. Grundlage derartiger Modelle sind stets Prozessparameter, die in Laborexperimenten ermittelt werden müssen. Laborexperimente auf dem jeweiligen Stand der Basiswissenschaften Chemie und Physik müssen die Basis einer jeden Modellentwicklung sein.

In der Abteilung Physik wird im Bereich der Laborexperimente eine Vielzahl von Messmethoden entwickelt, die zur Partikelcharakterisierung in boden- und luftgestützten Feldmesskampagnen eingesetzt werden. Im Einzelnen betreffen diese Arbeiten die Weiterentwicklung von DMA-basierenden (Differentieller Mobilitätsanalysator) Größenspektrometern sowie Sammelsysteme zur physikalischen und chemischen Charakterisierung

situ measurements (EUSAAR), and presently coordinates European lidar activities as a support to the space-borne CALIPSO lidar mission of NASA. Furthermore, the IfT hosts the WMO World Calibration Centre for physical in-situ aerosol measurements to assure high quality standards at national and international observatories.

Laboratory experiments

In atmospheric research, there is a continuous development of physico-chemical models for the description of the most relevant process. These models are based on process parameters, which need to be determined in laboratory experiments performed according to the state of the art in the basic sciences chemistry and physics.

In the physics section of the institute, laboratory experiments cover the development of a large number of methods to characterize atmospheric particles and droplets. In particular, DMA-based (Differential Mobility Analyzer) size spectrometers and sampling systems for the characterization of cloud droplets and interstitial aerosol particles are designed. Spectroscopic techniques such as the Differential Optical Absorption Spectroscopy have been developed for the analysis of trace gases and aerosol particles. Multi-wavelength aerosol LIDAR (Light Detection and Ranging) systems are

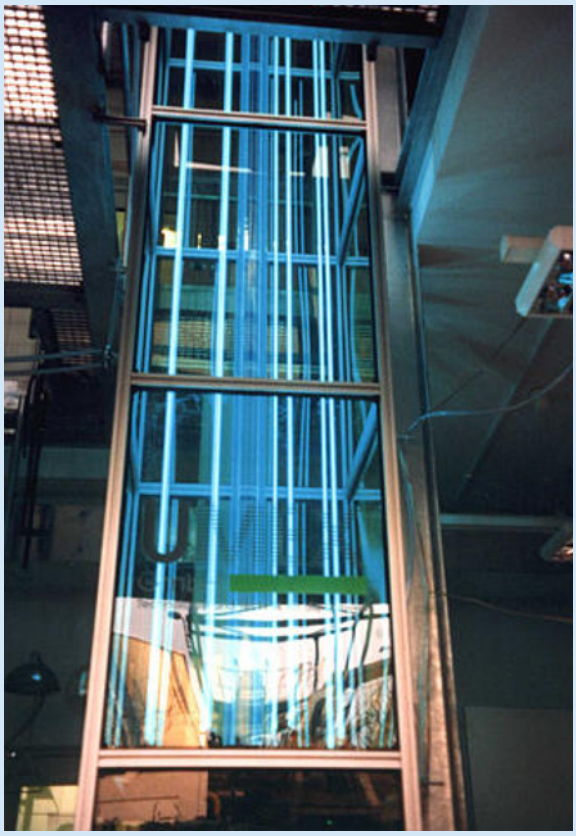

Fig. / Abb. 11: *The IfT laminar flow tube reactor (IfT-LFT). / Der laminare Rohrreaktor des IfT.*

Fig. / Abb. 12: *Mini Raman lidar Polly XT in an air-conditioned cabinet. / Mini-Ramanlidar Polly XT im klimatisierten Gehäuse.*

von Wolkentröpfchen und dem interstitiellen Aerosol, also denjenigen Aerosolpartikeln, die innerhalb von Wolken neben den Wolkentröpfchen selbst in der Gasphase suspendiert sind.

Optische Messmethoden werden zur Bestimmung der Extinktion von Partikeln und der Absorption von Spurengasen und Radikalen mittels der differentiellen Absorptionsspektroskopie (DOAS) angewendet. Mehrwellenlängenlidare und ein Windlidar werden zur Bestimmung von Aerosoleigenschaften, Aerosolflüssen und meteorologischen Parametern wie Temperatur, Feuchte und Wind im Labor weiterentwickelt und im Felde eingesetzt. Die Anteile „schwarzen Kohlenstoffs“ und mineralischer Aerosolkomponenten in Aerosolproben werden durch spektrale Absorptionsmessungen bestimmt.

In zwei Bereichen werden prozessorientierte Laboruntersuchungen gemeinsam von den Abteilungen Physik und Chemie durchgeführt. Diese abteilungsübergreifenden Aktivitäten betreffen einen als Laminarströmungsrohr ausgeführten Reaktor, an dem die Bildung von Partikeln aus SO_2 untersucht wird. Im Jahr 2005 nahm das IfT das neue Wolkenlabor rund um den Strömungsreaktor LACIS in Betrieb. Untersuchungen von LACIS betreffen das hygroskopische Wachstum von Aerosolpartikeln unterschiedlichster chemischer Zusammensetzung, deren Aktivierung zu Wolkentröpfchen, sowie deren Gefrieren. Ziele dieser Untersuchungen sind die Erlangung eines besseren Prozessverständnisses auf fundamentaler Ebene, die Identifikation kritischer und kontrollierender Parameter und die Entwicklung geeigneten Parametrisierungen zur Beschreibung der unterschiedlichen Prozesse in Modellen.

In der Abteilung Chemie werden Gasphasenreaktionen der Radikale OH und NO_3 in Strömungsreaktoren und der Leipziger Aerosolkammer (LEAK) untersucht. Diese Reaktionen sind von Interesse für die Ozon- und Partikelbildung, verur-

developed in the field for measuring atmospheric state parameters such as temperature, wind and relative humidity besides aerosol-optical characteristics and aerosol fluxes. Black carbon and mineral, light absorbing aerosol components are quantified with spectroscopic methods in aerosol and cloud samples.

The physics and chemistry sections in two main areas are carrying out process-oriented laboratory studies jointly. The first of these activities concerns a laminar flow tube reactor in which particle formation from SO_2 is being investigated. With the large Leipzig Aerosol Cloud Simulator LACIS and related instrumentation, the hygroscopic growth of aerosol particles, their activation to cloud droplets and the freezing of cloud droplets are considered. Goals of these investigations are achieving a better understanding concerning the underlying fundamental processes, the identification of critical and controlling parameters, and the development of parameterizations for use in atmospheric models.

The chemistry department conducts several process-oriented laboratory studies. Gas phase reactions of the radicals OH and NO_3 are being investigated in flow reactors. These reactions are important for ozone and particle formation caused by biogenic and anthropogenic emissions of volatile hydrocarbons. These investigations are also done in collaboration with the Physics Department determining hygroscopic growth and cloud droplet activation of the particles formed. The chemical identity of atmospheric particles is being characterized in the Leipzig Aerosol Chamber (LEAK). In a single drop experiment, phase transfer parameters of trace gases and radicals are being determined for different chemical species and surfaces. Experiments with radical reactions in the liquid phase form a core activity of the laboratory

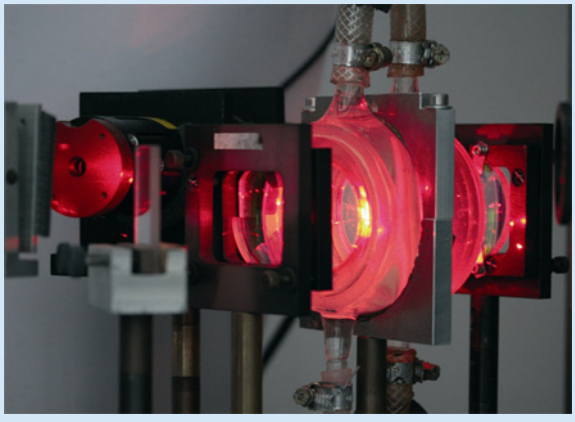

Fig. / Abb. 13: *Experimental set-up including White cell optics, reaction cell and solid state laser for the kinetic investigation of nitrate-radical (NO_3) reactions in aqueous solution. / Versuchsaufbau zur Messung der Kinetik von Nitratradikalreaktionen (NO_3) in wässriger Lösung mit Festkörperlaser, Whitespiegel-Konfiguration und Reaktionszelle.*

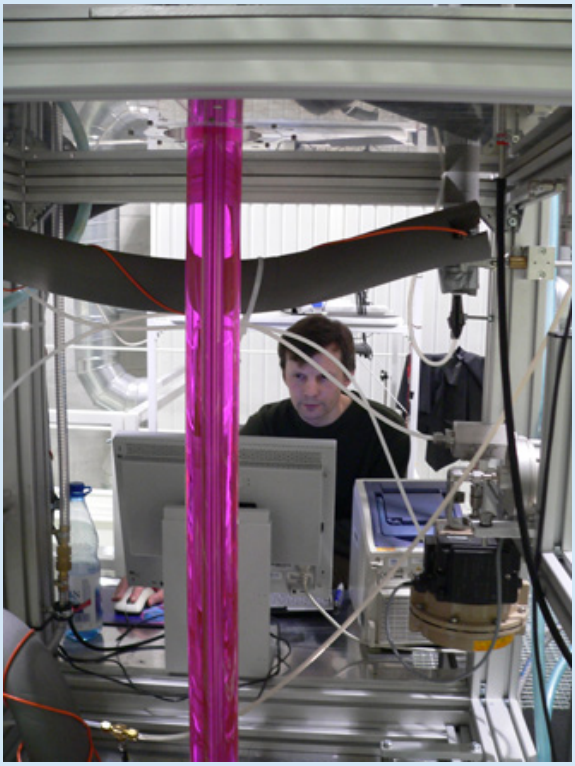

Fig. / Abb. 14: *The "Leipzig Aerosol Cloud Interaction Simulator" (LACIS). / Der Wolkenkanal (LACIS).*

sacht durch anthropogene oder biogene flüchtige Kohlenwasserstoffe. Die Untersuchungen laufen auch in Zusammenarbeit mit der Abteilung Physik zur Bestimmung des Feuchtewachstums und der Tropfenaktivierung der erzeugten Partikel.

In einem Einzeltropfenexperiment werden Phasentransferparameter für Spurengase und Radikale untersucht. Die Bestimmung von Phasentransferparametern und reaktiven Aufnahmekoeffizienten wird dabei auf bisher nicht betrachtete chemische Spezies und komplexe Oberflächen ausgeweitet. Im Bereich von Flüssigphasenmechanismen werden Reaktionen von vorwiegend radikalischen Oxidantien mit zeitaufgelösten optischen Nachweistechniken untersucht. Diese Reaktionen laufen in den Tröpfchen von Wolken, Regen und Nebel sowie in wässrigen Aerosolpartikeln ab. Hier werden zum Verständnis der Oxidation organischer Spurengase im troposphärischen Mehrphasensystem eine Vielzahl von Reaktionen der Radikale OH und NO_3 sowie Reaktionen von halogenhaltigen Oxidantien untersucht. Letztere Spezies sind von Interesse bei der Freisetzung von Halogenverbindungen aus maritimen Seesalzpartikeln, der so genannten Halogenaktivierung.

In der analytischen Messtechnik werden in Laborexperimenten Verfahren zur besseren chemischen Charakterisierung der organischen Bestandteile von Aerosolpartikeln entwickelt und getestet. Diese Techniken beruhen zumeist auf massenspektrometrischen Verfahren, die in ver-

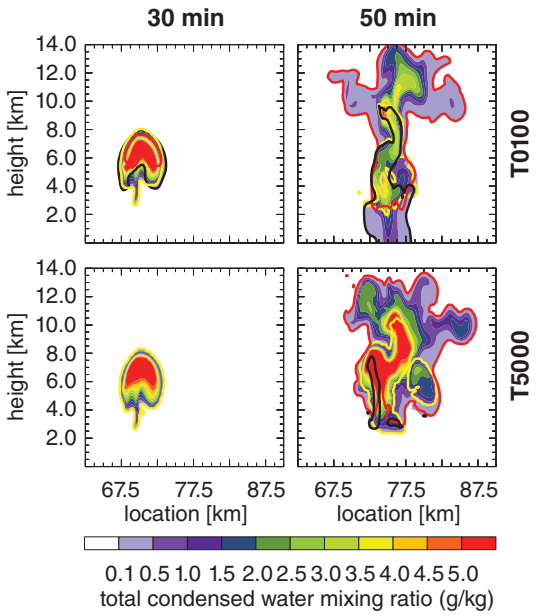

Fig. / Abb. 15: *Modelled convective cloud in clean (T0100) and polluted atmosphere (T5000) after 30 and 50 min. Contours: mixing ratio of 0.1 g/kg for cloud water (yellow), rain water (black) and cloud ice (red). / Modellierte konvektive Wolke in sauberer (T0100) und verschmutzter Atmosphäre (T5000). Konturen: 0.1 g/kg Mischungsverhältnis für Wolkenwasser (gelb), Regen (schwarz) und Wolkeneis (rot).*

experiments, because of their importance for processes in haze particles, fog and cloud droplets as well as in deliquescent aerosol particles. For the understanding of the oxidation of organic trace gases in the tropospheric multi-phase system, a large number of reactions with the OH and NO_3 radicals are being studied as well as reactions of halogenated oxidants. The latter species are of interest for the emission of reactive halogen compounds from sea salt particles.

Several laboratory experiments are dedicated to the chemical characterization of atmospheric organic aerosol components. Besides the conventional combustion techniques, mass spectroscopic and chromatographic techniques coupled directly to analysis by mass spectrometry or capillary electrophoresis with different sampling and segregation techniques are being developed.

Modeling

For the description of complex atmospheric processes, model systems of varying dimensions and complexity for micro- and mesoscale problems are developed, tested and applied using data of field experiments and satellite measurements.

One focal point of research is the description of cycle, interaction and phase transfer between aerosol particles, gases and clouds. This results in an improvement of understanding of the tropospheric multiphase processes.

schiedenen Kopplungstechniken eingesetzt werden. Im Bereich der Probenahmetechniken gibt es auch hier eine enge Kooperation mit der Abteilung Physik zur Entwicklung einer gezielten Abscheidung von Partikeln bestimmter Größe und deren chemischer Analyse.

Modellierung

Zur Beschreibung der komplexen atmosphärischen Vorgänge werden Modellsysteme verschiedener Dimension und Komplexität für die Mikro- bis Mesoskala entwickelt, überprüft und angewendet auch in Kombination mit Daten aus Feldmessungen und aus satellitengestützten Fernerkundungen.

Ein Forschungsschwerpunkt ist, die Kreisläufe, Wechselwirkungen und Phasenübergänge zwischen Aerosolpartikeln, Gasen und Wolken zu beschreiben, um so zu einer Verbesserung des Systemverständnisses troposphärischer Mehrphasensysteme zu gelangen.

Zentrales „Werkzeug“ ist das am IfT entwickelte vollprognosefähige 3D-Modellsystem **COSMO-MUSCAT**. Seine Brauchbarkeit zur Simulation des Ausbreitungsverhaltens von Photooxidantien und Partikeln auf regionaler Skala wurde in mehreren internationalen Modellvergleichen und bei der Bearbeitung von Fragen zur Luftqualität im legislativen Bereich bewiesen. In mehreren Projekten wird die Dynamik primärer und sekundärer Aerosolpartikel simuliert und deren Rückkopplungseffekte auf die Strahlung untersucht. Für weitere Anwendungsmöglichkeiten wird zusätzlich eine „urbanisierte“ Version von COSMO-MUSCAT entwickelt, die eine

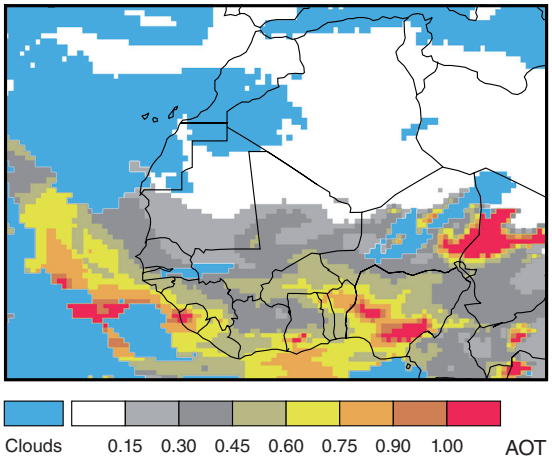

Fig. / Abb. 16: *Horizontal distribution of Saharan dust and biomass burning aerosol in terms of model-derived aerosol optical thickness (550 nm) on 31 January 2008 at 12:00 UTC. / Horizontale Verteilung des Saharastaubs sowie der Aerosolpartikel aus der Biomassenverbrennung am 31. Januar 2008, 12:00 UTC. Dargestellt ist die modellierte optische Dicke von Staub und Biomassenverbrennugsaerosol bei 550 nm Wellenlänge.*

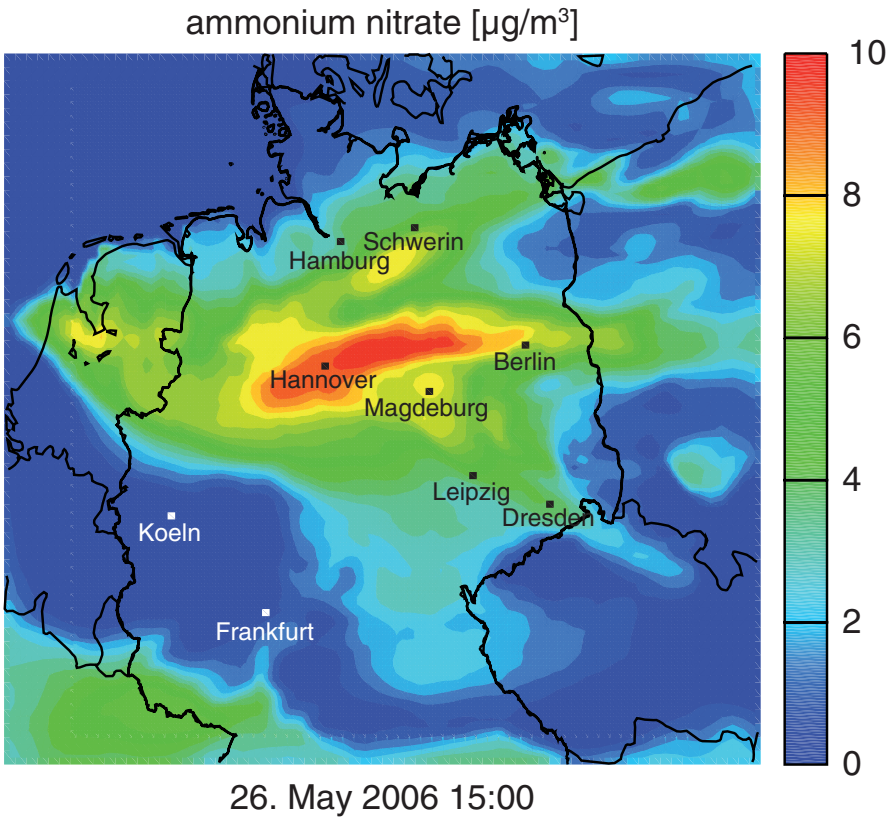

Fig. / Abb. 17: *Ammonium nitrate concentration over Germany simulated with the chemistry transport model COSMO-MUSCAT. / Mit dem Chemie-Transport Modell COSMO-MUSCAT simulierte Ammoniumnitrat-Konzentation über Deutschland.*

Main tool is the forecastable three-dimensional modeling system **COSMO-MUSCAT**, developed at the IfT and used for simulation of transport of photo oxidants and particles in a mesoscale region.

The model system was tested with success in many international model intercomparisons and was applied as a toolbox for legal tasks on the field of air quality. In many projects the dynamic of primary and secondary particles was simulated and their feedback on the radiative budget was investigated. For further investigations an “urbanized” version of COSMO-MUSCAT will be developed with a horizontal resolution up to 180x180m. In order to estimate the influence of future climate change on the budget of trace elements.

The model **ASAM** (**A**ll **S**cale **A**tmospheric **M**odel) indicates future developments, applicable from the micro to the global scale. It realized cut cells in a Cartesian grid for the description of orography and obstacles. It is currently mainly used for simulations of transport of particles in the microscale domain (urban canyons and urban districts).

One- and two-dimensional models are developed for process modeling. **SPECS** (**SPEC**tral bin cloud microphysic**S**) can be used for the investigation of cloud processes with a detailed description of condensation, collision or freezing. **SPACCIM** (**SP**ectral **A**erosol **C**loud **C**hemistry **I**nteraction

horizontale Auflösung bis hinab zu 180x180 m gestattet. Damit werden auch Untersuchungen zum Einfluss der regionalen Klimavarabilität auf Spurenstoffhaushalte durchgeführt.

Mit **ASAM** (**A**ll **S**cale **A**tmospheric **M**odel) steht ein zukunftsweisendes, noch in der Weiterentwicklung befindliches Modell zur Verfügung, dessen dynamischer Kern für Anwendungen vom mikroskaligen bis zum globalen Maßstab eingesetzt werden kann und das in einem kartesischen Gitter mit angeschnittenen Zellen für die Darstellung von Orographie und Hindernissen realisiert wurde. Es wird gegenwärtig vor allem zur Simulation der Ausbreitung von Partikeln im mikroskaligen Bereich (Straßenschluchten, Stadtquartiere) genutzt.

Daneben wurden und werden ein- und zweidimensionale Prozess-Modelle entwickelt bzw. weiterentwickelt. SPECS (SPECtral bin cloud microphysicS) dient zur Beschreibung von Wolkenprozessen. Es erlaubt eine explizite und sehr genaue Berechnung der Prozesse Kondensation, Kollision oder Gefrieren. SPACCIM (SPectral Aerosol Cloud Chemistry Interaction Model) ist ein Parcel Model zur gekoppelten größenaufgelösten Beschreibung von Mikrophysik und Mehrphasenchemie. Beide Module können sowohl in einer Box zur Prozess-Modellierung als auch gekoppelt an das mesoskalige COSMO-Modell zur Untersu-

Model**)** is a parcel model, which combines detailed microphysics with a complex multiphase chemistry.

Both modules can be applied to for process modeling in an one-dimensional box as well as coupled with the mesoscale model COSMO for the investigation of real situations. The process modeling will be realized in connection with experiments at LACIS (**L**eipzig **A**erosol **C**loud **S**imulator).

The model simulation of tropospheric multiphase systems is numerically highly demanding. The models need to be sufficiently accurate and numerically efficient to be used productively on existing computer systems. To this end the modeling department conducts an ongoing development.

chung von realen Situationen verwendet werden. Die Prozessmodellierungen werden auch im Zusammenhang mit den Experimenten am Wolkenkanal LACIS durchgeführt.

Die modelltechnische Behandlung eines so umfassenden atmosphärischen Systems ist numerisch sehr aufwendig. Die zu entwickelnden Modelle müssen hinreichend genau sein und numerisch sehr effizient den jeweils zur Verfügung stehenden Rechnerarchitekturen angepasst werden. Zur Optimierung der verwendeten numerischen Verfahren und Parallelisierungsstrategien liefert die Abteilung Modellierung ebenfalls wesentliche Beiträge.

Overview of the individual contributions

The work at the institute is structured into three major research themes:

1. *Evolution, transport and spatiotemporal distribution of the tropospheric aerosol*
2. *Effect of tropospheric aerosol on clouds and on the radiation budget*
3. *Chemical processes in tropospheric multiphase systems*

The goal of the corresponding studies is to explore significant processes in the troposphere and to improve their forecast skills by means of detailed process studies.

The work in the departments "Physics" and "Atmospheric Modeling" are aiming in about equal parts mostly at the first two research topics whereas the "Chemistry" department naturally mostly covers topic 3. On top of that a number of comprehensive studies exist in all departments and for all research topics. The present annual reports introduces the work at the IfT in the time period 2008 – 2009 by means of four extended and 15 short contributions.

The participation in the construction and operational use of two observatories on the Cape Verde Islands marks a further mile stone in the long-term work of the Physics and Chemistry department on Saharan dust, and contributes to the previous and continuing research within the DFG research group SAMUM and the EU-projects SOPRAN and TENATSO. **Müller et al.** report on the newly built research stations CVAO and CVOO and the IfT-contributions with respect to physico-chemical studies of atmospheric chemical processes under marine tropical conditions, which includes the upload of Saharan dust or the emission of organic aerosol components from the ocean.

Mineral dust particles like those from the Sahara are not transported passively by the troposphere but undergo a number of physical and chemical processes, which may have a considerable effect on their nucleation behaviour, i.e. on their ability to form hydrometeors. By means of laboratory studies and accompanying modeling **Niedermeier et al.** investigate the effect of different mineral dust particle films on the temperature depending ability of these particles to act as ice nuclei. The comparison with numerical simulations based on the classical nucleation theory provided a new parameterization of the immersion freezing of coated mineral particles.

The interplay between experiment, theory and modeling generally plays a decisive role in the process studies at the IfT. In a fundamental theoretical study **Hellmuth et al.** describe the previously only experimentally known hysteresis-effect during growth- and shrink-processes of

Übersicht der Einzelbeiträge

Die Arbeiten des Instituts sind in drei übergeordnete Forschungsthemen gegliedert:

1. *Evolution, Transport und raumzeitliche Verteilung des troposphärischen Aerosols*
2. *Einfluss des troposphärischen Aerosols auf Wolken und Strahlungshaushalt*
3. *Chemische Prozesse in troposphärischen Mehrphasenwolken*

Das Ziel der damit verbundenen Arbeiten ist es, signifikante Prozesse in der Troposphäre zu erkunden und durch detaillierte Prozess-Studien die Vorhersage troposphärischer Mehrphasensysteme zu verbessern.

Die Arbeiten der Abteilungen „Physik" und „Atmosphärische Modellierung" zielen zu etwa gleichen Teilen zumeist auf die ersten beiden Forschungsthemen ab, während die Abteilung „Chemie" naturgemäß hauptsächlich Thema 3 abdeckt. Darüber hinaus gibt es eine Vielzahl abteilungsübergreifender Arbeiten in allen Abteilungen und zu allen Themenbereichen. Der vorliegende Jahresbericht stellt in vier längeren und 15 Kurzbeiträgen einige ausgewählte Arbeiten des IfT im Zeitraum 2008 bis 2009 dar.

Die mehrjährigen Arbeiten zur Physik und Chemie des Saharastaubes passieren mit der Beteiligung am Aufbau und Betrieb zweier Observatorien auf den Kapverdischen Inseln einen weiteren Meilenstein und ergänzen die bisherigen und andauernden Forschungen der DFG-Forschergruppe SAMUM sowie der EU-Projekte SOPRAN und TENATSO. **Müller et al.** berichten über die neu geschaffenen Forschungsstationen CVAO und CVOO und über die IfT-Beiträge zu physiko-chemischen Untersuchungen der atmosphärenchemischen Prozesse unter maritimen tropischen Bedingungen. Hierzu gehört z. B. der Eintrag von Saharastaub oder die Emission organischer Aerosolkomponenten aus dem Ozean.

Mineralstaubpartikel wie etwa aus der Sahara werden in der Troposphäre nicht passiv transportiert, sondern durchlaufen eine Reihe von physikalischen und chemischen Prozessen, die einen erheblichen Einfluss auf deren Nukleationsverhalten, also auf die Bildung von Hydrometeoren haben können. Mittels Laborstudien und begleitender Modellierung untersuchen **Niedermeier et al.** den Einfluss verschiedener Mineralstaub-Beschichtungen auf die temperaturabhängige Eiskeimfähigkeit dieser Partikel. Aus dem Vergleich mit numerischen Simulationen auf der Basis der klassischen Nukleationstheorie konnte eine neue Parametrisierung des Immersionsgefrierverhaltens beschichteter Mineralstaubpartikel gewonnen werden.

hydroscopic particles. Thus, the situation that the growth rate of hydrometeors not only depends on the thermodynamic properties of their environment but also on their previous history can be accounted for in future numerical cloud resolving models for the first time.

Due to the heterogeneous conditions for emission, reaction and deposition the tropospheric aerosol is characterized by a strong spatial and temporal variability. Therefore, monitoring of aerosol is highly demanding in terms of logistics and measurement techniques. Since the end of 2008 IfT is coordinating the operation of the German Ultrafine Aerosol Network (GUAN). **Birmili et al.** introduce this unique network of ground-based in-situ observations as well as several applications ranging from health aspects to model validation to the impact of aerosol on climate.

The gas-to-particle conversions as well as the mostly complex organic chemical reactions within aerosol and cloud particles and their effect on activation and growth processes resemble general questions in our understanding of the aerosol and cloud evolution. With the application of new state-of-the-art particle counters **Bernd et al.** prove the existence of homogeneous nucleation of smallest H_2SO_4 particles with diameter as small as 1.5 nm. The authors also provide a parameterization of nucleation rates for application in atmospheric models. Based on experiments in the Leipzig aerosol chamber (LEAK) **Böge et al.** experimentally investigate the genesis and development of compounds that partition into the particle phase as well as their effect on the genesis of secondary organic aerosol. **Weller and Herrmann** measure photochemical reactions of iron complexes in water and their influence on the production of radicals and the redox cycle of the element iron, the latter being a continuous part in the atmosphere due to emissions of mineral dust. The reaction speeds of organic compounds in cloud droplets are determined by **Schäfer et al.** by means of a laser-photolysis long-distance absorption device. The herby earned data on the kinetic and product distribution are put into the Chemical Aqueous Phase Radical Mechanism (CAPRAM) of the IfT.

The experimentally based investigations of the burdened troposphere in highly relevant regions like in China, the Amazon, but also at local emission spots plays a central role in field studies performed by the IfT. **Henning et al.** report first results of the physical and chemical aerosol characterizations in the North East of China, which have been carried out in the framework of the DFG project “Hace in China” (HaCi). **Baars et al.** show results of aerosol profiling in the Amazon rain forest that have been performed with the automatic multiple-wavelength Raman lidar PollyXT. The characteristics of aerosols from the increasingly burning of wood for

Das Wechselspiel zwischen Experiment, Theorie und Modellierung spielt generell eine entscheidende Rolle in den Prozessstudien am IfT. In einer grundlegenden theoretischen Arbeit beschreiben **Hellmuth et al.** den bislang nur experimentell nachgewiesenen Hysterese-Effekt während des Wachstums- und Schrumpfungsprozesses hygroskopischer Partikel. Damit kann in Zukunft der Umstand, dass die Wachstumseigenschaften von Hydrometeoren nicht allein von deren thermodynamischen Umgebungsbedingungen, sondern auch vom früheren Verlauf des Wachstumsprozesses abhängen, erstmalig in wolkenauflösenden Modellen berücksichtigt werden.

Bedingt durch heterogene Emissions-, Reaktions- und Depositionseigenschaften zeichnet sich das troposphärische Aerosol durch eine hohe räumliche und zeitliche Variabilität aus. Deren Erfassung ist eine Herausforderung an Logistik und Messtechnik. Seit Ende 2008 koordiniert das IfT den Betrieb des Deutschen Beobachtungsnetzes für Ultrafeine Aerosolpartikel (GUAN – German Ultrafine Aerosol Network). **Birmili et al.** stellen dieses einzigartige Netz bodengestützter In-situ-Beobachtungen und deren Anwendungen vor. Letztere reichen von Gesundheitsaspekten über Modellvalidierung bis zur Klimawirksamkeit des Aerosols.

Die Partikelneubildung aus der Gasphase sowie die größtenteils komplexen organisch-chemischen Reaktionen in den Aerosol- und Wolkenpartikeln und deren Einfluss auf Aktivierungs- und Wachstumsprozesse stellen grundlegende Probleme in der Aerosol- und Wolkenentstehung dar. Durch den Einsatz neuartiger Partikelzähler weisen **Berndt et al.** die homogene Kondensation kleinster H_2S0_4-Partikel bis zu einem Durchmesser von 1.5 nm nach und stellen eine Parametrisierung der Nukleationsraten zur Anwendung in der Atmosphärenmodellierung vor. **Böge et al.** untersuchen mit Experimenten in der Leipziger Aerosolkammer (LEAK) die Bildung und Entwicklung partikulär gebundener organischer Verbindungen und deren Einfluss auf die Entstehung sekundärer organischer Aerosole. **Weller und Herrmann** messen photochemische Reaktionen organischer Eisenkomplexe in wässrigen Partikeln und deren Einfluss auf die Produktion von Radikalen und den Redoxkreislauf des Elementes Eisen. Letzteres ist aufgrund von Mineralstaubeinträgen ein steter Bestandteil der Atmosphäre. Die Reaktionsgeschwindigkeiten organischer Verbindungen in Wolkentropfen bestimmen **Schäfer et al.** mit der Laser-Photolyse-Langwegsabsorptionsapparatur. Die so gewonnenen Daten zur Kinetik und Produktverteilung gehen in das Multiphasen-Reaktionsschema CAPRAM (Chemical Aqueous Phase Radical Mechanism) des IfT ein.

Die experimentelle Erfassung der belasteten Troposphäre in hochrelevanten Regionen wie etwa

heating purposes are described by **Poulain et al.** in the framework of an aerosol campaign in Saxony in winter 2007/2008.

Besides local sources the transport of aerosol is required for our understanding of the global aerosol distribution. From lidar observations in Leipzig **Mattis et al.** find volcanic aerosol above the tropopause which were found to origin from volcanic eruptions in the Aleutians, Kurils, Alaska and Kamchatka. In the framework of the intensive measurement campaign IMPACT IfT investigates nearly all micro-/physical properties relevant for cloud processes with the help of the helicopter-based measurement platform ACTOS. **Wehner et al.** manage to explore boundary layer regions with increased concentration of ultrafine particles that are probably originated from turbulence-induced local supersaturation of precursor gases. **Siebert et al.** discover local supersaturations with respect to water vapour which are also induced by turbulences and which have an equally large effect on the droplet activation than the chemical and physical properties of the aerosol itself. The overall topic of cloud processes under turbulent environmental conditions will play a central role in future cloud microphysical studies.

The modeling activities integrate the results from various field- and laboratory studies and enable a more complete view on spatial pattern and most of all on dynamical tropospheric processes. The regional meteorological model COSMO, coupled with the chemistry module MUSCAT provides the basis of various model activities. **Tegen et al.** determine the influence of observed spectral surface reflectivities on the radiative forcing of modelled Saharan dust fields. Locally they find a larger effect due to the choice of surface types than due to the choice of the optical properties of the dust clouds themselves. **Schepanski et al.** develop a new dust source map from satellite data from Meteosat Second Generation. They find an enhanced dust mobilization in the morning hours, which they can explain by the dynamics of the boundary layer jet stream. Another fruitful alliance between surface measurements, satellite observations and regional modeling is introduced in the work by **Meier et al**., who apply ground- and satellite based lidar measurements to initiate and validate the modeling of aerosol transport. **Hinneberg and Wolke** utilize COSMO-MUSCAT to calculate potential emission scenarios of particulate matter. **Horn and Knoth** make use of the technical development of modern graphic boards to efficiently realize the calculations of the dynamics of complex three-dimensional Cumulus cloud fields in real time.

in China, dem Amazonas, aber auch an regionalen Emissionsorten spielt eine zentrale Rolle in den Feldstudien des IfT. **Henning et al.** berichten über erste Ergebnisse der physiko-chemischen Aerosolerfassung im Nordosten Chinas, die im Rahmen des DFG-Projektes „Hace in China“ (HaChi) durchgeführt werden. **Baars et al.** stellen Ergebnisse zur Aerosolprofilierung im Amazonas-Regenwald mit den am IfT entwickelten automatischen Mehrwellenlängen-Raman-Lidars PollyXT vor. Die Charakteristika des Aerosols aus der zunehmenden Holzverbrennung zu Heizzwecken beschreiben **Poulain et al.** anhand einer Aerosolkampagne im Winter 2007/2008 in Sachsen. Neben den lokalen Quellen ist der Transport des Aerosols zum Verständnis der globalen Aerosolverteilung entscheidend. **Mattis et al.** erkennen in Lidarmessungen in Leipzig vulkanisches Aerosol oberhalb der Tropopause, deren Ursprünge auf Vulkanausbrüche auf den Aleuten und Kurilen sowie in Alaska und Kamtschatka zurückzuführen sind.

Im Rahmen der Intensiv-Kampagne IMAPCT untersucht das IfT mit Hilfe der hubschraubergetragenen Messplattform ACTOS nahezu alle zur Wolkenbildung relevanten mikro-/physikalischen Größen. **Wehner et al.** gelingt der Nachweis von Grenzschichtbereichen erhöhter Konzentration ultrafeiner Partikel, die vermutlich aus der turbulenzinduzierten lokalen Übersättigung von Vorläufergasen entstanden ist. **Siebert et al.** entdecken lokale Wasserdampfübersättigungen, die ebenfalls turbulenzbedingt sind und die einen ebenso hohen Einfluss auf die Tröpfchenaktivierung haben können, wie die chemischen und physikalischen Eigenschaften des Aerosols selbst. Insgesamt wird das Thema der Wolkenbildung unter turbulenten Umgebungsbedingungen in Zukunft eine zentrale Rolle in den wolkenmikrophysikalischen Arbeiten einnehmen.

Die Arbeiten im Bereich der Modellierung integrieren die Ergebnisse der unterschiedlichen Feld- und Laborstudien und ermöglichen eine räumlich vollständigere und vor allem eine dynamische Sicht troposphärischer Prozesse. Das regionale meteorologische Modell COSMO, gekoppelt mit dem Chemie-Modul MUSCAT, stellt dabei die Grundlage vieler Modellierungsaktivitäten dar. **Tegen et al.** bestimmen den Einfluss gemessener spektraler Bodenalbeden auf den Strahlungsantrieb modellierter Saharastaubfelder und finden lokal einen größeren Effekt durch die Wahl der Bodenalbedo als durch die Wahl der optischen Eigenschaften der Staubwolken selbst. **Schepanski et al.** entwickeln eine neue Staubquellenkarte aus den Satellitendaten des Meteosat Second Generation und finden eine erhöhte Staubmobilisierung in den Morgenstunden, die sie mit der Dynamik des Grenzschichtstrahlstroms erklären können. Eine weitere fruchtbare Verknüpfung zwischen Boden-

Fig. / Abb. 18: *Planned Extension Building. / Geplanter Erweiterungsbau.*

messungen, Satellitenbeobachtung und regionaler Modellierung wird in der Arbeit von **Meier et al.** vorgestellt, die Lidarmessungen vom Boden und aus dem Weltraum zur Initialisierung und Validierung des Aerosoltransports im Modell nutzt. **Hinneburg und Wolke** verwenden COSMO-MUSCAT zur Berechnung von möglichen Feinstaub-Emissionsszenarien. **Horn und Knoth** nutzen die technische Entwicklung moderner Grafikkarten zur effizienten numerischen Umsetzung von Large-Eddy-Simulationen, die unter anderem die Berechnung der dynamischen Entwicklung komplexer dreidimensionaler Cumulus-Wolkenfelder in Echtzeit ermöglichen.

Articles

CVAO and CVOO – two new research sites with IfT contributions at Cape Verde

Konrad Müller, Wadinga Fomba, Sandra Lehmann, Conny Müller, Bernd Heinold, Ina Tegen, Nicole Niedermeier, Thomas Müller, Thomas Gnauk, Dominik van Pinxteren, Alfred Wiedensohler, Hartmut Herrmann

Die neu geschaffenen Forschungsstationen CVAO und CVOO auf der Kapverdeninsel São Vicente stellen eine neue Stufe in der Zusammenarbeit zwischen ozeanischer und Atmosphärenforschung dar. Das BMBF, die Leibniz-Gesellschaft und die EU stellen dafür erhebliche Mittel bereit, um Infrastruktur zu schaffen und Forschungen zu ermöglichen. Hier werden von internationalen Forscherteams Langzeituntersuchungen der Atmosphäre und des Ozeans durchgeführt. Das IfT beteiligt sich mit physiko-chemischen Aerosoluntersuchungen, die atmosphärenchemische Prozesse und den Eintrag von Saharastaub erforschen sowie die Emission organischer Aerosolkomponenten aus dem tropischen Nordatlantik zu Thema haben. Die Chemie der Halogenverbindungen über dem tropischen Nordatlantik, die Identifizierung von Eisenspezies im Aerosol sowie der Eintrag organischer Spurenstoffe aus dem Ozean in die Atmosphäre sind dabei Schwerpunkte. Alle experimentellen Daten werden zur Modellverifizierung genutzt. Die wissenschaftliche Zusammenarbeit mit dem INDP und dem INMG unterstützt auch kapverdische Forschungsaktivitäten. Erste Ergebnisse der Forschungen sind hier in Auszügen zusammengestellt.

Introduction

Atmospheric chemistry and physics in the marine boundary layer (mbl) in the tropics has received increased attention in the last years. Marine aerosol composition continues to represent a large source of uncertainty in the study of climate and atmospheric chemistry. Chemical processes were induced by the emission of Cl^- and Br^- species from sea salt. Halogen chemistry is one topic of recent research in the mbl von [*Glasow et al.* 2002 a, b; *Sander et al.*, 2003]. Interactions between halogen compounds, sulfur species, hydrocarbons and other organic matter from the ocean can contribute to formation of particulate matter. The position of the Cape Verde archipelago allows investigations in the mbl with only small influences of anthropogenic activities. The influence of Saharan dust on the chemical processes in the atmosphere and the ocean, as well as the interaction between these two compartments is a further important research goal. A detailed chemical and physical characterization of the dust particles is necessary. The Sahara desert is well known as the world largest natural source of atmospheric dust [*Heintzenberg,* 2009]. The dust emission and the atmospheric transport of dust are important sources of the iron nutrient for the subtropical and tropical North Atlantic Ocean and also for the Amazon basin [*Martin,* 1990]. In turn, oceanic emissions influence atmospheric properties, e. g. cloud formation [*Charlson et al,* 1987; *Kettle and Andreae,* 2000]. SAMUM experiments (http://samum.tropos.de) have brought new knowledge from the source region as well as from the Cape Verde islands.

The interaction between the atmosphere and the surface layer of the ocean is an object of research for a while now. To better study the influence of dust on the ocean and the ocean's influence on the atmosphere, the construction of the atmospheric observatory (CVAO) and the oceanic observatory (CVOO) at the Cape Verde Island São Vicente started in 2006. UK SOLAS, the German ministry for education and research (BMBF), the Leibniz-Institutes IfM-GEOMAR (Kiel) and IfT (Leipzig), the EU funded project TENATSO as well as the German Max-Planck-Society are the major founders of this research activity in close collaboration with the Cape Verde Instituto Nacional de Meteorologia e Geofísica (INMG) and the Instituto Nacional de Desenvolvimento das Pescas (INDP) in the northern tropical Atlantic Ocean (http://www.york.ac.uk/capeverde/).

CVAO links with the international program SOLAS, the EU-funded TENATSO (Tropical Eastern North Atlantic Time-Series Observatory) project, and with the German SOPRAN (Surface Ocean Processes in the Anthropocene) project of the German Ministry for Research and Education.

Fig. 1: *CVAO photo (T. Müller) with wind mill (left), 30m-tower, and research containers from December 2009.*

Contributions to the British RHaMBLe campaign (Reactive Halogens in the Marine Boundary Layer) in spring 2007 were the first important field activity with PM characterization at CVAO.

The CVAO exists to advance understanding of climatically-significant interactions between the atmosphere and ocean and to provide a regional focal point and long-term data context for field campaigns. Measurements of O_3, CO, NO, NO_2, NO_y, VOC began at the site in October 2006 and recent data can be found at the British Atmospheric Data Centre (BADC). Chemical characterization of aerosol measurements and flask sampling of greenhouse gases began in November 2006, halocarbon measurements in May 2007, physical aerosol characterization in May 2007, and on-line measurements of greenhouse gases in October 2008.

The implementation of the CVAO and CVOO

The Cape Verde Islands are a volcanic archipelago 700 km off the west coast of Africa. The CVAO on the north-eastern coast of the island São Vicente (16°51'50" N, 24°52'2" W, 10 m a. s. l.), 70 m from the coastline and the CVOO (investigation site: 17.4° N 24.5° W; 3600 m water depth, about 84 km in northern direction of São Vicente in the ocean, not influenced by the coastline; laboratory at the INDP) are parts of a bilateral German-UK initiative to undertake long-term ground- and ocean-based observations in the tropical Eastern North Atlantic Ocean region. Prevailing north-eastern trade winds heading from the Canary Islands and the North African continent are blowing directly off the ocean. On the coast, influences from the island itself like dispersed dust, orographic influences in dust sedimentation or anthropogenic emissions are negligible. The climate on São Vicente is arid with a maximum of 50 mm rainfall per year. Therefore, dominantly dry deposition of mineral dust is expected. The annual average temperature is about 25 °C.

Using the CVAO research site, the chemical and physical characterization of PM (particulate matter) near the surface will be carried out for several years to identify the transport of Saharan dust into the Atlantic Ocean, to investigate biogenic oceanic contributions to the aerosol and to support the model verification by long-term data from a region heavily influenced by Saharan dust deposition.

São Vicente is far from source regions and about 900 km in the main wind direction off the coast of West Africa (Mauretania and West Sahara). For the aerosol measurements, a 30 m high tower was built to reduce the strong influence of the sea spray on the samples (inlet height: 32 m).

A high volume Digitel filter sampler DHA-80 with PM10-inlet was installed on top of the 30 m high tower. Samples were collected on annealed 150 mm quartz fiber filters with an average flow rate of 500 l/min. For the size-resolved samples, a 5-stage-Berner impactor made of stainless steel was mounted in 31 m height too. It was operated with a flow rate of 75 l/min. As substrate material, annealed aluminum foils were used. Additional Nuclepore polycarbonate foils for the determination of metals were exposed on each stage (stage 1: 0.05 – 0.14 µm, stage 2: 0.14 – 0.42 µm, stage 3: 0.42 – 1.2 µm, stage 4: 1.2 – 3.5 µm, stage 5: 3.5 – 10 µm). A PM10 isokinetic inlet was mounted on the impactor. The inlet of the physical PM characterization was mounted at the same height at the tower. In the Ift-container a SMPS, an APS, a MAAP, and SOAP were operated. Outside the container, a visibility sensor was employed.

During intensive measurement campaigns, the aerosol was investigated in five size fractions with respect to the analysis of mass, concentration of ionic components, organic and elemental carbon (OC; EC), iron, and organic single compounds (MSA and dicarboxylic acids). Furthermore, hygroscopic particle growth factors for particles in the micrometer size range were measured. Such complex data sets were often requested [*e.g., Mahowald et al.,* 2005]. Only a few data actually exist from source regions but not from the main deposition region in the tropical North Atlantic. Exceptions are the work of [*Chiapello et al.* 1995], some ship cruises in this region and short time aerosol data [*e.g., Chen and Siefert,* 2004, *Rijkenberg et al.,* 2008].

For future modeling, long term experimental data of the total dust deposition and its size-resolved chemical composition are needed.

Aerosol Chemistry

Masses were determined by the use of micro-balances at the IfT in Leipzig. For chemical analyses the filters were divided into quarters. The size-segregated samples were divided by the number of particle spots, differing between size fractions (38 – 53 % for ion analysis, 25 – 40 % for OC/EC analysis, 7 – 10 % for metal analysis, and 8 – 28 % for organic single species analysis).

During the first two years, we have collected 31 samples with more than 90 µg/m³ PM, 22 in winter, four in spring and fall each, and one in summer. From the size segregated samples, it is known that OC and other non-sea-salt (nss) components were found mainly in the three fractions below 1 µm diameter and sea salt as well as Saharan dust particles were found in the three size fractions between 0.42 and 10 µm.

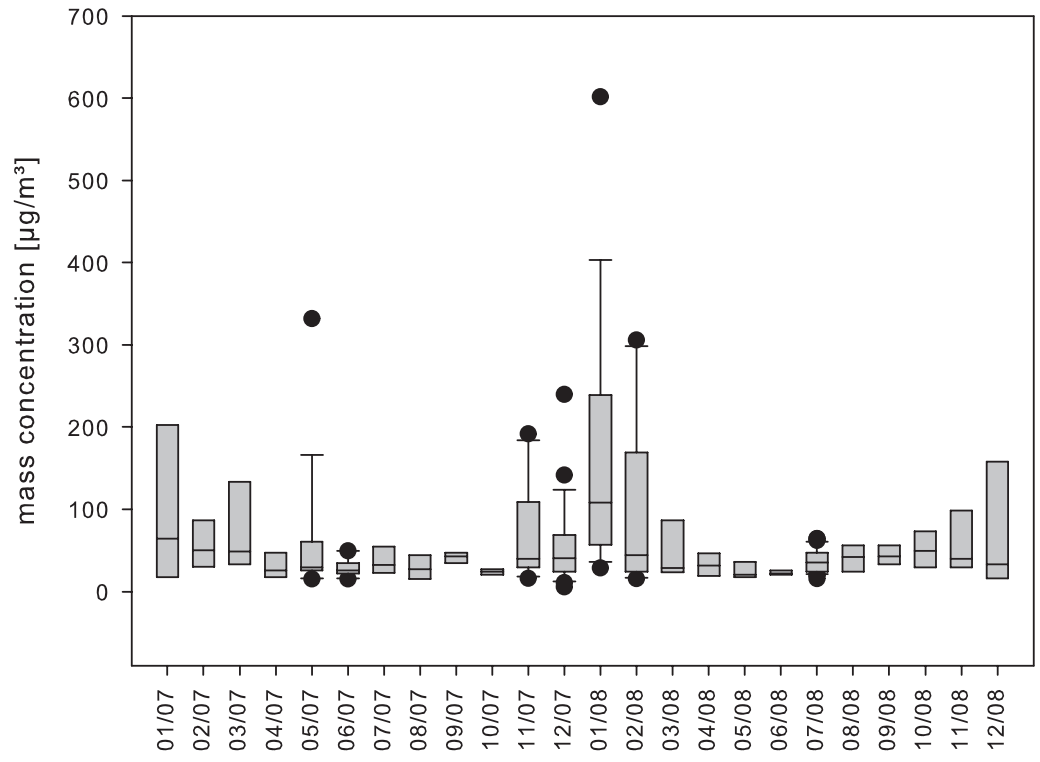

Fig. 2: *Monthly averages of aerosol mass concentration of the first two years of filter sampling (grey bars represent the 25/75 % range, dots represent extreme values).*

In contrast to the constitution of continental aerosol, an extremely low concentration of ultra fine particles (0.05 – 0.14 µm) was found in all samples. In the two smallest size fractions the mass concentrations were below 0.2 µg/m³ for 0.05 – 0.14 µm and up to 1.7 µg/m³ in the 0.14 – 0.42 µm fraction and consisted mostly of OC and nss-components. Low concentrations of elemental carbon from this PM long range transported were observed. Ammonium and nss-sulphate are the major ions. Besides sea salt nss-sulphate, nitrate, and ammonium were found. Traces of bromide, dicarboxylic acids (DCA) and methanesulfonic acid (MSA) were detected in nearly all samples, too. Between MSA and nss-sulphate, a good correlation was observed in spring 2007 *[Müller et al.,* 2009b] whereas dimethyl sulfide not correlates. Seasonal differences were found for MSA and malonate with factor of 2 higher concentrations during summer than in winter while for oxalate a factor of 1.5 was detected. Not only Saharan dust but also anthropogenically emitted or influenced PM was found during episodes with transport of continental aerosols to Cape Verde.

Metals and iron redox states characterization of Saharan dust

The investigation of various metals that may be relevant for the understanding and prediction of the dust input into the oceans and for the modeling of the various ocean and atmospheric interactions is important. Dust deposition provides mineral nutrients for oceanic microorganisms and terrestrial vegetation, therefore influencing the global carbon cycle and consumption of CO_2. Iron is one of the most important nutrients for marine biota. The Saharan Desert is a known source of iron into the oceans via dust deposition [*Buck et al,* 2008]. In SOPRAN, we characterize the metal content of the aerosol at the CVAO with emphasis on iron and its red-ox states.

During the transportation of dust, chemical transformations occur that can lead to a much greater solubility of iron than in the Saharan source regions [*Baker and Jickells,* 2006]. There is an ongoing scientific discussion about iron solubility from emitted and processed mineral dust. The solubility of anthropogenic and natural aerosol iron was determined in a wide range between 0.01 and 80 % [*Baker et al.* 2006; *Solmon et al.* 2009] and appears to be strongly dependent on acidity [*Mancinelli et al.,* 2005]. Furthermore, organic ligands, like oxalate in aerosols or siderophores in seawater, do enhance the solubility of iron significantly [*Kraemer,* 2004].

The total metal content of the aerosol is analyzed using Total Reflection X-Ray Fluorescence (TXRF, S2-PICOFOX, BRUKER) technique from impactor samples. The Saharan

	Size fraction µm	Ca µg/m³ (%)	K µg/m³ (%)	Fe µg/m³ (%)
High dust	0.05 – 0.14	0.004 (1.54)	0.001 (0.31)	0.002 (0.66)
	0.14 – 0.42	0.006 (0.30)	0.010 (0.51)	0.008 (0.39)
	0.42 – 1.2	0.080 (1.18)	0.025 (0.37)	0.035 (0.51)
	1.2 – 3.5	0.527 (2.01)	0.216 (0.82)	0.331 (1.26)
	3.5 – 10	0.388 (2.05)	0.225 (1.19)	0.305 (1.61)
Low dust	0.05 – 0.14	0.001 (0.67)	0.000 (0.00)	0.001 (0.32)
	0.14 – 0.42	0.002 (0.12)	0.003 (0.19)	0.002 (0.10)
	0.42 – 1.2	0.017 (1.04)	0.013 (0.80)	0.008 (0.50)
	1.2 – 3.5	0.056 (0.82)	0.031 (0.44)	0.017 (0.24)
	3.5 – 10	0.002 (0.04)	0.001 (0.02)	0.002 (0.04)

Tab. 1: *Content of calcium, potassium and iron in impactor samples for two main groups (high dust – low dust) of samples during May/June 2007. The percentage in brackets refers to the impactor stage mass.*

dust was found mainly in the three fractions between 0.42 and 10 µm with a maximum in the fraction 1.2 – 3.5 µm. The Table 1 shows the difference of metal concentrations for potassium, calcium and iron during dusty and non-dusty periods in spring 2007.

Iron is found in the atmosphere mostly in the Fe(III) oxidation state, but in the presence of UV radiation in aqueous media, Fe(III) is reduced to Fe(II) [*Chen and Siefert,* 2004; *Jickells et al.* 2005]. This process is also expected to occur when Saharan dust containing Fe(III) travels over long transportation paths, over the Atlantic Ocean to CVAO. Thus, it is expected that both Fe(III) and Fe(II) are deposited into the oceans. Fe(II) is the most soluble and hence most bioavailable form of iron, which is needed for marine biota. However, Fe(III) is more abundant than Fe(II), and Fe(II) concentration decreases with ocean depth [*Hansard et al.* 2009] leading to its scarcity in the ocean. Hence, investigating the amount of Fe(II) deposition will increase the understanding of the various rate limiting processes that affect the ocean vegetation.

The characterization of soluble iron redox states is done using ion chromatography and post-column derivatization, (ICS 900, DIONEX). The method for the characterization has recently been developed and implemented at IfT.

Aerosols samples were collected on quartz fiber filters and thereafter leached with DI water (pH 5.5) and the extracts analyzed. Figure 3 shows the total iron, soluble Fe(III) and Fe(II) concentrations obtained for two sampling periods. The results show that only about 20 % of the total iron was soluble, while the rest was found to be insoluble. This is not unusual for urban aerosols (Majestic et al. 2007). A clear picture of the Fe(II), Fe(III) ratio was not established which is not unexpected since the Fe(II) production depends on the exposure of the Fe(III) to UV radiation. Thus, lower Fe(II) concentrations are to be expected on less sunny days and vice versa. Similar measurements are being performed at the CVAO now.

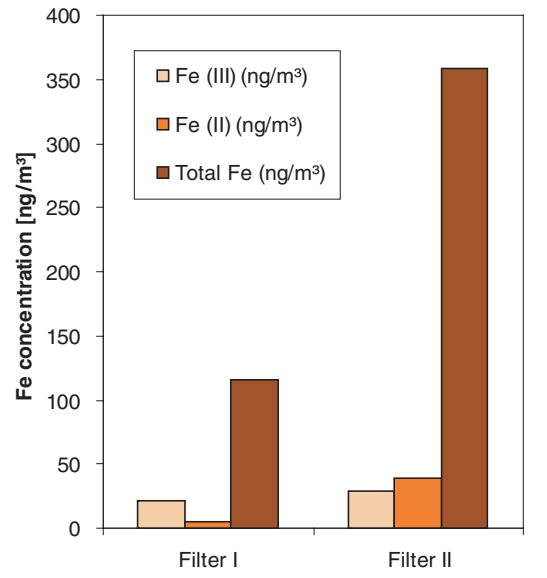

Fig. 3: *Total Fe, Fe(II), and Fe(III) from two different measuring periods during method development in Leipzig.*

Analysis of aliphatic amines in aerosols

In addition to the metal analysis, single organic compound analysis was performed to characterize the marine aerosol composition and its composition on the ocean atmosphere interaction. The chemical analysis revealed small highly volatile aliphatic amines (methylamine (MA), dimethylamine (DMA) and diethylamine (DEA)) that were concentrated in sub micrometer particles [*Müller et al.,* 2009a] (Fig. 4). Typically,

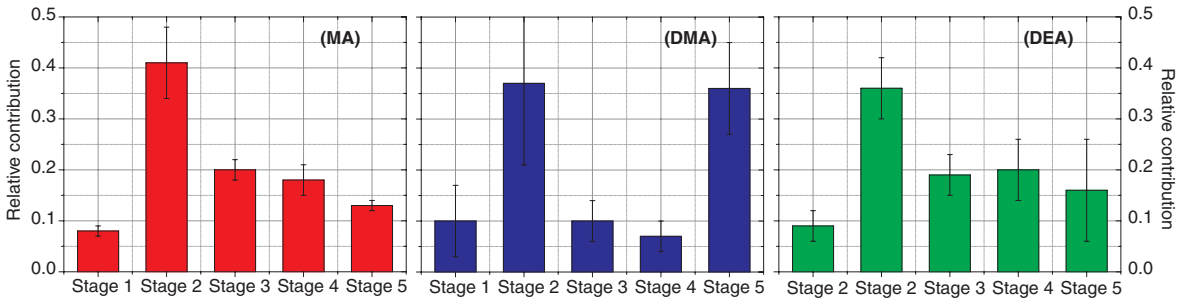

Fig. 4: *Relative contribution of methylamine (MA), dimethylamine (DMA) and diethylamine (DEA) to the five stage Berner impactor samples (50 % cut-off diameters – stage 1: 0.14 µm, stage 2: 0.42 µm, stage 3: 1.2 µm, stage 4: 3.5 µm, stage 5: 10 µm) with air masses originating from the open North Atlantic Ocean.*

marine aerosols in sub micrometer size ranges are formed by the gas to particle conversion process of the gas-phase sulfuric acid and ammonia [*Kulmala,* 2003]. In addition, it is known that the gas-phase amines react rapidly with sulfuric acid, leading to secondary aerosol. For this reason, it has been suggested that the detected aliphatic amines are present in the particle phase as organic sulfate salts [*Facchini et al.,* 2008a; *Müller et al.,* 2009a]. The importance of the low molecular weight aliphatic amines in the marine aerosol is unknown at this point. However, it is known that small changes in the chemical composition of marine aerosol can have large influence on the physicochemical character of the particles.

The detected amines contribute non negligible amounts to the organic carbon (OC) content in small particles (0.42 µm), ranging up to 2.5 %C in the winter months. In addition, aliphatic amines add up to 1.5 %N to the nitrogen content (sum parameter of ammonium, nitrate and amines) in sub micrometer particles [*Müller et al.,* 2009a]. This suggests that the detected amines may play a non negligible role in the nitrogen cycle as well as in the carbon cycle in the remote marine environment.

A comparison between satellite chlorophyll-a (Chl-a) data and the aliphatic amine concentration shows the connection between the marine bio productivity and the detected amine concentrations at the Cape Verde islands. In Fig. 5 the seasonal variation of the aliphatic amines is shown. In the spring 2007 and the winter 2007/2008 the measured aliphatic amine concentrations were higher than the rest of the measurement periods. The comparison with the calculated monthly Chl a (MODIS satellite data, Giovanni, NASA) values shows high amine

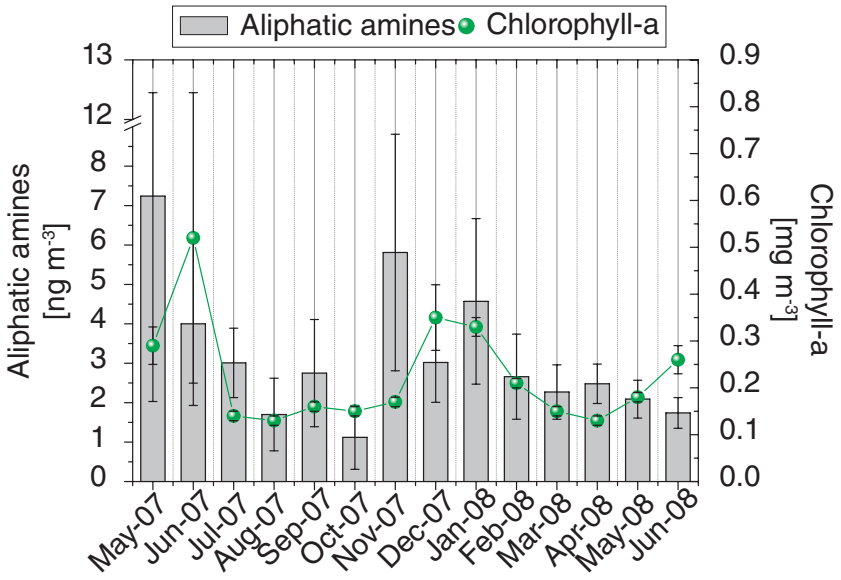

Fig.5: *Monthly averages and standard deviation of aliphatic amine concentrations (grey bars, sum of methylamine, dimethylamin and diethylamine) detected in quartz fiber filters from high volume samplers and the MODIS ocean color base time series of average Chl a concentrations (green filled circles, error bars indicating 1/10 of the variability).*

concentrations during high biological activity periods. Similar observations were performed by [*Facchini et al.* 2008a] for the Mace Head region.

Interestingly, high amine values were observed simultaneously to the winter algal bloom in the region. The marine bio productivity is expected to be high in spring and low in the wintertime though it is likely that there is a process that supports wintertime algal bloom in the region. The main influencing parameter of the marine biomass production is the available nutrient content. Two mechanisms exist in the Cape Verde region that can increase the nutrient content in the surface water during the wintertime. One is the upwelling process and the other one is the dust deposition process. The measured ocean temperature depth profile during the winter algal bloom shows a mixed layer deepening which indicates upwelling of cooler nutrient rich deep sea water. Additionally, dust deposition was measured in the winter time at the CVAO. It is likely that the anomalous algal bloom in the winter 2007/2008 was related to both the process, entrainment of nutrient into the oceanic mixed layer as well as dust deposition from the atmosphere.

Physical aerosol characterization and determination of deposition flux

Instruments for physical aerosol characterization are housed in an air conditioned container. The aerosol inlet consists of a PM10 inlet at top of the tower and a 30 m stainless steel pipe for transporting the aerosol into the container. In the container, the aerosol is dried to relative humidities below 40 %. Instruments for physical aerosol characterization are downstream of the dryer. Particle number size distributions (PNSD) were measured with a Scanning Mobility Particle Sizer (SMPS; after [*Wang and Flagan,* 1989]) in the size range from 10 nm to 800 nm and with an Aerodynamic Particle Sizer (APS; TSI 3320, TSI Inc., St. Paul Minnesota, USA) in the size range from 700 nm to 10 µm. With a dust particle density of 2.4 g/cm³ the total mass concentration was determined. A comparison with gravimetrically measured mass concentrations of samples of a five stage Berner impactor showed a good agreement (Fig. 6). Number fractions of salt and dust were measured using a H-DMA-APS (Leinert and Wiedensohler, 2008) at aerodynamic diameters of 600, 800 and 1000 nm. Combining the dust number fraction, the particle number size distribution, and the dust particle density a dust mass size distribution and dust mass concentration are derived.

Another method to measure dust mass concentrations was the optical absorption spectroscopy. A Spectral Optical Absorption Photometer (SOAP) measured the particle absorption coefficient in the wavelength range from 300 to 800 nm. Reference absorption spectra and mass absorption coefficients for mineral dust were measured during the SAMUM-1 campaign in the Saharan desert in Morocco [*Müller et al. 2009c, Schladitz et al* 2009]. Comparing measured absorption spectra with reference spectra yields the dust mass concentration. This method is sensitive the main absorbers of the particulates, which in case of mineral dust are iron oxide. The method implies that the iron concentrations for sample and reference measurements are the same. A comparison of dust mass concentrations measured with

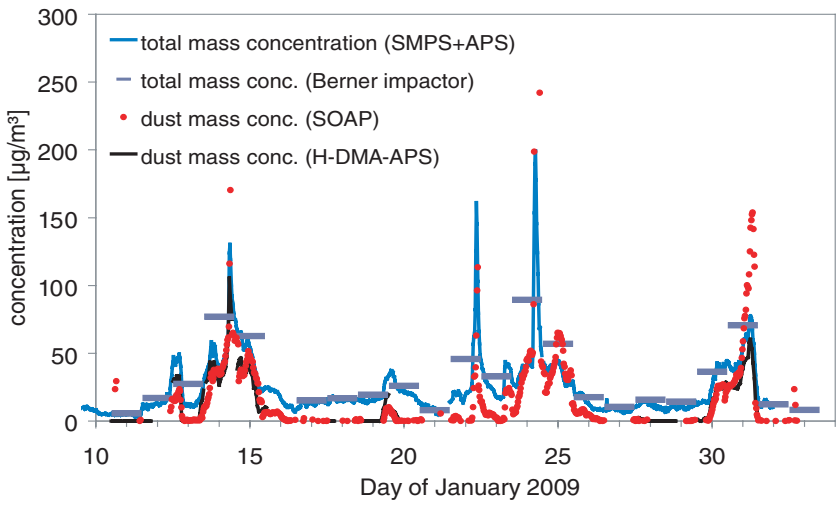

Fig.6: *Total mass concentrations (PM10) calculated from particle density and particle number size concentrations and gravimetric analysis (Berner impactor). Also shown are dust mass concentrations determined by SOAP and H-TMD-APS.*

optical absorption spectroscopy and determining dust masses by hygroscopicity measurements show a good agreement (Fig. 6), although the total dust mass is determined by measuring different chemical and physical properties. Differences between physical measurements of dust concentrations can be easily explained by their method. The optical spectroscopic method (SOAP) is sensitive to the absorption characteristics of aerosols. A characteristic spectral feature of mineral dust is the strong absorption in the ultra-violet region, while in the near infrared red the absorption is relatively small [*Müller et al.,* 2009c]. Since the optical absorption of mineral dust is dominated by iron oxides, the dust concentration derived by SOAP is sensitive to the abundance of iron oxides in the sample. Differences in dust concentrations can be thus caused by different chemical and mineralogical particle composition.

Particle dry deposition was determined using a parameterization after [*Zhang et al.* 2001]. The parameterization calculates particle dry deposition velocities as a function of particle size and density as well as meteorological variables. From parameters measured with a sonic anemometer (Gill Instruments Limited) and size resolved particle number size distribution the dry particle deposition velocity was calculated. Another way for getting the relevant meteorological parameters was by measuring the horizontal wind speed and direction in heights at of 4 m and 10 m with vane anemometers and in 30 m height with a cup anemometer. Using the parameterization after Zhang et al. (2001) and the particle dust size distribution, this 'gradient' technique also yields a dry deposition flux. A third method is to use micrometeorology measured with the sonic and mass concentration measured with SOAP.

Regional modeling of Saharan dust transport towards the tropical Atlantic (SOPRAN)

Within SOPRAN, Saharan dust transport and deposition into the tropical North Atlantic Ocean are simulated with the regional model system COSMO-MUSCAT [*Heinold et al.,* 2007]. Its components are the mesoscale meteorological model COSMO (former Lokal-Modell, LM) of the German Weather Service (Deutscher Wetterdienst, DWD) and the MUltiScale Chemistry Aerosol Transport Model (MUSCAT). The dust emission scheme based on [*Tegen et al.* 2002] is implemented in the model. Dust emission, transport, and deposition are simulated using meteorological and hydrological fields from COSMO including the computation of the direct dust radiative effect on atmospheric dynamics. Surface properties (vegetation, surface roughness, soil texture) and the location of potential dust sources derived from Meteosat Second Generation (MSG) satellite observations [*Schepanski et al.,* 2007] are taken into account for dust emission calculations. The model-predicted dust is transported as passive tracer in five independent size classes between 0.1 µm and 25 µm radius. The processes that remove dust from the atmosphere are dry and wet deposition. Dry deposition depends on particle size, density and relevant meteorological parameters. It is due to gravitational settling, which is most relevant for particles larger than 2 µm, and turbulent mixing. The parameterization of wet deposition accounts for rain-out and wash-out. The model domain covers an area with lower left corner at (0.2°N, 32.3°W) and an upper right corner at (41.1°N, 32.9°E) with 28 km horizontal grid resolution and 40 vertical layers.

Saharan dust transport and deposition into the tropical Atlantic Ocean have been simulated for specific dust transport events during the intensive SOPRAN campaigns from 2007 to 2009. The model results were evaluated based on satellite dust indices within dust source regions, sun photometer observations, and chemical and physical measurements of Saharan desert aerosol at the Cape Verde Atmospheric Observatory (CVAO). Initial detailed comparisons of modeled dust concentrations and particle size distributions with observations at Cape Verde for May 2007 and January 2009 show promising agreement, indicating that the model reproduces size resolved dust deposition fluxes realistically. Tests of the model performance during the other intensive campaigns will be completed susequentially.

The simulations performed within SOPRAN confirm the findings of a previous COSMO-MUSCAT study by [*Schepanski et al.* 2008] providing additional case studies. Over the Atlantic, mineral dust is transported within the Saharan Air Layer (SAL), which is a well-defined layer with low relative humidity (< 40 %) and high dust particle concentration. Saharan dust transport in Northern Hemisphere winter months occurs below 2 km height, which leads to efficient dry deposition. In summer, dust transport occurs above the marine boundary layer at 3 – 5 km height, and dry deposition events over the ocean are related to sinking of dust-containing air masses. During this season, deposition fluxes in the Cape Verde region are low and influenced by both dry and wet processes. While areas dominated by wet deposition are related to wet convective precipitation in the intertropical convergence zone, in the Cape Verdes dry deposition processes of dust dominate during most of the year.

For the intensive campaign in January 2009, estimates of dry deposition fluxes at the CVAO are

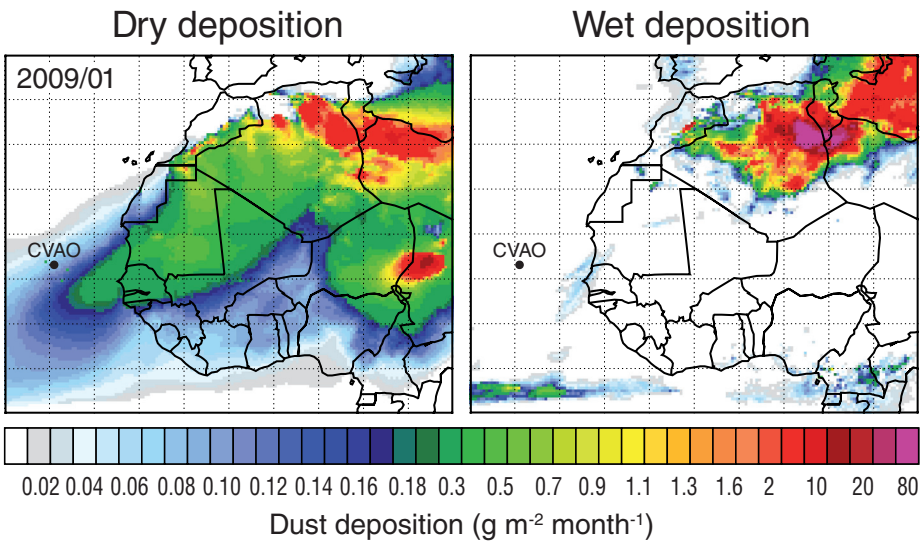

Fig. 7: *Total dry (left) and wet (right) deposition of Saharan dust [g m^{-2}] for January 2009 as simulated by COSMO-MUSCAT.*

available from microphysical measurements (see above/below for the description). Within this period dust deposition in the Cap Verde region was influenced only by dry processes (Fig. 7). Fluxes of up to 0.1 µg m^{-2} s^{-1} were observed during three dust episodes (Fig. 9). A comparison with the model can be considered as a test for the method to determine the dry deposition fluxes.

In order to ensure that COSMO-MUSCAT provides realistic dust fields, the model results are evaluated using, e.g., sun photometer measurements from Aerosol Robotic Network (AERONET) stations within relevant dust source regions. The model matches the aerosol optical depth (AOD) of dust fairly well at Tamanrasset throughout the whole period (Fig. 8a). At Agoufou, a good agreement is found after the 20 January (Fig. 8b). In the days before, an Ångström exponent greater than 1 was observed indicating that the high AOD before 20 January was not related to desert aerosol. In addition, the comparison of the model-derived dust optical thickness with AOD data at the AERONET station Sal indicates that the model is able to reproduce the mineral dust load over the neighboring island (Fig. 8c). Considering the fact that the measured AOD is influenced also by biomass burning aerosol from West Africa, the modeled dust optical thickness agrees well for the first and the last dust event, but is slightly overestimated in between.

Since desert dust deposition to the ocean surface cannot be measured directly by remote sensing and direct dust deposition measurements with marine sediment traps are sparse and uncertain, the input of Saharan dust into the tropical Atlantic can be described only by a combination of measurements and modeling for this region. The regional model COSMO-MUSCAT

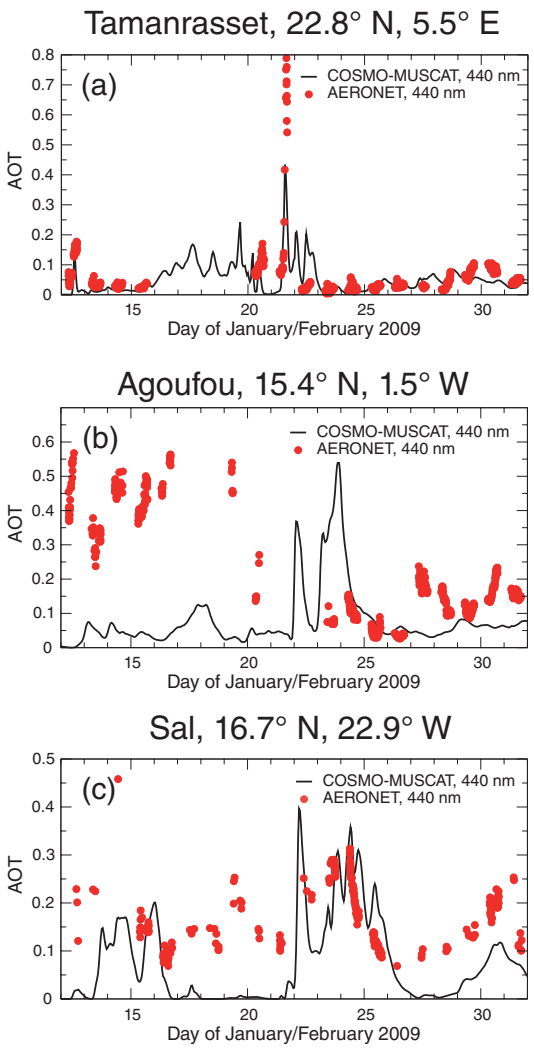

Fig. 8: *Comparison of the model-derived dust aerosol optical thickness (440 nm; black line) thickness provided by AERONET (red symbols) at Tamanrasset (a), Agoufou (b), and Sal (c).*

is suitable to investigate relevant processes for emission, transport, and deposition of dust. It will be used for ongoing simulations of Saharan aerosol transport towards the tropical Atlantic Ocean and will provide spatial context to the dry deposition fluxes obtained from microphysical measurements at the CVAO.

Comparison of measured and modeled deposition flux

Dust deposition flux determined by three experimental methods and a regional dust transport model have been compared. The measurements were performed in January 2009, a period of the West African Harmattan active season (October to May) [*McTainsh et al.,* 1997].

A time series of dust deposition fluxes is shown in Fig. 9. There is a good agreement between the experimental techniques 'sonic', 'profile' and 'SOAP'. The comparison of the dry deposition fluxes from COSMO-MUSCAT with the experimental methods shows a good agreement for the first dust event from 12 to 16 January, except for the last day of this episode. Significant discrepancies occur for the second dust outbreak between 22 and 26 January with about three times higher values determined by the model. The analysis of satellite dust indices points towards an overestimation by the model of dust emissions in Algeria due to a winter cyclone. As mentioned before, the modeled AOD is too high on Sal Island. Again, reasonable agreement is found for the end of January 2009. On the other hand, there is a strong lateral gradient in the dust deposition flux near CVAO, which causes high uncertainties in estimating the deposition flux. A more detailed analysis using the dust transport model (COSMO-MUSCAT) showed that from January 12 to 15 the ground station was in a region of small lateral gradients. At January 16, there was a large lateral gradient. Similar gradients were found for the other dust periods. Despite the discrepancies, which are caused by special meteorological conditions, there is a promising agreement between experimental and model determined dust deposition fluxes.

Outlook

Starting in 2010, in close connection to the UK SOLAS activities the CVAO and the CVOO will be improved by the Leibniz SAW project INFRA-CV being granted by the Leibniz Society and lead by IfT. New laboratory capacities will be constructed at the INDP as well as new equipments for the research vessel "Islandia", the CVOO and the CVAO will be installed during the next three years. In parallel, the SOPRAN-II project will continue and improve the research activities at the two research sites at Cape Verde.

A new part of the SOPRAN II will be named: ***Ocean export of organic matter***. Thereby, the work will be focusing on the export of organic material from the ocean surface into the particle phase. Because, recent studies have shown that the water insoluble organic carbon (WISOC) content can contribute up to 60 % [*Cavalli et al.,* 2004; *O'Dowd et al.,* 2004, *Facchini et al.,* 2008a] of the particle mass in marine sub micrometer particles. The organic material is suggested of

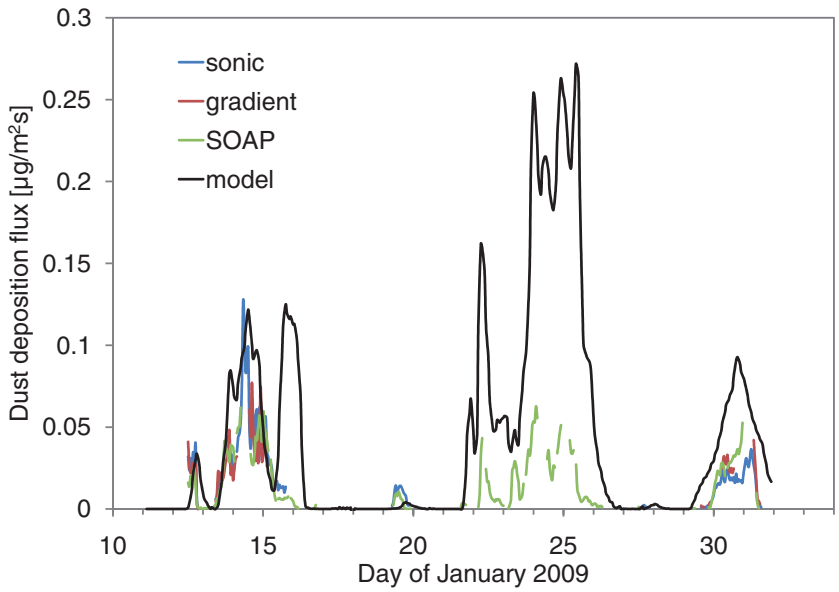

Fig. 9: *Dry deposition fluxes at CVAO derived from experimental methods 'sonic', 'gradient', and 'SOAP' SMPS-APS and as well as from COSMO-MUSCAT simulations.*

marine bio productivity origin but the chemical composition as well as the transport processes are still not well known.

The main aim of this project part is the chemical characterization of inorganic and organic fractions of marine particles. The organic fraction will be analyzed for the water soluble and the water insoluble fractions. The influence of the seasonal biomass production on the chemical composition of the marine aerosol will be addressed. In order to achieve the objective of the proposal, field campaigns and laboratory studies utilising mesocosms will be performed with

- Analysis of water soluble organic and water insoluble organic fractions
- Chemical analysis of organic compounds: carboxylic acids and fatty acids, amino compounds (amino acids and aliphatic amines) and monosaccharides
- Identification of marine biomarkers in the particle phase
- Size-segregated sampling to select the marine originating aerosol
- Analysis of inorganic compounds (anion/cations).

In future intensive experiments more analytical methods will be applied immediately after sampling the PM to avoid chemical transformations during storage and transport of samples.

There will be ongoing simulations of Saharan dust transport to the Tropical Atlantic Ocean for future intensive SOPRAN campaigns using the regional model COSMO-MUSCAT. Information on dust source regions obtained from the model results can help to interpret the mineralogical and physico-chemical particle properties. In turn measurements of the Saharan desert aerosol at the CVAO together with satellite dust indices will be needed for further model evaluations. A fully automated multi wavelengths absorption photometer will be installed. Radiative particle properties near ground will be calculated from measured spectral absorption and ongoing measurements of particle number size distributions and chemical composition. Additionally dust concentrations will be derived from absorption spectra with high temporal resolution. Measurement of dust concentrations near ground and satellite dust indices help to evaluate dust transport models. As part of the new topic within SOPRAN-II, the export of organic matter from ocean surface will be modelled with COSMO-MUSCAT. In order to estimate the source strength of organic compounds of marine aerosol we plan to implement and test a parameterization of organic aerosol emissions from ocean surface films in the regional model, as first approach, assuming a similar mechanism as the generation of sea salt particles.

In addition, a Lagrangian model study is planned to investigate dust surface chemistry and the conversion of iron oxides during dust transport from source to oceanic sink. Initially, cloud contact and in-cloud residence time will be used as indicator for changes in iron speciation and solubility. The measurements of the particle and gas phase at the SOPRAN field site will provide the basis to validate the model results.

References

Baker, A. R., and T. D. Jickells (2006), Mineral particle size as a control on aerosol iron solubility, *Geophys. Res. Lett.*, *33* (17), -, L17608, doi:10.1029/2006GL026557.

Baker, A. R., T. D. Jickells, M. Witt, and K. L. Linge (2006), Trends in the solubility of iron, aluminium, manganese and phosphorus in aerosol collected over the Atlantic Ocean, *Mar. Chem.*, *98* (1), 43-58.

Buck, C. S., W.M. Landing, J.A. Resing, C.I. Measures (2008), The solubility and deposition of aerosol Fe and other trace elements in north atlantic ocean: Observations from the A16N CLIVAR/CO2 repeat hydrography section, *Mar. Chem.*, doi:10.1016/j.marchem.2008.08.003, 2008.

Cavalli, F., M. C. Facchini, S. Decesari, M. Mircea, L. Emblico, S. Fuzzi, D. Ceburnis, Y. J. Yoon, C. D. O'Dowd, J. P. Putaud, and A. Dell'Acqua (2004), Advances in characterization of size-resolved organic matter in marine aerosol over the North Atlantic, *J. Geophys. Res. - Atmos.*, *109* (D24), -, D24215, doi:10.1029/2004jd005137.

Charlson, R. J., J. E. Lovelock, M. O. Andreae, and S. G. Warren (1987), Oceanic Phytoplankton, Atmospheric Sulfur, Cloud Albedo and Climate, *Nature*, *326* (6114), 655-661.

Chen, Y., and R. L. Siefert (2004), Seasonal and spatial distributions and dry deposition fluxes of atmospheric total and labile iron over the tropical and subtropical North Atlantic Ocean, *J. Geophys. Res. - Atmos.*, *109* (D9), -, D09305, doi:10.1029/2003JD003958.

Chiapello, I., G. Bergametti, L. Gomes, B. Chatenet, F. Dulac, J. Pimenta, and E. S. Suares (1995), An Additional Low Layer Transport of Sahelian and Saharan Dust over the North-Eastern Tropical Atlantic, *Geophys. Res. Lett.*, *22* (23), 3191-3194.

Facchini, M. C., S. Decesari, M. Rinaldi, C. Carbone, E. Finessi, M. Mircea, S. Fuzzi, F. Moretti, E. Tagliavini, D. Ceburnis, and C. D. O'Dowd (2008a), Important Source of Marine Secondary Organic Aerosol from Biogenic Amines, *Environ. Sci.Technol.*, *42* (24), 9116-9121, doi:10.1021/Es8018385.

Facchini, M. C., M. Rinaldi, S. Decesari, C. Carbone, E. Finessi, M. Mircea, S. Fuzzi, D. Ceburnis, R. Flanagan, E. D. Nilsson, G. de Leeuw, M. Martino, J. Woeltjen, and C. D. O'Dowd (2008b), Primary submicron marine aerosol dominated by insoluble organic colloids and aggregates, *Geophys. Res. Lett.*, *35* (17), -, L17814, doi:10.1029/2008gl034210.

Hansard, S. P., W. M. Landing, C. I. Measures, and B. M. Voelker (2009), Dissolved iron(II) in the Pacific Ocean: Measurements from the PO2 and P16N CLIVAR/CO2 repeat hydrography expeditions, *Deep-Sea Res. Pt. I*, *56* (7), 1117-1129.

Heinold, B., J. Helmert, O. Hellmuth, R. Wolke, A. Ansmann, B. Marticorena, B. Laurent, and I. Tegen (2007), Regional modeling of Saharan dust events using LM-MUSCAT: Model description and case studies, *J. Geophys. Res. - Atmos.*, *112* (D11), -, D11 204, doi:10.1029/2006JD007443.

Heinrich, D. H., and K. T. Karl Tropospheric Halogen Chemistry, edited, pp. 1-67, Pergamon, Oxford.

Heintzenberg, J. (2009), The SAMUM-1 experiment over Southern Morocco: overview and introduction, *Tellus B*, *61* (1), 2-11.

Jickells, T. D., Z. S. An, K. K. Andersen, A. R. Baker, G. Bergametti, N. Brooks, J. J. Cao, P. W. Boyd, R. A. Duce, K. A. Hunter, H. Kawahata, N. Kubilay, J. laRoche, P. S. Liss, N. Mahowald, J. M. Prospero, A. J. Ridgwell, I. Tegen, and R. Torres (2005), Global iron connections between desert dust, ocean biogeochemistry, and climate, *Science*, *308* (5718), 67-71.

Kettle, A. J., and M. O. Andreae (2000), Flux of dimethylsulfide from the oceans: A comparison of updated data seas and flux models, *J. Geophys. Res. - Atmos.*, *105* (D22), 26793-26808.

Kraemer, S. M. (2004), Iron oxide dissolution and solubility in the presence of siderophores, *Aquat. Sci.*, *66* (1), 3-18.

Kulmala, M. (2003), How particles nucleate and grow, *Science*, *302* (5647), 1000-1001.

Leinert, S., and A. Wiedensohler (2008), A DMA and APS based technique for measuring aerodynamic hygroscopic growth factors of micrometer-size aerosol particles, *J. Aerosol Sci.*, *39* (5), 393-402.

Mahowald, N. M., A. R. Baker, G. Bergametti, N. Brooks, R. A. Duce, T. D. Jickells, N. Kubilay, J. M. Prospero, and I. Tegen (2005), Atmospheric global dust cycle and iron inputs to the ocean, *Global Biogeochem. Cy.*, *19* (4), -, doi: 10.1029/2004GB002402.

Majestic, B. J., J. J. Schauer, and M. M. Shafer (2007), Application of synchrotron radiation for measurement of iron red-ox speciation in atmospherically processed aerosols, *Atmos. Chem. Phys.*, *7* (10), 2475-2487.

Mancinelli, V., S. Decesari, M. C. Facchini, S. Fuzzi, and F. Mangani (2005), Partitioning of metals between the aqueous phase and suspended insoluble material in fog droplets, *Ann. Chim. - Rome*, *95* (5), 275-290.

Martin, J. H. (1990), Glacial-interglacial CO_2 change:The iron hypothesis, *Paleoceanogr.*, *5*, 14.

McTainsh, G. H., W. G. Nickling, and A. W. Lynch (1997), Dust deposition and particle size in Mali, West Africa, *Catena*, *29* (3-4), 307-322.

Müller, C., Y. Iinuma, J. Karstensen, D. van Pinxteren, S. Lehmann, T. Gnauk, and H. Herrmann (2009a), Seasonal variation of aliphatic amines in marine sub-mictometer particles at the Cape Verde islands, *Atmos. Chem. Phys.*, *9* (24), 9587-9897.

Müller, K., S. Lehmann, D. van Pinxteren, T. Gnauk, N. Niedermeier, A. Wiedensohler, H. Herrmann (2009b), Particle characterization at the Cape Verde atmospheric observatory during the 2007 RHaMBLe intensive, *Atmos. Chem. Phys. Discuss.*, *9*, 34.

Muller, T., A. Schladitz, A. Massling, N. Kaaden, K. Kandler, and A. Wiedensohler (2009c), Spectral absorption coefficients and imaginary parts of refractive indices of Saharan dust during SAMUM-1, *Tellus B*, *61* (1), 79-95.

O'Dowd, C. D., M. C. Facchini, F. Cavalli, D. Ceburnis, M. Mircea, S. Decesari, S. Fuzzi, Y. J. Yoon, and J. P. Putaud (2004), Biogenically driven organic contribution to marine aerosol, *Nature*, *431* (7009), 676-680, doi:10.1038/Nature02959.

Rijkenberg, M. J. A., C. F. Powell, M. Dall'Osto, M. C. Nielsdottir, M. D. Patey, P. G. Hill, A. R. Baker, T. D. Jickells, R. M. Harrison, and E. P. Achterberg (2008), Changes in iron speciation following a Saharan dust event in the tropical North Atlantic Ocean, *Mar. Chem.*, *110* (1-2), 56-67.

Sander, R., W. C. Keene, A. A. P. Pszenny, R. Arimoto, G. P. Ayers, E. Baboukas, J. M. Cainey, P. J. Crutzen, R. A. Duce, G. Honninger, B. J. Huebert, W. Maenhaut, N. Mihalopoulos, V. C. Turekian, and R. Van Dingenen (2003), Inorganic bromine in the marine boundary layer: a critical review, *Atmos. Chem. Phys.*, *3*, 1301-1336.

Schepanski, K., I. Tegen, B. Laurent, B. Heinold, and A. Macke (2007), A new Saharan dust source activation frequency map derived from MSG-SEVIRI IR-channels, *Geophys. Res. Lett.*, *34* (18), -, L18 803, doi:10.1029/2007GL030168.

Schepanski, K., I. Tegen, and A. Macke (2009), Saharan dust transport and deposition towards the tropical northern Atlantic, *Atmos. Chem. Phys.*, *9* (4), 1173-1189.

Schladitz, A., T. Muller, N. Kaaden, A. Massling, K. Kandler, M. Ebert, S. Weinbruch, C. Deutscher, and A. Wiedensohler (2009), In situ measurements of optical properties at Tinfou (Morocco) during the Saharan Mineral Dust Experiment SAMUM 2006, *Tellus B*, *61* (1), 64-78.

Solmon, F., P. Y. Chuang, N. Meskhidze, and Y. Chen (2009), Acidic processing of mineral dust iron by anthropogenic compounds over the north Pacific Ocean, *J. Geophys. Res. - Atmos.*, *114*, -, D02305, doi:10.1029/2008JD010417.

Tegen, I., S. P. Harrison, K. Kohfeld, I. C. Prentice, M. Coe, and M. Heimann (2002), Impact of vegetation and preferential source areas on global dust aerosol: Results from a model study, *J. Geophys. Res. - Atmos.*, *107* (D21), -, 4576, doi: 10.1029/2001JD000963.

von Glasow, R., R.Sander, A. Bott, P.J. Crutzen (2002), Modelling halogen chemistry in the marine boundary layer 1.Cloud-free MBL, *J. Geophys. Res. - Atmos.*, *107* (D17), 4341, doi:10.1029/2001JD000942.

von Glasow, R., R.Sander, A. Bott, P.J. Crutzen (2002), Modeling halogen chemistry in the marine boundary layer 2.Interactions with sulfur and the cloud-covered MBL, *J. Geophys. Res. - Atmos.*, *107* (D17), 4323, doi:10.1029/2001JD000943.

Wang, S. C., and R. C. Flagan (1989), Scanning Electrical Mobility Spectrometer, *J. Aerosol Sci.*, *20* (8), 1485-1488.

Zhang, L. M., S. L. Gong, J. Padro, and L. Barrie (2001), A size-segregated particle dry deposition scheme for an atmospheric aerosol module, *Atmos. Environ.*, *35* (3), 549-560.

Funding
- Federal Ministry of Education and Research, BMBF (SOPRAN)
- European Commission (TENATSO)
- Scientific Community Gottfried Wilhelm Leibniz, WGL (CV-INFRA)

Cooperation
- University of York, Great Britain
- IfM-Geomar, Kiel, Germany
- Instituto Nacional de Meteorologia e Geofísica INMG, Mindelo, Cape Verde
- Instituto Nacional de Desenvolvimento das Pescas INDP, Mindelo, Cape Verde
- IOM Warnemünde, Germany
- MPI for Biogeochemistry, Jena, Germany

Heterogeneous freezing of droplets with immersed surface modified mineral dust particles

Dennis Niedermeier[1], Susan Hartmann[1], Frank Stratmann[1], Heike Wex[1], Tina Clauss[1], Alexei Kiselev[1], Eva Hallbauer[1], Laurent Poulain[1], Raymond A. Shaw[1,2], Ryan Sullivan[3], Paul DeMott[3], Olaf Stetzer[4], Bernd Reimann[5], Ulrich Bundke[5], David Covert[6], Berko Sierau[4], Thomas F. Mentel[7], Paul Reitz[8,9], Johannes Schneider[8]

[1] Leibniz Institute for Tropospheric Research (IfT), Leipzig, Germany
[2] Department of Physics, Michigan Technological University, Houghton, Michigan, USA
[3] Department of Atmospheric Science, Colorado State University, Fort Collins, Colorado, USA
[4] Institute of Atmospheric and Climate Science, ETH Zurich, Zurich, Switzerland
[5] Institute for Atmospheric and Environmental Sciences, Goethe University, Frankfurt/Main, Germany
[6] Joint Institute for the Study of the Atmosphere and Ocean, University of Washington, Seattle, Washington, USA
[7] ICG-2: Troposphere, Research Center Jülich, Jülich, Germany
[8] Particle Chemistry Department, Max Planck Institute for Chemistry, Mainz, Germany
[9] Institute for Atmospheric Physics, Johannes Gutenberg University, Mainz, Germany

Im Rahmen der internationalen Messkampagnen FROST I und II (FReezing Of duST) wurde das Immersionsgefrierverhalten von chemisch und physikalisch oberflächenbehandelten Mineralstaubpartikel (Arizona Test Dust) untersucht. Hierfür wurde erstmalig die erweiterte Version des Wolkensimulators LACIS (Leipzig Aerosol Cloud Interaction Simulator) eingesetzt. Um die Alterung von Mineralstaubpartikel in der Atmosphäre zu simulieren, wurden die Arizona Test Dust Partikel mit verschiedenen Substanzen (Schwefelsäure, Ammoniumsulfat und Bernsteinsäure) beschichtet. Dabei wurden ausschließlich atmosphärisch relevante Schichtdicken untersucht. Zusätzlich wurde die Oberfläche der beschichteten und unbeschichteten Arizona Test Dust Partikel mit einem Thermodenuder thermisch behandelt. Mit LACIS wurde die temperaturabhängige Eiskeimfähigkeit im Temperaturbereich von 233 K bis 239 K untersucht. Unter Verwendung der gewonnenen experimentellen Ergebnisse und numerischer Simulationen konnte auf Basis der klassischen Nukleationstheorie eine Parametrisierung zur Beschreibung des Immersionsgefrierverhaltens der untersuchten Mineralstaubpartikel abgeleitet werden.

Introduction

Ice formation in the atmosphere may take place via homogeneous or heterogeneous nucleation processes, with the latter process being induced by a foreign insoluble substance called an ice nucleus (IN) [*Cantrell and Heymsfield*, 2005]. Four different heterogeneous freezing modes are distinguished in the literature: Deposition nucleation mode as well as condensation, immersion and contact freezing mode [*Pruppacher and Klett*, 1997].

In general, our understanding of the physical and chemical processes underlying heterogeneous ice formation is limited. Therefore, more scientific work, both theoretical and experimental, is necessary to elucidate the fundamental physical mechanisms, as well as to develop adequate parameterizations that are suitable for use in e.g., cloud and global models [*Cantrell and Heymsfield*, 2005; *Kärcher and Lohmann*, 2003].

Various atmospheric observations of droplet freezing through heterogeneous ice nucleation show that in the atmosphere insoluble substances, especially mineral dust particles, serve effectively as IN [*Cziczo et al.,* 2004; *DeMott et al.*, 2003a,b; *Richardson et al.*, 2007]. As a result mineral dust particles indirectly influence cloud properties, precipitation, and therefore earth's climate [*DeMott et al.*, 2003a,b; *Zuberi et al.*, 2002]. Mineral dust particles originate from desert regions like the Sahara and the Gobi desert and can be lifted into the free troposphere during storm events. Subsequently, the dust particles can be transported over large distances [*Prospero*, 1999; *DeMott et al.*, 2003a] and undergo aging processes e.g., through coatings with sulfates and other electrolytes [*Zuberi et al.*, 2002]. As a result of these aging processes IN ability may change.

During the measurement campaigns FROST I and II (FReezing Of duST), which took place in April 2008 and 2009, respectively, the ability of mineral dust particles (Arizona Test Dust, ATD) to function as IN was investigated and quantified. FROST I and II comprised hygroscopic growth measurements with H-TDMA and HH-TDMA (Humidity- and High Humidity-Tandem Differential Mobility Analyzer, *Hennig et al*. [2005]), the determination of critical supersaturation for droplet activation with a CCN counter (Cloud Condensation Nucleus counter, Droplet Measurement Technologies, *Roberts and Nenes* [2005]), as well as AMS (Aerosol Mass Spectrometers, *Jayne et al.* [2000]) and ATOFMS (Aerosol Time-Of-Flight Mass Spectrometer, *Prather et al.*, [1994]) measurements to determine particle composition. By means of a Transmission

Electron Microscopy the particle morphology was analyzed. The IN ability of the particles was investigated for different freezing modes. For the immersion freezing mode, the Leipzig Aerosol Cloud Interaction Simulator (LACIS, *Stratmann et al.* [2004]), the Continuous Flow thermal gradient Diffusion Chamber (CFDC, *Rogers* [1988]) and the Fast Ice Nucleus Chamber Counter [*Bundke et al.*, 2008] were applied. The deposition nucleation was studied with the Portable Ice Nucleation Chamber (PINC, *Stetzer et al.* [2008]) and the CFDC instrument. Here we will mainly concentrate on the findings and results emerging from with investigations performed with LACIS during FROST I and II and thereafter.

LACIS allows the investigation of immersion freezing processes, such that the influence of size segregated particles on the freezing behavior of droplets can be measured, where only one particle is immersed in each droplet. Ice fractions as function of temperature were determined. From these, nucleation rates can be derived, which are not instrument specific and therefore generally comparable. Arizona Test Dust (ATD) was used as a surrogate for mineral dust for the freezing experiments during the FROST measurement campaigns. To simulate atmospheric aging processes, the ATD particles were coated with various substances such as ammonium sulfate ($(NH_4)_2SO_4$), sulfuric acid (H_2SO_4, three different coating conditions) and succinic acid ($C_4H_6O_4$). The coating amounts are in the range observed in the atmosphere [*Mertes et al.*, 2005, *Yuskiewicz et al.*, 1999]. Additionally, the coated and uncoated particles were treated thermally in order to evaporate the coating material and/or to stimulate chemical reactions at the particle surface. Thus, the influence of surface modifications on the freezing behavior was investigated. In the experiments quasi monodisperse particles with a mobility diameter of 300 nm were considered.

Operating LACIS in the immersion freezing mode, the temperature dependent ice fractions were determined in a temperature range between 233 K and 239 K. From this data, assuming a stochastic nature of the freezing process, a parameterization based on a classical nucleation theory (CNT) has been derived to quantify the immersion freezing behavior of the pure and treated mineral dust particles. Additionally, numerical simulations with Fluent/FPM were performed in order to evaluate the parameterization derived from the experiments and to test the applicability of CNT for describing the ice nucleation processes (homogeneous and heterogeneous) simulated in LACIS.

Experimental Set-up

Particle Generation. The ATD particles were dispersed using a fluidized bed generator. As a result of friction in the fluidized bed the particles were highly charged and a self-built Corona discharger was applied for reducing the charge level. Then, particles with an aerodynamic diameter larger than 560 nm were removed from the aerosol flow by means of a Micro-Orifice Uniform-Deposit Impactor (MOUDI). A Krypton 85 neutralizer was applied to establish a bipolar equilibrium charge distribution on the particles. Subsequently, particles were coated with different substances and coating amounts ($C_4H_6O_4$, H_2SO_4 at three different coating temperatures leading to three different coating amounts) in vapor diffusion tubes. For $(NH_4)_2SO_4$ coating, the ATD particles were first coated with H_2SO_4. Then, the aerosol flow was humidified to saturation and ammonia gas was added. In a three meter reaction tube the neutralization of the particulate H_2SO_4 by ammonia gas took place. After that the aerosol flow was dried using a diffusion dryer. Downstream the coating devices particles could be passed through a thermodenuder, in which the volatile fraction of the aerosol particles was removed. In its heating section a temperature of 250 °C was applied. Finally a DMA (Differential Mobility Analyzer; [*Knutson and Whitby*, 1975]; type 'Vienna Medium') was used for selecting a quasi-monodisperse particle size fraction. For the freezing experiments, particles with a mobility diameter of 300 nm were selected. A CPC was used to determine the particle concentration and an aerosol flow of 0.08 l/min was fed into LACIS.

Leipzig Aerosol Cloud Interaction Simulator. The laminar flow diffusion cloud chamber LACIS was constructed to investigate cloud microphysical processes like hygroscopic growth and droplet activation of aerosol particles under atmospheric relevant conditions [*Stratmann et al.*, 2004]. Basically, LACIS is a laminar flow tube of variable length consisting of a variable number of 1 m long tube segments (also called sections). In order to study homogeneous and heterogeneous ice nucleation, LACIS was brought up to its full length by adding cooling sections covering the supercooled temperature range $T < T_0 = 273.15$ K, where ice nucleation may occur. Inside LACIS super-saturation with respect to water and/or ice are achieved by a combined heat and vapor diffusion process. The temporal and spatial scales of the new developed long version of LACIS range from about 10 to 30 s and 1 to 7 m, respectively. Temperature can be varied from 298 down to 223 K under operational pressures from 700 hPa to ambient values.

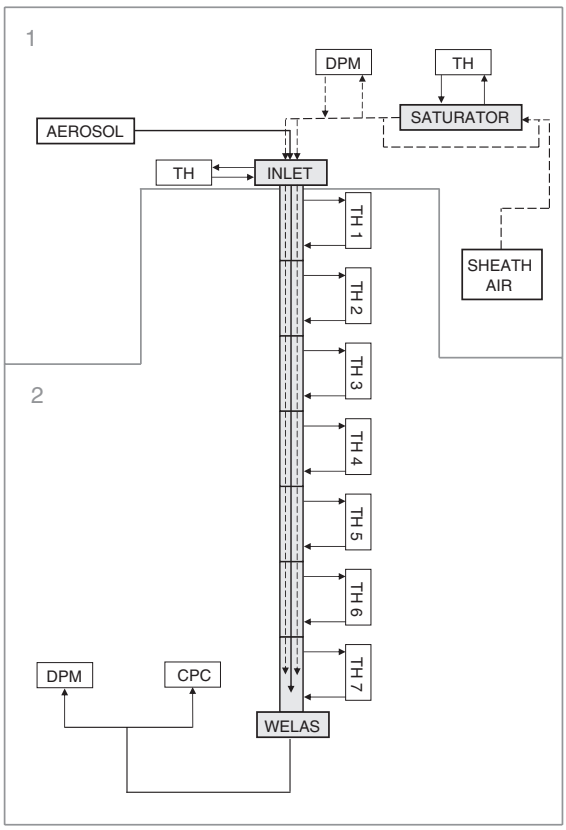

Fig. 1: *The schematic of LACIS set-up with conditioning part (item 1), laminar diffusion cloud chamber (item 2) and optical particle detection system (WELAS, white-light aerosol spectrometer).*

The schematic of the LACIS set-up is given in Fig. 1. The inlet temperature, the humidity and the volume flow of the aerosol and sheath air flows are conditioned prior to entering LACIS. The particle free sheath air flow is humidified by a saturator. In order to achieve dew point temperatures below 275.15 K, this humidified air flow is mixed with a dry air flow. An inline-connected chilled mirror dew point hygrometer (DPM) monitors the dew point temperature of the mixed air flow. The aerosol flow remains dry. The aerosol and sheath air flow are combined in the inlet section of LACIS (Fig. 1). Additionally, the inlet serves as heat exchanger (temperature controlled by a thermostat) for harmonizing the temperatures of both flows. The volume flows of aerosol (0.08 l/min) and sheath air flow (4.00 l/min) are controlled by a mass flow controller at the LACIS outlet. Entering the flow tube, the sheath air surrounds the aerosol air flow forming an about 2 mm in diameter aerosol particle beam at the flow tube center. The temperatures of the inner walls of the seven tube sections are adjusted separately by thermostats (TH). In order to monitor and control the wall temperatures, additional temperature sensors in form of external resistance thermometers are used to measure the refrigerant temperature in the return line of the cooling cycle of each tube section. With this configuration a wall temperature accuracy of 0.1 K, stability of ±0.01 K for section 1 to 5 and for the last two tube sections an accuracy of 0.3 K with a stability of ±0.05 K is attained. The flow inside LACIS is fully developed, laminar and axis symmetric [*Stratmann et al.,* 2004].

To detect particles at the outlet of LACIS, the white light-scattering spectrometer WELAS (Fig. 1) is installed. Downstream of WELAS, a Condensation Particle Counter (CPC), operating at 1.0 l/min, is used to measure the particle number concentration and a Dew Point Mirror (DPM), operating at 0.7 l/min, monitors the outlet dew and frost point temperatures.

Theory and numerical model

Because of the complex coupled fluid and particle dynamical processes taking place in LACIS, a numerical model (Fluent/FPM, *Fluent* [2001], FPM developed at IfT, *Wilck et al.* [2002], *Particle Dynamics* [2005]) is applied to design experiments and interpret the experimental data gained. This includes also the evaluation of different theoretical approaches to determine homogeneous and heterogeneous ice nucleation rates and the development of parameterizations.

Numerical model. Considering freezing experiments in LACIS, the main fluid dynamical processes taking place in LACIS are fluid flow, and heat and mass transfer. Concerning particle dynamics, transport and phase transitions processes need to be considered. These processes are mathematically described by fluid and particle dynamics equations such as the momentum, the vapor mass transport, the energy equation and the conservation equations for e.g., particle number and mass [*Stratmann et al.,* 2004]. The particle dynamical equations account for transport due to convection, diffusion and external forces (thermophoresis, sedimentation), as well as phase transition processes such as condensation/evaporation and ice nucleation. The respective equations are coupled through latent heat release and vapor depletion resulting from the phase transition processes.

The newly developed implementation of the ice phase into the numerical model i.e., Fluent/FPM, allows the consideration of water-to-ice phase transition processes and ice covered tube walls.

The numerical model is half quantitative at the current state, which means that it includes the main occurring physical processes, but not in their full complexity. The following assumptions and simplifications are made: constant wall temperature, mass accommodation coefficient of

1 and a spherical ice crystal shape for ice crystal growth.

For all simulations, monodisperse (diameter 300 nm), spherical, internally mixed seed particles consisting of ATD with a soluble mass fraction of 0.019 ammonium sulfate were assumed. The amount of ammonium sulfate coating was chosen to match the activation behavior observed in droplet activation measurements with a CCN counter. Additionally, an ice saturation of 1 was assumed as wall boundary condition for sections with ice covered tube walls.

Nucleation theory. In the numerical model the water-to-ice phase transition is simulated adopting two different approaches. First, Classical Nucleation Theory (CNT) is applied for homogeneous and heterogeneous ice nucleation [B]. For the second approach, a parameterization for immersion freezing derived from LACIS measurements [A] [*Niedermeier et al.*, 2009] is implemented into the numerical model.

According to CNT [*Pruppacher and Klett*, 1997; *Seinfeld and Pandis*, 1998] the homogeneous and heterogeneous nucleation rate coefficient j_{hom} [#/m³s] and j_{het} [#/m²s] which are defined as number of nucleation events per time and total volume of the droplet population or as number of nucleation events per time and total insoluble particle surface, [B] are defined as

$$j_{hom/het}(T) = \frac{k_B T}{h} exp\left(-\frac{\Delta F_{diff}}{k_B T}\right) N_v / N_s \, exp\left(-\frac{\Delta G_{hom} f(\Theta)}{k_B T}\right) \quad (1)$$

with Boltzmann constant k_B, absolute temperature T, Planck constant h, the diffusion energy across the water-ice interface ΔF_{diff}, the number density of molecules in the bulk water N_v (typical value of $3.1 \cdot 10^{28}$ m^{-3}, *Marcolli et al.*, [2007]), the number density of liquid molecules in contact with IN surface N_s (typical value of about 10^{19} m^{-2}, *Zobrist et al.* [2007]), the critical Gibbs free energy ΔG_{hom} and the reduction factor $f(\Theta)$ including the contact angle Θ. The unknown thermodynamic quantities such as diffusion energy across water-ice interface, ratio of water to ice saturation vapor pressures and the interfacial free energy between liquid water and ice (included in ΔG_{hom}) are parameterized according to *Zobrist et al.* [2007] and references therein. In the view of CNT, the only difference between homogeneous and heterogeneous ice nucleation is that the IN increases the likelihood to form a critical embryo by reducing energy barrier, but the ice nucleus does not disturb the stochastic nature of the freezing process. Therefore the concept of a contact angle is adopted and values between 0 and 180° are assumed, whereas in the former case the energy barrier vanishes and the latter case corresponds to homogeneous ice nucleation.

As second approach, a parameterization for the heterogeneous ice nucleation coefficient derived from the LACIS measurements concerning immersion freezing described below, is implemented into the numerical model [A]. The derivation is explained in *Niedermeier et al.* (2009). The respective heterogeneous ice nucleation rate coefficient $j_{het,LACIS}$ [#/m²s] is given by

$$j_{het,LACIS} = \frac{a}{S_P} \exp\left(-C_2 \frac{\left(1-\frac{\Delta T_S}{C_1}\right)^3}{\Delta T_S^{\,2}} f_{het}\right) \quad (2)$$

with temperature independent parameters a (includes total particle surface and kinetic effects) and f_{het} (reduction factor, includes surface properties and thermodynamic effects). The insoluble surface of a single seed particle and the supercooling temperature are given by S_P and $\Delta T_S = T_0 - T_{axis}$, respectively. $C_1 = 8.24 \cdot 10^1$ K and $C_2 = 5.00 \cdot 10^5$ K² are constants. This formula is valid in a supercooling temperature range of $34 \le \Delta T_S < 38$ K.

Assuming a stochastic nature of the immersion freezing process and constant supercooling temperature during the time of ice nucleation t, the heterogeneous ice nucleation rate coefficient $j_{het,LACIS}$ can be connected to the ice fraction f_{ice}, which is the number of frozen droplets N_f per total number N_0 of the initial droplet population, as measured with LACIS:

$$f_{ice} = \frac{N_f}{N_0} = 1 - \exp\left(-S_P j_{het}(\Delta T_S) t\right). \quad (3)$$

LACIS operational mode

Simulating the immersion freezing behavior of aerosol particles under atmospheric relevant conditions, LACIS can be operated in water and ice super-saturated mode. During the FROST measurement campaigns, the first ice nucleation measurements at LACIS were performed. Therefore, a straightforward and simple measurement setup was used. The following parameters were applied: an inlet temperature

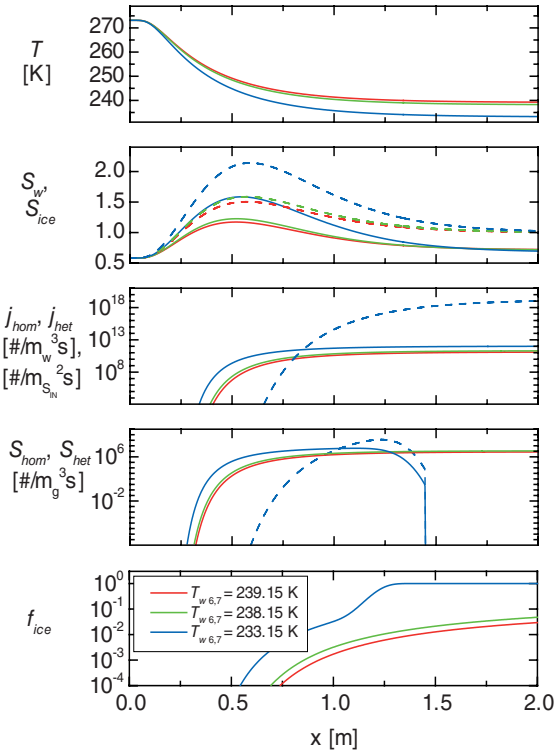

Fig. 2: *Thermodynamic conditions and water-to-ice phase transition parameters at the centerline of LACIS. Temperature profiles (panel 1), saturation wrt. water (solid lines) and ice (dashed lines) profiles (panel 2), homogeneous (dashed lines) and heterogeneous (solid lines) ice nucleation rate coefficients (panel 3), the source terms for homogeneous and heterogeneous ice mode (panel 4) and the ice fraction (panel 5) are shown for different wall temperature settings.*

of 293.15 K, an inlet dew point temperature of 265.95 K, the wall temperature of section 1 of 293.15 K, wall temperatures of section 2 – 5 of 273.15 K and the wall temperatures of section 6 – 7 range between 233.15 K and 239.15 K. For sections with wall temperatures below 273.15 K, the corresponding inner tube walls were coated with ice by cooling the respective sections down to 233.15 K for 5 min prior to measurement start. This procedure was necessary to ensure well-defined and reproducible wall boundary conditions.

Model calculations with Fluent/FPM assuming similar initial and boundary conditions as in the experiment were carried out. The resulting profiles at the centerline of LACIS are shown in Fig. 2 for the last two sections only. Starting at 273.15 K, the temperatures (illustrated in the first panel of Fig. 2) decrease very steeply within the sixth section and approach the set wall temperatures in the seventh section, in which the temperatures at the centerline are almost constant. In the supercooled temperature range the vapor pressure over ice is smaller than over liquid water. The second panel of Fig. 2 depicts the temperature dependent saturation profiles wrt. water (solid lines) and ice (dashed lines). For both cases the saturation rises strongly until a maximum is reached, then the saturation decreases and approaches constant value close to the outlet of LACIS. The lower the adjusted wall temperature the higher is the maximum of the saturation profile. Because of these thermodynamic conditions, the ATD particles grow hygroscopically at first and as soon as the saturation increases sufficiently all the particles become activated to liquid water droplets. These droplets grow dynamically by diffusion until water saturation falls below 1. Then the supercooled droplets start to evaporate in an ice super- and water sub-saturated environment. At sufficiently low temperature (approx. 244 K), heterogeneous ice nucleation starts and increases with decreasing temperature. This is illustrated in panel 3, 4 and 5 of Fig. 2. Panel 3 shows that the homogeneous (dashed line) and heterogeneous (solid line) nucleation rate coefficient j_{het} rise very steeply in the sixth section and are almost constant in the seventh tube section. In order to model the water-to-ice phase transition the total liquid water volume in the homogeneous and the total insoluble particle surface in the heterogeneous case have to be accounted for. This is realized in the source terms S_{hom} and S_{het} for the ice mode in the Fluent/FPM, which are given in panel 4. Because of similar units, S_{hom} and S_{het} are now directly comparable. For the wall temperature $T_{w6,7}$ = 233.15 K, the homogeneous source term becomes larger than the heterogeneous one at a temperature of 235.75 K i.e., homogeneous ice nucleation is dominant for T < 235.75 K. In this case, all supercooled droplets freeze and the source term drops to zero as soon as all droplets are frozen. The resulting ice fractions for the different wall temperature settings are shown in the last panel of Fig. 2. For all wall temperature settings f_{ice} increases along the centerline, in which for $T_{w6,7}$ = 233.15 K an abrupt rise caused by incipient homogeneous ice nucleation can be seen. The most ice is formed in the seventh section for all adjusted wall temperatures, where the heterogeneous ice nucleation rate coefficient is almost constant.

In practice, LACIS settings were chosen such that the supercooled water droplets, which do not freeze, evaporate completely before passing the outlet of LACIS. As a consequence, only frozen droplets and seed particles remain which be easily distinguished with the WELAS instrument by size. Ice fractions can be determined from the number of frozen droplets and seed particles.

Results and Discussion

Figure 3 presents the determined ice fraction values as function of supercooling temperature

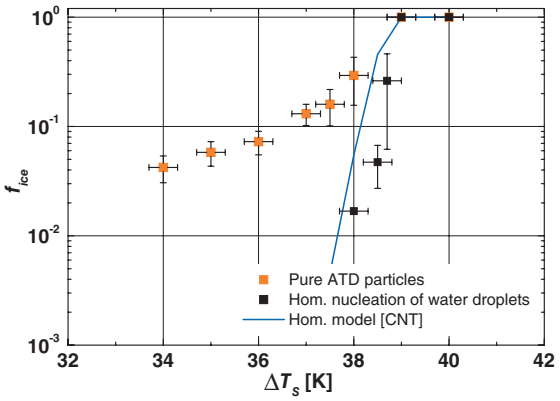

Fig. 3: *Heterogeneous (on the left) and homogeneous (on the right) freezing mode. Ice fraction at different ΔT_S resulting from freezing of droplets with an immersed ATD particle (orange squares) and from freezing of highly diluted ammonium sulfate solution droplets (black squares). The blue curve present Fluent/FPM simulation results assuming a homogeneous ice nucleation model according to CNT.*

ΔT_S ranging from 34 K to 40 K using pure ATD particles as seed particles. Again, the supercooling temperature is defined as $\Delta T_S = T_0 - T_{axis}$. The error bars represent the respective standard deviations. With increasing ΔT_S the ice fraction increases and reaches a value of 1 at ΔT_S = 39 K. Homogeneous freezing occurs for $\Delta T_S \geq$ 38K and is the dominating nucleation process for higher supercooling temperatures. This conclusion results from additional freezing measurements of highly diluted ammonium sulfate solution droplets and is supported by Fluent/FPM simulation results assuming the homogeneous ice nucleation model according to CNT. For ΔT_S < 38 K, ice formation occurs due to heterogeneous ice nucleation in particular through immersion freezing.

Ice fraction values for the coated and uncoated seed particles are presented in Fig. 4 for given LACIS supercooling temperatures. For all particle types, the ice fraction values increase with increasing ΔT_S, but in a different manner. Uncoated particles and those with $C_4H_6O_4$ coatings or with small amounts of H_2SO_4 (1) start to act as IN at lower ΔT_S compared to particles with larger amounts of H_2SO_4 [(2) and (3)] or with $(NH_4)_2SO_4$ coating. In general, the higher the amount of H_2SO_4 coating on the particles, the lower is the observed ice fraction for all $\Delta T_S \leq$ 35 K. For this supercooling temperature range pure ATD particles feature the largest ice fraction i.e., IN efficiency.

For the investigated temperature range the supercooled droplets are activated and highly diluted when freezing occurs. Consequently, the differences in the determined ice fractions are not caused by a freezing point depression due to dissolved coating material. It is much more likely that alterations of surface properties during the coating procedure are causing the reduced IN efficiency.

For $\Delta T_S \geq$ 35 K, all particles show a similar IN efficiency except for the $(NH_4)_2SO_4$ coated ones which are the most ineffective IN. The exposure of the sulfuric acid to water vapor, which occurs before the addition of ammonia to form $(NH_4)_2SO_4$, may accelerate reactions with the mineral dust, leading thereby to the greatest reduction in nucleating efficiency.

Additional thermodenuder treatment of the particles causes a further decrease of the IN ability (Fig. 5) for the H_2SO_4 coated particles. The higher the amount of H_2SO_4 on the ATD particles the more decreased is the IN efficiency after thermal treatment. The thermal treatment seems not to lead to a removal of the coating material, since the IN ability does not increase to ice fraction values obtained for pure ATD particles. More presumably, the thermodenuder seems to cause an enhancement of reactions between coating and particle, changing and destroying surface features effectively.

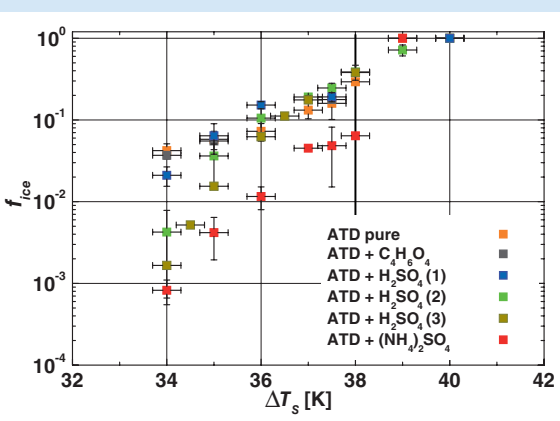

Fig. 4: *Immersion freezing behavior of all particle types. The determined ice fraction f_{ice} is plotted versus the supercooling temperature ΔT_S. The line at ΔT_S = 38 K separates the heterogeneous (on the left) and homogeneous (on the right) freezing modes.*

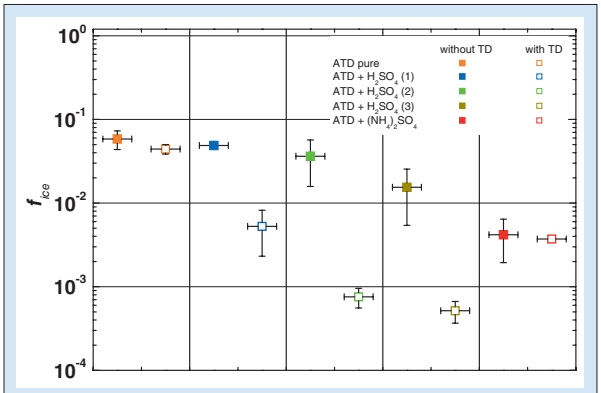

Fig. 5: *Ice fractions of pure and coated ATD particles (filled squares) and additional thermally treated pure and coated ATD particles by means of thermodenuder at 250°C (blank squares) for ΔT_S = 35 K.*

For $(NH_4)_2SO_4$ coated particles, the thermodenuder treatment does not decrease the IN efficiency further. As mentioned above, already the procedure for $(NH_4)_2SO_4$ coating may cause irreversible IN surface changes. Consequently, the thermal treatment probably does not cause further particle surface alteration.

The simplified CNT parameterization (Eq. 2) was applied to determine the parameters *a* and f_{het} for all investigated particle types. This was done by matching ice fractions calculated applying Eq. 2 to the experimentally determined ones by adjusting *a* and f_{het}. Deriving this parameterization, it was assumed that the major part of ice is formed in section 7 where the supercooling temperature and therefore j_{het} are almost constant. The residence time within the last section is about 1.6 s and this time is assumed to be the ice nucleation time *t*. In Table 1 it is shown that both parameters, *a* and f_{het}, change for the different IN types. The factor f_{het} is smallest for pure ATD particles and highest for ATD particles coated with the largest amount of H_2SO_4 (3). That means that the energy barrier which has to be overcome to form a critical ice embryo on the particle surface which initiates freezing, is lowest for the former and highest for the latter case. This suggests that surface properties have been altered i.e., in context of CNT, the interfacial free energy or contact angle have been changed. Microscopically, this could be viewed as defects being blocked, changed or destroyed due to the coating procedure. This finding confirms the assumption made above. Concerning parameter *a*, the lowest value is also obtained for pure ATD particles and the highest value for ATD particles coated with the largest amount of H_2SO_4 (3). Overall the nucleation rate coefficient decreases as *a* increases. Since *a* includes information about the total particle surface and kinetic effects, the increase can be interpreted as an increased (ice active) surface area per particle, or as an increase in the rate at which molecules can be transferred from liquid water to ice phase. Since both values, *a* and f_{het}, change in comparable manner but with opposite tendencies for the nucleation rate coefficient, it appears that the thermodynamic effect is most dominant for the change in immersion freezing behavior. However, the meaning of the parameters *a* and f_{het} should not be over-interpreted at the current stage, because the assumptions made during the derivation of Eq. 2 might include too strong simplifications. To clarify this, further investigations are required.

Particle Type	*a* [s^{-1}]	f_{het}
ATD	1,31E+0	4,51E-2
ATD + $C_4H_6O_4$	8,46E+0	6,83E-2
ATD + H_2SO_4 (1)	1,57E+1	7,79E-2
ATD + H_2SO_4 (2)	5,71E+2	1,35E-1
ATD + H_2SO_4 (3)	8,22E+3	1,78E-1
ATD + $(NH_4)_2SO_4$	1,31E+2	1,40E-1

Tab. 1: *Parameters a and f_{het} of the CNT type nucleation rate expression for the immersion freezing of supercooled water droplets containing different types of IN.*

Inserting the determined values for *a* and f_{het} into Eq. 2 and assuming that all particles are spherical with a mass equivalent diameter of 300 nm, the corresponding nucleation rate coefficients can be calculated (Fig. 6). Since the nucleation rate coefficients are not instrument specific, they can be compared to values determined by other measurement methods. E.g., *Archuleta et al*. [2005] determined nucleation rate coefficients for sulfuric acid coated iron and aluminium oxide particles from Continuous-Flow Ice-thermal Diffusion Chamber studies. Their coefficients show a similar increase with increasing ΔT_S and have values comparable to our results.

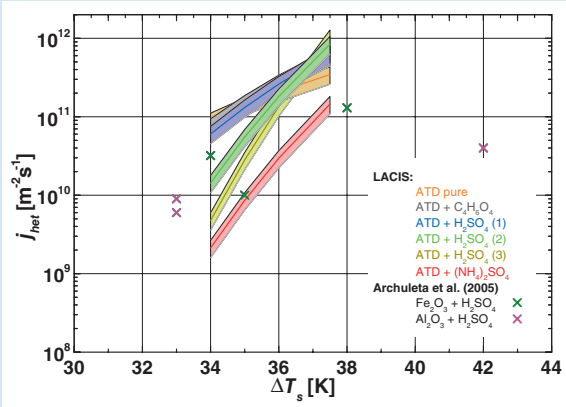

Fig. 6: *Nucleation rate coefficients j_{het} for all particle types. The crosses represent nucleation rate coefficients for sulfuric acid coated iron and aluminium oxide particles determined by Archuleta et al. (2005).*

A comparison of experimentally determined ice fractions and results from Fluent/FPM simulations is illustrated in Fig. 7. The combined model [A] (red curve), which accounts for homogeneous ice nucleation according to CNT and heterogeneous ice nucleation according to LACIS derived parameterization for immersion freezing, agrees within the measurement uncertainties with the experimental data. The small differences of the ice fractions result from the fact that for the LACIS derived parameterization a constant temperature is assumed during the time where ice nucleation takes place. In contrast, Fluent/FPM accounts for the temperature profile and therefore the ice fraction is slightly underestimated by the model.

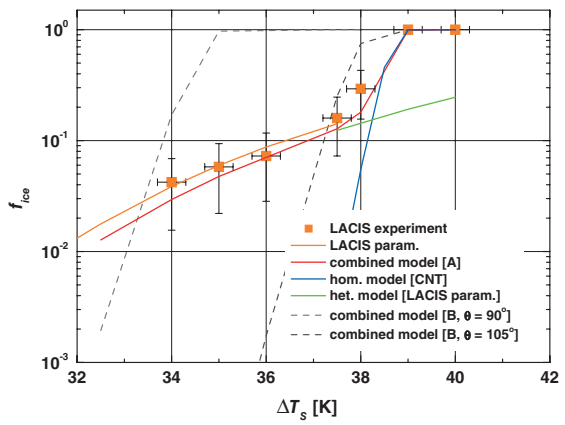

Fig. 7: *Comparison of LACIS immersion freezing experiments (orange cubes) and derived immersion freezing parameterization (orange line) [Niedermeier et al., 2009] with Fluent/FPM simulations. For the simulations a homogeneous ice nucleation model according to CNT (blue line), a heterogeneous ice nucleation model with implemented immersion freezing parameterization derived from LACIS measurements (green line), the combined model [A] (LACIS derived immersion freezing parameterization for the heterogeneous and CNT for the homogeneous ice mode, red line) and combined model [B] (CNT for both freezing modes, Eq. 2) for different contact angles (grey dashed line) are applied.*

However, the assumptions of the LACIS derived parameterization are appropriate.

Separate model simulations for homogeneous (according to CNT, blue curve) and immersion freezing (according to LACIS derived parameterization for immersion freezing, green curve) are shown to elucidate the supercooling temperature ranges where different freezing mechanisms are important. As to be seen from Fig. 7 for ΔT_S < 37.5 K immersion freezing is the dominant ice nucleation process while for ΔT_S > 38.5 K freezing is due to homogeneous ice nucleation. Interestingly, homogeneous freezing is not suppressed by the heterogeneous freezing mechanism. The results of the combined model [B] (homogeneous and heterogeneous ice nucleation according to CNT, Eq. 1) simulations suggest a much steeper slope than observed for the experimentally determined ice fractions, i.e. the temperature dependence of the heterogeneous nucleation rate coefficient is overestimated when using CNT. A constant contact angle as single free parameter is insufficient to fit the measured temperature dependence of the experimentally determined ice fractions with a CNT model [B]. From this it follows that a model description based on CNT with constant contact angle is inappropriate to describe our experimental findings.

Conclusion and Outlook

During the measurement campaigns FROST I and II the ability of size-segregated, surface modified mineral dust particles (ATD) to function as IN in the immersion freezing mode was investigated at LACIS. The particles were coated with ammonium sulfate, sulfuric acid (three different coating thicknesses) and succinic acid. Additionally, all particles besides of the succinic acid coated ones were treated thermally in a thermodenuder. Thus, the influence of various surface modifications on the freezing behavior was investigated. Using LACIS, ice fractions were determined in a supercooling temperature range between 34 K and 40 K. For ΔT_S < 35 K all coatings depressed the IN ability compared to pure ATD particles, e.g. the higher the amount of H_2SO_4 on the particles the lower the IN ability. Similar IN ability was observed for all particle types for $\Delta T_S \geq 35$ K except for the $(NH_4)_2SO_4$ coated ones which were found to be the most ineffective IN. The observed decreases of IN ability are most likely caused by particle surface modification due to reactions of the coating materials with substances contained in the dust particles. Additional thermodenuder treatments resulted in a further decrease of the IN ability for the H_2SO_4 coated particles. This suggests that the thermal treatment enhances the chemical reactions between coating and particle at the particle surface, changing or destroying ice forming surface features more effectively. In general, surfaced modification did lead to a decreased IN ability compared to the pure dust particles. This suggests that the chemical aging processes taking place in the atmosphere will lead to a decreased IN efficiency of mineral dust particles in the immersion and deposition (not shown here) freezing modes. Therefore, decreased IN concentrations due to particle aging processes have to be considered in e.g., cloud and global models.

For use in such models, based on CNT, a parameterization was developed to describe the behavior of uncoated and coated dust particles in the immersion freezing mode. The parameterization suggests that due to the surface modification, the energy barrier, which has to be overcome to initiate freezing, is increased. The parameterization also suggests that the total particle surface and/or kinetic effects are also affected. However, it appears that the thermodynamic effect is most dominant.

Comparing experimental results and model predictions, we found that a CNT-based homogeneous ice nucleation model describes the experimental results with good accuracy. In contrast, for freezing in the immersion mode, the CNT-based heterogeneous ice nucleation model overestimates the temperature dependence. Here, the model based on a parameterization derived from LACIS experiments was found to provide encouraging results. Combining the CNT-based homogeneous ice nucleation model with

the LACIS data based parameterized immersion freezing model we were able to reproduce the experimental data over the whole temperature range investigated.

Future investigations will concentrate on the ice nucleation behavior of surface modified IN such as other dusts, single minerals, soot particles, etc., the further development and testing of the parameterization concept suggested here, and the evaluation of different approaches to heterogeneous ice nucleation theory i.e., testing of the singular versus the stochastic hypothesis.

References

Archuleta, C. M., P. J. DeMott, and S. M. Kreidenweis (2005), Ice nucleation by surrogates for atmospheric mineral dust and mineral dust/sulfate particles at cirrus temperatures, *Atmos. Chem. Phys.*, *5*, 2617-2634.

Bundke, U., B. Nillius, R. Jaenicke, T. Wetter, H. Klein, and H. Bingemer (2008), The fast Ice Nucleus chamber FINCH, *Atmos. Res.*, *90* (2-4), 180-186, doi:10.1016/j.atmosres.2008.02.008.

Cantrell, W., and A. Heymsfield (2005), Production of ice in tropospheric clouds - A review, *Bull. Amer. Meteor. Soc.*, *86* (6), 795-+, doi:10.1175/bams-86-6-795.

Cziczo, D. J., D. M. Murphy, P. K. Hudson, and D. S. Thomson (2004), Single particle measurements of the chemical composition of cirrus ice residue during CRYSTAL-FACE, *J. Geophys. Res. - Atmos.*, *109* (D4), 13, D04201, doi:10.1029/2003jd004032.

DeMott, P. J., D. J. Cziczo, A. J. Prenni, D. M. Murphy, S. M. Kreidenweis, D. S. Thomson, R. Borys, and D. C. Rogers (2003a), Measurements of the concentration and composition of nuclei for cirrus formation, *Proc. Natl. Acad. Sci. USA*, *100* (25), 14655-14660, doi:10.1073/pnas.2532677100.

DeMott, P. J., K. Sassen, M. R. Poellot, D. Baumgardner, D. C. Rogers, S. D. Brooks, A. J. Prenni, and S. M. Kreidenweis (2003b), African dust aerosols as atmospheric ice nuclei, *Geophys. Res. Lett.*, *30* (14), 4, 1732, doi:10.1029/2003gl017410.

Durant, A. J., and R. A. Shaw (2005), Evaporation freezing by contact nucleation inside-out, *Geophys. Res. Lett.*, *32* (20), 4, L20814, doi:10.1029/2005gl024175.

Dynamics, P. (2005), FPM User's Guide, *www.particle-dynamics.de*.

Fletcher, N. H. (1969), Active sites and ice crystal nucleation, *J. Atmos. Sci.*, *26* (6), 1266-&.

FLUENT (2001), FLUENT 6 user's guide, *FLUENT Inc.*

Hennig, T., A. Massling, F. J. Brechtel, and A. Wiedensohler (2005), A tandem DMA for highly temperature-stabilized hygroscopic particle growth measurements between 90% and 98% relative humidity, *J. Aerosol. Sci.*, *36* (10), 1210-1223, doi:10.1016/j.jaerosci.2005.01.005.

Hirst, E., P. H. Kaye, R. S. Greenaway, P. Field, and D. W. Johnson (2001), Discrimination of micrometre-sized ice and super-cooled droplets in mixed-phase cloud, *Atmos. Environ.*, *35* (1), 33-47.

Hung, H. M., A. Malinowski, and S. T. Martin (2003), Kinetics of heterogeneous ice nucleation on the surfaces of mineral dust cores inserted into aqueous ammonium sulfate particles, *J. Phys. Chem. A*, *107* (9), 1296-1306, doi:10.1021/jp021593y.

Jayne, J. T., D. C. Leard, X. F. Zhang, P. Davidovits, K. A. Smith, C. E. Kolb, and D. R. Worsnop (2000), Development of an aerosol mass spectrometer for size and composition analysis of submicron particles, *Aerosol Sci.Technol.*, *33* (1-2), 49-70.

Karcher, B., and U. Lohmann (2003), A parameterization of cirrus cloud formation: Heterogeneous freezing, *J. Geophys. Res. - Atmos.*, *108* (D14), 15, 4402, doi:10.1029/2002jd003220.

Knopf, D. A., and T. Koop (2006), Heterogeneous nucleation of ice on surrogates of mineral dust, *J. Geophys. Res. - Atmos.*, *111* (D12), 10, D12201, doi:10.1029/2005jd006894.

Knutson, E. O., and K. T. Whitby (1975), Aerosol classification by electric mobility: apparatus, theory, and applications, *J. Aerosol. Sci.*, *6* (6), 443-451.

Lohmann, U. (2006), Aerosol effects on clouds and climate, *Space Sci. Rev.*, *125* (1-4), 129-137, doi:10.1007/s11214-006-9051-8.

Marcolli, C., S. Gedamke, T. Peter, and B. Zobrist (2007), Efficiency of immersion mode ice nucleation on surrogates of mineral dust, *Atmos. Chem. Phys.*, *7* (19), 5081-5091.

Megahed, K. (2007), The Impact of Mineral Dust Aerosol Particles on Cloud Formation, Dissertation thesis, 207 pp, Rheinischen Friedrich-Wilhelms-Universitaet Bonn, Bonn.

Mertes, S., D. Galgon, K. Schwirn, A. Nowak, K. Lehmann, A. Massling, A. Wiedensohler, and W. Wieprecht (2005), Evolution of particle concentration and size distribution observed upwind, inside and downwind hill cap clouds at connected flow conditions during FEBUKO, *Atmos. Environ.*, *39* (23-24), 4233-4245, doi:10.1016/j.atmosenv.2005.02.009.

Niedermeier, D., Hartmann, S., Shaw, R. A., Covert, D., Mentel, Th. F., Schneider, J., Poulain, L., Reitz, P., Spindler, C., Clauss, T., Kiselev, A., Hallbauer, E., Wex, H., Mildenberger, K. and F. Stratmann (2009), Heterogeneous freezing of droplets with immersed mineral dust particles – measurements and parameterization, *Atmos. Chem. Phys. Discuss.*, *9*, 15827-15865.

Prather, K. A., T. Nordmeyer, and K. Salt (1994), REAL-TIME CHARACTERIZATION OF INDIVIDUAL AEROSOL-PARTICLES USING TIME-OF-FLIGHT MASS-SPECTROMETRY, *Anal. Chem.*, *66* (9), 1403-1407.

Prospero, J. M. (1999), Long-term measurements of the transport of African mineral dust to the southeastern United States: Implications for regional air quality, *J. Geophys. Res. - Atmos.*, *104* (D13), 15917-15927.

Pruppacher, H. R., and J. D. Klett (1997), *Microphysics of Clouds and Precipitation*, Kluwer Academic Publishers, Dordrecht, The Netherlands.

Rogers, D. C. (1988), Development of a continuous flow thermal gradient diffusion chamber for ice nucleation studies, *Atmos. Res.*, *22*, 149-181.

Seinfeld, J. H., and S. N. Pandis (1998), *Atmospheric Chemistry and Physics – From Air Pollution to Climate Change*, 1326 pp., Wiley-Interscience.

Shaw, R. A., A. J. Durant, and Y. Mi (2005), Heterogeneous surface crystallization observed in undercooled water, *J. Phys. Chem. B*, *109* (20), 9865-9868, doi:10.1021/jp0506336.

Stetzer, O., B. Baschek, F. Luond, and U. Lohmann (2008), The Zurich Ice Nucleation Chamber (ZINC) - A new instrument to investigate atmospheric ice formation, *Aerosol Sci. Technol.*, *42* (1), 64-74, doi:10.1080/02786820701787944.

Stratmann, F., A. Kiselev, S. Wurzler, M. Wendisch, J. Heintzenberg, R. J. Charlson, K. Diehl, H. Wex, and S. Schmidt (2004), Laboratory studies and numerical simulations of cloud droplet formation under realistic supersaturation conditions, *J. Atmos. Ocean. Tech.*, *21* (6), 876-887.

Vali, G. (1994), Freezing rate due to heterogeneous nucleation *J. Atmos. Sci.*, *51* (18), 2683-2683.

Vali, G. (2008), Repeatability and randomness in heterogeneous freezing nucleation, *Atmos. Chem. Phys.*, *8* (16), 5017-5031.

Wilck, M., F. Stratmann, and E. R. Whitby (2002), A fine particle model for FLUENT: Description and application., paper presented at Proc. Sixth Int. Aerosol Conf., Chinese Association for Aerosol Research in Taiwan/International Aerosol Research Assembly, Taipei, Taiwan.

Yuskiewicz, B. A., F. Stratmann, W. Birmili, A. Wiedensohler, E. Swietlicki, O. Berg, and J. Zhou (1999), The effects of in-cloud mass production on atmospheric light scatter, *Atmos. Res.*, *50* (3-4), 265-288.

Zobrist, B., T. Koop, B. P. Luo, C. Marcolli, and T. Peter (2007), Heterogeneous ice nucleation rate coefficient of water droplets coated by a nonadecanol monolayer, *J. Phys. Chem. C*, *111* (5), 2149-2155, doi:10.1021/jp066080w.

Zobrist, B., C. Marcolli, T. Peter, and T. Koop (2008), Heterogeneous ice nucleation in aqueous solutions: the role of water activity, *J. Phys. Chem. A*, *112* (17), 3965-3975, doi:10.1021/jp7112208.

Zuberi, B., A. K. Bertram, C. A. Cassa, L. T. Molina, and M. J. Molina (2002), Heterogeneous nucleation of ice in (NH4)(2)SO4-H2O particles with mineral dust immersions, *Geophys. Res. Lett.*, *29* (10), 4, 1504, doi:10.1029/2001gl014289.

Funding

- German Research Foundation (DFG), Bonn, Germany (DFG project under contract HE 939/21-1)
- Helmholtz Association, Bonn, Germany (Helmholtz Virtual Institute “Aerosol-Cloud Interactions”)
- the EC 6th Framework Programme, Wuppertal, Germany (research project EUROCHAMP, Section “Support for Research Infrastructures – Integrated Infrastructure Initiative”)
- Alexander von Humboldt Foundation

Cooperation

- Department of Physics, Michigan Tech University, Houghton, Michigan, USA
- ICG-II, Research Centre Juelich, Juelich, Germany
- Particle Chemistry Department, Max Planck Institute for Chemistry, Mainz , Germany
- Institute for Atmospheric Physics, Johannes Gutenberg University, Mainz, Germany
- Department of Atmospheric Science, Colorado State University, Fort Collins, Colorado, USA
- Institute of Atmospheric and Climate Science, Swiss Federal Institute of Technology Zurich, Zurich, Switzerland
- Institute for Atmospheric and Environmental Sciences, Goethe University, Frankfurt am Main, Germany
- Joint Institute for the Study of the Atmosphere and the Ocean, University of Washington, Seattle, Washington, USA

Deliquescence/efflorescence hysteresis of hygroscopic particles

Olaf Hellmuth[1], Alexander K. Shchekin[2], Ilya V. Shabaev[2], Jeannine Katzwinkel[1]

[1] Leibniz Institute for Tropospheric Research (IfT), Leipzig, Germany
[2] St. Petersburg State University, St. Petersburg, Russia

Auf der Grundlage einer verallgemeinerten thermodynamischen Theorie sowie der klassischen Nukleationstheorie werden Untersuchungen zum Wachstum/Schrumpfen von hygroskopischen Partikeln während der Hydrierung/Dehydrierung in der Atmosphäre durchgeführt. Das spezielle Interesse gilt hierbei der Beschreibung des „Memory"-Effektes, der durch die Deliqueszenz/Effloreszenz-Hysterese während des Wachstums- und Schrumpfungsprozesses in einer turbulenten Umgebung verursacht wird. Die Theorie gestattet die Bestimmung messbarer physikalischer Eigenschaften, wie des Feuchtewachstumsfaktors als Funktion der relativen Feuchte sowie der Deliqueszenz- und Effloreszenzfeuchte. Es werden Ergebnisse für einen aquatischen NaCl-Lösungstropfen diskutiert.

Introduction

The atmospheric aerosol contains a significant fraction of soluble substances (mostly salts) having a strong affinity for moisture. Due to their ability to absorb water molecules from the ambient air, such substances are called hygroscopic. When the ambient relative humidity (RH) is sufficiently high, the water uptake continues until the hygroscopic particle completely dissolves in the absorbed water, in this way forming a pure solution droplet. The transition from partial to complete dissolution is called deliquescence, and the RH threshold at which a soluble particle completely dissolves is called deliquescence humidity (DRH). Deliquescence of particles of highly soluble substances occurs at subsaturation of the ambient water vapor with respect to a flat surface of pure bulk water. We will show, that the deliquescence sets in at water vapor saturation with respect to the curved surface of the solution droplet. This stage corresponds to the point of intersection of the condensate chemical potential curve with the line of the vapor chemical potential. The reverse process, called efflorescence (or crystallization), leads to hydrosol formation by precipitation of solid crystals from the solution within evaporating droplets. Crystallization performs via two steps: homogeneous nucleation of a supercritical nanocrystal from solute molecules and its subsequent growth. The crystallization is driven by the supersaturation of the solution, which depends on ambient temperature and ambient relative humidity. The ambient relative humidity at which efflorescence sets in at a fixed temperature, is called efflorescence humidity (ERH).

The difference between DRH and ERH results in a hysteresis effect during hydration and dehydration of a hygroscopic particle. Due to this hysteresis effect the aggregate state of atmospheric particles depends not only on thermodynamic state parameters but also on their anamnesis. In this way, the evolution of hygroscopic particles is affected by a memory effect.

The aggregate state of hygroscopic particles has a strong impact on atmospheric radiation and chemistry [*Wang et al.,* 2008a,b]. Solid particles may serve as ice nuclei and influence cirrus formation. Aqueous particles have larger mass extinction efficiency but a smaller backscattered fraction than their solid counterparts. Furthermore, they may act as chemical microreactors for hydrolysis, secondary organic aerosol formation, micellization, heterogeneous surface reactions etc. Owing to the high variability of the relative humidity in the planetary boundary layer, hysteresis effects were found to effectively impact the partitioning between solid and aqueous phases of tropospheric sulphate-ammonium particles on a global scale [*Wang et al.,* 2008a]. Moreover, such effects were reported to have a significant impact on the sulphate direct climate forcing (SDFC). Depending on how these effects were parameterized in a global 3-D chemical transport model, an uncertainty in the SDFC of 23 % on the global scale, but of much higher values on regional scales have been found from sensitivity studies [*Wang et al.,* 2008b].

Here, we employ a theoretical approach to determine both the hygroscopic growth factor of a hygroscopic particle as a function of ambient vapor saturation ratio, as well as the vapor saturation thresholds at the deliquescence and efflorescence transition. The present theory dispenses the application of the capillary approximation and employs instead of this the mechanical and thermodynamic concept of the disjoining pressure. The approach is based on the thermodynamic theory of thin solution films developed by *Djikaev* [2002], *Djikaev et al.* [2001a,b], *Kuni et al.* [2001], *Shchekin and Rusanov* [2008], *Shchekin et al.* [1993, 2008],

Tatianenko et al. [2000], and on the classical nucleation theory (CNT) [*Seinfeld and Pandis*, 1998, Chapter 10, *Pruppacher and Klett*, 1998, Chapter 7] . The predictive power of the present approach is examined for a sodium chloride particle in a water vapor environment.

Basic scenario and assumptions

We will use a three-phase model of *Shchekin et al.* [2008], which is based on the following geometrical, thermodynamical, and physicochemical assumptions (cf. Fig. 1):

1. In the initial state, the system consists of a solid soluble core of phase γ, which is embedded in a solvent vapor of phase β. The whole system captures the volume V and has the temperature T. In the equilibrium state, the system consists of a droplet, which is embedded in the solvent vapor of phase β, whereas the droplet consists of a partially dissolved residual core (condensation nucleus (CN)) of phase γ, enveloped by a thin liquid film of phase α. The three phases are separated from each other by interfaces, which are fully characterized by the bulk surface tensions of the liquid/vapor, vapor/solid, and liquid/solid interfaces, $\sigma_{\alpha\beta}^{(\infty)}$, $\sigma_{\beta\gamma}^{(\infty)}$, and $\sigma_{\alpha\gamma}^{(\infty)}$, as well as by the disjoining pressure of a thin liquid film, Π_D. If the chemical potential of the solvent vapor approaches a certain threshold value, the residual core completely dissolves forming a solution droplet. This is the deliquescence transition. If the chemical potential of the solvent vapor decreases below another certain threshold value, a new germ of phase γ will reappear and rapidly grow to form a new core within a droplet. This is the efflorescence transition.
2. The volume V, the temperature T, and the number of molecules of every component stay fixed in both states of the system.
3. The initial solid core, its residue, and the equilibrium droplet are assumed to have a spherical form. The initial core has the radius R_n and volume $V_{R_n} = 4\pi R_n^3/3$, its residue the radius R_n' and volume $V_{R_n'} = 4\pi R_n'^3/3$, and the droplet the radius R (equal to the radius of the outer surface of the film) and volume $V_R = 4\pi R^3/3$. The numbers of solute molecules in the initial core, ν_n, of solute molecules in the residual core, ν_n', and of solvent molecules in the condensate film, ν, obey the law of mass conservation:

$$\nu\left(R, R_n'\right) = \frac{V_R - V_{R_n'} - \upsilon_n^{\alpha}\left(\nu_n - \nu_n'\right)}{\upsilon^{\alpha}}, \qquad (1)$$

$$\nu_n = \frac{4\pi R_n^3}{3\upsilon_n}, \quad \nu_n'\left(R_n'\right) = \frac{4\pi R_n'^3}{3\upsilon_n}.$$

Here, υ^{α} denotes the volume of a solvent molecule in the film, υ_n^{α} the volume of a solute molecule in the film, and υ_n the volume of a molecule of the substrate matter of the core. The film thickness is given by $h = R - R_n'$. The liquid film forms a solution with the relative solute concentration (molality), x, which is defined by the number of solute molecules per number of solvent molecules:

$$x\left(R, R_n'\right) = \frac{\nu_n - \nu_n'\left(R_n'\right)}{\nu\left(R, R_n'\right)}. \qquad (2)$$

The disjoining pressure of a thin liquid film, Π_D, is approximated by the following function [*Derjaguin*, 1987, *Marčelja and Radić*, 1976]:

$$\Pi_D\left(R, R_n'\right) \approx K^{(*)} \exp\left(-\frac{R - R'}{l^{(*)}}\right), \qquad (3)$$

$$K^{(*)} = \frac{s}{l^{(*)}}, \quad s = \sigma_{\beta\gamma}^{(\infty)} - \left(\sigma_{\alpha\beta}^{(\infty)} + \sigma_{\alpha\gamma}^{(\infty)}\right).$$

Here, $K^{(*)}$ denotes a characteristic pressure scale, $l^{(*)} \propto \left(\upsilon^{\alpha}\right)^{1/3}$ a characteristic correlation length scale of the condensation film around the nucleus (order of the intermolecular separation), and s is the spreading coefficient. A spreading coefficient $s > 0$ refers to complete wetting of the core surface by the liquid film, $s = 0$ to the formation of the equilibrium film, and $s < 0$ to the disappearance of the film and the formation of a lens-like cluster of the new phase on the surface of the pre-existing core (Young equilibrium, contact angle concept, cf. *Pruppacher and Klett* [1998, Sections 9.1.3.1-9.1.3.2]).

4. The matter of the soluble condensation nucleus is an electrolyte, which dissociates into ions under dissolution in a polar condensate. For a solute molecule AB, which is dissolved in a solvent and thereby dissociates into a number z_+ of cations A^+ and a number z_- of anions B^- the dissociation equilibrium reads:

$$AB \rightleftarrows z_+ A^+ + z_- B^-$$

5. The liquid film and the solid nucleus are assumed to be incompressible.
6. The bulk surface tensions of the liquid/vapor, vapor/solid, and liquid/solid interfaces and the partial molecular volumes are assumed to be independent of the solution concentration.
7. The dependence of the disjoining pressure, required to describe the specific properties of a thin liquid film, on the solution concentration is neglected. This is justified by the fact, that the solution concentration in thin films is almost constant and approaches the solubility of the nucleus matter at equilibrium with a flat interface between the solid phase of the nucleus substance and the solution.

The equilibrium conditions

Based on the assumptions above, the theory predicts two equilibrium conditions to fully characterize the droplet in thermodynamic equilibrium [*Shchekin et al.*, 2008, *Hellmuth et al.*, 2009]:

a) the "external solvent equilibrium" between the solvent in the vapor phase β and the solvent in the liquid phase α,

b) the "internal solute equilibrium" between the solute in the residual solid phase γ and the solute in the liquid phase α.

To describe the external equilibrium one arrives at a generalization of the Gibbs-Kelvin-Köhler (GKK) equation of the theory of nucleation on wettable soluble particles, here formulated in the form of an implicit function F_{GKK} [cf. *Hellmuth et al.,* 2009, Eq. (41) therein]:

$$F_{\mathrm{GKK}}\left(S^{\beta},R,R'_{\mathrm{n}}\right)\Big|_{\substack{T=\mathrm{const}\\R_{\mathrm{n}}=\mathrm{const}}} = -k_{\mathrm{B}}T\ln S^{\beta} - k_{\mathrm{B}}T\left(z_{+}+z_{-}\right)x\left(R,R'_{\mathrm{n}}\right)+\frac{2\sigma^{(\infty)}_{\alpha\beta}\upsilon^{\alpha}}{R} - \left(\frac{R'_{\mathrm{n}}}{R}\right)^{2}\frac{s\upsilon^{\alpha}}{l^{(*)}}\exp\left(-\frac{R-R'_{\mathrm{n}}}{l^{(*)}}\right)=0. \tag{5}$$

Here, k_{B} denotes the Boltzmann constant, $S^{\beta}=p^{\beta}/p^{\beta}_{\infty}$ is the vapor saturation ratio, i.e., the ratio of the actual vapor pressure p^{β} to the equilibrium vapor pressure over a flat surface of the pure liquid p^{β}_{∞}, and x_{∞} is the solubility of the core matter at equilibrium with a flat interface between the solid phase of the core substance and the solution.

Determination of the vapor condensation growth factor

To determine the dependence of the droplet radius R on the vapor saturation ratio S^{β} at equilibrium between the droplet and the ambient vapor we have to distinguish the following cases:

1. If the initial core is only partially dissolved in the solution film (corresponding to the existence of an equilibrium residual core), we have to determine the thermodynamic conditions for both the external and internal equilibrium. Replacing R'_{n} in the Gibbs-Kelvin-Köhler Eq. (5) by the relation $R'_{\mathrm{n}}(R)$ from the Ostwald-Freundlich Eq. (6) provides a relation to determine $R\left(S^{\beta}\right)$:

$$\begin{aligned} F_{\mathrm{GKK}}\left(S^{\beta},R,R'\right)\Big|_{\substack{T=\mathrm{const}\\R_{\mathrm{n}}=\mathrm{const}}} &= 0\\ F_{\mathrm{OF}}\left(R,R'_{\mathrm{n}}\right)\Big|_{\substack{T=\mathrm{const}\\R_{\mathrm{n}}=\mathrm{const}}} &= 0\\ \hline F_{\mathrm{GKK+OF}}\left(S^{\beta},R\right)\Big|_{\substack{T=\mathrm{const}\\R_{\mathrm{n}}=\mathrm{const}}} &= 0. \end{aligned} \tag{7}$$

For given vapor saturation ratio S^{β} the droplet radius R is numerically determined as the root of the transcendental equation $F_{\mathrm{GKK+OF}}\left(S^{\beta},R\right)=0$ in Eq. (7) at fixed values of temperature T and initial core radius R_{n}. The solution of Eq. (7) directly provides the relation $R=f_{1}\left(T,R_{\mathrm{n}},S^{\beta}\right)$.

To describe the internal equilibrium one arrives at a generalization of the Ostwald-Freundlich (OF) equation of the theory of solutions, given in the form of an implicit function F_{OF} [cf. *Hellmuth et al.*, 2009, Eq. (42) therein]:

$$F_{\mathrm{OF}}\left(R,R'_{\mathrm{n}}\right)\Big|_{\substack{T=\mathrm{const}\\R_{\mathrm{n}}=\mathrm{const}}} = -k_{\mathrm{B}}T\left(z_{+}+z_{-}\right)\ln\left(\frac{x\left(R,R'_{\mathrm{n}}\right)}{x_{\infty}}\right)+\frac{2\upsilon_{\mathrm{n}}}{R'_{\mathrm{n}}}\left[\sigma^{(\infty)}_{\alpha\gamma}+s\exp\left(-\frac{R-R'_{\mathrm{n}}}{l^{(*)}}\right)\right] - \frac{2\sigma^{(\infty)}_{\alpha\beta}}{R}\left(\upsilon^{\alpha}_{\mathrm{n}}-\upsilon_{\mathrm{n}}\right)+\frac{s}{l^{(*)}}\exp\left(-\frac{R-R'_{\mathrm{n}}}{l^{(*)}}\right)\left[\upsilon_{\mathrm{n}}-\left(\frac{R'_{\mathrm{n}}}{R}\right)^{2}\left(\upsilon_{\mathrm{n}}-\upsilon^{\alpha}_{\mathrm{n}}\right)\right]=0. \tag{6}$$

2. If the initial core is completely dissolved in the solution droplet, we have to determine the thermodynamic conditions for the external equilibrium only. Considering $R_n' = 0$ (or $\nu_n' = 0$), the Gibbs-Kelvin-Köhler Eq. (5) reduces to:

$$F_{GKK}\left(S^\beta, R\right)\Big|_{\substack{T=\text{const}\\ R_n=\text{const}}} = 0\,. \tag{8}$$

Here, the second term on the right-hand side of Eq. (5) containing the relative solute concentration $x = \nu_n / \nu$ is retained, but the fourth term containing the disjoining pressure vanishes because of $R_n' = 0$. Then, the solution of Eq. (8) directly provides the relation $R = f_2\left(T, R_n, S^\beta\right)$.

3. If the initial core is insoluble we also have to determine the thermodynamic conditions for the external equilibrium only. Considering $R_n' = R_n$ (or $\nu_n' = \nu_n$) and $x = 0$, the Gibbs-Kelvin-Köhler Eq. (5)) reduces to:

$$F_{GKK}\left(S^\beta, R\right)\Big|_{\substack{T=\text{const}\\ R_n=\text{const}}} = 0\,. \tag{9}$$

Here, the second term on the right-hand side of Eq. (5) containing the relative solute concentration vanishes because of $x = 0$, but the fourth term containing the disjoining pressure is retained because of $\Pi_D \neq 0$. Then, the solution of Eq. (9) directly provides the relation $R = f_3\left(T, R_n, S^\beta\right)$.

Knowing the relation $R = f_i\left(T, R_n, S^\beta\right)$, the measurable vapor condensation growth factor GF can be determined as follows:

$$\mathrm{GF} = \frac{R}{R_n} = R_n^{-1} f_i\left(T, R_n, S^\beta\right), \quad i = 1,\ldots,3\,. \tag{10}$$

Determination of the deliquescence barrier of the vapor saturation ratio

Now, we want to determine the thermodynamic condition for the prompt transition from the equilibrium state with the partially dissolved residual core to the equilibrium state with the completely dissolved residual core (deliquescence stage) (cf. Fig. 1, middle and right picture). We recall, that the existence of an equilibrium aerosol state with a partially dissolved condensation nucleus requires the coeval fulfillment of both an external and an internal equilibrium condition (cf. Eqs. (5), (6)).

The generalized Ostwald-Freundlich Eq. (6) determines the number of solvent molecules, ν, as a function of the number of solute molecules in the residual core, ν_n', at which the residual core is in thermodynamic equilibrium with the enveloping solution film. The function $\nu\left(\nu_n'\right)$ reveals a maximum value ν_i, above which the condition for the internal equilibrium Eq. (6) is not satisfied any longer and the residual core will inevitably disappear. This maximum value sets an upper limit for the number of solvent molecules, at which the internal equilibrium with a residual core is fulfilled at a specified initial core radius R_n and temperature T.

The chemical potentials of the solvent molecules in the vapor phase, μ^β, and in the liquid phase, μ^ν, respectively, in thermal units $k_B T$, b^β and b_ν read (cf. *Hellmuth et al.* [2009, Eqs. (47)-(49) therein]):

$$b^\beta = \frac{\mu^\beta - \mu_\infty}{k_B T} = \ln S^\beta \tag{11}$$

By virtue of the validity of Eqs. (1), (2), and (6), the chemical solvent potential is a function of the number of solvent molecules $b_\nu = b_\nu(\nu)$ at fixed radius R_n and temperature T. One can show, that Eq. (12) has a maximum at certain $\nu = \nu_{th} < \nu_i$. This value establishes a threshold value S_{th}^β in such a way, that there is no solution of Eq. (5) at $S^\beta > S_{th}^\beta$. The property S_{th}^β defines the threshold, above which the prompt barrierless transition to the deliquescence stage sets in. Employing the external equilibrium condition $b_\nu = b^\beta$, the deliquescence threshold of the chemical potential of the solvent vapor, b_{th}^β, reads [cf. *Hellmuth et al.*, 2009, Eq. (50) therein]:

$$b_\nu = \frac{\mu_\nu - \mu_\infty}{k_B T} = -\left(z_+ + z_-\right)\left(\frac{\nu_n - \nu_n'\left(R_n'\right)}{\nu\left(R, R_n'\right)}\right) + \frac{\upsilon^\alpha}{k_B T}\left[\frac{2\sigma_{\alpha\beta}^{(\infty)}}{R} - \left(\frac{R_n'}{R}\right)^2 \left(\frac{s}{l^{(*)}}\right) \exp\left(-\frac{R - R_n'}{l^{(*)}}\right)\right]. \tag{12}$$

$$b_{th}^\beta = b_\nu\left(\nu_{th}\right) = -\left(z_+ + z_-\right)\left(\frac{\nu_n - \nu_n'\left(\nu_{th}\right)}{\nu_{th}}\right) + \frac{\upsilon^\alpha}{k_B T}\left[\frac{2\sigma_{\alpha\beta}^{(\infty)}}{R} - \left(\frac{R_n'\left(\nu_{th}\right)}{R\left(\nu_{th}\right)}\right)^2 \left(\frac{s}{l^{(*)}}\right) \exp\left(-\frac{R\left(\nu_{th}\right) - R_n'\left(\nu_{th}\right)}{l^{(*)}}\right)\right]. \tag{13}$$

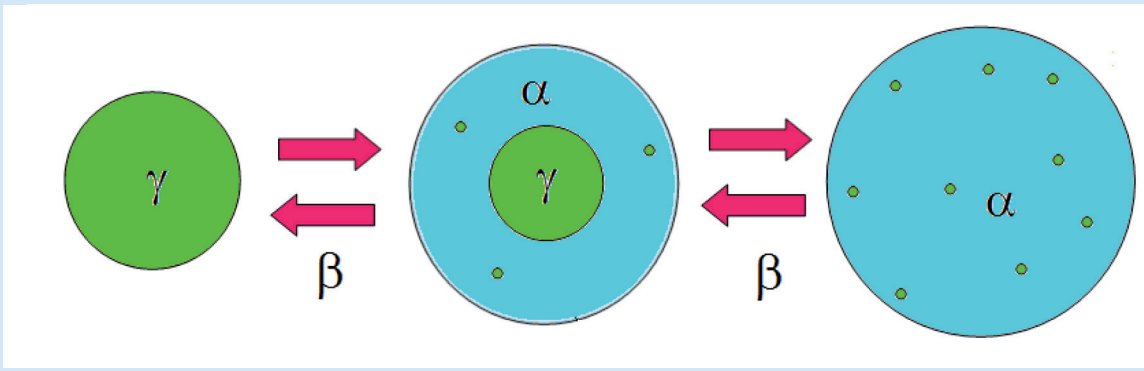

Fig. 1: Core-shell aggregate in an ambient vapor. Initial state (left): solid soluble core (phase γ) with radius R_n, embedded in a solvent vapor (phase β). Equilibrium state I (middle): ambient vapor (phase β) enclosing a droplet with radius R, which consists of a residual core (phase γ) with radius R_n' and an enveloping thin liquid film (phase α) with thickness $h = R - R_n'$. Equilibrium state II (deliquescence transition, right): ambient vapor (phase β) enclosing a solution droplet (phase α) with radius R, corresponding to a completely dissolved residual core at a chemical potential of the solvent vapor above a well-defined threshold value. By decreasing the chemical potential of the solvent vapor below another well-defined threshold value the system moves to the efflorescence transition.

Correspondingly, the deliquescence vapor saturation ratio is given by:

$$S_{th}^{\beta} = S_{del}^{\beta} = \exp\left(b_{th}^{\beta}\right) . \qquad (14)$$

Efflorescence behavior from classical nucleation theory

Basic scenario and assumptions. The prompt transition from a droplet with a homogeneous solution to a solution droplet with a stable crystal core is called efflorescence transition. It performs via homogeneous crystallization, i.e., the precipitation of solute crystals from a supersaturated solution droplet. We assume, that efflorescence is the result of only one successful crystallization event inside the solution droplet. This assumption implies, that the growth rate of a single supercritical solute crystal is very large at the solution supersaturation, at which homogeneous crystallization takes place. Thus, the first supercritical crystal germ formed can grow quickly enough to aggregate a stable equilibrium core inside the droplet before any other supercritical crystal germ is formed. Additionally it can be assumed, that the primary germ formation is favored over the secondary one due to the latent heat release during germ growth, which immediately raises the temperature of the solution in the droplet. This reduces the solution supersaturation and, consequently, the rate of homogeneous crystallization to a very small value. Moreover, homogeneous nucleation considered here performs in a very small volume (like in a molecular dynamics cell). In such an environment the formation of a single supercritical embryo is sufficient to decrease the solution supersaturation and to prevent further nucleation events.

Efflorescence condition. Employing the classical nucleation theory (CNT), the efflorescence condition reads [cf., e. g, *Gao et al.,* 2007, *Onasch et al.,* 2000]:

$$J_{hom}\big|_{effl} = \frac{1}{V_R\big|_{effl}\, t_{ind}} . \qquad (15)$$

Here, J_{hom} denotes the rate of homogeneous crystallization, $V_R\big|_{effl} = 4\pi R_{effl}^3/3$ the volume of the solution droplet at the onset of efflorescence, and t_{ind} the induction time, defined as the time the system spent at constant droplet composition prior to nucleation. The time t_{ind} can be considered as the latency time required for the appearance of a supercritical embryo.

The rate of homogeneous crystallization is obtained from the CNT:

$$J_{hom} = J_{hom,0} \exp\left(-\frac{\Delta F^*}{k_B T}\right) , \quad J_{hom,0} = n_n \left(\frac{k_B T}{h}\right) \exp\left(-\frac{\Delta g}{k_B T}\right) , \qquad (16)$$

$$\frac{\Delta F^*}{k_B T} = \frac{16\pi}{3} \frac{\left(\sigma_{\alpha\beta}^{(\infty)}\right)^3 \upsilon_n^3}{\left(k_B T\right)^3 \left(\ln S^{\alpha}\right)^3} , \quad S^{\alpha} \approx \frac{x}{x_{\infty}} .$$

In Eq. (16) the symbol $J_{hom,0}$ denotes the kinetic prefactor of the homogeneous nucleation rate, and the term $\Delta F^* / \left(k_B T\right)$ the free energy in thermal units, required to form a critical embryo of the new phase (crystal) from its mother phase (solution).

In the expression for the kinetic prefactor, the property $n_n = 1/\upsilon_n$ denotes the molecular concentration of the solute in the crystalline nucleus (with υ_n the already introduced molecular volume of the substrate matter). The terms $k_B T/h$ and $\Delta g/k_B T$ are the frequency and free energy barrier in thermal units of a solute molecule to jump from the solution to the crystalline nucleus. The critical formation work ΔF^* is a nonlinear function of the solution saturation ratio S^α, which is determined by the ratio of the relative solute concentration to the solubility of the substrate matter. The other symbols have been introduced above.

Combining Eqs. (15) and (16), we obtain a transcendental equation for the determination of the relative solute concentration at the efflorescence transition, x_{effl}:

$$\left.\begin{aligned} F_{nuc}\left(R\left(x_{effl}\right)\right)\Big|_{\substack{T=const\\R_n=const\\R_n'=0}} &= 0 \\ F_{GKK}\left(S^\beta_{effl}, R_{effl}, x_{effl}\right)\Big|_{\substack{T=const\\R_n=const\\R_n'=0}} &= 0 \\ F_{sphere}\left(R_{effl}, x_{effl}\right)\Big|_{\substack{T=const\\R_n=const\\R_n'=0}} &= 0 \\ \hline F_{nuc+GKK+sphere}\left(S^\beta_{effl}\right) &= 0\,. \end{aligned}\right. \qquad (20)$$

Combining the first three equations yields a transcendental equation (cf. last equation), the root of which is the efflorescence vapor saturation ratio S^β_{effl}.

$$F_{nuc}\left(R\left(x_{effl}\right)\right)\Big|_{\substack{T=const\\R_n=const\\R_n'=0}} = \left[\frac{16\pi}{3}\left(\frac{\sigma^{(\infty)}_{\alpha\beta}}{k_B T}\right)^3 \frac{\upsilon_n^2}{\ln\left[\frac{4\pi}{3}\left(R\left(x_{effl}\right)\right)^3 J_{hom,0}\, t_{ind}\right]}\right]^{1/2} - \ln\left(\frac{x_{effl}}{x_\infty}\right) = 0\,. \qquad (17)$$

To find the root of Eq. (17) the dependence of the droplet radius on the relative solute concentration, $R\,(x)$, must be known. The inverse function, $x\,(R)$, is given by the generalized Gibbs-Kelvin-Köhler equation for the completely dissolved residual core, Eq. (5):

$$F_{GKK}\left(S^\beta, R, x\right)\Big|_{\substack{T=const\\R_n=const\\R_n'=0}} = -k_B T \ln S^\beta - k_B T\left(z_+ + z_-\right)x + \frac{2\sigma^{(\infty)}_{\alpha\beta}\upsilon^\alpha}{R} = 0\,. \qquad (18)$$

Equation (18) is also valid at the relative solute concentration at the efflorescence transition, i. e., at x_{effl}. Both Eqs. (17) and (18) are two equations for the three unknown variables x_{effl}, R_{effl}, and S^β_{effl}, i. e., the problem is underdetermined. To close the system, we employ the law of mass conservation given by Eqs. (1) and (2):

$$F_{sphere}\left(R, x\right)\Big|_{\substack{T=const\\R_n=const\\R_n'=0}} = x - \frac{\upsilon^\alpha R_n^3}{\upsilon_n R^3 - \upsilon_n^\alpha R_n^3} = 0\,. \qquad (19)$$

With Eqs. (17), (18), and (19) , we have three equations to determine the relative solute concentration x_{effl}, the droplet radius R_{effl}, and the vapor saturation ratio S^β_{effl} at the onset of efflorescence:

Application to the sodium-chlorid/water aerosol system

Model setup. The model parameters for the determination of the vapor condensation growth factor and the deliquescence/efflorescence vapor saturation ratios for the sodium chloride (NaCl)/water system are given in Tab. 1.

From laboratory studies *Biskos et al.* [2006] derived the following power law fits to describe the size dependence of the deliquescence and efflorescence relative humidity values, DRH and ERH, of NaCl particles with dry mobility equivalent diameters in the range 6 nm < $D_{m,dry}$ < 60 nm:

$$\frac{DRH_{Biskos}}{[\%]} = 213\left(\frac{D_{m,dry}}{[nm]}\right)^{-1.6} + 76\,, \qquad (21)$$

$$\frac{ERH_{Biskos}}{[\%]} = 213\left(\frac{D_{m,dry}}{[nm]}\right)^{-1.65} + 44\,.$$

For the present purposes we replace the dry mobility equivalent diameter, $D_{m,dry}$, by the dry volume equivalent diameter, $D_{V,dry}$.

The saturation ratio of the solvent molecule activities in the droplet, $S_\nu = \exp(b_\nu)$, according to the generalized Ostwald-Freundlich Eq. (6)

Parameter	Value	Reference
T	= 298 K	Prescribed
R_n	= 15 x 10^{-9} m	Prescribed
z_+	= 1	Prescribed
z_-	= 1	
υ_n	= 4.49 x 10^{-29} m^3	Table values
υ_α	= 3.0 x 10^{-29} m^3	
υ_n^α	= 3.06 x 10^{-29} m^3	
$l^{(*)}$	= 3 x 10^{-10} m	Marčelja and Radić [1976]
$\sigma_{\alpha\beta}^{(\infty)}$	= 0.083 ± 0.002 J/m^2	Russell and Ming [2002]
$\sigma_{\beta\gamma}^{(\infty)}$	= 0.213 (0.1-0.27) J/m^2	Russell and Ming [2002]
$\sigma_{\alpha\gamma}^{(\infty)}$	= 0.029 ± 0.020 J/m^2	Russell and Ming [2002]
$\sigma_{\alpha\gamma}^{(\infty)}$	= 0.0895 J/m^2	Gao et al. [2007]
x_∞	$= 0.1805 - 5.310\times10^{-4}T + 9.965\times10^{-7}T^2$ $x_\infty(T = 298\,\mathrm{K}) = 0.111$	Seinfeld and Pandis [1998]
x_∞	= 0.20	Russell and Ming [2002]
$\Delta g/k_B T$	= 6	Onasch et al. [2000]
t_{ind}	= 1 s	Gao et al. [2007]

Tab. 1: *Specification of the model parameters for the NaCl/H_2O system.*

Results. Numerical studies revealed a high sensitivity of the DRH on x_∞ and of the ERH on $\sigma_{\alpha\gamma}^{(\infty)}$. Therefore, we varied both parameters within their limits (cf. Tab. 1) to approach the observed values of DRH and ERH. The best agreement between the model and the observations was obtained for $x_\infty = 0.17$ and for $\sigma_{\alpha\gamma}^{(\infty)} = 0.0711\,\mathrm{J/m^2}$. With these parameters the predicted deliquescence relative humidity amounts $DRH_{Model} = 75.6\,\%$, which is close to the experimental value $DRH_{Biskos} = 76.9\,\%$. The predicted efflorescence humidity amounts $ERH_{Model} = 44.8\,\%$, which agrees with the experimental value $ERH_{Biskos} = 44.8\,\%$.

The solution of the generalized Ostwald-Freundlich Eq. (6) is shown in Fig. 2. The relation $\nu = \nu(\nu_n')$ represents the number of solvent molecules in the liquid solution film as the function of the number of solute molecules in the residual core at which the internal thermodynamic equilibrium is fulfilled. The number ν_i denotes the upper limit of the number of solvent molecules, above which the equilibrium with a core does not hold any longer and the residual core disappears.

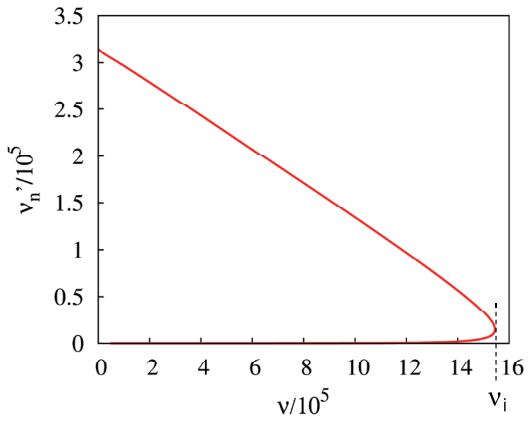

Fig. 2: *Solution $\nu = \nu(\nu_n')$ of the generalized Ostwald-Freundlich Eq. (6), and the value ν_i.*

and Eq. (12) is depicted in Fig. 3. The disjoining pressure vanishes for a bulk liquid film, but becomes important for very thin films. According to Eq. (12), the term containing the disjoining pressure enters the chemical potential of the

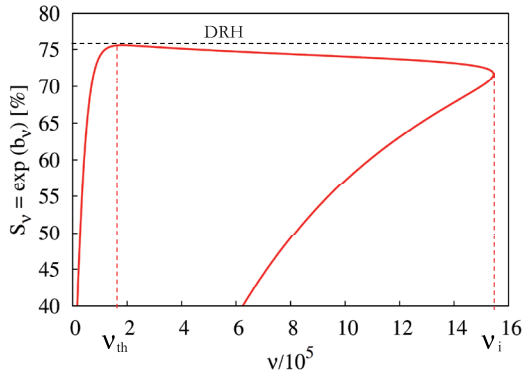

Fig. 3: *Saturation ratio of the solvent molecule activities in the liquid phase, S_ν, according to Eq. (12), and deliquescence threshold of the saturation ratio of the solvent vapor,* $\mathrm{DRH} = S^{\beta}_{del}$, *from Eqs. (13) and (14).*

solvent in the liquid phase, b_ν, with a negative sign. In this way, b_ν can assume very low values, i. e., well below the chemical potential of the solvent vapor, especially at the beginning of water adsorption at the surface of a hygroscopic particle, when the film is very thin. This fact is the *conditio sine qua non* for the water adsorption in the early stage of hygroscopic growth. Without the consideration of the disjoining pressure it is not possible to describe this early stage within the framework of classical thermodynamics. Also presented in Fig. 3 is the deliquescence barrier of the saturation ratio of the solvent vapor, $\mathrm{DRH} = S^{\beta}_{del}$, which is obtained from Eqs. (13) and (14).

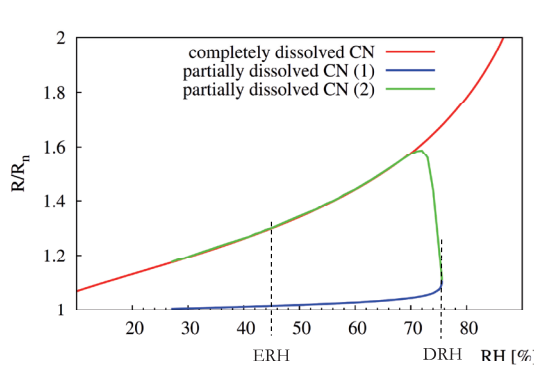

Fig. 4: *Hygroscopic growth factor,* $\mathrm{GF} = R/R_n$, *according to Eq. (10), determined from the solutions of the generalized Gibbs-Kelvin-Köhler and Ostwald-Freundlich equations, Eqs. (5) and (6), the deliquescence relative humidity,* $\mathrm{DRH} = S^{\beta}_{del}$, *from Eqs. (13) and (14), and the efflorescence relative humidity, the efflorescence relative humidity,* $\mathrm{ERH} = S^{\beta}_{effl}$, *as the solution of Eq. (20). Blue (1) and green graphs (2): partially dissolved residual core according to the conditions in Section 4, item 1. Red graph: completely dissolved residual core according to the conditions in Section 4, item 2.*

The hygroscopic growth factor $\mathrm{GF} = R/R_n$ (from Eqs. (5), (6), and (10)), the deliquescence relative humidity $\mathrm{DRH} = S^{\beta}_{del}$ (from Eqs. (13) and (14)), and the efflorescence relative humidity $\mathrm{ERH} = S^{\beta}_{effl}$ (from Eq. (20)), are shown in Fig. 4. The blue (1) and green graphs (2) represent the growth factors for the aerosol with the partially dissolved residual core according to item 1 in Section 4, the red graph the one with the completely dissolved residual core according to item 2 of Section 4. At RH < ERH, there exist two physically sound equilibrium states of the aerosol (graph (1) and (2), core-shell aggregate), in the range ERH < RH < DRH there are three different equilibrium states (core-shell-aggregate and solution droplet), and at RH > DRH there exists only one equilibrium state (solution droplet).

Conclusions

In an ambient atmosphere of a solvent vapor with turbulence-induced temperature and humidity fluctuations the particle may undergo a strongly nonlinear hygroscopic growth:

1. Starting with the dry particle, GF=1, the hygroscopic growth follows the blue graph in Fig. 4 for RH < DRH.
2. At RH=DRH the growth factor performs a jump and increases further along the red graph for RH > DRH. Decreasing RH below DRH again, the hygroscopic growth remains on the red graph until RH=ERH.
3. At RH=ERH efflorescence sets in and the growth factor follows the green line for ERH < RH < DRH.

The present approach provides a generalized theoretical framework to describe the hysteresis effects during hydration/dehydration of hygroscopic salts. The model was found to be very sensitive against the solubility of the hygroscopic condensation nucleus and the surface tension of the solid/liquid interface. By means of the present approach, these parameters can be estimated on the basis of observed values of the DRH and ERH.

Acknowledgement

I. Shabaev thanks for support by the Russian Fond for Basic Research (Grant No. 09-03-01005-a) and the Government of St. Petersburg (Grant 2.4/04-05/092).

References

Biskos, G., A. Malinowski, L. M. Russell, P. R. Buseck, and S. T. Martin (2006), Nanosize effect on the deliquescence and the efflorescence of sodium chloride particles, *Aerosol Sci. Technol.*, *40* (2), 97-106, doi:10.1080/02786820500484396.

Derjaguin, B. V., N. V. Churaev, and V. M. Muller (1987), *Surface forces*, Consultants Bureau, New York.

Djikaev, Y. S. (2002), Kinetics of fluctuational deliquescence, *J. Chem. Phys.*, *116* (22), 9865-9874.

Djikaev, Y. S., R. Bowles, and H. Reiss (2001a), Role of constraints in the thermodynamics of heterogeneous condensation on solid soluble particles: Failure of the capillarity approximation, *Physica A*, *298*, 155-176.

Djikaev, Y. S., R. Bowles, and H. Reiss (2001b), Theory of size dependent deliquescence of nanoparticles: Relation to heterogeneous nucleation and comparison with experiments, *J. Phys. Chem. B*, *105*, 7708-7722.

Gao, Y., S. B. Chen, and L. E. Yu (2007), Efflorescence relative humidity of airborne sodium chloride particles: A theoretical investigation, *Atmos. Environ.*, *41*, 2019-2023, doi:10.1016/j.atmosenv.2006.2012.2014.

Hellmuth, O., A. K. Shchekin, and I. Shabaev (2009), Deliquescence/efflorescence hysteresis of hygroscopic particles: Deductions from thermodynamic and kinetic theory, *Atmos. Res.*, submitted (Ms. Ref. No. ATMOSRES-D-09-0035).

Kuni, F. M., A. K. Shchekin, and A. P. Grinin (2001), Theory of heterogeneous nucleation for vapour undergoing a gradual metastable state formation process, *Physics Uspekhi*, *44* (4), 331-370.

Marčelja, S., and N. Radić (1976), Repulsion of interfaces due to boundary water, *Chem. Phys. Lett.*, *42* (1), 129-130.

Onasch, T. B., R. McGraw, and D. Imre (2000), Temperature-dependent heterogeneous efflorescence of mixed ammonium sulfate/calcium carbonate particles, *J. Phys. Chem. A*, *104* (46), 10797-10806, doi:10.11021/jp0024064.

Pruppacher, H. R., and J. D. Klett (1997), *Microphysics of clouds and precipitation*, Kluwer Academic Publishers, Dordrecht ; Boston.

Russell, L. M., and Y. Ming (2002), Deliquescence of small particles, *J. Chem. Phys.*, *116* (1), 311-321, doi:10.1063/1061.1420727.

Seinfeld, J. H., and S. N. Pandis (1998), *Atmospheric chemistry and physics : From air pollution to climate change*, John Wiley & Sons, New York.

Shchekin, A. K., and A. I. Rusanov (2008), Generalization of the Gibbs-Kelvin-Köhler and Ostwald-Freundlich equations for a liquid film on a soluble nanoparticle, *J. Chem. Phys.*, *129*, 154116, doi:10.151063/154111.2996590.

Shchekin, A. K., A. I. Rusanov, and F. M. Kuni (1993), Thermodynamics of condensation on soluble nuclei of colloidal surfactants, *Colloid Journal of the Russian Academy of Sciences*, *55* (2), 227-234.

Shchekin, A. K., I. V. Shabaev, and A. I. Rusanov (2008), Thermodynamics of droplet formation around a soluble condensation nucleus in the atmosphere of a solvent vapor, *J. Chem. Phys.*, *129*, 214111, doi:10.1063/1.3021078.

Tatianenko, D. V., A. K. Shchekin, and F. M. Kuni (2000), On the conditions imposed on the spreading coefficient and the nucleus size in the theory of nucleation on wettable insoluble nuclei, *Colloid Journal*, *62* (4), 479-486.

Wang, J., A. A. Hoffmann, R. J. Park, D. J. Jacob, and S. T. Martin (2008a), Global distribution of solid and aqueous sulfate aerosols: Effect of the hysteresis of particle phase transitions, *J. Geophys. Res.*, *113* (D11), D11206, doi:10.11029/12007JD009367.

Wang, J., D. J. Jacob, and S. T. Martin (2008b), Sensitivity of sulfate direct climate forcing to the hysteresis of particle phase transitions, *J. Geophys. Res.*, *113* (D11), D11207, doi:10.11029/12007JD009368.

Cooperation

- St. Petersburg State University, Research Institute of Physics, Department of Statistical Physics, St. Petersburg, Russia
- Bogoliubov Laboratory of Theoretical Physics, Joint Institute for Nuclear Research, Dubna, Russia

The first year of continuous aerosol observations in the German Ultrafine Aerosol Network (GUAN)

Wolfram Birmili[1], Kay Weinhold[1], Stephan Nordmann[1], Alfred Wiedensohler[1], Stephan Mertes[1], Gerald Spindler[1], Konrad Müller[1], Hartmut Herrmann[1], Thomas Gnauk[1], Mike Pitz[2], Josef Cyrys[2], Harald Flentje[3], Carmen Nickel[4], Thomas A.J. Kuhlbusch[4], Gunter Löschau[5], Frank Meinhardt[6], Andreas Schwerin[6], Ludwig Ries[6], Klaus Wirtz[6]

[1] Leibniz Institute for Tropospheric Research (IfT), Leipzig, Germany
[2] German Research Center for Environmental Health (HZM), Neuherberg, Germany
[3] German Weather Service (DWD), Hohenpeissenberg, Germany
[4] Institute of Energy and Environmental Technology (IUTA), Duisburg, Germany
[5] Saxonian office for the Environment, Agriculture, and Geology (LfULG), Dresden, Germany
[6] German Federal Environment Agency (UBA), Messnetzzentrale, Langen, Germany

Seit Ende 2008 koordiniert das IfT den Betrieb des Deutschen Beobachtungsnetzes für Ultrafeine Aerosolpartikel (GUAN - German Ultrafine Aerosol Network). Dieses weltweit einzigartige Netz bodengestützter In-Situ-Beobachtungen zielt auf eine genauere Beschreibung des atmosphärischen Aerosols sowohl bezüglich seiner Gesundheits- als auch Klimaauswirkungen ab. Zu den gemessenen Parametern gehören die Partikelanzahlgrößenverteilung, die Massenkonzentration von Ruß und die größenaufgelöste chemische Zusammensetzung der Partikel an bis zu dreizehn Beobachtungspunkten in Deutschland. Datenerfassung, Datenauswertung und Qualitätssicherung finden erstmals unter einem Dach statt und sichern eine hohe Qualität und Vergleichbarkeit der Daten. Intensive Feldmesskampagnen zur Erlangung eines besseren Prozessverständnisses runden die Aktivitäten ab. Die Beobachtungen des ersten kompletten Jahres 2009 zeigen den hohen Wert der Messdaten, standortabhängige wie auch jahreszeitliche Trends im atmosphärischen Aerosol über Mitteleuropa zu verstehen. Hauptresultat ist, dass die Partikelanzahl durch lokale Prozesse, die Partikelmasse durch Prozesse auf der synoptischen Skala bestimmt wird. Die Rußmassenkonzentration wird durch Prozesse auf beiden Skalen bestimmt. Die kontinuierlich gesammelten Daten eignen sich ideal zur Validierung regionaler und globaler Aerosoltransportmodelle im Hinblick auf Klima- und Gesundheitseffekte in Mitteleuropa.

Introduction

Aerosol particles, or particulate matter (PM), are essential constituents in the atmosphere influencing global climate [*Forster et al.*, 2007], and human health [*Peters et al.*, 2005; *Dockery and Stone*, 2007]. In the European Union, the mass concentrations of PM_{10} and $PM_{2.5}$ serve as a legal metric to assess a population's exposure to ambient particles (European Council, 2008/50/EC). Substantial research has been directed towards elucidating the sources and behavior of PM_{10}, including concrete administrative measures to reduce the numerous exceedances of the daily limit value of 50 µg m^{-3} (allowed for no more than 35 days) in urban and even rural areas. Meanwhile, it has become obvious that the mass-based metrics might not be appropriate to appraise the PM-induced health effects [*HEI*, 2002]. Mass concentration measurements are, in particular, not sufficient to account for the effects of carbonaceous particles or ultrafine particles (diameter < 100 nm), which are emitted by anthropogenic combustion processes such as industry, traffic and domestic heating. While there is little doubt about the potential health effects of these particles [*Wichmann*, 2004], their relatively low mass concentration makes them largely inaccessible for mass-based measurements. To date, PM can be characterized in very much detail, including size-resolved number concentration and chemical composition, or individual particle analysis. The process of implementing novel measurement techniques in regular air quality monitoring, however, is relatively new because in the past, it was hampered by the required investments, and limited measurement reliability and standardization.

In 2008, the Leibniz Institute for Tropospheric Research (IfT) and the German Federal Environment Agency (UBA) organized a new Germany-wide network for the characterization of fine and ultrafine particles in the atmosphere. The network involves many of UBA's manned background monitoring stations [*UBA*, 2009], and more sites operated by IfT, LfULG Dresden, GAA Hildesheim, the German Meteorological Service (DWD), the Helmholtz Research Center for Environmental Health (HMGU), and IUTA Duisburg (see Fig. 1). Continuous measurements of sub-µm particle number size distributions and soot mass concentrations (determined from light absorbing fine and ultrafine particles) were installed at eleven observation sites. The continuous physical measurements are complemented by an intermittent chemical characterization using

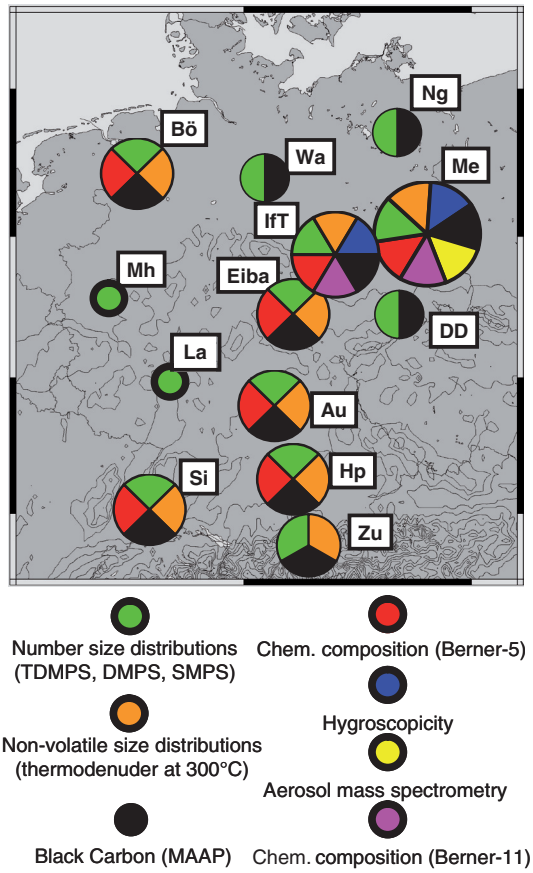

Fig. 1: *Observation sites in the German Ultrafine Aerosol Network (GUAN). Continuous measurements include particle number size distributions (unconditioned and non-volatile) and black carbon. Chemical composition is measured at multiple sites on selected days. Hygroscopicity and aerosol mass spectrometry are studied during intensive periods at Leipzig-IfT and Melpitz.*

low pressure impactors. Furthermore, intensive field campaigns are dedicated to specialized particle properties (hygroscopicity, highly time-resolved chemical composition), which will add to the scientific basis necessary for a more comprehensive understanding of the life-cycle of ambient fine and ultrafine particles. This article presents an overview of the first year of the spatial observations, 2009.

The German Ultrafine Aerosol Network (GUAN)

Overview. The German Ultrafine Aerosol Network (GUAN) combines federal and state air quality monitoring stations and observatories as well as atmospheric observation sites run by various research institutes. State-of-the-art aerosol characterization equipment has been installed at twelve observation sites. Figure 1 provides an overview of the measurement program and sites. Full details can be found in *Birmili et al.* [2009a].

Continuous and semi-continuous measurements. Particle number size distributions are measured at all eleven observation sites using mobility size spectrometers. Most instruments are Scanning Mobility Particle Sizers (SMPS) or Twin Differential Mobility Particle Sizers [*TDMPS*; *Birmili et al.*, 1999] developed and constructed at IfT. At Mülheim-Styrum and Zugspitze commercially available SMPS systems (TSI model 3080, St. Paul, USA) are deployed. The most commonly used particle size ranges are 3 – 800 nm and 10 – 800 nm depending on whether a dual or a single instrument is deployed. Recent instrumental improvements include a closed-loop sheath flow arrangement, and desiccation devices for the sheath flow and aerosol inlet flows. The comparability of the measurements is assured by central comparison workshops [*Helsper et al.*, 2008], and also by in-situ comparisons with total particle counters at Hohenpeissenberg and Zugspitze.

Non-volatile particle number size distributions are recorded at eight stations, with thermodenuders being operated upstream of the differential mobility particle sizers. In the thermodenuder, aerosol particles are heated to 300 °C, and volatile substances are evaporated. Downstream of the thermodenuder, the size distribution of non-volatile residues is recorded, in an alternating fashion with the unconditioned size distribution [*Engler et al.*, 2007]. The thermodenuder measurements allow for the quantification of refractory particle cores, which are presumed to play a crucial role with respect to particle health effects upon inhalation as well as light absorption.

The mass concentration of airborne soot is quantified at nine sites by Multi-Angle Absorption Photometers [*MAAP*; *Petzold et al.*, 2004]. The MAAP converts the light attenuation through a particle-laden quartz fiber filter into an absorption coefficient, and finally into a soot mass concentration using an experimentally determined specific attenuation cross-section of 6.6 $m^2\,g^{-1}$ at a wavelength of 637 nm. Because the MAAP performs an integral aerosol measurement, the upper cut-off size in the aerosol sampling inlet is important. At present, this cut-off size is not uniform, and varies between no cut-off (Zugspitze), 10 µm (Melpitz, Leipzig-IfT, Hohenpeissenberg), 2.5 µm (Augsburg), and 1 µm (Bösel, Leipzig-Eisenbahnstraße, Schauinsland). To provide accurate and comparable measurements under dry sample conditions, most MAAP aerosol inlets have been equipped with membrane dryers.

To enable spatially resolved measurements as well as particle size-segregated chemical information, Berner low-pressure impactors were installed at seven sites (cf. Fig. 1). The five stage

Berner impactor classifies particles into five size fractions between 0.05 and 10 µm, which are to be analyzed separately [*Herrmann et al.*, 2006]. A total of 40 sampling events – each across the whole of Germany and lasting 24 hours, is envisaged. Fifteen of these sampling events have been completed in 2009, and are currently under evaluation (Dr. Konrad Müller). To capture as many contrasting air masses even with a limited number of samples, the sampling events are not statically fixed, but will be triggered after five-day meteorological forecasts.

All aluminum impactor foils and quartz fiber filter samples are analyzed at IfT's chemistry department for water-soluble inorganic ions by standard ion chromatography, elemental (EC) and organic carbon (OC) by thermographic analysis, and selected organic trace species by gas chromatography/mass spectrometry. Details of the corresponding analytical procedures and methods are summarized in *Herrmann et al.* [2006]. First data from the impactors on elemental carbon are shown below in this article.

Additional campaign measurements. The hygroscopic properties of sub-µm aerosol particles were determined at Melpitz using a HTDMA (Hygroscopicity Tandem Differential Mobility Analyser) [*Massling et al.*, 2005], and at Leipzig-IfT using a HDMPS (Humidifying Differential Mobility Particle Sizer) [*Birmili et al.*, 2009b]. Hygroscopic particle growth factors were determined at 90 % relative humidity, and were conducted between 6/2008 and 6/2009. The hygroscopic measurements serve to identify the external mixture of the aerosol (more and less hygroscopic particles) as well as the particles' ability to take up water. Both parameters are of interest for the assessment of the particle health as well as climate effects. The hygroscopicity measurements are currently evaluated in a Master thesis (Friederike Kinder).

A high resolution time-of-flight aerosol mass spectrometer (AMS; Aerodyne Research, Inc., Billerica, USA) was deployed at Melpitz to characterize the size-segregated chemical composition of ambient aerosol particles (0.2 – 2 µm) at high time resolution (~15 min). Campaigns lasting for six and ten weeks were started in June 2008, September 2008, and spring 2009. The evaluation of these data is ongoing (Dr. Laurent Poulain). The AMS measurements are designed to drastically improve our understanding of aerosol formation and transformation processes. In addition, a ten-stage Berner impactor has been deployed to collect highly size-fractionated particles at Melpitz and Leipzig-IfT, which allows to collect ultrafine particles down to sizes of 0.018 µm for chemical analysis.

Particle Size Distributions

Figure 2 illustrates the annual cycle of integral aerosol parameters derived from the particle number size distributions in the year 2009. Time series of 14-day floating average values are generally displayed. Figure 2a shows that particle number differs significantly between the 10 sites across Germany. A trend can be seen from low particle numbers at rural sites (Zugspitze) towards high numbers at urban and roadside sites (Leipzig-Eisenbahnstrasse). A prime cause for these differences are anthropogenic emissions of ultrafine particles, such as from traffic. The role of secondary particle formation events, in turn, is more difficult to evaluate, since they take place only part of the measurement time (primarily under the assistance of sunlight).

Figure 2b illustrates the annual cycle of particle mass (PM_1 range, i.e. diameters < 1 µm), calculated here under the assumption of spherical particles and a material density of 1.6 g cm^{-3}. The Particle mass shows a variable annual cycle with several individual maxima. These maxima represent cycles in the synoptic situation over Central Europe. Periods with continental inflow (high particle mass) change with periods of maritime influence (low particle mass). It is worth to note that all stations under investigation correlate highly in these maxima. Our data set allows to describe the spatial extent of these continental air masses, as well as the representativity of individual sites. In the cold season, the mountain sites (Zugspitze, Hohenpeissenberg, Schauinsland) show low aerosol mass concentrations due to the presence of free tropospheric air.

Figure 2c displays the non-volatile volume fraction of particles. This was calculated by dividing the particle volume downstream the thermodenuder by the volume upstream the thermodenuder. In the thermodenuder particles are heated to 300 °C in the airborne state; the residuals of this process are expected to represent mainly non-volatile carbon, crustal material and traces of sea salt. The annual time series shows that the highest non-volatile fractions occur in the urban atmosphere, which is not surprising in view of the high number of diffuse sources, such as motor vehicles. A relatively low fraction of non-volatile particles was found at the station Bösel. This can be taken as indicative of a high proportion of volatile secondary aerosols.

The spatial variability of the atmospheric particle number size distribution in the lower boundary layer is depicted in Fig. 3. Three cases are illustrated, each lasting around 4 weeks. Figure 3a represents a continental aerosol in the end of winter. The mountain sites show low values

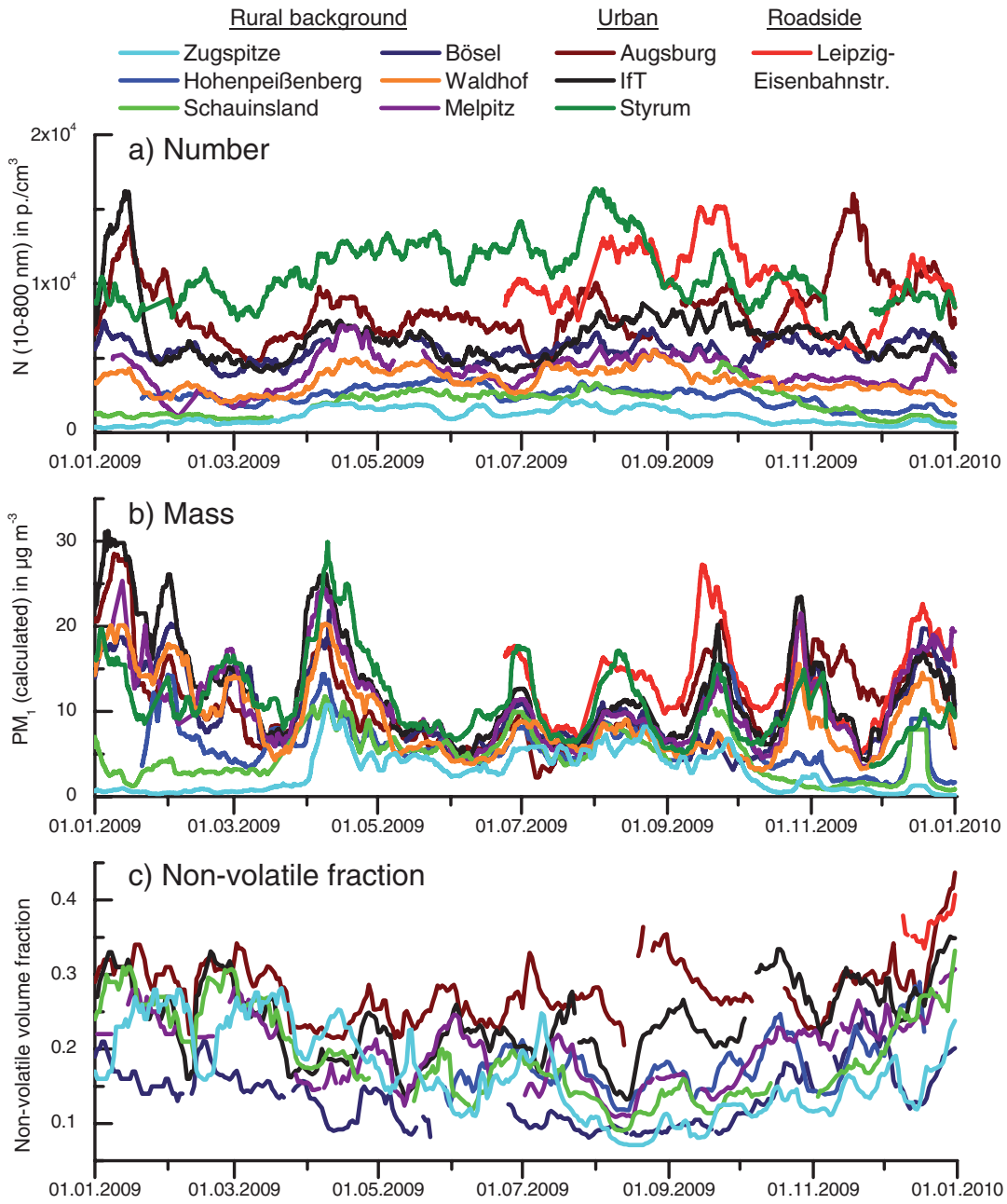

Fig. 2: *Annual time series of aerosol parameters derived from number size distribution measurements across the GUAN network: a) Particle number (10 nm < diameter < 800 nm), b) calculated PM1 mass concentration (assuming a particle density of 1.6 g cm^{-3}), c) the non-volatile particle volume fraction, calculated as the ratio of total particle volume downstream and upstream of a thermodenuder (300°C).*

because they reside mainly above the mixing layer. Figure 3b shows a coherent period with clean maritime inflow in summer 2009. Here, the aerosol size distribution is very homogeneous across entire Germany. Figure 3c displays another period with continental inflow in autumn 2009, where higher spatial heterogeneity can be seen. It is worth to note that the mean accumulation mode diameters differ between the continental and maritime cases, as indicated by vertical lines: Continentally aged aerosols can be found at higher diameters (ca. 300 nm compared to 200 nm in the marine case) and reflect, for instance, the predominant absence of the effective wet deposition mechanism in these air masses. The differences in mean particle diameter are relevant for later calculations of radiative forcing.

Diurnal cycles of particle number and mass (2009 averages) are shown in Fig. 4. The graphs highlight once more the different levels in particle number concentration and mass. In urban areas, a morning and afternoon peak can be seen. These are indicative of the interaction of urban emissions with the dynamics of the boundary layer. Four types of behavior can be distinguished from the cycles of particle number: 1) traffic sites (Leipzig-

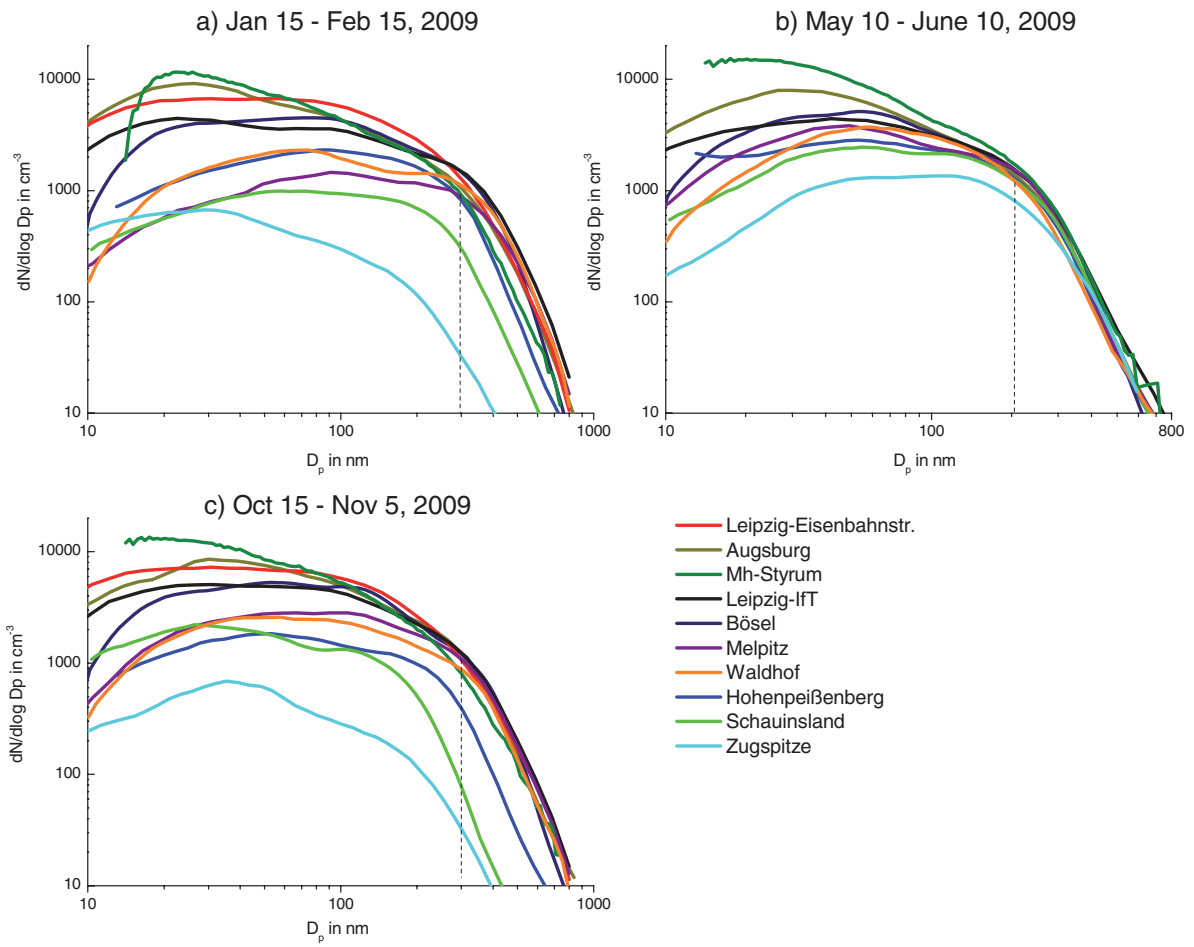

Fig. 3: *Spatial variability of the particle number size distribution in the GUAN network during selected periods. a) a coherent period with continental air masses in late winter 2008/09, b) a period with clean maritime inflow in summer 2009, and c) another period with continental inflow in autumn 2009. Vertical lines indicate the approximate mean size of the accumulation mode.*

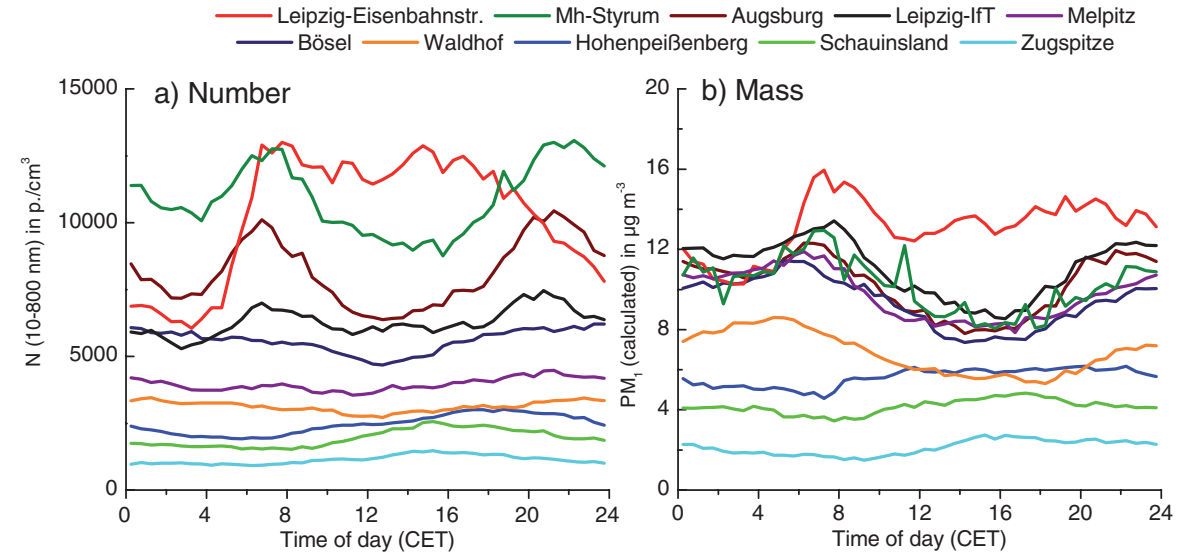

Fig. 4: *Diurnal cycle of total particle number (10 nm < diameter < 800 nm) and calculated particle mass concentration (PM_1 range) in the GUAN network. Averages for the complete year 2009 are shown for all sites except Leipzig-Eisenbahnstr. (2 months only).*

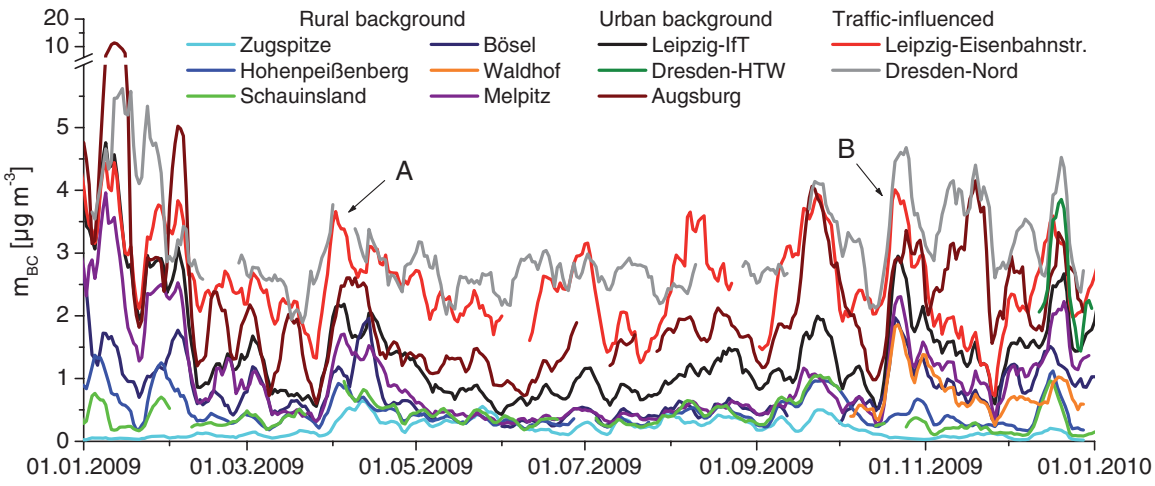

Fig. 5: *Annual time series of the black carbon (BC) concentration across the GUAN network. The measurements were made with Multi-Angle Absorption Photometers (MAAP) using a default mass absorption efficiency of 6.6 $m^2 g^{-1}$. A and B indicate periods of high soot concentrations as a result of the long-lasting inflow of continental air.*

Eisenbahnstraße), dominated by the diurnal cycle of traffic emissions, 2) urban background sites (Augsburg, Mülheim-Styrum, Leipzig-IfT), featuring a double-peaked structure of urban emissions, 3) rural lowland sites (Melpitz, Bösel, Waldhof), featuring a concentration minimum at mid-day, 4) mountain sites (Schauinsland, Hohenpeißenberg, Zugspitze) showing a maximum in particle number in the afternoon. A similar picture is valid for particle mass; here, the distinction between urban background sites and rural lowland site disappears.

Characterization of Black Carbon

Many efforts have been devoted to monitor various parameters of the aerosol component colloquially known as "soot". Different measurement techniques were applied to quantify graphitic carbon (by Raman analysis), light-absorbing carbon (by multi-angle absorption photometry; MAAP), elemental carbon (by thermographic analysis), and the non-volatile particle volume (by using a thermodenuder in conjunction with the particle mobility spectrometers.) For details on the various procedures, see *Nordmann et al.* [2009]. Here, the key results are presented.

Annual cycle of black carbon in Central Europe. The MAAP was used to quantify "light-absorbing carbon" (LAC), or "black carbon" (BC). Figure 5 displays the continuous time series of black carbon (daily averages) at 11 sites in Germany. As in the case of total particle mass (Fig. 2), distinct maxima can be seen throughout the year, which coincide at most stations. Two of the distinct maxima are marked in the Figure and correspond to long-lasting episodes of continental inflow. As was the case for total particle mass, the mountain stations feature low soot concentrations in the cold season due to their location above the mixing layer. Besides, there is the usual gradient between remote sites (low BC concentrations) and urban sites (high BC concentrations).

The diurnal cycle of BC is scrutinized in Fig. 6 with regard to the influence of urban emissions: The rural background level of BC in East Germany (Melpitz) is about 1 µg m^{-3}. Urban background levels rise to about 1.4 µg m^{-3} and at roadside to 2.5 µg m^{-3}. This suggests that the contribution of soot from the vehicular exhaust gas amounts to ca. 1 – 2 µg m^{-3} on average. This is the

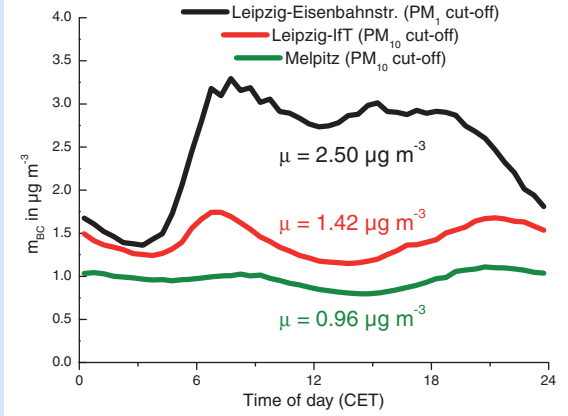

Fig. 6: *Effects of urban sources – particularly traffic, on the diurnal cycle of black carbon (BC). The diurnal cycle at roadside (Leipzig-Eisenbahnstr.) closely follows that of the traffic volume (daily sum about 12 000 veh). Urban background concentrations (Leipzig-IfT; distant at 1.5 km) and regional background concentrations (Melpitz; distant at 50 km) are added for comparison. The data cover the entire year 2009. The PM_1 cut-off at the traffic site ensures that primarily the particulate components of the vehicle exhaust are sampled, and resuspended components are omitted.*

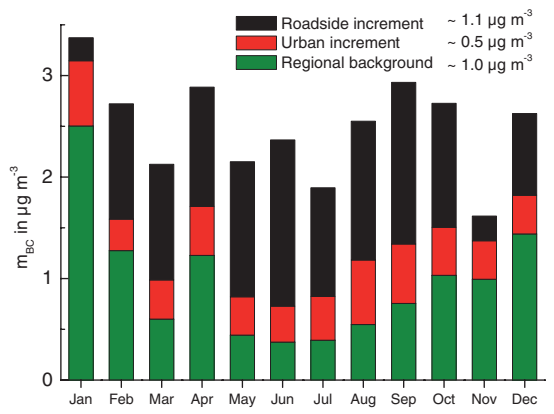

Fig. 7: *Monthly average levels in 2009 of the regional background in lack carbon (BC) at Melpitz, compared to the increments observed in the urban background (Leipzig-IfT) and at roadside (Leipzig-Eisenbahnstr.). Importantly, the regional background concentration of BC is more variable throughout the year than the individual source contributions within a city, or in a street canyon.*

maximum concentration of PM mass that can be removed in the street canyon, for example, by a rigorous cleaning of the vehicles' exhaust gas. Figure 7 displays the annual context of the data; interestingly, the roadside increment seems to be less variable than the regional background. This highlights the importance of specific winter-time aerosol sources on the levels of soot in Central Europe.

Raman analysis. Raman analysis was conducted with spots of particles deposited on the MAAP's glass fibre filter. Raman analysis allows to determine the graphitic carbon (GC) mass concentrations from the integrated G-band intensity [*Nordmann et al.*, 2009]. As the Raman analysis of one single filter spot requires substantial time (~ 1 h), our initial work concentrated on filter spots from three exemplary GUAN sites, Bösel (rural), Leipzig-IfT (urban background), and Leipzig-Eisenbahnstr. (street canyon).

Figure 8a shows daily averages of the absorption coefficient σ_{ap} and the GC mass concentration m_{GC} between March 25 and April 10, 2009. The beginning of the measurement period was characterized by clean Atlantic air and westerly wind directions. The values of m_{GC} were between 0.29 and 0.67 µg m^{-3} at Bösel, and between 0.66 and 0.94 µg m^{-3} at Leipzig-IfT. The street canyon (Leipzig-Eisenbahnstr.) featured even higher levels. After March 29, the wind direction switched to easterly winds that were associated with continental air and thus higher soot concentrations. m_{GC} reached values up to 3.0 µg m^{-3} at Bösel and 4.3 µg m^{-3} at Leipzig-IfT. A close time correlation can be seen between m_{GC} and σ_{ap}.

Figure 8b shows the absorption efficiency δ_{GC}, defined as the quotient σ_{ap}/m_{GC}. δ_{GC} indicates the ability of an aerosol sample to absorb light in relation to its GC mass concentration, and

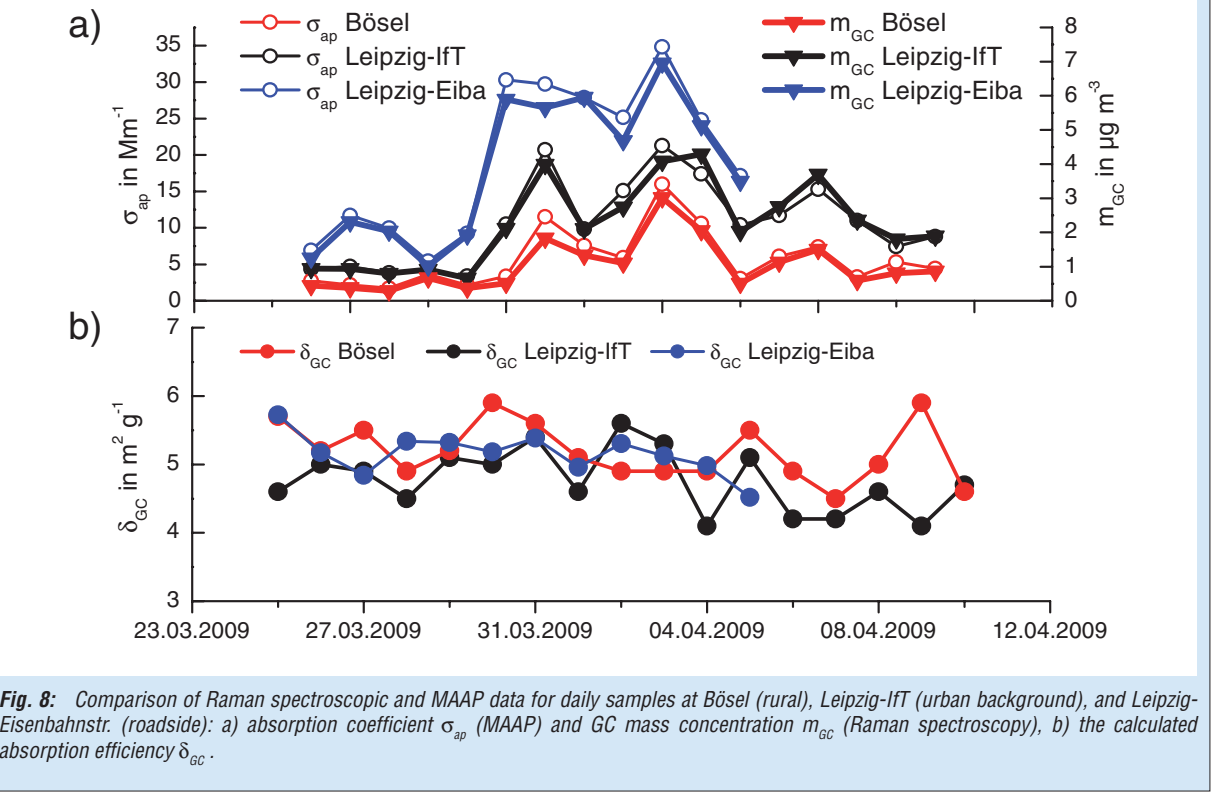

Fig. 8: *Comparison of Raman spectroscopic and MAAP data for daily samples at Bösel (rural), Leipzig-IfT (urban background), and Leipzig-Eisenbahnstr. (roadside): a) absorption coefficient σ_{ap} (MAAP) and GC mass concentration m_{GC} (Raman spectroscopy), b) the calculated absorption efficiency δ_{GC}.*

is highly relevant for a correct estimation of the radiative effects of soot in atmospheric climate modeling. In practice, δ_{GC} may vary from site to site, and even from sample to sample depending on the state of mixture of GC, and the size distribution of the absorbing particles. The change in air masses around March 30 has no obvious effect on δ_{GC}. At this early stage of the data evaluation we are unable to conclude whether this rural/urban difference is significant. The absorption efficiencies are in the lower range of data reported in the literature for various types of soot [*Bond et al.*, 2006]. During the ongoing research project, it is planned to analyze more MAAP glass fiber filters from all GUAN sites with Raman analysis, and extend the comparison to samples from all seasons.

Comparison between black carbon and thermographic EC analysis. In GUAN, the chemical composition of size-fractionated aerosol particles is determined at seven observation sites in Germany (Fig. 1). Berner impactor samples are taken over 24 hours on pre-selected days, and at all stations simultaneously. Between December 12, 2008 and August 6, 2009, we conducted 16 sampling events on the basis of weather forecasts with the aim of meeting the following criteria: Stable synoptic weather situation over several consecutive days, homogeneous wind direction over Germany, absence of rain (which would infringe on the quality of the five-stage impactor sampling).

Figure 9 shows the EC mass concentration obtained from thermographic analysis [*Herrmann et al.*, 2006] and the light absorption coefficient σ_{ap} for a total of 94 atmospheric samples. Site-specific linear regression analyses yield a span of R^2 between 0.60 and 0.88, and an R^2 value of 0.63 for the total data set. Linear fits for $\sigma_{ap}(m_{EC})$ yield slopes between 2.3 and 7.4 and considerable axis offsets. Trend lines are indicated in Fig. 8 for a rough orientation in the data set. The ratio σ_{ap}/m_{EC} is, like σ_{ap}/m_{GC}, an absorption efficiency. Although its median value of 7.5 $m^2\ g^{-1}$ is again in the range of previously published values [*Bond et al.*, 2006], it shows considerable variation across the data set (quartile range: 4.2 – 14 $m^2\ g^{-1}$). At the current stage of the data analysis the reasons for the scattering of the data are not evident. A very basic interpretation is that MAAP and thermographic analysis measure two apparently different aspects of the carbonaceous aerosol content. While the MAAP measures the particles optical absorption properties the thermographic analysis examines the temperature-dependent properties of bulk particle samples deposited on aluminum foils. A limitation of the thermographic method used here is that it cannot be operated with optical charring

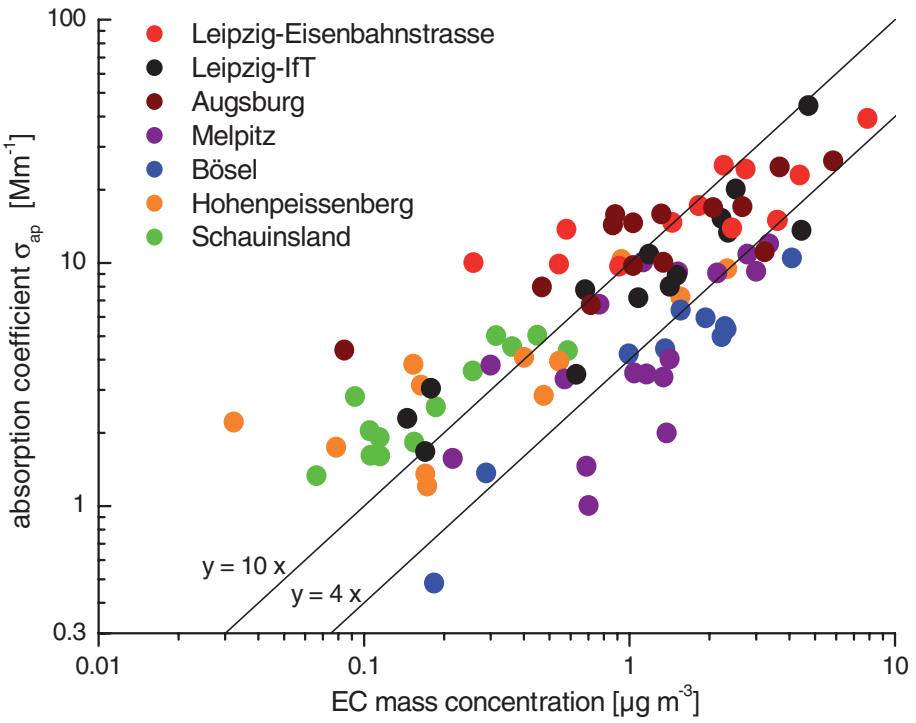

Fig. 9: *Comparison between elemental carbon (EC) mass concentrations from thermographic analysis and the absorption coefficients for 7 observation sites in GUAN. Trend lines are indicated for orientation. Figure reproduced from Nordmann et al. [2009] by permission of Springer-VDI-Verlag, Düsseldorf.*

correction due to the collection of particles on impactor foils rather than on homogeneously loaded quartz fiber filters.

Comparison of black carbon and the non-volatile particle volume. As elemental carbon is a major non-volatile constituent in the atmospheric sub-µm aerosol, we checked the correspondence between the non-volatile particle volume derived from mobility spectrometers/thermodenuders (Sect. 3) and light absorbing aerosol constituents. Figure 10 shows a scatter plot for the non-volatile particle volume (< 1 µm aerodynamic size) and the aerosol absorption measured by the MAAP for four GUAN sites (Leipzig-IfT and Augsburg: urban background; Bösel: rural; Zugspitze: high alpine background) for the period March 24 – April 10, 2009. Due to the combination of maritime, continental, and free tropospheric air, the data set spans more than three orders of magnitude in concentration. As can be seen in Fig. 9, the data collective follows a similar trend. Linear regression of a straight line with no axis intercept yielded linear slopes of 3.95 (Zugspitze), 4.22 (Bösel), 3.99 (Leipzig-IfT), 5.13 (Augsburg), and 4.48 (all data), with corresponding R^2 values of 0.96, 0.92, 0.93, 0.87, and 0.90.

The results indicate a close correlation between light-absorbing carbon (LAC) from the MAAP instrument and the non-volatile particulate volume in the sub-µm range. Since LAC could be attributed largely to GC during the same measurement period, we conclude that the non-volatile particle volume is associated mostly with GC. Under the assumption of a mass absorption efficiency of 4.8 $m^2\ g^{-1}$, both non-volatile volume and LAC would be consistent using an effective particle density in the range 0.82 – 1.06 g cm^{-3}. Effective particle densities < 1 g cm^{-3} are possible for fractal agglomerates. Our data show that a size distribution measurement of non-volatile particle residues can act as a surrogate measurement for soot in the sub-µm range. A more extended data set, however, will be evaluated to substantiate the conclusions.

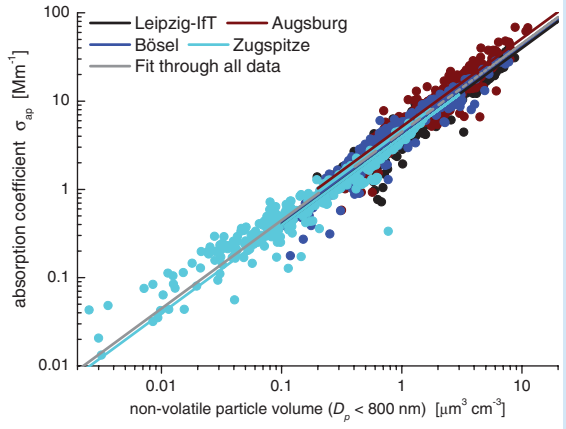

Fig. 10: *Comparison between the non-volatile particle volume and the aerosol absorption coefficient for hourly data at four GUAN sites between March 24 and April 10, 2009. Linear trend lines are added.*

Conclusions and Outlook

Since the end of 2008 the German Ultrafine Aerosol Network (GUAN) is operational. This nation-wide network of several institutions is designed to establish a new body of atmospheric long-term observations. The network represents a comprehensive effort aiming at a better description of the environmental aerosol (PM), particularly endorsing new particle metrics that are of relevance for health-related exposure but also climate effects. Continuous measurements of number size distributions and soot at up to thirteen measurement sites are complemented by an intermittent size-segregated chemical characterization and additional campaign measurements.

The first measurements presented here show marked contrasts between different observation sites particularly in terms of particle number. Differences in particle mass occur to a minor degree, but particle mass shows a significant variation throughout the year. The main variation in particle mass is due to synoptic scale meteorology, governing Central Europe by maritime and continental air masses in an alternating fashion. Measurements of black carbon (BC) provide vital information on the abundance and behavior of this important light-absorbing constituent. First comparisons between different measurement techniques suggested a rather uniform mass absorption coefficient of BC around 5 $m^2\ g^{-1}$. This experimental finding allows to constrain future simulations of radiative transfer in the atmosphere.

Current plans suggest the body of measurements to continue until the end of 2010. The anticipated multi-annual series as well as the planned chemical characterization will allow deeper conclusions about the sources and processes of soot and ultrafine particles in Germany. The measurement data are planned to be used for several purposes: Besides phenomenological studies discussing the spatio-temporal variations of the aerosol in relation to meteorological processes, an assessment of the particle health effects based on soot, particle mass and number exposure will be conducted. We also see GUAN as part of the emerging European observation network (EUSAAR, EMEP), where experimental methods are homogenized and data made available to public and research users.

Within European research activities (EUCAARI), GUAN data will also be used to validate climate models describing the sources, processes and climate effects of atmospheric aerosols, and thus help to understand the regional and global implications of ultrafine particles and soot in the Central European atmosphere.

Acknowledgements

This work has been funded by BMU grant F&E 370343200 (Title: "Erfassung der Zahl feiner und ultrafeiner Partikel in der Außenluft"). We acknowledge many colleagues who also contributed to the ongoing project: André Sonntag, Andrea Haudek, Laurent Poulain, Thomas Müller, Andreas Nowak, Thomas Tuch, Achim Grüner (all IfT), Franck Nordmann und Dirk Haase (GAA Hildesheim), Hartmut Walter (Bösel), Christian Plaß-Dülmer (DWD), Ralf Sohmer (UBA Zugspitze), and Markus Wallasch (UBA Langen). We express our thanks to the NRW State Agency for the Nature, Environment, and Consumer Protection (LANUV-NRW) who sponsor the measurements in Mülheim-Styrum. The measurements in Augsburg were exclusively supported by the Helmholtz-Zentrum München.

References

Birmili, W., F. Stratmann, F., and A. Wiedensohler, Design of a DMA-based size spectrometer for a large particle size range and stable operation, *J. Aerosol Sci., 30,* 549–553, 1999.

Birmili, W., H. Berresheim, C. Plass-Dülmer, T. Elste, S. Gilge, A. Wiedensohler, and U. Uhrner, The Hohenpeissenberg aerosol formation experiment (HAFEX): a long-term study including size-resolved aerosol, H2SO4, OH, and monoterpenes measurements, *Atmos. Chem. Phys., 3,* 361-376, 2003.

Birmili, W., K. Weinhold, S. Nordmann, A. Wiedensohler, G. Spindler, K. Müller, H. Herrmann, T. Gnauk, M. Pitz, J. Cyrys, H. Flentje, C. Nickel, T.A.J. Kuhlbusch, G. Löschau, D. Haase, F. Meinhardt, A. Schwerin, L. Ries, and K. Wirtz, Atmospheric aerosol measurements in the German Ultrafine Aerosol Network (GUAN): Part 1 – soot and particle number size distributions, *Gefahrst. Reinhalt. L., 69* (4), 137-145, 2009a.

Birmili, W., K. Schwirn, A. Nowak, T. Petäjä, J. Joutsensaari et al., Hygroscopic growth of atmospheric particle number size distributions in the Finnish boreal forest region, *Boreal Environ. Res., 14*, 458–480, 2009b.

Bond, T.C., and R.W. Bergström, Light absorption by carbonaceous particles: An investigative review, *Aerosol Science and Technology, 40*, 27-67, 2006, doi:10.1080/02786820500421521.

Dockery, D. W., and P.H. Stone, Cardiovascular risks from fine particulate air pollution, *New Engl. J. Med., 356,* 511-513, 2007.

European Commission: Council Directive 2008/50/EC of 21/05/2008 on ambient air quality and cleaner air for Europe. Official Journal, L152: 1-44, 11/06/2008.

EMEP Particulate Matter Assesment Report: Convention on long-range transboundary air pollution. EMEP/CCC-Report 8/2007. Edited by Aas, W., P. Bruckmann, R. Derwent, N. Poisson, J.-P. Putaud, L. Rouil, S. Vidic, K-E. Yttri, 2007, Download at http://www.nilu.no/projects/ccc/reports/cccr8-2007.pdf

Engler, C., D. Rose, B. Wehner, A. Wiedensohler, E. Brüggemann, et al., Size distributions of non-volatile particle residuals (Dp < 800 nm) at a rural site in Germany and relation to air mass origin *Atmos. Chem. Phys.*, *7*, 5785-5802, 2007.

Forster, P., V. Ramaswamy, P. Artaxo, T. Berntsen, R. Betts et al., Changes in Atmospheric Constituents and in Radiative Forcing. In: Climate Change 2007: The Physical Science Basis. Contribution of Working Group I to the Fourth Assessment Report of the Intergovernmental Panel on Climate Change [Solomon, S., D. Qin, M. Manning, Z. Chen, M. Marquis, M. et al. (eds.)]. Cambridge University Press, Cambridge, United Kingdom 2007. Available at http://www.ipcc.ch.

HEI: Understanding the health effects of components of the particulate matter mix: progress and next steps. Tech. Rep. 4, Health Effects Institute, Boston (MA), USA, 2002.

Helsper, C., H.-G. Horn, F. Schneider, B. Wehner, A. Wiedensohler, Intercomparison of five mobility size spectrometers for measuring atmospheric submicrometer aerosol particles. *Gefahrst. Reinhalt. L., 68* (11/12), 475-481, 2008.

Herrmann, H., E. Brüggemann, U. Frank, T. Gnauk, G. Löschau et al., A source study of PM in Saxony by size-segregated characterisation, *J. Atmos. Chem., 55,* 103-130, 2006, doi: 10.1007/s10874-006-9029-7.

Massling, A., M. Stock and A. Wiedensohler, Diurnal, weekly, and seasonal variation of hygroscopic properties of submicrometer urban aerosol particles, *Atmos. Environ., 39*, 3911-3922, 2005, doi: 10.1016/j.atmosenv.2005.03.020.

Nordmann, S., W. Birmili, K. Weinhold, A. Wiedensohler, S. Mertes, K. Müller, T. Gnauk, H. Herrmann, M. Pitz, J. Cyrys, H. Flentje, L. Ries, K. Wirtz, Atmospheric aerosol measurements in the German Ultrafine Aerosol Network (GUAN) – Part 2: Comparison of measurements techniques for graphitic, light-absorbing, and elemental carbon, and the non-volatile particle volume under field conditions, *Gefahrst. Reinhalt. L., 69* (11/12), 469-474, 2009.

Peters, A., S. von Klot, M. Heier, I. Trentinaglia, J. Cyrys et al., Particulate air pollution and nonfatal cardiac events. Part I: air pollution, personal activities, and onset of myocardial infarction in a case-crossover study. HEI Research Report, *124*, 1-82, 2005.

Petzold, A. and M. Schönlinner, Multi-angle absorption photometry – a new method for the measurement of aerosol light absorption and atmospheric black carbon, *J. Aerosol Sci., 35*, 421-441, 2004, doi: 10.1016/j.jaerosci.2003.09.005.

Turpin, B.J., and J.J. Huntzicker, Identification of secondary organic aerosol episodes and quantification of primary and secondary organic aersol concentrations during SCAQS, *Atmos. Environ., 29*, 3527-3544, 1995.

UBA (2009) Air and air pollution control: air quality monitoring networks, see http://www.umweltbundesamt.de/luft/luftmessnetze/index.htm

Wichmann, H.-E., Health effects of particles in ambient air, *Int. J. Hyg. Envir. Heal., 207*, 399-407, 2004.

Funding
- Bundesministerium für Umwelt, Naturschutz und Reaktorsicherheit, Forschungs- und Entwicklungsvorhaben 3703 43 200, Titel „Erfassung der Zahl feiner und ultrafeiner Partikel in der Außenluft“
- Deutsche Bundesstiftung Umwelt (DBU), AZ 20008/960

Cooperation
- The Federal Environmental Agency (UBA); Messnetzzentrale Langen
- Helmholtz Zentrum München, German Research Center for Environmental Health (GmbH)
- Universität Augsburg, Wissenschaftszentrum Umwelt
- German Meteorological Service (DWD), Meteorological Observatory Hohenpeissenberg
- Sächsisches Landesamt für Umwelt, Landwirtschaft und Geologie (LfULG), Dresden
- Institut für Energie- und Umwelttechnik e. V. (IUTA), Duisburg
- Staatliches Gewerbeaufsichtsamt (GAA) Niedersachsen, Hildesheim

New particle formation from the reaction of OH radicals with SO_2

Torsten Berndt, Mikko Sipilä, Frank Stratmann

Die Partikelneubildung in der unteren Troposphäre ist an das Vorhandensein von H_2SO_4 in Konzentrationen von 10^5 – 10^7 Moleküle cm^{-3} gebunden. Unter Laborbedingungen gelang es bisher lediglich für H_2SO_4 Konzentrationen von etwa 10^7 Moleküle cm^{-3} Partikelbildung qualitativ nachzuweisen. Der Einsatz neuartiger Partikelzähler erlaubt den Nachweis von neu gebildeten Partikeln bis zu einem Durchmesser von etwa 1.5 nm. Dies ist nahe der Größe des kritischen Clusters. Damit ist es nahezu möglich, alle neu gebildeten Partikel zu erfassen. Messverfälschungen, bedingt durch unzureichendes Partikelwachstum bis hin zur Nachweisgrenze gebräuchlicher Partikelzähler (2.5 – 3 nm), werden minimiert bzw. eliminiert. Die auf diesem Weg ermittelten Partikelbildungsgeschwindigkeiten stimmen gut mit beobachteten Werten in der Troposphäre überein. Abgeleitete Parametrisierungen können in der Atmosphären-Modellierung verwendet werden. Die Messungen zeigen einen deutlichen Beitrag des H_2O für das Partikelwachstum.

Introduction

Simultaneous measurements of newly formed ultra-fine particles and H_2SO_4 in the lower troposphere reveal that new particle formation is strongly connected to the occurrence of H_2SO_4 with concentrations of about 10^5 – 10^7 molecule cm^{-3}. The production rate of new particles can be described by a power law equation for H_2SO_4 with an exponent in the range of 1 – 2 [*Weber et al.*, 1996, *Riipinen et al.*, 2007]. However, laboratory experiments have failed to demonstrate H_2SO_4 particle formation rates as high as those observed in the atmosphere. By means of commonly used particle counters (detection limit: particle diameter ≥ 2.5 – 3 nm), up to now, we were able to observe new particle formation starting for H_2SO_4 concentrations of about 10^7 molecule cm^{-3} [*Berndt et al.*, 2005]. Here, measurements of new particles observed immediately after their formation with diameters down to about 1.5 nm are reported. In these measurements a pulse height condensation particle counter, PH-CPC, [*Sipilä et al.*, 2009] as well as a mixing-type condensation particle counter, M-CPC, [*Verhanen*, 2009] came into operation.

The nucleation experiments have been carried out in the atmospheric pressure flow-tube *IfT*-LFT (i. d. 8 cm; length 505 cm) at 293 ± 0.5 K. H_2SO_4 is continuously produced via the reaction of OH radicals with SO_2 in the presence of water vapour. The H_2SO_4 concentrations were measured at the outlet of *IfT*-LFT with a Chemical Ionization Mass Spectrometer, CI-MS.

Results and Discussion

Figure 1 shows nucleation rates as a function of H_2SO_4 concentrations derived from particle measurements by means of the PH-CPC and the M-CPC at r. h. = 22 %.

Using these high sensitivity counters there exists no clear dependence of the nucleation rates on the residence time in the flow tube. Obviously, in this case, particle growth is not the limiting step and the counting efficiency is high enough that the majority of formed particles can be detected. Regression analysis according to

$$J = k\,([H_2SO_4] / \text{molecule cm}^{-3})^{\alpha} \qquad \text{(I)}$$

(J: nucleation rate)

yields $\alpha = 1.80 \pm 0.06$ and $k = 1.3 \cdot 10^{-12}$ $cm^{-3}s^{-1}$ (full line in Fig. 1). Setting $\alpha = 2$ as a fixed value, $k = 4.2 \cdot 10^{-14}$ $cm^{-3}s^{-1}$ follows (dashed line in Fig. 1). For the individual data series in Fig. 1, α is in the range of 1.7 – 2.1. Constraining α to an integer value, i.e. $\alpha = 1$ or 2, a number of one or two H_2SO_4 molecules in the critical cluster follows assuming that the nucleation step is rate limiting. The presence of one or two H_2SO_4

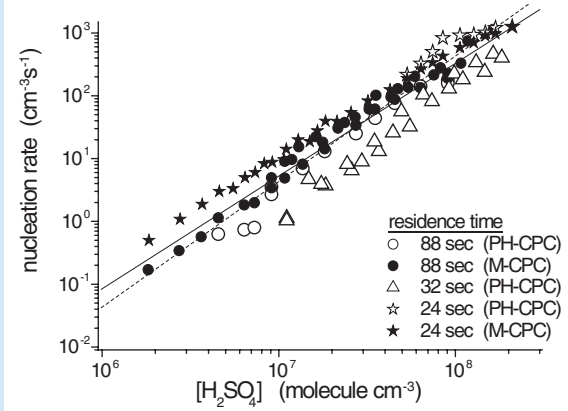

Fig. 1: *Nucleation rate as a function of H_2SO_4 concentration for different residence times in the irradiated middle section of the IfT-LFT; r.h. = 22 %. Full line represents the overall best fit according to equation (I), dashed line stands for the fitting result constraining the exponent for H_2SO_4 at 2.*

molecules in the critical cluster is in agreement with observations in the atmosphere [*Weber et al.*, 1996, *Riipinen et al.*, 2007, *Kuang et al.*, 2008].

In a next set of experiments, for a fixed residence time of 88 sec, the relative humidity was varied in the range 22 – 61 %. The measurements showed a clear increase of the nucleation rate with increasing H_2O vapour concentration. The exponents for H_2SO_4 (α) and for H_2O vapour (β) were determined simultaneously according to equation (II) using all data available.

$$J = k\ ([H_2SO_4] / \text{molecule cm}^{-3})^{\alpha}\ ([H_2O] / 10^{15}\ \text{molecule cm}^{-3})^{\beta} \qquad \text{(II)}$$

As a result of parameter fitting $\alpha = 1.86 \pm 0.03$, $\beta = 3.08 \pm 0.09$ and $k = (1.05 \pm 0.98)\ 10^{-19}\ \text{cm}^{-3}\text{s}^{-1}$ were found. The exponent for H_2O vapour, $\beta = 3.08$, points at a strong promoting effect of H_2O vapour for nucleation. Analysis of atmospheric nucleation, however, shows an inhibiting overall effect of H_2O vapour on the nucleation process being in disagreement with the result of this study. On the other hand, from other laboratory experiments also an enhancing effect of H_2O vapour is reported.

Simulated nucleation rates according to equation (II) for r. h. = 22 % ($[H_2O] = 1.3 \cdot 10^{17}$ molecule cm^{-3}) and r. h. = 61 % ($[H_2O] = 3.5 \cdot 10^{17}$ molecule cm^{-3}) have been compared with atmospheric nucleation rates as observed in Heidelberg and Hyytiälä [*Riipinen et al.*, 2007]. The agreement between simulation and atmospheric observations is good suggesting applicability of this parameterisation in the framework of atmospheric nucleation modelling.

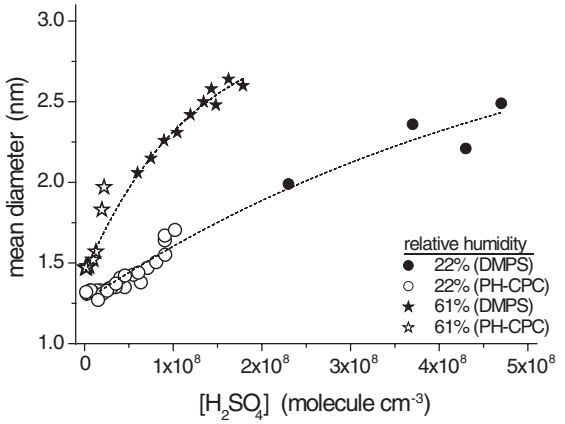

Fig. 2: *Detected mean particle diameters from DMPS and PH-CPC measurements as a function of H_2SO_4 concentration; r.h. 22 % or 61 %, residence times in the irradiated middle section of 88 sec.*

As a result of PH-CPC analysis an increase of the mean particle diameter with increasing r. h. was observed also, i.e. beside the nucleation rate the growth process is significantly enhanced by H_2O vapour as well. In Fig. 2 the PH-CPC data along with results from DMPS measurements for elevated H_2SO_4 concentrations are depicted. Qualitatively, mean particle diameters derived by both techniques show a similar trend.

References

Berndt, T., O. Boge, F. Stratmann, J. Heintzenberg, and M. Kulmala (2005), Rapid formation of sulfuric acid particles at near-atmospheric conditions, *Science*, *307* (5710), 698-700.

Kuang, C., P. H. McMurry, A. V. McCormick, and F. L. Eisele (2008), Dependence of nucleation rates on sulfuric acid vapor concentration in diverse atmospheric locations, *J. Geophys. Res. - Atmos.*, *113* (D10), -, D10209, doi:10.1029/2007JD009253, 2008.

Riipinen, I., S. L. Sihto, M. Kulmala, F. Arnold, M. Dal Maso, W. Birmili, K. Saarnio, K. Teinila, V. M. Kerminen, A. Laaksonen, and K. E. J. Lehtinen (2007), Connections between atmospheric sulphuric acid and new particle formation during QUEST III-IV campaigns in Heidelberg and Hyyti, *Atmos. Chem. Phys.*, *7* (8), 1899-1914.

Sipilä, M., K. Lehtipalo, M. Attoui, K. Neitola, T. Petäjä, P. Aalto, D. O'Dowd, and M. Kulmala (2009), Laboratory verification of PH-CPC's ability to monitor atmospheric sub-3nm cluster, *Aerosol Sci. Technol.*, *43*, 126-135.

Vanhanen, J. (2009), Mixing-type CPC detecting charged clusters down to 1.05 nm, paper presented at ICNAA, Prague.

Weber, R. J., J. J. Marti, P. H. McMurry, F. L. Eisele, D. J. Tanner, and J. A. (1996), Measured atmospheric new particel formation rates: Implications for nucleation mechanisms, *Chem. Eng. Comm.*, *151*, 53-64.

Aerosol chamber studies of the formation of secondary organic particle phase compounds from terpene oxidation

Olaf Böge, Yoshiteru Iinuma, Ariane Kahnt, Anke Heinold, Hartmut Herrmann

*Es wurden Laborexperimente in der **Le**ipziger **A**erosol**k**ammer (LEAK) ausgeführt. Dabei wurde die Bildung partikulär gebundener sekundärer organischer Verbindungen ausgehend von α-Pinen und β-Pinen in der Reaktion mit Ozon sowie die heterogenen Reaktionen bekannter semivolatiler Reaktionsprodukte dieser Terpene untersucht. Schwerpunkt der Experimente war die Untersuchungen des Einflusses der Partikelacidität auf die partikulär gebundenen Produkte. Hierbei zeigte sich, dass saure Sulfatpartikel zur Entstehung von partikulären Organosulfaten in der Ozonolyse von α-Pinen und β-Pinen führen. Experimente zum reaktiven Uptake bekannter semivolatiler Ozonolyseprodukte der Terpene legen den Schluss nahe, dass die Terpenoxide die wichtigsten Vorläufer für die Organosulfate sind. Weiterhin wurden Terpensäuren mit Lactonstruktur wie Terpenylsäure und Diaterpenylsäureacetat als neue partikuläre Produkte der Ozonolyse von α-Pinen gefunden, welche einen wesentlichen Einfluss auf die Entstehung sekundärer organischer Aerosole aus biogenen Vorläufern haben.*

Introduction

It is well recognized that secondary organic aerosol (SOA) plays an important role in the global climate and regional air quality. Monoterpenes are among the most important class of SOA precursor compounds as they react rapidly with atmospheric oxidants (O_3, OH and NO_3 radicals) to form low volatile compounds that partition into the particle phase. Additionally, after methane and isoprene the terpenes are the organic compounds with the highest global emission.

Fig. 1: *The IfT aerosol chamber LEAK.*

The identification and quantification of reaction products from the oxidation of terpenes in the gas phase as well as in the particle phase has been received great attention over the past two decades. Recently, organosulfates have been shown to occur in laboratory-generated SOA from the oxidation of terpenes [*Surratt et al*.,2007; *Surratt et al*., 2008; *Iinuma et al*., 2007a; *Iinuma et al*., 2007b]. Field evidence suggests that organosulfates contribute substantially to ambient SOA, ranging from 6 – 12 % [*Lukács et al*., 2009] or as high as 30 % [*Surratt et al*., 2008] of total sulfur concentration in summer in K-puszta, Hungary.

In the chamber experiments the reactive uptake of β-pinene oxide, which was postulated to be a precursor for β-pinene-derived organosulfates [*Iinuma et al*., 2007a], was studied. Furthermore, α-pinene oxide, campholenic aldehyde and carveol as known semivolatile terpene oxidation products were investigated for their organosulfate formation potentials.

Additionally, α-pinene ozonolysis in LEAK accompanied by extensive analysis of formed particulate products has been performed to get a comprehensive view on this process.

Experimental

The experiments were carried out in the IfT aerosol chamber LEAK (Fig. 1). The chamber has a cylindrical geometry, a volume of 19 m^3 and is made of Teflon FEP film. LEAK is equipped with a humidifier, an ozone and a particle generator. Outlets of the chamber are connected with a condensation particle counter (CPC), a continuous monitoring ozone analyzer and a particle sampling filter device with a fixed integrated annular denuder to avoid gaseous contamination of the deposited particles during sampling. The size distributions of particles in the aerosol chamber as a function of

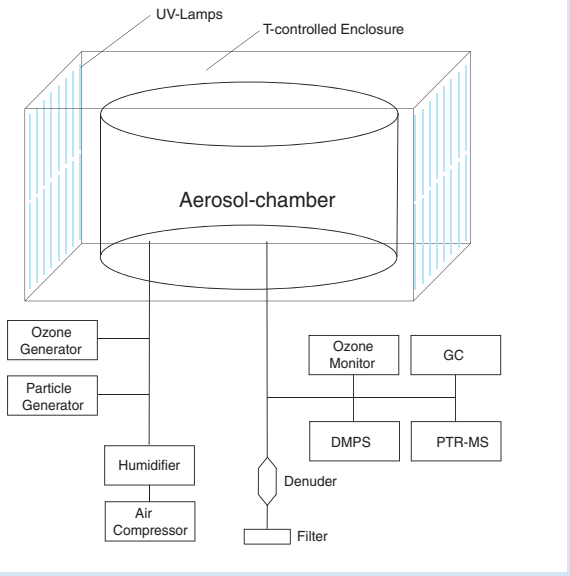

Fig. 2: *Block diagram of the gas- and aerosol-phase instrumentation of the new IfT aerosol chamber.*

time are measured by a differential mobility particle sizer (DMPS). An Agilent gas chromatograph (GC) with flame ionization detector and a PTR-MS (Ionicon) monitor gas-phase hydrocarbon concentrations in the chamber. A scheme of the experimental set-up is given in Fig. 2.

The chamber was flushed for a minimum of 18 h with clean dry air before each experiment. Afterwards the chamber was flushed with humidified air until a relative humidity of 50 % was reached. The chamber was thermostated (22 °C) to avoid RH and temperature fluctuation during the experimental runs. Organic precursors were injected into the chamber from an injection port using an unheated syringe at 200 L min^{-1} of air for 1 min. Seed particles were generated atomizing a solution containing the seed particle constituents. Particle size distributions were monitored using a differential mobility particle sizer system (DMPS, 3 – 900 nm). The initial mean peak diameter was 45 – 50 nm for both acidic and neutral seed particles. Wall loss for aerosol growth was corrected from blank experiments by measuring the decays of seed particles. The mixing ratio of the organic precursor was monitored using the proton transfer reaction-mass spectrometer. Particle-phase products were collected on borosilicate glass fibre filter coated with fluorocarbon (47 mm diameter, PALLFEX T60A20, Pall, NY, USA) after a reaction time of 1 h. Gas-phase compounds were collected using an annular denuder (5 channel, 400 mm length, URG, Chapel Hill, NC, U.S.A.) coated with XAD-4 resin (Sigma-Aldrich). The filter and denuder samples were collected for 1 h with total sampling volumes of 1.8 m^3. The filter samples were stored in a freezer (-22 °C) until analysis.

The chemical analysis was performed using a high performance liquid chromatography instrument coupled to an electrospray ionization time-of-flight mass spectrometer (HPLC/ESI-TOFMS). The electrospray was operated at the negative mode to detect deprotonated compounds (M_w-1).

Results

Organosulfate formation from reactive uptake of semivolatile terpene oxidation products. A detectable increase in the particle volume and hence the organic mass was observed for all experiments in the presence of acidic sulfate seed particles [*Iinuma et al*., 2009]. In particular, β-pinene oxide showed significantly higher increases in the ΔV values than α-pinene oxide, campholenic aldehyde and carveol. In contrast, no increase in ΔV was observed for the experiments with neutral seed particles regardless of organic precursors used.

In the chemical analysis β-pinene oxide was found to form notably higher amounts of organosulfates than α-pinene oxide and campholenic aldehyde in the presence of acidic sulfate seed particles. Additionally α-pinene oxide forms campholenic aldehyde on the wet (acidic) particle surface. Carveol, which is an alcohol isomer of α-pinene oxide, did not yield

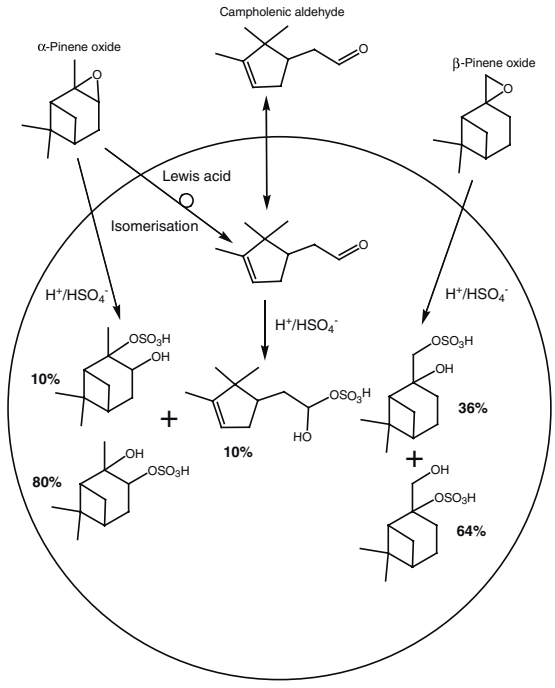

Fig. 3: *Feasible formation pathways and the fraction of α-pinene-derived organosulfates and the β-pinene-derived organosulfates. The fractions shown are from the experiments with 50 ppb organic precursors.*

organosulfates regardless of seed particle acidity. The results are summarized in Fig. 3.

Products from the oxidation of α-pinene. In the ozonolysis of α-pinene, novel SOA products (terpenylic acid and diaterpenylic acid acetate) have been found [*Claeys et al.*, 2009]. The amounts of terpenylic acid and diaterpenylic acid acetate are considerably higher than the amounts of the previously known oxidation products such as norpinonic, pinic and hydroxypinonic acid cf. Fig. 4. The structural elucidation performed based on MS data obtained in the (-)ESI mode and comparison of MS and LC data with synthesized reference compounds.

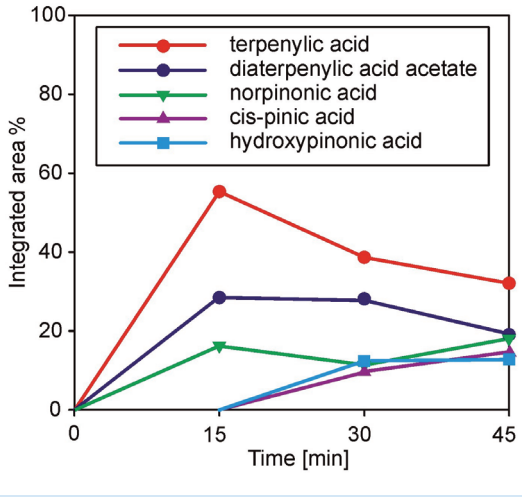

Fig. 4: *Time courses of α-pinene SOA products during an ozonolysis experiment where no OH scavenger was used.*

Summary

In the first part of this study, organosulfate formation was observed from reactive uptake of monoterpene oxides (α-pinene oxide and β-pinene oxide) and, to a lesser extend, campholenic aldehyde, indicating that epoxides most likely serve as precursors for some of the organosulfates reported from both ambient and laboratory SOA samples. It is likely that other epoxides also play an important role for the formation of organosulfates under atmospheric conditions.

In the second part of this study, novel secondary SOA products from the atmospheric oxidation of α-pinene have been identified as lactone-containing terpenoic acids, i.e., terpenylic and hydroxyterpenylic acid, and diaterpenylic acid acetate. Terpenylic acid and diaterpenylic acid acetate are early oxidation products, while hydroxyterpenylic acid formation can be explaind by further oxidation of terpenylic acid. The newly characterized compounds will serve as specific monoterpene SOA tracers for fine PM characterization, a topic of great interest, since knowledge of aerosol sources is essential towards improving air quality.

References

Claeys, M., Y. Iinuma, R. Szmigielski, J. D. Surratt, F. Blockhuys, C. Van Alsenoy, O. Böge, B. Sierau, Y. Gomez-Gonzalez, R. Vermeylen, P. Van der Veken, M. Shahgholi, A. W. H. Chan, H. Herrmann, J. H. Seinfeld, and W. Maenhaut (2009), Terpenylic Acid and Related Compounds from the Oxidation of alpha-Pinene: Implications for New Particle Formation and Growth above Forests, *Environ. Sci. Technol.*, *43* (18), 6976-6982.

Iinuma, Y., O. Böge, A. Kahnt, and H. Herrmann (2009), Laboratory chamber studies on the formation of organosulfates from reactive uptake of monoterpene oxides, *Phys. Chem. Chem. Phys.*, *11* (36), 7985-7997.

Iinuma, Y., C. Müller, T. Berndt, O. Böge, M. Claeys, and H. Herrmann (2007a), Evidence for the existence of organosulfates from beta-pinene ozonolysis in ambient secondary organic aerosol, *Environ. Sci.Technol.*, *41* (19), 6678-6683.

Iinuma, Y., C. Müller, O. Böge, T. Gnauk, and H. Herrmann (2007b), The formation of organic sulfate esters in the limonene ozonolysis secondary organic aerosol (SOA) under acidic conditions, *Atmos. Environ.*, *41* (27), 5571-5583.

Lukacs, H., A. Gelencser, A. Hoffer, G. Kiss, K. Horvath, and Z. Hartyani (2009), Quantitative assessment of organosulfates in size-segregated rural fine aerosol, *Atmos. Chem. Phys.*, *9* (1), 231-238.

Surratt, J. D., Y. Gomez-Gonzalez, A. W. H. Chan, R. Vermeylen, M. Shahgholi, T. E. Kleindienst, E. O. Edney, J. H. Offenberg, M. Lewandowski, M. Jaoui, W. Maenhaut, M. Claeys, R. C. Flagan, and J. H. Seinfeld (2008), Organosulfate formation in biogenic secondary organic aerosol, *J. Phys. Chem. A*, *112* (36), 8345-8378.

Surratt, J. D., J. H. Kroll, T. E. Kleindienst, E. O. Edney, M. Claeys, A. Sorooshian, N. L. Ng, J. H. Offenberg, M. Lewandowski, M. Jaoui, R. C. Flagan, and J. H. Seinfeld (2007), Evidence for organosulfates in secondary organic aerosol, *Environ. Sci.Technol.*, *41* (2), 517-527.

Iron complex photochemistry in the atmospheric aqueous phase

Christian Weller, Hartmut Herrmann

Photochemie von organischen Eisenkomplexen spielt in Wolkentröpfchen und luftgetragenen wässrigen Partikeln in der Atmosphäre eine wichtige Rolle als Quelle für Radikale und den Redoxkreislauf des Elementes Eisen. Der Aspekt der Radikalproduktion ist wichtig für Stoffabbau und -umwandlungen, da diese in der Atmosphäre oft durch Radikalkettenreaktionen erfolgen. In der vorliegenden Arbeit wurden Photolyse-Quantenausbeuten von einer Reihe umweltrelevanter Eisen-Komplexe mit den organischen Liganden Oxalat, Malonat, Succinat, Glutarat, Tartronat, Gluconat, Pyruvat und Glyoxalat experimentell gemessen.

Introduction

Iron is always present in the atmosphere in concentrations from ~10^{-9} M (clouds, rain) up to ~10^{-3} M (fog, particles). Sources are mainly mineral dust emissions. Iron complexes are very good absorbers in the UV-VIS actinic region and thus photo-chemically reactive. Iron complex photolysis leads to radical production (see Fig. 1) and can initiate radical chain reactions, which is related to the oxidizing capacity of the atmosphere. These radical chain reactions are involved in the decomposition and transformation of a variety of chemical compounds in cloud droplets and deliquescent particles. Additionally, the photochemical reaction itself represents a degradation pathway for organic molecules with the ability to bind iron [*Deguillaume et al.*, 2005].

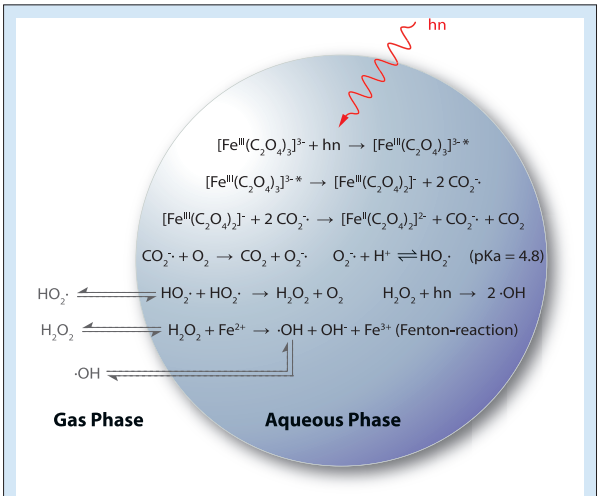

Fig. 1: *Photolysis of Fe(III)-oxalato complex, including subsequent reactions.*

The Fe^{2+} budget is important for the Fenton-reaction, which can be a considerable in-situ OH source. The iron redox cycling depicted in Fig. 1 is simplified and has additional pathways that are not shown. This is addressed in chemistry models that can be used to evaluate the role of certain chemical pathways. Iron-complex photolysis modelling is currently only included in the atmospheric chemistry mechanism CAPRAM (Chemical Aqueous Phase Radical Mechanism) [*Herrmann et al.*, 2005]. This mechanism so far considers only iron-oxalato and iron-inorganic complexes. Model runs with CAPRAM show that oxalate is consumed through Fe-oxalato photolysis, which results in a net destruction of oxalate. This is a contradiction to field measurements, where substantial amounts of oxalate are found. Other models do not include Fe-oxalato photolysis and over-predict oxalate. Iron-oxalate photolysis is either overestimated or other photochemical reaction partners of iron are missing in the picture. To understand the complicated interaction of the photochemical redox cycling of iron with other atmospheric aqueous phase reactions it is necessary to quantify the efficiency of the photochemical reactions with the quantum yield. This can be achieved with laboratory investigations of the iron complex photoreactions. A review of scattering quantum yield measurements (Fig. 2) in the case of iron-oxalate shows the necessity of a reinvestigation of the subject. Photochemical data for other relevant iron-complexing compounds are also scarce.

Laboratory investigations of Iron complex photochemistry

Iron-complexes of environmentally relevant coordination compounds like oxalate, malonate, succinate, glutarate, tartronate, gluconate, pyruvate and glyoxalate have been investigated. Iron speciation depends on the iron-ligand ratio and the pH. The most suitable experimental conditions were calculated with a speciation program. Iron oxalate solutions were bubbled with argon to minimize the oxygen content of the solutions to avoid secondary reactions of photolysis products with oxygen. The solutions were transferred to a 1 cm quartz cuvette and flash-photolyzed with an excimer laser at wavelengths 308 or 351 nm. Photochemically

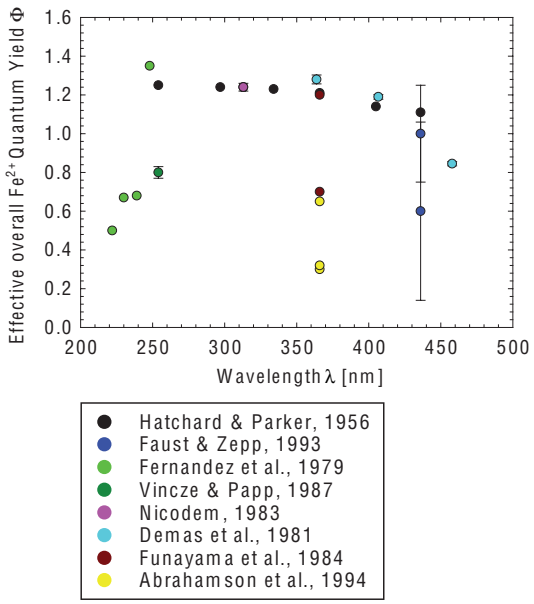

Fig. 2: *Literature overview of experimental Fe-oxalato quantum yields.*

(Fig. 3) in agreement with other studies (Hatchard and Parker 1956, Nicodem 1983). In and above milimolar concentrations the Fe-oxalate system is reliably used as chemical actinometer. But there is a marked concentration dependence below

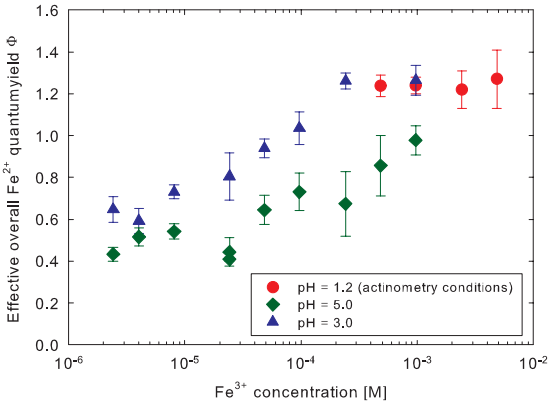

Fig. 3: *Dependence of overall Fe^{2+} quantum yield on initial Fe^{3+} concentration, Fe-oxalato flash photolysis at 308 nm.*

produced Fe^{2+} has been measured by spectrometry at 510 nm as $Fe(phenantroline)_3^{2+}$. The concentration of Fe^{2+} was determined with the Lambert-Beer law from the absorbance readings at 510 nm and the well known extinction coefficient of $Fe(phenantroline)_3^{2+}$. Fe^{2+} overall effective quantum yields have been calculated with the concentration of photochemically produced Fe^{2+} and the measured energy of the excimer laser pulse. The laser pulse energy was measured with a pyroelectric sensor.

Results of photolysis experiments

From $6 \cdot 10^{-3}$ M down to approximately $5 \cdot 10^{-4}$ M and also at higher concentrations the overall quantum yield of iron oxalate complexes is independent of the initial Fe^{3+} concentration

$5 \cdot 10^{-4}$ M for the measurement series at pH = 3. This behavior could be explained as follows. Two $CO_2^{-\cdot}$ radicals per photon can be produced (see Fig. 1), one reacts instantly with Fe(III)species, yielding one Fe^{2+} and the other can subsequently react: (i) with another Fe(III)species (secondary thermal reduction), yielding more Fe^{2+}, (ii) with itself (recombination) or traces of oxygen in the solution. Lowering the concentration of Fe(III)species could make reaction path (i) less effective, leading to a decrease of Φ. Quantum yield measurements at pH = 5 are generally lower compared to pH = 3 and show also a clear dependence on initial Fe^{3+} concentration. The explanation for the concentration dependence is the same as for pH = 3. The difference in quantum yield between pH 3 and 5 is due to a shift in the coordination of iron with oxalate from an excess

System with Fe^{3+}	Φ attributed to individual complex (species contains > 95 % Fe^{3+})	Effective overall Fe^{2+} quantum yield Φ		
		308 nm	351 nm	366 nm (literature)
malonic acid	$[Fe\text{-}(malonato)_2]^-$	0.024 ± 0.001	0.040 ± 0.003	0.027 (Faust and Zepp 1993)
succinic acid	mixed species	0.24 ± 0.02	0.16 ± 0.02	0.13 (Abrahamson 1994)
glutaric acid	$[Fe\text{-}(glutarato)_2]^-$	0.021 ± 0.001	0.017 ± 0.002	-
pyruvic acid	$[Fe\text{-}(pyruvato)]^{2+}$	0.28 ± 0.03	0.42 ± 0.02	-
glyoxylic acid	$[Fe\text{-}(glyoxalato)_2]^-$	0.64 ± 0.08	0.55 ± 0.01	-
tartronic acid	$[Fe\text{-}(tartronato)_2]^-$	0.44 ± 0.03	0.78 ± 0.02	-
gluconic acid	$[Fe\text{-}(OH)_3(gluconato)_2]^{2-}$	0.076 ± 0.003	0.10 ± 0.03	-

Tab. 1: *Effective overall quantum yields of carboxylic acid iron-complexes obtained from excimer laser flash photolysis, solutions contained oxygen under atmospheric pressure.*

of the [Fe-(oxalato)$_2$]$^-$ species at pH 3 towards an excess of the [Fe-(oxalato)$_3$]$^{3-}$ species at pH 5.

In the case of malonic, glutaric, pyruvic and glyoxalic acid the quantum yields could be attributed to individual complexes with known stoichiometry whereas the value for succinic acid was measured for a mixture of complexes (Tab. 1). The quantum yields of the complexes differ between 308 and 351 nm which might be due to a difference in the electronic transitions at higher wavelengths. The Quantum yields of atmospherically relevant carboxylic acid complexes with iron other than oxalic are sufficiently high to play a role for atmospheric chemistry. Out of the investigated compounds, [Fe-(glyoxalate)$_n$]^m complexes have the highest stability constants compared to Fe-oxalate and the other Fe-carboxylate complexes which makes them suitable candidates for atmospheric aqueous phase photochemistry.

References

Abrahamson, H. B., A. B. Rezvani, and J. G. Brushmiller (1994), Photochemical and Spectroscopic Studies of Complexes of Iron(III) with Citric-Acid and Other Carboxylic-Acid, *Inorg. Chim. Acta*, *226* (1-2), 117-127.

Deguillaume, L., M. Leriche, K. Desboeufs, G. Mailhot, C. George, and N. Chaumerliac (2005), Transition metals in atmospheric liquid phases: Sources, reactivity, and sensitive parameters, *Chem. Rev.*, *105* (9), 3388-3431.

Demas, J. N., W. D. Bowman, E. F. Zalewski, and R. A. Velapoldi (1981), Determination of the Quantum Yield of the Ferrioxalate Actinometer with Electrically Calibrated Radiometers, *J. Phys. Chem.*, *85* (19), 2766-2771.

Faust, B. C., and R. G. Zepp (1993), Photochemistry of Aqueous Iron(III) Polycarboxylate Complexes - Roles in the Chemistry of Atmospheric and Surface Waters, *Environ. Sci. Technol.*, *27* (12), 2517-2522.

Fernandez, E., J. M. Figuera, and A. Tobar (1979), Use of the Potassium Ferrioxalate Actinometer Below 254-Nm, *J. Photochem.*, *11* (1), 69-71.

Funayama, H., K. Ogiwara, T. Sugawara, and H. Ohashi (1984), Dependence of Quantum Yield on Concentration in Potassium Trisoxalatoferrate Chemical Actinometer, *Kagaku Kogaku Ronbunshu*, *10* (4), 534-536.

Hatchard, C. G., and C. A. Parker (1956), A New Sensitive Chemical Actinometer 2. Potassium Ferrioxalate as a Standard Chemical Actinometer, *Proceedings of the Royal Society of London Series a-Mathematical and Physical Sciences*, *235* (1203), 518-536.

Herrmann, H., A. Tilgner, P. Barzaghi, Z. Majdik, S. Gligorovski, L. Poulain, and A. Monod (2005), Towards a more detailed description of tropospheric aqueous phase organic chemistry: CAPRAM 3.0, *Atmos. Environ.*, *39* (23-24), 4351-4363.

Nicodem, D. E., and O. M. V. Aquilera (1983), Standardization of the Potassium Ferrioxalate Actinometer over the Temperature-Range 5-Degrees-C 80-Degrees-C, *J. Photochem.*, *21* (3), 189-193.

Vincze, L., and S. Papp (1987), Individual Quantum Yields of $Fe^{3+}Ox_n^{2-}H_m^+$ Complexes in Aqueous Acidic Solutions (Ox^{2-}=(C_2O_4)O^{2-}, N = 1 - 3, M = 0,1), *J. Photochem.*, *36* (3), 289-296.

Funding

- TRACES (Ocean-Atmosphere-Land Impacts on Tropical Atlantic Ecosystems), WGL-SAW- Project

Cooperation

- TRACES: Leibniz Institute for Baltic Sea Research (IOW), Leibniz Institute of Marine Sciences (IFM-GEOMAR), Potsdam Institute for Climate Impact Research (PIK)

Laboratory Studies on the Multiphase Chemistry of Isoprene and Acetone: Kinetic and Product Studies

Thomas Schaefer, Dirk Hoffmann, Luisa Schöne, Hartmut Herrmann

Für Reaktionen von Oxidationsprodukten des Isoprens und des Acetons mit atmosphärisch relevanten Radikalen wurden temperaturabhängige Geschwindigkeitskonstanten in wässriger Lösung mittels einer Laser-Photolyse-Langwegsabsorptionsapparatur ermittelt. Weiterhin konnten durch Modifizierung dieser Apparatur UV-Absorptionsspektren kurzlebiger Reaktionsprodukte (organische Peroxyradikale) aufgezeichnet werden. Mit den erhaltenen spektroskopischen Daten werden unter anderem Rekombinationsreaktionen der Peroxyradikale untersucht. Ergänzt wurden die kinetischen und spektroskopischen Untersuchungen durch Produktstudien. Die ermittelten Daten zur Kinetik und Produktverteilung werden in den Ausbau und die Verbesserung des Multiphasenmechanismus CAPRAM 3.0 (Chemical Aqueous Phase RAdical Mechanism) einfliessen.

Introduction

The atmospheric conversion and degradation of volatile organic compounds (VOCs) is often initiated by radical reactions in all phases including the aqueous phase (clouds, rain and deliquescent particles) [*Herrmann*, 2003]. In order to describe the aqueous phase oxidation processes more detailed, information on the reactivity, on transient species (i.e., peroxy radicals), on reaction end products and on the product distribution are needed. Within the DFG projects ACETOX (The atmospheric multiphase oxidation of acetone) and MISOX (Tropospheric Multiphase Processing of Isoprene Oxidation Products) aqueous phase oxidation processes of acetone, isoprene as well as important oxidation products were investigated.

Experimental

The kinetic and spectroscopic measurements of the radical reactions have been done as a function of the temperature (278 K ≤ T ≤ 318 K) and the pH value (0.5 ≤ pH ≤ 9) using a Laser-Photolysis-Long-Path-Absorption (LP-LPA) setup (Fig. 1). For the kinetic measurement of the OH radicals, which was formed by photolysis of H_2O_2 at λ = 248 nm, a competition kinetics method applying the thiocyanate reference system [*Gligorovski and Herrmann*, 2004; *Hoffmann et al.,* 2009] was used. In contrast to this, the rate constants for NO_3 and SO_4^- reactions were determined by direct measurements following the decay of the radical concentration as a function of the time and the reactant concentrations. The NO_3 radical was produced by both photolysis of nitrate anions at λ = 248 nm under acidic conditions (pH = 0.5) and photolysis of peroxodisulphate anions at λ = 248 nm in presence of nitrate anions [*de Semainville et al.*, 2007]. SO_4^- radicals were formed by the photolysis of peroxodisulphate anions at λ = 248 nm.

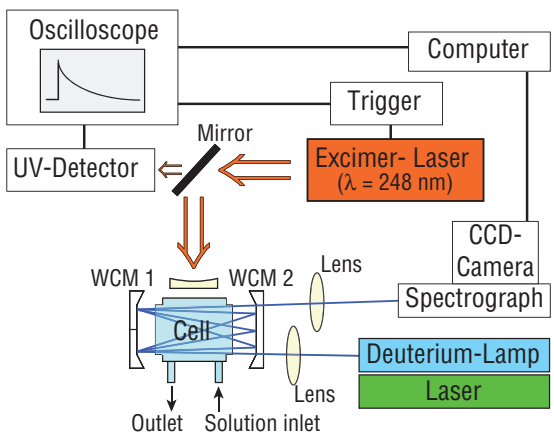

Fig. 1: *Laser-Photolysis – Long-Path-Absorption set-up coupled with a CCD-camera / grating combination for the kinetic and spectroscopic investigations in aqueous solution.*

The peroxy radicals in aqueous solution have been generated by the reaction of the OH radical with the parent organic compounds via H-atom abstraction mechanism in presence of oxygen. In order to characterize the optical properties of these transient species the (LP-LPA) setup (Fig. 1) was coupled with a CCD-camera / grating combination. The analytical light source was a water-cooled 150 W deuterium lamp. With this setup time resolved absorption spectra (at different delay times after the excimer laser pulse) of the reactants and products were recorded (see Fig. 2).

Results

Kinetic studies. Temperature dependent rate constants for the reaction of OH, NO_3 and SO_4^- radicals with water soluble oxidation products of acetone and isoprene have been measured. The investigated reactants include small and highly functionalized carboxylic acids, carbonyls and alcohols as well as unsaturated compounds such as methacrolein and methyl vinyl ketone from the isoprene oxidation. Additionally, kinetic measurements of acidic reactants were done at

compound	$k_{OH,\ 298\ K}$ [$M^{-1}\ s^{-1}$]	E_A [kJ mol^{-1}]	A [$M^{-1}\ s^{-1}$]	pH
OH + small organic compounds				
1.3-dihydroxyacetone	$(1.7 \pm 0.3) \cdot 10^9$	13 ± 3	$(3.5 \pm 0.2) \cdot 10^{11}$	6
1.3-butanediol	$(2.5 \pm 0.2) \cdot 10^9$	10 ± 4	$(1.2 \pm 0.1) \cdot 10^{11}$	6
2.3-butanediol	$(2.0 \pm 0.04) \cdot 10^9$	10 ± 3	$(1.1 \pm 0.1) \cdot 10^{11}$	6
OH + isoprene oxidation products				
acrylic acid	$(5.4 \pm 0.8) \cdot 10^9$	7 ± 1	$(1.1 \pm 0.01) \cdot 10^{11}$	1
acrylic acid	$(6.5 \pm 1.0) \cdot 10^9$	3 ± 1	$(2.4 \pm 0.1) \cdot 10^{11}$	8
NO_3 + isoprene oxidation products				
methacroleine	$(3.0 \pm 0.6) \cdot 10^7$	4 ± 4	$(1.5 \pm 0.1) \cdot 10^8$	1
methylvinylketone	$(1.9 \pm 0.3) \cdot 10^7$	15 ± 2	$(6.9 \pm 0.3) \cdot 10^9$	1
acrylic acid	$(2.2 \pm 0.1) \cdot 10^7$	28 ± 7	$(1.6 \pm 0.2) \cdot 10^{12}$	1
methacrylic acid	$(1.1 \pm 0.2) \cdot 10^8$	21 ± 17	$(8.1 \pm 2.0) \cdot 10^{11}$	1

Tab. 1: *Kinetic data and activation parameters of investigated OH and NO_3 reactions with organic compounds in aqueous solution.*

two different pH-values to measure the reactivity of the dissociated and the undissociated form. Some results of the kinetic measurements from both DFG-projects are summarized in Tab. 1.

Spectroscopic studies. Within the ACETOX project spectroscopic investigations were performed in order to study the formation of transient reaction products such as organic peroxy radicals. After an intensive characterization of both the measurement method and the measurement setup, absorption spectra of the organic reactants, radicals and organic peroxy radicals were measured. Figure 2 shows the absorption spectra of the organic peroxy radical formed after the oxidation of the following carbonyl compounds by OH radicals in presence of oxygen (a) acetone, (b) hydroxyacetone and (c) methylglyoxal. In the case of the acetonylperoxy radical the resulting spectrum (Fig. 2A) is in a good agreement with the absorption spectrum obtained by [*Zegota et al.*, 1986]. The spectroscopic information's

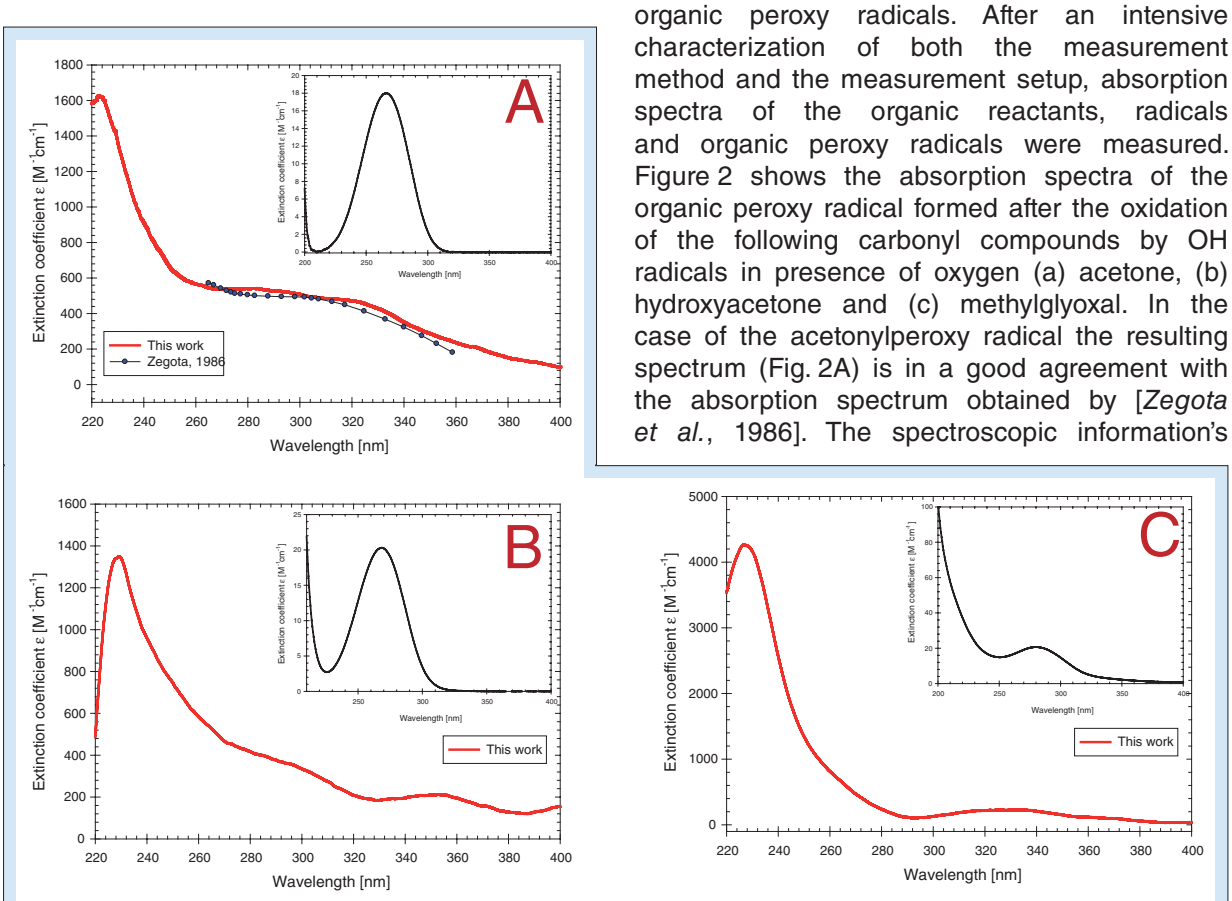

Fig. 2: *Spectrum of the observed peroxy radical A) acetonylperoxy radical, B) hydroxyacetonylperoxy radical and C) methylglyoxylperoxy radical measured in a oxygen saturated aqueous solution. The spectrum of A) acetone, B) hydroxyacetone and C) methylglyoxal is shown in the insets.*

obtained are necessary to study radical recombination reactions in the next step.

Product studies. Kinetic measurements of the isoprene oxidation products methacrolein and methyl vinyl ketone were supplemented by product studies. For the product studies methacrolein and methyl vinyl ketone were oxidized in aqueous solution by OH radicals. The reaction solutions were subsequently analyzed using different hyphaneted analytical techniques such as HPLC-MS, CE-UV and CE-MS. Identified reaction products were highly functionalized carbonyls and acids including pyruvic acid, methylglyoxal and hydroxyacetone. Informations on the reaction products will allow a better description of the isoprene degradation sequence in future versions of the CAPRAM mechanism.

Summary

Results obtained indicate the importance of aqueous phase processes for conversion and degradation reactions of VOCs. Furthermore, radical reactions in aqueous solution can represent an effective source for the formation of known atmospheric particle constituents such as mono- and dicarboxylic acids. The obtained data will be used to improve the multiphase mechanism CAPRAM [*Herrmann et al.*, 2005].

References

de Semainville, P. G., D. Hoffmann, C. George, and H. Herrmann (2007), Study of nitrate radical (NO3) reactions with carbonyls and acids in aqueous solution as a function of temperature, *Phys. Chem. Chem. Phys.*, *9* (8), 958-968.

Gligorovski, S., and H. Herrmann (2004), Kinetics of reactions of OH with organic carbonyl compounds in aqueous solution, *Phys. Chem. Chem. Phys.*, *6* (16), 4118-4126.

Herrmann, H. (2003), Kinetics of aqueous phase reactions relevant for atmospheric chemistry, *Chem. Rev.*, *103* (12), 4691-4716.

Herrmann, H., A. Tilgner, P. Barzaghi, Z.-T. Majdik, S. Gligorovski, L. Poulain, and A. Monod (2005), Towards a more detailed description of tropospheric aqueous phase organic chemistry: CAPRAM 3.0, *Atmos. Environ.*, *39* (23-24 (Special Issue: FEBUKO and MODMEP)), 4351-4363.

Hoffmann, D., B. Weigert, P. Barzaghi and H. Herrmann (2009), Reactivity of poly-alcohols towards OH, NO_3 and $SO4^-$ in aqueous solution, *Phys. Chem. Chem. Phys.*, *11* (41), 9351-9363.

Zegota, H., Schuchmann, M.N., Schulz, D., von Sonntag, C., (1986), Acetonylperoxyl Radicals, $CH_3COCH_2O_2$: A Study on the γ-Radiolysis of Acetone in Oxygenated Aqueous Solutions, *Z. Naturforsch.*, *41b* (8), 1015-1022

Funding
- German Research Foundation (DFG), Bonn, Germany

Hygroscopicity at High Relative Humidities, Activation Properties, and Chemical Composition of Anthropogenic Influenced Aerosol in China

Silvia Henning[1], Andreas Nowak[1], Katrin Mildenberger[1], Eike Sommerhage[1], Eva Hallbauer[1], Tina Göbel[1], Bettina Nekat[1], Dominik van Pinxteren[1], Zhaoze Deng[2], Pengfei Liu[2], Nan Ma[2], Chunsheng Zhao[2], Hartmut Herrmann[1], Alfred Wiedensohler[1], Frank Stratmann[1]

[1] Leibniz Institute for Tropospheric Research (IfT), Leipzig, Germany
[2] Department of Atmospheric Sciences, School of Physics, Peking University, Beijing, China

Der Nordosten Chinas und insbesondere die Region zwischen Beijing und Tianjin weist in den letzten Jahrzehnten sowohl ein starkes Wirtschafts- als auch Bevölkerungswachstum auf, verknüpft mit einer hohen Siedlungsdichte und einer starken Luftverschmutzung mit sehr geringen Sichtweiten. Die Luftverschmutzung hat nicht nur negative Auswirkungen auf die Gesundheit des Menschen, sondern wirkt sich auch in der Strahlungsbilanz der Erde aus.

Im Rahmen des DFG Projekts HaChi (Haze in China) wurden im Winter und Sommer 2009 das Partikelwachstum bei sehr hohen relativen Feuchten, die Wolkentropfen-Aktivierbarkeit, die chemische Zusammensetzung sowie die optischen Partikeleigenschaften bestimmt. Diese Messungen wurden in Kooperation mit dem Institut für Atmosphärenphysik an der Peking Universität durchgeführt. Basierend auf den Messungen wird eine Parametrisierung des hygroskopischen Partikelwachstums und der Aktivierung erarbeitet, welche in einem Boxmodell zur Beschreibung von Partikel-, Wolken- und Strahlungswechselwirkungen Anwendung finden wird. Erste Ergebnisse zeigen eine starke Abhängigkeit der Hygroskopizität von der Partikelgröße. Außerdem wurde für alle Größen eine hydrophobe Partikelfraktion (extern gemischter Ruß) beobachtet. Beides muss in bei der Vorhersage der Anzahl von Wolkenkondensationskeimen berücksichtigt werden, da sonst große Fehler in Abhängigkeit von der Partikelgrößenverteilung auftreten können.

Introduction

North Eastern China, especially the area around Beijing and Tianjin, frequently suffers from heavy air pollution (both gaseous and particulate) and low visibility caused by a strong economic and population growth in the last two decades. The pollution has consequences for human health, the formation of cloud droplets due to the condensation nuclei, and the radiative properties of the atmosphere. The strength and direction of the aerosol effect on climate depends on the physical and chemical properties or the aerosol particles. However, detailed knowledge concerning these properties and their effects on the optical properties of the atmosphere is mainly limited to urban studies in Beijing, because the characterization of the regional aerosol was limited so far to the CAREBeijing study in 2006.

In the framework of the DFG project HaChi (Haze in China), comprehensive measurements concerning aerosol particle hygroscopicity at high relative humidity, CCN ability, chemical composition, and optical properties were taken in winter and summer 2009. These investigations were conducted in collaboration with the Departments of Atmospheric Physics of Peking University, Beijing, China. Here, a conclusive parameterization of aerosol hygroscopicity and activation data is aimed for; it will then be implemented in a box model to investigate aerosol-cloud-radiation interactions.

Experimental

During two intensive campaigns in March and July/August 2009, in-situ aerosol measurements were performed in an air-conditioned mobile laboratory next to the Wuqing Meteorological Station (39°23'8.53"N, 117°1'25.88"E), located between Beijing and Tianjin, which is an ideal regional site in this megacity region. In the report at hand, we focus on data from the winter campaign.

Particle number size distributions (TDMPS and APS), light scattering and absorption coefficients (MAAP and integrating nephelometer) and hygroscopic properties (growth and mixing state) at high RH (HH-TDMA, LACIS-mobile) were characterized as well as their size-resolved cloud nucleating properties above supersaturation (DMA-CCNC). All these instruments were connected to a PM_{10} inlet mounted on the roof of the mobile laboratory followed by a aerosol drier unit [*Tuch, et al.*, 2009].

Both, HH-TDMA [*Hennig, et al.*, 2005] and LACIS-mobile [*Stratmann, et al.*, 2004; *Wex, et al.*, 2006] measured size-resolved hygroscopic properties at several relative humidities for selected particle sizes in the ranges 50 – 250 nm and 200 – 250 nm, respectively. The relative humidities were 90 to 99 % for the HH-TDMA and 97.5 to 99.6 % RH for LACIS-mobile. The CCNC instrument [*Roberts and Nenes*, 2005] was operated in combination with a DMA for monodisperse activation measurements.

For chemical composition, 24 h PM_1 particle samples were continuously collected over the two campaigns in winter and summer using a DIGITEL high volume sampler (DHA-80). Additionally, two 6h size-resolved samples (day-time and night-time) were collected each day applying a 11-stage Berner impactor. The size selection of HH-TDMA, LACIS and the CCNC was synchronized with the impactor stages.

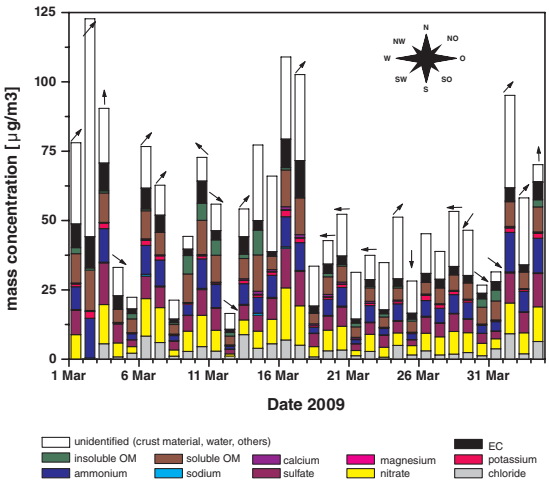

Fig. 1: *hemical composition of PM_1 aerosol mass (DIGITEL). Samples were taken for 24h starting midnight LT. Arrows indicate the prevailing wind direction for days with relatively stable conditions.*

First Results - Winter Campaign

Figure 1 shows the chemical mass balance of the PM_1 aerosol for the winter campaign. Usually, the highest aerosol mass concentrations were observed during periods with air masses from southern areas, while northern wind directions led to significantly lower concentrations. As shown in Fig. 1, the main chemical compounds were inorganic ions such as secondary formed ammonium nitrate und ammonium sulfate, as well as carbonaceous material. The organic carbon fraction was mostly dominated by water soluble organic carbon (80 % on average). A detailed analysis was done for dicarboxylic acids, fatty acids, sugars and sugar-related compounds. High concentrations of tracers such as the anhydrosugar levoglucosan [*Iinuma, et al.*, 2007] suggest biomass burning emissions as a dominant source of organic particles in the area. A significant mass fraction remained unidentified and consisted most likely of crustal material such as dust, and of particle-bound water.

Size-resolved hygroscopicity and activation were measured during the whole winter campaign covering one month. The time resolution was between 8 min and 30 min depending on the ambient particle number concentration. Figure 2

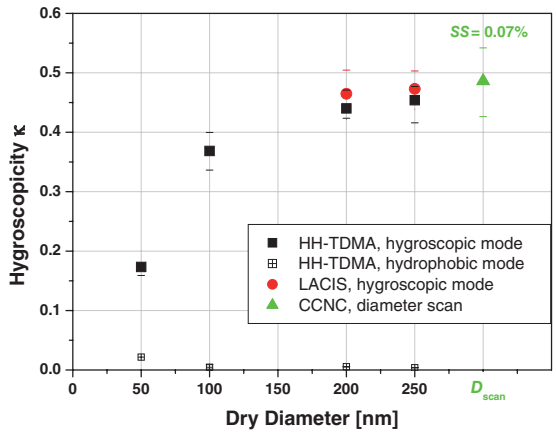

Fig. 2: *Median values over the whole winter campaign of the hygroscopicity parameter κ versus the dry particle diameter for 99 % RH. Values are derived from HH-TDMA, LACIS-mobile and CCNC measurements. Upper and lower lines give 25 and 75 percentile value, respectively.*

provides an overview over the winter campaign in form of the hygroscopicity parameter κ following *Petters and Kreidenweis* [2007].

The HH-TDMA hygroscopic growth spectra were divided into three ranges: hydrophobic (0 – 20 % of hygroscopic growth of pure ammonium sulfate), intermediate (20 – 80 %), and hygroscopic (80 – 100 %). Generally particles of a certain size were externally mixed. On average κ in the hydrophobic mode was about 0.02 with no size-dependence. Also on average approximately 15 % of the particles were of hydrophobic nature over all sizes. The frequent presence of hydrophobic soot particles is consistent with biomass burning being one of the dominant sources of organics. For larger hygroscopic particles, LACIS-mobile and the HH-TMDA detected high κ-values of about 0.47, close to ammonium sulfate with a κ of 0.53 [*Petters and Kreidenweis*, 2007] (cf. Fig. 3). This observation is in agreement with the activation-measurement-derived κ-value of 0.49. For the hygroscopic particles, a strong size-dependence of κ on particle size was observed, with small particles being less hygroscopic than larger ones. This fact and the hydrophobic and intermediate particle fractions have to be considered for CCN predictions. Applying κ 0.47 for all sizes may lead to an overestimation of 50 %, and neglecting the hydrophobic and the intermediate particle fraction may result in an overprediction of the CCN number concentration (calculated for SS = 0.1 %, case study March 11, 2009).

Two different closure studies were performed with respect to the particle activation. For one, the hygroscopicity parameter κ as derived from the hygroscopic growth measurements was used to predict SS_{crit}. For the second, a standard Köhler model was used, together with information on the

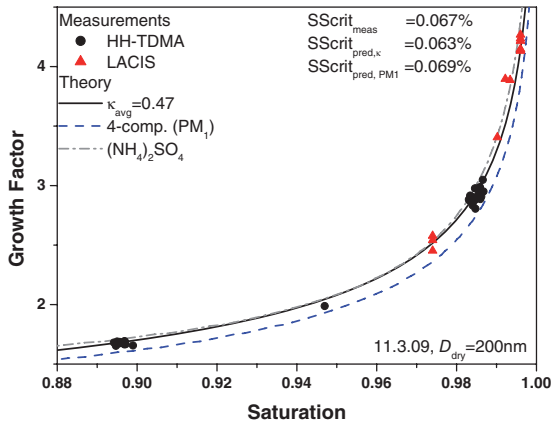

Fig. 3: Measured growth factors (GF) for a dry particle diameter of 200 nm in relation to saturation at March 11, 2009. The lines give the Köhler curves calculated for the HH-TMDA and LACIS derived kappa of 0.47 (black), a 4-component chemistry model based on the chemical composition of PM_1 (dashed blue) and for ammonium sulphate (grey).

4 major aerosol components as obtained from the chemical analysis of the DIGITEL samples to predict SS_{crit}. We selected March 11, 2009 (Fig. 3) for a case study. On this day the maximum of the volume size distribution ranged between 200 and 250 nm, and the submicrometer chemical composition was dominated by particles in this size range. GFs measured with HH-TDMA and LACIS for particles of a dry size of 200 nm are shown in Fig. 3 as function of saturation. The κ-value for HH-TDMA and LACIS measurements was derived to $\kappa_{avg} = 0.47$, and the associated Köhler curve was calculated (black line). SS_{crit} was predicted to 0.063 %, which agrees well with the CCNC-determined SS_{crit} of 0.067 %.

In the second approach the mass of 4 major components, namely ammonium sulfate, ammonium nitrate, sodium chloride and soluble organic matter, was used as input parameter of a standard Köhler model including an insoluble core. The resulting Köhler curve is given as dashed blue line. The hygroscopic growth of the particles is underestimated by about 6 %, but considering the assumptions made (bulk chemistry, 4-components included), the agreement is still good. The activation point was well predicted with 0.069 %.

Outlook

Future work will focus on the development of an improved CCN prediction model by considering the aerosol mixing state and size-dependent particle hygroscopicity. For the hygroscopicity closure, size-resolved chemical composition will be included in the parameterization. The challenge will be the mixing state of elemental carbon. Furthermore, the hygroscopic properties will be related to the air mass origin and if possible to sources applying a cluster analysis. The hygroscopicity data will also be investigated for seasonal influences on air chemistry. The hygroscopicity results and the number size distributions will be employed e.g. in a box model to simulate the radiative effect of the haze layer and to predict the cloud activation.

References

Hennig, T., A. Massling, F. J. Brechtel, and A. Wiedensohler (2005), A tandem DMA for highly temperature-stabilized hygroscopic particle growth measurements between 90% and 98% relative humidity, *J. Aerosol Sci.*, *36* (10), 1210-1223.

Petters, M. D., and S. M. Kreidenweis (2007), A single parameter representation of hygroscopic growth and cloud condensation nucleus activity, *Atmos. Chem. Phys.*, *7* (8), 1961-1971.

Roberts, G. C., and A. Nenes (2005), A continuous-flow streamwise thermal-gradient CCN chamber for atmospheric measurements, *Aerosol Sci. Technol.*, *39* (3), 206-221.

Stratmann, F., A. Kiselev, S. Wurzler, M. Wendisch, J. Heintzenberg, R. J. Charlson, K. Diehl, H. Wex, and S. Schmidt (2004), Laboratory studies and numerical simulations of cloud droplet formation under realistic supersaturation conditions, *J. Atmos. Ocean. Tech.*, *21* (6), 876-887.

Tuch, T. M., A. Haudek, T. Müller, A. Nowak, H. Wex, and A. Wiedensohler (2009), Design and performance of an automatic regenerating adsorption aerosol dryer for continuous operation at monitoring sites, *Atmos. Meas. Tech. (AMT)*, *2*, 417–422.

Wex, H., A. Kiselev, M. Ziese, and F. Stratmann (2006), Calibration of LACIS as a CCN detector and its use in measuring activation and hygroscopic growth of atmospheric aerosol particles, *Atmos. Chem. Phys.*, *6*, 4519-4527.

Funding
- German Research Foundation (DFG), Bonn, Germany

Cooperation
- Department of Atmospheric Sciences, Peking University, Beijing, China

Aerosol Raman lidar measurements in the Amazon rain forest

Holger Baars, Dietrich Althausen, Ronny Engelmann, Albert Ansmann, Detlef Müller

Mit dem automatischen Mehrwellenlängen-Raman-Lidar Polly^{XT} wurden erste Langzeituntersuchungen zur vertikalen Aerosolverteilung im Amazonasbecken durchgeführt. Die Messungen fanden 50 km nördlich von Manaus, Brasilien (2°S, 60°W) statt. Insgesamt konnten Messdaten über 2500 Stunden im Zeitraum von Januar bis November 2008, also sowohl während der Regen- als auch der Trockenzeit, erfasst werden. Aus diesem Datensatz wird ein Fallbeispiel (Trockenzeit) präsentiert und intensiv bezüglich optischer Aerosoleigenschaften und der Schichtstruktur diskutiert. Mit Polly^{XT} können vertikale Profile des Rückstreukoeffizienten bei 355, 532 und 1064 nm, des Extinktionskoeffizienten bei 355 und 532 nm und des Partikeldepolarisationsverhältnisses bei 355 nm bestimmt werden. Auch mikrophysikalische Eigenschaften, wie der effektive Radius und die Volumenkonzentration, werden mittels Inversion ermittelt und analysiert. Die Untersuchung des Fallbeispiels zeigt, dass hierbei Partikel von lokalen Biomasseverbrennungen beobachtet wurden.

Introduction

The Amazon basin with its extensions of more than six million square kilometres contains the worlds largest tropical rain forest. Investigations of aerosol characteristics in this large area are important for the understanding of the local and global influence of Amazonian aerosol on radiation budget and cloud formation. Compared to its global importance, knowledge on aerosols in this region is still inadequate. Efforts have been made in this region to characterize aerosol properties in the framework of the Large-Scale Biosphere-Atmosphere Experiment in Amazonia (LBA) but so far only a few studies of the vertical aerosol distribution were made. The vertical aerosol structure during the dry season was observed in Rondonia, south-west Brazil, during the Smoke, Aerosols, Clouds, Rainfall and Climate (LBA-SMOCC) campaign [*Chand et al.*, 2006]. Airborne measurements were used to characterize the aerosol within the planetary boundary layer (PBL) and within the free troposphere. Haze layers of biomass burning aerosol were frequently found above the PBL. Saharan dust and biomass-burning plumes from long-range transport were observed in the wet season during the Cooperative LBA Regional Experiment (CLAIRE98) in Surinam [*Formenti et al.*, 2001]. In spite of these interesting results there is still a lack of detailed knowledge of the vertical aerosol structure in this region. For the first time in Amazonia, long-term observations of the vertical aerosol structure were made for a period of almost one year in the framework of the European Integrated project on Aerosol Cloud Climate and Air Quality Interactions (EUCAARI).

Experiment

The lidar observations in Amazonia took place from January to November 2008. The experimental site was located ca. 50 km north of Manaus in the Brazilian part of the Amazon rain forest at 2° 35.5' S, 60° 2.3' W, 84 m a.s.l. Figure 1 shows the field site in Brazil. The satellite dish for the internet connection and Polly^{XT} are situated on a glade in the rain forest at the Silvicultura site of the National Institute for Amazonia Research (INPA). The main wind direction in this region is usually northeast to east, thus typically no pollution from the city of Manaus is expected. The general weather conditions are characterized by a wet season and a dry season. A high fire activity is typically observed in the dry season.

The automated polarization Raman lidar Polly^{XT} [*Althausen et al.*, 2009] was used to perform the measurements. With this instrument, vertical profiles of the backscatter coefficients can be derived at 355, 532 and 1064 nm. Profiles of extinction coefficients are determined from nighttime observations at 355 and 532 nm using the Raman scattered light at 387 and 607 nm. Crosspolarized light is detected at 355 nm and allows for the determination of the particle depolarization. The system is designed to

Fig. 1: *Field site with satellite dish for internet connection and lidar Polly^{XT}.*

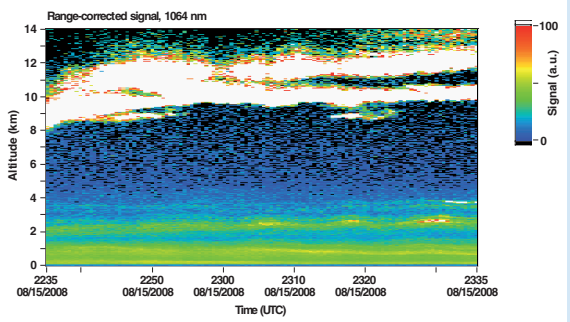

Fig. 2: Temporal development of range-corrected signal at 1064 nm on 15 August 2008.

measure 24 hours a day, 7 days a week and can be controlled remotely via internet. Additionally, the data are automatically transferred to a server and plots of the range-corrected signals are shown in near real time on a website (http://polly.tropos.de).

During the almost one-year period, lidar measurements were performed on 211 days resulting in more than 2500 hours of tropospheric observations in the Amazon rain forest. Nevertheless, fog development during night time at the canopy level prohibited detailed analysis of many observation cases during the wet season. At daytime the high frequency of low-level clouds and rain also caused problems in data analysis. Therefore only a few measurement cases of the wet season can be used for the detailed analysis of vertical aerosol profiles. During the dry season, fog, low-level clouds and rain also disturbed lidar observation, but the frequency of occurrence of such events is much lower than during the wet season. One example case of the dry season (15 August 2008) will be discussed in the following.

Case study

The temporal development of the range-corrected signal at 1064 nm between 2235 and 2335 UTC on 15 August 2008 is shown in Fig. 2. A complex aerosol layer structure was existent during the one-hour nighttime observation. Aerosol up to 5 km was observed. The residual layer extended up to ca. 1.6 km. A lofted aerosol layer centred at ca. 2.5 km can be seen. Diverse cloud layers were present above 9 km. Figure 3 shows the vertical profiles of backscatter and extinction coefficients, lidar ratios, and Ångström exponents at several wavelengths. The profiles of backscatter and extinction coefficient show a clear spectral behaviour. Maximum extinction coefficients of 130 Mm^{-1} and 80 Mm^{-1} at 355 and 532 nm, respectively, occur in the residual layer. Values up to 100 Mm^{-1} and 45 Mm^{-1} are observed in the lofted aerosol layer at 2.5 km. Integration of the extinction profile yields a particle optical depth of about 0.3 and 0.15 at the two wavelengths (assuming height independent extinction in the lowermost 1 km). The corresponding vertical profiles of the lidar ratio at the two wavelengths are almost spectral independent. The values vary between 35 and 55 sr. Relatively high extinction-related Ångström exponents (about two) indicate small aerosol particles. The inversion of the optical data set gives a rather low single scattering albedo (0.95±0.05) and small particle radii (0.13 ± 0.01 µm) for the residual layer and the lofted aerosol layer. These optical and microphysical properties are in good agreement with observations of local biomass burning smoke in Amazonia [*Reid et al.*, 1998]. Figure 4 shows the fire counts in northern South America

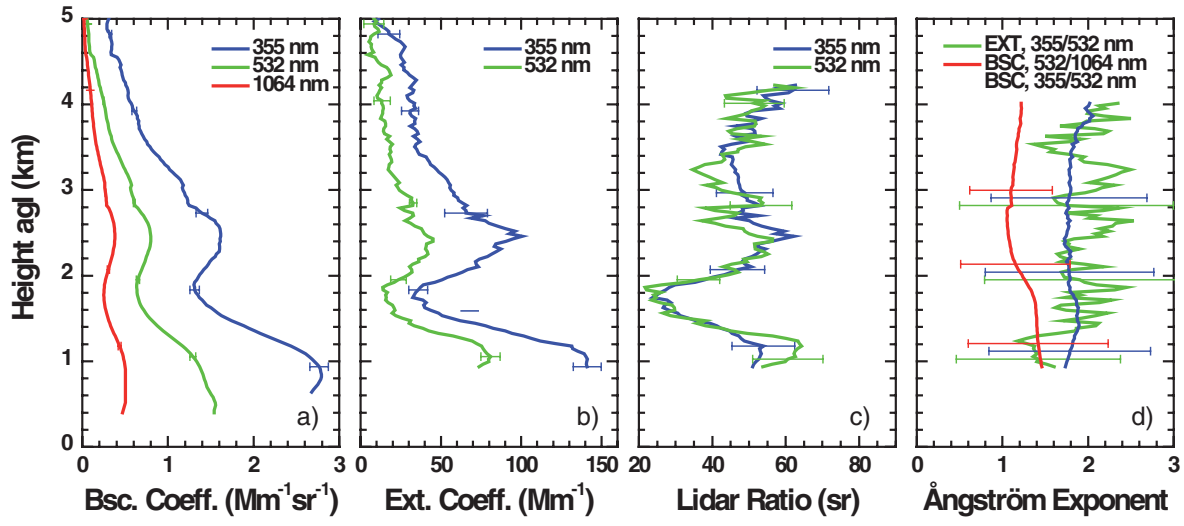

Fig. 3: Vertical profiles of a) backscatter coefficient, b) extinction coefficient, c) lidar ratio, and d) Ångström exponents on 15 August 2008 2235-2335 UTC.

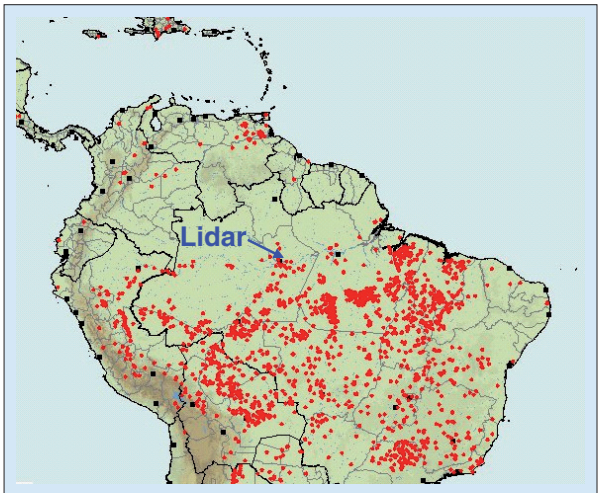

Fig. 4: *MODIS fire counts on 14-15 August 2008. Blue arrow shows the location of the lidar. (NASA/GSFC, MODIS Rapid Response:rapidfire.sci.gsfc.nasa.gov)*

on that day. A high burning activity can be seen in the south and southwest of the measurement site. Many fire spots were also detected close (around 100 km) to the field site. Therefore one can conclude, that local and/or regional biomass-burning aerosol dominated the optical aerosol properties on 15 August 2008.

Summary

Multiwavelength Raman lidar observations were performed in Amazonia for a period of almost one full year with about 2500 hours of observations time. In the wet season lots of cases with low-level clouds, fog and rain were observed. The aerosol layer height was typically between 1.5 and 3 km. Some cases of lofted layers (up to 4 km) were observed. Occasionally aged biomass-burning aerosol from Africa dominated optical aerosol properties at the measurement site [*Ansmann et al.*, 2009]. In the dry season the aerosol layer top was typically between 2.5 – 5.5 km. A frequent occurrence of lofted aerosol layers was observed. Biomass burning is the dominant aerosol source in this season, as shown for the example case of 15 August 2008.

References

Althausen, D., R. Engelmann, H. Baars, B. Heese, A. Ansmann, D. Müller, and M. Komppula (2009), Portable Raman Lidar Polly^{XT} for automated profiling of aerosol backscatter, extinction, and depolarization, *J. Atmos. Ocean. Tech.*, *26* (11), 2366-2378.

Ansmann, A., H. Baars, M. Tesche, D. Müller, D. Althausen, R. Engelmann, T. Pauliquevis, and P. Artaxo (2009), Dust and smoke transport from Africa to South America: Lidar profiling over Cape Verde and the Amazon rainforest, *Geophys. Res. Lett.*, *36*, L11802.

Chand, D., P. Guyon, P. Artaxo, O. Schmid, G. P. Frank, L. V. Rizzo, O. L. Mayol-Bracero, L. V. Gatti, and M. O. Andreae (2006), Optical and physical properties of aerosols in the boundary layer and free troposphere over the Amazon Basin during the biomass burning season, *Atmos. Chem. Phys.*, *6* (10), 2911-2925.

Formenti, P., M. O. Andreae, L. Lange, G. Roberts, J. Cafmeyer, I. Rajta, W. Maenhaut, B. N. Holben, P. Artaxo, and J. Lelieveld (2001), Saharan dust in Brazil and Suriname during the Large-Scale Biosphere-Atmosphere Experiment in Amazonia (LBA)-Cooperative LBA Airborne Regional Experiment (CLAIRE) in March 1998, *J. Geophys. Res.*, *106* (D14), 14919-14934.

Reid, J. S., P. V. Hobbs, R. J. Ferek, D. R. Blake, J. V. Martins, M. R. Dunlap, and C. Liousse (1998), Physical, chemical, and optical properties of regional hazes dominated by smoke in Brazil, *J. Geophys. Res.*, *103* (D24), 32059-32080.

Funding
- EUCAARI is funded by the European Union (Framework Programme 7, grant number 0368332)

Cooperation
- Institute of Physics, University São Paulo, Brazil
- National Institute for Amazonia Research (INPA), Brazil
- Amazon State University, Brazil
- AMAZE-08 Consortium
- EUCAARI Consortium

Biomass burning characterization at the village of Seiffen (Germany)

Laurent Poulain, Konrad Müller, Yoshiteru Iinuma, Hartmut Herrmann

In dieser Studie wurde eine intensive aerosol-charakterisierende Messkampagne zwischen Oktober 2007 und März 2008 in Seiffen, einem kleinen Dorf in Sachsen, durchgeführt. Ein HR-ToF-AMS wurde zwischen dem 10. Januar und dem 2. Februar 2008 zur Ergänzung eines alle vier Tage messenden Digitel High Volume PM Samplers eingesetzt.

Die AMS-Daten lieferten zeitlich hoch aufgelöste Informationen über den Einfluss der Holzverbrennung auf die lokalen PM_1-Werte. Mit Hilfe des AMS wurden ebenfalls detaillierte Informationen über die chemischen Bestandteile, wie z.B. Biomasseverbrennungsindikatoren auf die lokalen partikulären Konzentrationen erhalten. Die AMS Tagesmittelwerte von Kalium, PAH und Monosaccharid-Konzentrationen stimmten gut mit den PM_1-Filter-Konzentrationen überein. Damit konnten die AMS-Daten quantitativ zur unterstützenden Auswertung der Filterdaten verwendet werden. Sie zeigten einen starken Einfluss von Feuerholzverbrennung auf den PM am frühen Morgen und Abend. Weiterhin lieferten sie eine Reihe von hohen Levoglucosankonzentrationen in der Zeitreihe. Somit hat die lokale Rauchentwicklung durch Feuerholz einen stärkeren Einfluss auf die Luftqualität als die Emissionen von Luftschadstoffen oder der regionale Ferntransport in Seiffen.

Introduction

A recent trend in residential wood combustion for heating attracts a significant interest in characterizing its impact on air quality. In order to characterize the biomass burning aerosols, an intensive field campaign was performed in the small town of Seiffen during the winter 2007-2008. The sampling site was located in a mountain area (50°38'50" N, 13°27'08" E, and 647 m a.s.l.) at around 50 km southwest of Dresden.

An Aerodyne High Resolution Time of Flight Aerosol Mass Spectrometer (HR-ToF-AMS, [*DeCarlo et al.*, 2006]) was deployed from 10th January to 2nd February 2008 to compliment daily Digitel PM_1 filter sampling performed every four days during the whole winter season. The filters were analyzed using ion chromatography for main soluble inorganic ions, Curie Point Pyrolysis Gas Chromatography Mass Spectrometry (CPP-GC-MS) for PAH, and High Performance Anion Exchange Chromatography coupled to Pulse Amperometric Detector (HPAEC-PAD) for saccharidic wood smoke tracers (e.g. levoglucosan). A comparison of the AMS mass concentrations for different compounds (biomass burning organic aerosol tracers (BBOA), PAH and potassium) with PM_1 filter was performed to validate the AMS results and then to obtain the diurnal patterns of these compounds.

Results

AMS Time series. Average concentrations for organics, nitrate, sulfate, ammonium and non sea-salt chloride were 2.0, 1.1, 1.3, 0.6 and 0.07 µg m^{-3} during the AMS measurement period, respectively. Time series of these main particles components, wind direction and temperature are presented in Fig. 1. A comparison of the wind direction and temperature shows that periods of high particles concentrations correlate better with southeasterly wind and low temperature while periods with lower PM concentrations correspond to warmer conditions and northwesterly wind direction.

Comparison with off-line measurements. The AMS results for BBOA, PAH and potassium are compared with PM_1 filters. The AMS data are averaged over 24 hours (midnight to midnight) in order to have the same time resolution to PM_1 filter samples. Levoglucosan is known to be a good tracer for biomass burning and can be followed in the AMS mass spectrum by two specific fragments at *m/z* 60 ($C_2H_4O_2^+$) and *m/z* 73 ($C_3H_5O_2^+$) [*Schneider et al.*, 2006]. A linear relationship between these two fragments was observed during the measurement period. However, the ratio of these two fragments was clearly different from a standard of pure levoglucosan due to the presence of other sugars in the aerosol which also generate fragments at *m/z* 60 and *m/z* 73 with different ratios. Using the Positive Matrix Factorization method developed by [*Ulbrich et al.*, 2009] one factor was successfully assigned to Biomass Burning Organic Aerosol (BBOA). The resulting BBOA presents a similar time series to the fragment ($C_2H_4O_2^+$) as shown in Fig. 2, confirming the PMF assignment. Moreover, daily average BBOA concentrations are well correlated with the sum of the main biomass burning sugars (levoglucosan, mannosan and galactosan) identified by HPAEC-PAD in the PM_1 filter samples. This further supports the idea that fragments $C_2H_4O_2^+$ and $C_3H_5O_2^+$ originate not only from levoglucosan but also other saccharidic compounds originating from wood burning.

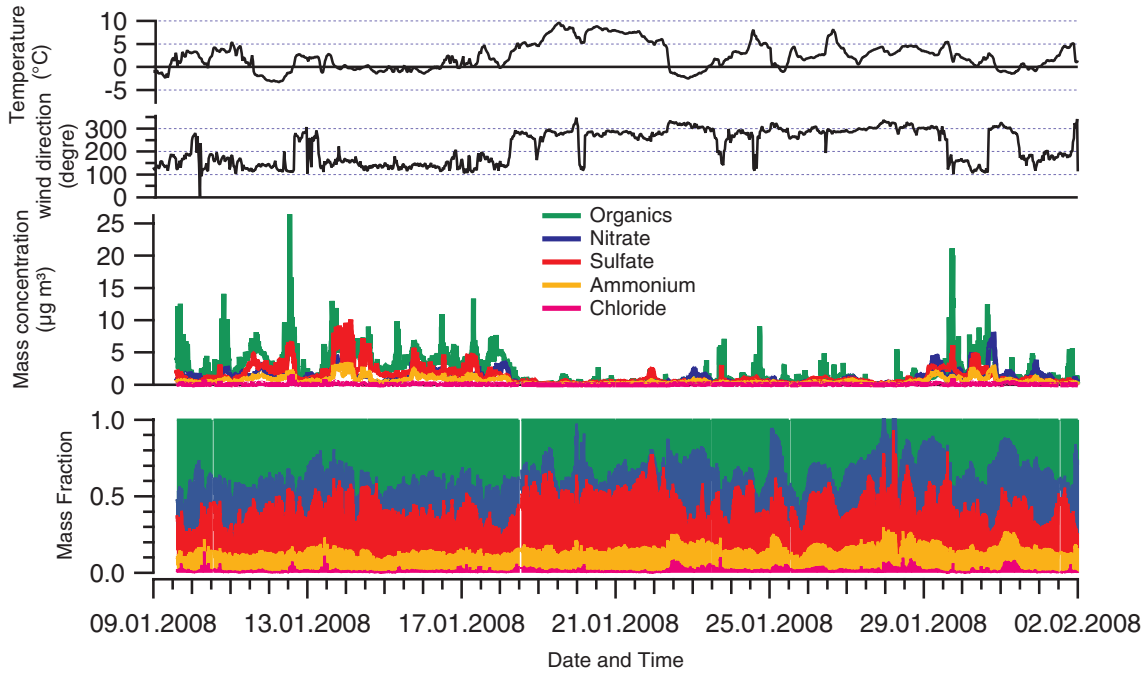

Fig. 1: *Temperature, wind direction, time series and mass fraction of the main non refractory PM_1 particle components during the whole campaign.*

A similar approach is used for the PAH according the PAH fragmentation table described in the literature [*Dzepina et al.*, 2007] and for potassium using the high time resolution of the AMS. The daily average results correlate well with total PAH determined from the filter samples considering the fact that the AMS-PAH concentrations have uncertainties of 35 – 38 % [*Dzepina et al.*, 2007]. A time series of the PAH shows the presence of very sharp spikes that may correspond to local emission sources such as car exhaust plumes. Moreover, periods with higher PAH concentrations were observed particularly at the beginning of the AMS measurement period when temperature was lower. The daily average of the AMS potassium signal correlates well with that of the PM_1 filter

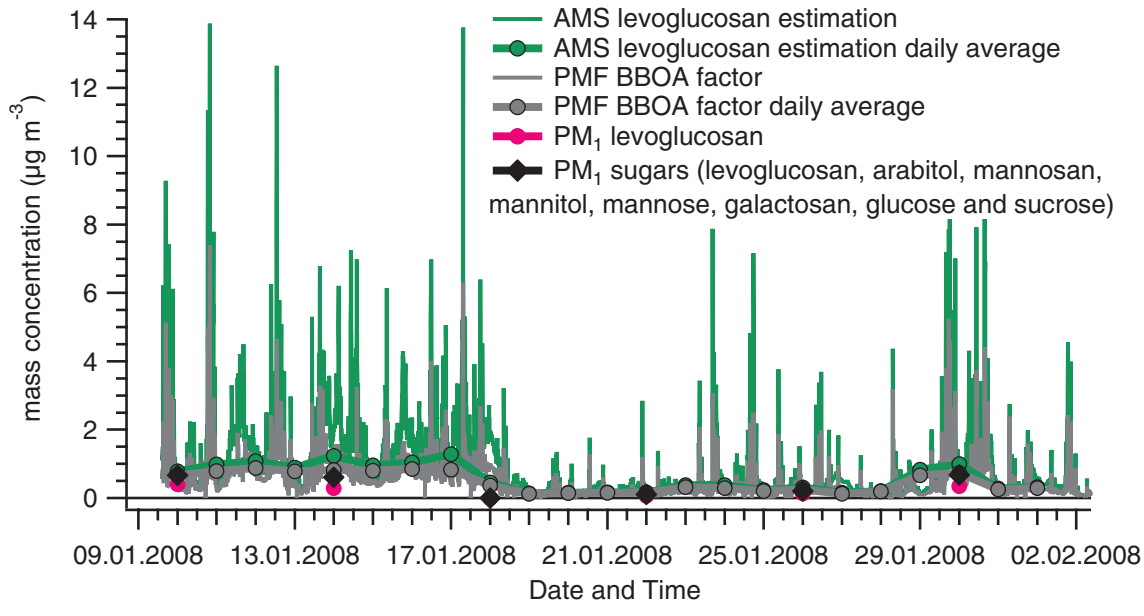

Fig. 2: *Time series of the estimated reconstructed levoglucosan and BBOA time series from PMF analysis. Levoglucosan and the sum of other sugars from PM_1 samples are also plotted.*

concentration. However, AMS results are not quantitative due to difficulties associating with the estimation of the potassium ionization efficiency which depends strongly on the form of potassium salts [*Takegawa et al.*, 2009].

The comparison between the daily average AMS data and the PM_1 filter data allows us to validate the AMS derived concentrations for a group of compounds, providing highly time resolved measurements for BBOA, PAH and potassium.

Diurnal profiles of the main particles components. A similar diurnal pattern is observed for organics, BBOA and potassium with two maxima: early morning and evening corresponding to the start of the day and the end of working hours/ home arrival. PAH correlates weakly with organics and BBOA which may be an indication for the existence of multiple sources of PAHs (fossil fuel based heating systems and car exhaust). These results indicate that the biomass burning has a significant influence on the organic fraction of the aerosol at Seiffen. Chloride also follows a pattern similar to the organics with a maximum only in the evening. Nitrate and sulfate behave differently from the organics and chloride, with a sulfate maximum and a nitrate minimum around the midday.

Summary. In this study, an intensive winter-time aerosol characterization campaign was carried out between October 2007 and March 2008 in the small village of Seiffen, Saxony. An HR-ToF-AMS was deployed between 10th January and 2nd February 2008 to compliment high volume PM samplers that were collected every four days between October 2007 and March 2008. The AMS data provides highly time resolved information about the influence of wood combustion to the local PM and PM_1 data provides more detailed information about chemical constituents such as biomass burning tracers in the local PM. The daily average AMS derived potassium, PAHs and monosaccharide concentrations agree well with that of PM_1 filter sample derived concentrations, indicating that the AMS data can be used quantitatively to support the filter data. The AMS data shows a strong influence of residential wood burning to the PM in the early morning and in the evening. The AMS data reveals a number of sharp levoglucosan peaks in the time series, indicating that the local wood smoke emission has a stronger impact on the biomass burning originating PM in Seiffen than the regional emissions or long range transport.

References

DeCarlo, P. F., J. R. Kimmel, A. Trimborn, M. J. Northway, J. T. Jayne, A. C. Aiken, M. Gonin, K. Fuhrer, T. Horvath, K. S. Docherty, D. R. Worsnop, and J. L. Jimenez (2006), Field-deployable, hight-resolution, time-of-flight aerosol mass spectrometer, *Anal. Chem.*, *78*, 8281-8289.

Dzepina, K., J. Arey, L. C. Marr, D. R. Worsnop, D. Salcedo, Q. Zhang, T. B. Onasch, L. T. Molina, M. J. Molina, and J. L. Jimenez (2007), Detection of particle-phase polycyclic aromatic hydrocarbons in Mexico City using an aerosol mass spectrometer, *Int. J. Mass. Spectrom.*, *263* (2-3), 152-170.

Schneider, J., S. Weimer, F. Drewnick, S. Borrmann, G. Helas, P. Gwaze, O. Schmid, M. O. Andreae, and U. Kirchner (2006), Mass spectrometric analysis and aerodynamic properties of various types of combustion-related aerosol particles, *Int. J. Mass. Spectrom.*, *258* (1-3), 37-49.

Takegawa, N., T. Miyakawa, M. Kuwata, Y. Kondo, Y. Zhao, S. Han, K. Kita, Y. Miyazaki, Z. Deng, R. Xiao, M. Hu, D. van Pinxteren, H. Herrmann, A. Hofzumahaus, F. Holland, A. Wahner, R. Blake, N. Sugimoto, and T. Zhu (2009), Variability of submicron aerosol observed at a rural site in Beijing in the summer of 2006, *J. Geophys. Res. - Atmos.*, *114*.

Ulbrich, I. M., M. R. Canagaratna, Q. Zhang, D. R. Worsnop, and J. L. Jimenez (2009), Interpretation of organic components from Positive Matrix Factorization of aerosol mass spectrometric data, *Atmos. Chem. Phys.*, *9*, 2891-2918.

Funding
- Sächsisches Lamdesamt für Umwelt und Geologie, Dresden, Germany, grand number 13-0345.42/275.

Volcanic aerosol layers observed with multi-wavelength Raman lidar over Europe since summer 2008

Ina Mattis, Patric Seifert, Detlef Müller, Matthias Tesche, Anja Hiebsch, Thomas Kanitz, Jörg Schmidt, Fanny Finger

Im Rahmen klimatologischer Lidarmessungen wurden über Leipzig seit Sommer 2008 Aerosolschichten in der oberen Troposphäre und unteren Stratosphäre beobachtet. Transportsimulationen zeigen, dass diese Schichten auf verschiedene Vulkanausbrüche auf den Aleuten und Kurilen sowie in Alaska und Kamtschatka zurückzuführen sind. Die Aerosolschichten reichten bis 30 km Höhe, wobei jedoch das Maximum der Partikelkonzentration im Tropopausenbereich zu finden war. Die optische Dicke der Schicht variierte zwischen 0.004 und 0.025 bei 532 nm.

Introduction

Regular multi-wavelength Raman lidar observations of the vertical aerosol distribution have been performed at the Leibniz Institute for Tropospheric Research (IfT), Leipzig, Germany since 1996. These measurements did not show any major event of volcanic aerosol pollution in the upper troposphere - lower stratosphere (UTLS) region [*Mattis et al.* 2008]. The situation changed due to a series of strong eruptions of volcanoes in the Aleutian Islands, Kamchatka, Alaska, and in the Kuril Islands since summer 2008. Table 1 lists the corresponding volcanoes, their location, and the estimated maximum height of the emitted gas or ash plumes. All volcanoes are located between 40 °N and 70 °N. The eruption dates can be seen from Fig. 1.

Previous major volcanic eruptions (e.g., El Chichon and Pinatubo) showed that the transport of volcanic aerosols from the stratospheric reservoir into the upper troposphere occurs quite slowly. Such aerosols can act as cloud condensation nuclei and may influence cloud properties in the upper troposphere over years.

After the eruption of Pinatubo it was possible for the first time to measure optical properties of volcanic aerosol in the stratosphere with the Raman method [*Ansmann et al.*, 1997]. The Raman method allows for an independent determination of extinction and backscatter coefficients. The particle extinction-to-backscatter (lidar) ratio contains information on particle size and particle light-absorption and thus allows for a rough estimation of

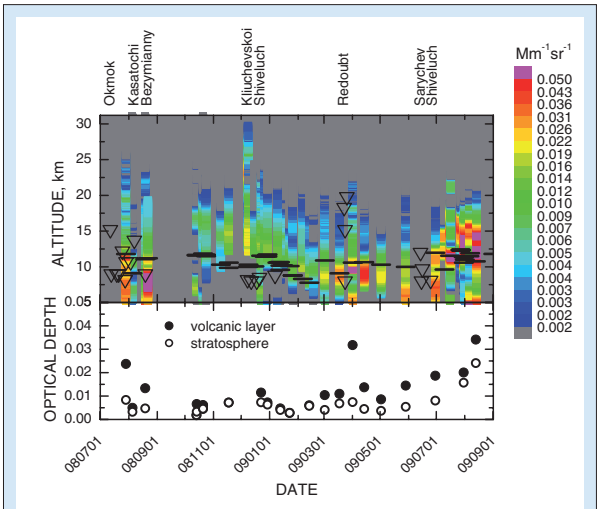

Fig. 1: *Time series of aerosol layers in the ULTS region in terms of backscatter coefficient at 1064 nm. Black horizontal bars indicate the tropopause in the individual observations. Triangles show the plume top heights of the different volcanic eruptions listed in Tab. 1. The particle optical depth at 532 nm (bottom) is computed for the entire volcanic aerosol layer (solid circles) and for the stratosphere (above the tropopause) only. The date is given in the format YYMMDD.*

Volcano	Latitude	Longitude	Height	Location
Okmok	53.43°N	168.13°W	1073 m	Aleutians
Kasatochi	52.17°N	175.51°W	314 m	Aleutians
Bezymianny	55.98°N	160.59°E	2882 m	Kamchatka
Kliuchevskoi	56.06°N	160.64°E	4835 m	Kamchatka
Shiveluch	56.65°N	161.36°E	3283 m	Kamchatka
Redoubt	60.49°N	152.74°W	3108 m	Alaska
Sarychev	48.09°N	153.20°E	1496 m	Kuriles

Tab. 1: *Volcanic eruptions in the northern hemisphere since July 2008 until the beginning of October 2009. The information is obtained from www.avo.alaska.edu and from www.volcanodiscovery.com.*

microphysical parameters of stratospheric aerosols [*Wandinger et al.,* 1995].

The volcanic layers of 2008 and 2009 can be studied in much more detail by the continental-scale network of multi-wavelength Raman lidars of the European Aerosol Research LIdar NETwork (EARLINET). The wavelength dependence of the backscatter and extinction coefficients and of the lidar ratios allow for a more detailed differentiation of aerosol types and for the direct retrieval of microphysical aerosol parameters like effective radius and single-scattering albedo. There was a major effort during the past years to extract characteristic optical properties for different aerosol types from multi-wavelength Raman lidar measurements [*Müller et al.*, 2007]. This kind of aerosol model is used, e.g., for the analysis of data from simple backscatter lidars like the CALIPSO lidar CALIOP. Unfortunately those aerosol models as well as the CALIPSO retrieval algorithm do not yet contain stratospheric aerosols. Studies on the 2008/2009 volcanic layers can fill this gap.

Instrumentation

From measurements with the IfT multi-wavelength Raman lidar we obtain vertical profiles of backscatter coefficients at 355, 532, and 1064 nm, extinction profiles at 355 and 532 nm as well as depolarization ratio profiles at 532 nm [*Mattis et al.*, 2002]. For aerosol observations in the free-troposphere the relative errors of the particle backscatter and extinction coefficients and the lidar ratio are of the order of 5 % – 20 %, 15 % – 40 %, and 20 % – 60 %, respectively. In some cases the Raman signals in the stratosphere are too noisy and do not allow for an calculation of backscatter and extinction coefficients with the Raman method. For the documentation of the temporal development of the stratospheric plume we calculated particle backscatter coefficients at 1064 nm.

The origin of the aerosol layers in the UTLS region was determined with FLEXPART simulations. FLEXPART is a Lagrangian particle dispersion model [*Stohl et al.*, 1999]. It treats long-range transport, dry and wet deposition, turbulent diffusion, and convection. The transport simulations are driven by meteorological analysis data from the Global Forecast Model (GFS) which have a horizontal resolution of 1°x1°. We used archived GFS data with a temporal resolution of 6 hours [http://dss.ucar.edu/datasets/ds083.2].

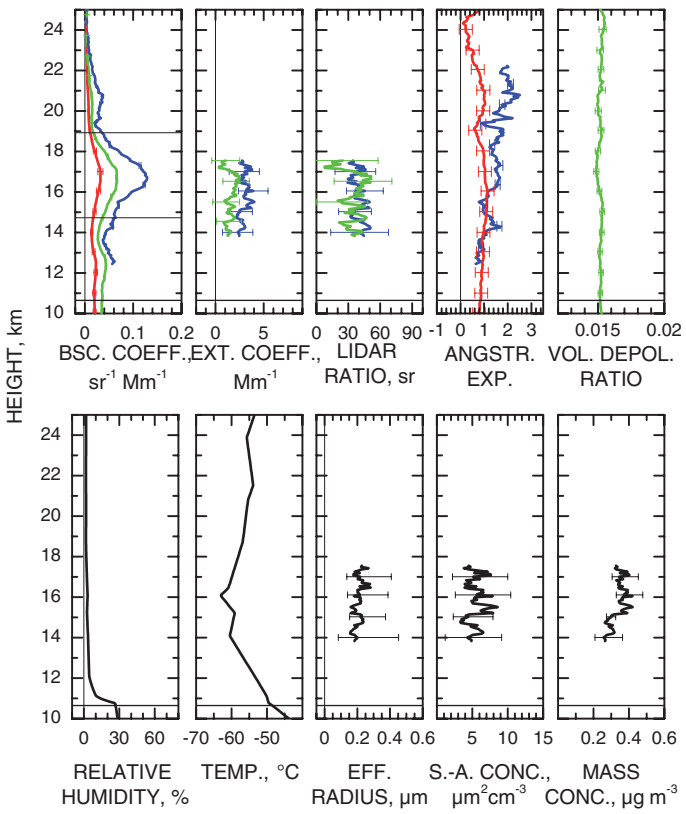

Fig. 2: *5–hour mean values of optical and microphysical properties derived from the Raman lidar measurements at Leipzig on August 31, 2009, 2058–0201 UTC. The tropopause is indicated by a thick horizontal line, bottom and top of the volcanic layer by thin, grey horizontal lines (in the backscatter plot). The vertical resolution of the backscatter profiles is 1260 m. The extinction coefficients and the microphysical properties have been obtained with a vertical resolution of 4 km. Error bars show the uncertainties introduced by signal noise and due to the uncertainty of the teperature profile.*

Observations

Time series. Figure 1 shows the temporal development of the aerosol load in the UTLS region from July 2008 to September 2009 in terms of backscatter coefficients at 1064 nm. The 532 nm particle optical depth, given at the bottom of Fig. 1, is computed from those profiles integrated from the bottom to the top of the identified UTLS aerosol layers by assuming a lidar ratio of 38 sr and an Ångström exponent of 1.05.

The plume height of each volcanic eruption is indicated by a triangle. The given tropopause heights (thick horizontal black bars) indicate that many strong aerosol layers occurred in the upper troposphere. The particle optical depth typically ranges from 0.004 – 0.025, and is sometimes larger than 0.03. The stratospheric aerosol optical depth is small with values from 0.001 – 0.01, and thus a factor of 10 – 20 smaller than the one observed during the first two years after the Pinatubo eruption [*Ansmann et al.*, 1997].

First traces of aerosols in the tropopause region were observed on July 28, 2008. Transport simulations indicate that these layers probably originated from the Okmok eruption. A very strong aerosol layer in the upper troposphere was detected on August 21, 2008. This layer probably came from the Kasatochi eruption.

The largest vertical extend of about 30 km could be observed on December 8, 2008. In November and December 2008 the upper troposphere was almost clean, but the aerosol content above the tropopause remained almost constant. Another strong increase of the aerosol load in the tropopause region occurred in spring 2009.

After the eruption of the Sarychev volcano in mid June 2009 we observed several very thin, separated aerosol layers in the stratosphere. The thin layers dispersed and layer depth increased up to 4 km by the end of July 2009 (see http://polly.tropos.de/martha).

Case study of a multi-wavelength Raman lidar measurement. On August 31, 2009, we observed a stratospheric volcanic aerosol layer from 15 – 19 km height (see Fig. 2). Peak volume extinction values in the stratospheric volcanic aerosol layer are 1.5 Mm^{-1} (532 nm) and 3 – 4 Mm^{-1} (355 nm), the respective Ångström exponent is 1.2. The backscatter-related Ångström exponents also vary around 1.0 – 1.5 in the center of the volcanic layer. The aerosol optical depth is roughly 0.01 (532 nm) and 0.015 (355 nm). According to the method of *Wandinger et al*. [1995], 355 nm lidar ratios around 10 – 30 sr and 50 – 60 sr indicate particle size distributions with effective radii of 0.3 – 0.5 µm and 0.1 – 0.2 µm, respectively. For the surface area and mass concentrations we found values of 5 – 10 $\mu m^2 cm^{-3}$ and 0.3 – 0.5 µg m^{-3}, respectively. By applying the inversion scheme [*Müller et al.*, 1999] to the full set of available backscatter and extinction coefficients similar results were obtained. The surface-area and mass concentrations are thus about a factor 10 – 20 lower than the respective values observed after the Mt. Pinatubo eruption in the years 1992 and 1993.

References

Ansmann, A., I. Mattis, U. Wandinger, F. Wagner, and J. Reichardt (1997), Evolution of the Pinatubo aerosol: Raman lidar observations of particle optical depth, effective radius, mass and surface area over central Europe at 53.4° N, *J. Atmos. Sci.*, *54* (22), 2630-2641.

Mattis, I., A. Ansmann, D. Müller, U. Wandinger, and D. Althausen (2002), Dual-wavelength Raman lidar observations of the extinction-to-backscatter ratio of Saharan dust, *Geophys. Res. Lett.*, *29*, doi:10.1029/2002GL014721.

Mattis, I., D. Müller, A. Ansmann, U. Wandinger, J. Preißler, P. Seifert, and M. Tesche (2008), Ten years of multiwavelength Raman lidar observations of free-tropospheric aerosol layers over Central Europe: Geometrical properties and annual cycle, *J. Geophys. Res.*, *113* (D20), D20202, doi:20210.21029/22007JD009636.

Müller, D., A. Ansmann, I. Mattis, M. Tesche, U. Wandinger, D. Althausen, and G. Pisani (2007), Aerosol-type-dependent lidar ratios observed with Raman lidar, *J. Geophys. Res.*, *112* (16), D16202, doi:16210.11029/12006JD008292.

Müller, D., U. Wandinger, and A. Ansmann (1999), Microphysical particle parameters from extinction and backscatter lidar data by inversion with regularization: Simulation, *Appl. Optics*, *38* (12), 2358-2368.

Stohl, A., and D. Thomson (1999), A density correction for lagrangian particle dispersion models, *Bound.-Lay. Meteorol.*, *90* (1), 155--167.

Wandinger, U., A. Ansmann, J. Reichardt, and T. Deshler (1995), Determination of stratospheric-aerosol microphysical properties from independent extinction and backscattering measurements with a Raman lidar, *Appl. Optics*, *34*, 8315-8329.

Observations of turbulence-induced new particle formation in the residual layer

Birgit Wehner, Holger Siebert, Albert Ansmann, Florian Ditas, Patric Seifert, Frank Stratmann, Alfred Wiedensohler, Raymond A. Shaw

Im Rahmen der Intensivkampagne IMPACT wurden während einer Fallstudie Aerosolmessungen mit der hubschraubergetragenen Meßplatform ACTOS und einem LIDAR in Cabauw (NL) durchgeführt. Dabei wurden innerhalb der Residualschicht Bereiche mit erhöhten Konzentrationen ultrafeiner Partikel gefunden, die kurz zuvor neu gebildet worden waren. Diese Bereiche zeigen Richardson-Zahlen unterhalb des kritischen Wertes sowie gleichzeitig erhöhte Turbulenz. Turbulente Mischung kann zu lokaler Übersättigung möglicher Vorläufergase führen was wiederum notwendige Voraussetzung für die Partikelneubildung ist. Nach Auflösung der nächtlichen Inversion wurden diese Partikel herunter gemischt und anschließend auch am Boden gemessen.

Introduction

New particle formation has a major influence on the concentration of atmospheric aerosol particles. This has been demonstrated by various ground-based measurements but also a small number of airborne case studies indicate new particle formation at elevated heights. However, the basic processes and locations within the boundary layer are still not well understood. Therefore, airborne measurements of aerosol number concentrations and additional parameters are essentially required. The former campaign SATURN showed increased number concentrations of ultrafine particles after break-up of the nocturnal inversion within the whole mixed layer and near the inversion.

This work presents a combination of in-situ measurements with the helicopter-borne payload ACTOS (Airborne Cloud Turbulence Observation System) and remote sensing observations performed by a ground-based lidar to investigate a case study with increased ultrafine particle concentrations at elevated heights [*Wehner et al.* 2010].

Measurements

Presented data were taken during the field campaign IMPACT, a part of the EU-project EUCAARI, performed at the Cabauw Experimental Site for Atmospheric Research (CESAR) in May 2008. Here, as a case study May 13 was selected.

ACTOS was used to perform temporal and spatial highly-resolved measurements in the PBL up to a height of 2000 m above ground. ACTOS is an autonomous system which is carried by means of a 140 m long rope as external cargo below a helicopter and flown with a true airspeed of about 20 m s^{-1} to ensure safe flights out of the helicopter's downwash [*Siebert et al.,* 2006a]. The payload is equipped with fast sensors for measuring the three-dimensional wind vector, temperature, static pressure, and humidity.

In addition, aerosol number size distributions (NSD; 6 nm – 2.5 µm, SMPS and OPC, time resolution 2 min) and total particle number concentrations (CPC, time resolution 1 s) have been measured [*Wehner et al.,* 2010].

The lidar CAELI (CESARWater Vapour, Aerosol and Cloud Lidar) is a high-performance, multiwavelength Raman lidar, capable of providing measurements of volume backscatter and extinction coefficients of aerosol particles, the depolarisation ratio, and water-vapor-to-dry-air mixing ratio and was operated by (the National Institute for Public Health and the Environment, Bilthoven, NL).

Results

On May 13, 2008, the weather was sunny in the morning leading to an undisturbed boundary layer (BL) development. Polluted air masses were advected from central Europe to the field site. The evolution of the aerosol layers (developing convective BL at ground and residual layer on top) in the morning of May 13 is presented in Fig. 1. This Figure shows the time series of the backscattered lidar signal at 1064 nm below 2000 m between 7:15 and 9:45 UTC including the ACTOS-flight-pattern. The top of the convectively active BL was around 220 m at 7:15 UTC and increased to 500 m two hours later. After 9:35 UTC, the BL was well-mixed so that wave-structured layers as found from 7:40 – 8:10 UTC (around 700 m height) and from 8:40 – 9:00 UTC (800 – 900 m height) are no longer detected. Note that the lidar signal strength increased above 1000 m height (above the local residual layer) caused by the advection of aged anthropogenic haze from the European continent to the east.

Vertical profiles of selected parameters measured by ACTOS complete the picture of vertical stratification. Figure 2 shows the total particle number concentration N and potential temperature Θ measured during the first ascent

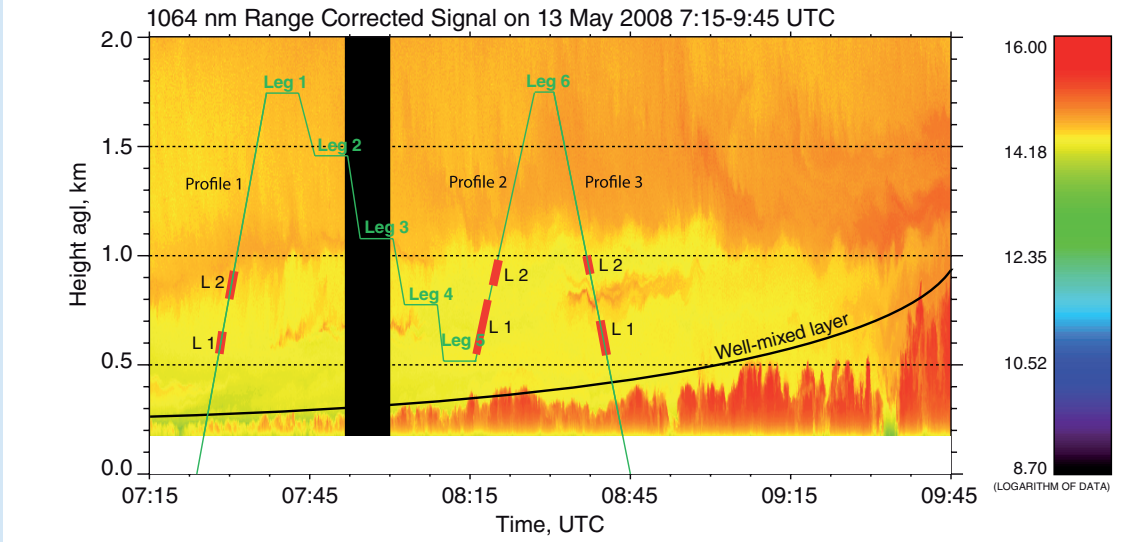

Fig. 1: *Evolution of the boundary layer and lofted aerosol layers on May 13, 2008, from 7:15-9:45 UTC in terms of the range-corrected 1064 nm lidar signal. The vertical resolution is 7.5 m and the temporal resolution 10 s. Lidar signals are not trustworthy below 150 m because of the incomplete transmitter-receiver overlap. The ACTOS-flight pattern is marked by the green line, the profiles and horizontal legs are labeled accordingly. L1 and L2 indicate layers with significantly increased particle number concentrations (see Fig. 2).*

(profile 1) and the last descend (profile 3). A strong temperature inversion is visible up to a height of 300 m during profile 1 with a shallow unstable surface layer above ground. Above the inversion, the temperature gradient was gradually decreasing (but still positive) up to a height of about 500 m followed by an almost neutrally stratified layer.

In the well-mixed layer (the lowermost 200 m), *N* was height-constant with concentrations of $N \approx 6 * 10^3$ cm^{-3}, above the inversion *N* significantly decreased with some variations above. The most obvious features are two layers with local maxima where *N* increased by a factor of 2 – 3 (marked areas L1 and L2 in Fig. 2). About one hour after take-off, the final descent (profile 3) was flown showing a well-mixed layer from the surface up to ≈ 280 m. *N* increased significantly in L1 and L2, while L2 was slightly lifted up in the mean-time.

Horizontal flight legs were flown at 5 different heights between 500 and 1800 m (cf. Fig. 1) including typically 2 – 3 NSDs during each leg. Averaged NSDs are given in *Wehner et al.* [2010]. Significant variations in the nucleation but also in the Aitken mode were found for the different measurement heights. Leg 4 showed a clearly developed nucleation mode with a maximum around 10 nm. The corresponding measurement height level (770 m) was in the region of increased *N* in profile 2 (not shown here), which was flown less than 10 min after leg 4. Legs below and above the layer of increased *N* show much lower concentrations in the nucleation mode. Thus, we can conclude that the high particle number concentrations between 550 and 800 m were caused by particles in the nucleation mode range, i.e. particles which have been formed by nucleation recently and grew up to around 10 nm.

To understand this feature, we analyzed the turbulence structure by means of local energy dissipation ε_τ. Here, ε_τ is derived from so-called second-order structure functions $S^{(2)}$ estimated from short, non-overlapping, subrecords of length $\tau = 2$ s (see *Siebert et al.* [2006b], and references therein). Figure 2 shows the profiles of ε_τ taken during the first ascent (profile 1, left panel) and the last descent (profile 2, middle panel). Both ε_τ profiles show comparably high values in the highly turbulent well-mixed layer where production of turbulent kinetic energy due to convection is already dominant. Above the well-mixed layer, the damping influence of the temperature inversion increases which results in decreasing turbulence. In the last profile this decrease is almost three orders of magnitude. In the two layers (L1 and L2) with increased particle number concentration we observe a different behavior of ε_τ during the two profiles. During profile 1, ε_τ shows a local maximum in both layers L1 and L2 with an increase by a factor of ≈ 2 indicating a more turbulent layer compared to the background. Even though this increase of turbulence is not very strong, the correlation of increased ε_τ and increased *N* in L1 and L2 is remarkable.

For the last descent, the profile of ε_τ in the region of new-particle formation gives a slightly different picture. In particular for the region L1, an increase of ε_τ of nearly two orders of magnitude was measured but the maximum values are shifted more to the upper and lower boundaries of L1. For L2, the picture is quite similar but much less pronounced. The increase of ε_τ above

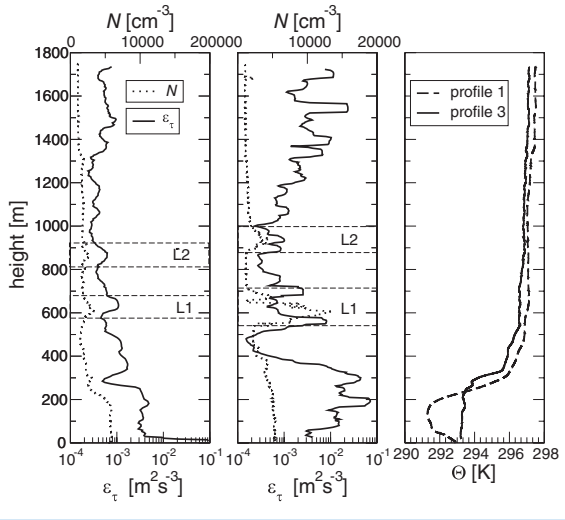

Fig. 2: *Vertical profiles of the local energy dissipation rate ε_τ (black lines) and the particle number concentration N (dashed lines) for profile 1 (left) and profile 3 (middle). The right-hand plot shows the corresponding profiles of the potential temperature Θ.*

and below L1 is obviously due to shear-induced turbulence.

Conclusions

This study presents a unique combination of in-situ measurements with high temporal and spatial resolution at heights up to 1800 m covering meteorological and aerosol parameters, and continuous measurements of a lidar. While the in-situ measurement provides a very detailed snapshot of a certain measurement point in time and space, the lidar follows the development of the vertical structure of the backscatter signal above one location during the measurement period.

The observations show the occurrence of nucleation mode particles (< 20 nm) within distinct layers inside the residual layer. These layers showed only slight differences of mean thermodynamic and dynamic parameters compared to the surrounding regions but were characterized by increased turbulence. Thus, we can conclude that mainly turbulent layers were responsible for creating favorable thermodynamic conditions (e.g., supersaturation of precursor gases due to non-linear mixing). Particle measurements at ground level show a rapid increase of nucleation mode particles just at the time when the well-mixed layer ranges from ground up to 800 m, which corresponds to the height where the enhanced number concentration of ultrafine particles was found. Thus, it is very likely that these particles observed at the ground were formed at higher altitudes and mixed downwards.

The combination of ground-based, remote sensing (lidar) and airborne in-situ measurements with high spatial resolution clearly indicate a step forward to understanding the complex interaction between boundary layer dynamics, turbulence, and new particle formation. However, the nucleation process itself seems still an unsolved issue since precursor gas measurements are still missing in this context.

Acknowledgements

The authors thank all those people from KNMI which were involved in the IMPACT campaign for organization and all kinds of support before, during, and after the intensive campaign and colleagues from the enviscope, rotorflug, and HeliHolland companies.

References

Siebert, H., H. Franke, K. Lehmann, R. Maser, E. W. Saw, D. Schell, R. A. Shaw, M, Wendisch (2006a), Probing Finescale Dynamics and Microphysics of Clouds with Helicopter-Borne Measurements, *Bull. Amer. Meteor. Soc.*, *87* (12), 1727–1738.

Siebert, H., K. Lehmann and M. Wendisch (2006b), Observations of small scale turbulence and energy dissipation rates in the cloudy boundary layer, *J. Atmos. Sci.*, *63*, 1451 - 1466.

Wehner, B., H. Siebert, A. Ansmann, F. Ditas, P. Seifert, F. Stratmann, A. Wiedensohler, A. Apituley, R. A. Shaw, H. E. Manninen, and M. Kulmala (2010), Observations of turbulence-induced new particle formation in the residual layer, *Atm. Chem. Phys. Discuss.*, *10*, 327 - 360.

Funding
- EU

Cooperation
- RIVM - National Institute for Public Health and the Environment, Bilthoven, The Netherlands
- Department of Physics, Michigan Technological University, Houghton, Michigan, USA
- Department of Physics, University of Helsinki, Helsinki, Finland
- Enviscope GmbH, Frankfurt/Main, Germany

Small-scale variability of the water vapor field near cloud base

Holger Siebert, Florian Ditas, Raymond A. Shaw, Frank Stratmann, Birgit Wehner

Für die Enstehung von konvektiver Bewölkung ist das Wasserdampffeld an der Wolkenbasis von zentraler Bedeutung. Kleinste Änderungen in der relativen Feuchte (rH) entscheiden ob aus einem Partikel ein Wolkentropfen entsteht oder ob z.B. gerade gebildete Tropfen wieder verdunsten. Die relative Feuchte ist eine Funktion der aktuellen Temperatur T und des Wasserdampffeldes (z.B. beschrieben durch den Wasserdampfpartialdruck e). Beide Parameter sind turbulente Zustandsgrößen und vor allem auf Grund der Nichtlinearität des Sättigungsdampfdruckes in T ist auch rH ein turbulenter Parameter mit einer erhöhten Wahrscheinlichkeit für das lokale und sporadische Auftreten von Extremwerten.

Das Feuchtefeld im Bereich des Kondensationsniveaus von konvektiver Grenzschichtbewölkung wurde im Rahmen der IMPACT-Kampagne im Mai 2008 mit der Hubschrauberschleppsonde ACTOS untersucht und entsprechende Schlussfolgerungen für mögliche Übersättigungen gezogen. Es wurden lokal auftretende hohe Übersättigungen von bis zu 2 % beobachtet welche einen ebenso hohen Einfluss auf die Aktivierung von Kondensationskernen haben können wie deren chemische oder physikalische Eigenschaften.

Introduction

The water vapor field and its turbulent characteristics near cloud base is essential for the condensation process and the onset of cumulus convection. In general, the supersaturation $s = e / E(T) - 1$ depends on the water vapor field (here described by the partial pressure e of the water vapor) and the saturation pressure $E(T)$, which is a function of temperature T. That is, s depends nonlinearly on T and linearly on e; because both parameters are known to be highly turbulent in the atmosphere we can expect that s is also a highly turbulent parameter, which will exhibit even more extreme fluctuations due to its nonlinear behavior [e.g., *Shaw*, 2000]). On the other hand, s will respond to possible condensation of cloud droplets according to the following differential equation $ds/dt = \omega - s/\tau_p$, where ω describes the change in s due to vertical translation of a cloud parcel. Therefore, ω is a function of the vertical velocity and other thermodynamic state parameters, and τ_p is the phase relaxation time depending on the droplet size and droplet number concentration (see textbook of *Rogers and Yau* [1989] for more details). In principle, τ_p describes the typical time scale at which the supersaturation field adjusts in a field of droplets growing by condensation. At cloud base with relatively low droplet number concentration and small droplets, τ_p can be easily in the order of a few to tens of seconds whereas in higher cloud levels τ_p is closer to the order of one second. In other words, at cloud base we can expect more intense fluctuations of s compared to relatively low and uniform supersaturation inside a cloud. This may have significant consequences for the activation process.

However, a problem still unsolved in cloud physics is the fast and precise measurement of humidity or supersaturation in the presence of cloud droplets. Even though this quantity plays a key role in the development of a cloud, it is only modeled rather than measured [e.g., *Gerber*, 2004].

This paper describes first airborne in-situ observations with high temporal and spatial resolution of temperature, humidity, and cloud droplets, just a few minutes after the onset of cumulus convection. Measurements were made during the IMPACT field campaign in May 2008 around Cabauw, The Netherlands.

Observations

The data presented in this paper were taken with the helicopter-borne payload ACTOS (Airborne Cloud Turbulence Observation System, *Siebert et al.*, [2006]) on May 20th, 2008 around the Cabauw tower in The Netherlands. During take-off at 09:15 local time, cloud-free conditions were observed. A first vertical profile with ACTOS indicated a well-mixed layer up to 750 m (see Fig. 1) with slightly stable conditions above. While taking this profile, the well-mixed layer evolved and a field of small cumulus clouds popped up at a height of about 1100 to 1200 m (see photo from the on-board camera in Fig. 2). Therefore, horizontal legs were flown at the condensation level immediately after finishing the first profile.

Figure 3 presents a 15-s-long example of this flight leg corresponding to a flight path of approximately 300 m (true airspeed of ACTOS was 20 m/s). The top panel shows the actual temperature T as measured with a fast-response fine wire sensor (UltraFast Thermometer, UFT) which is protected against droplet impaction

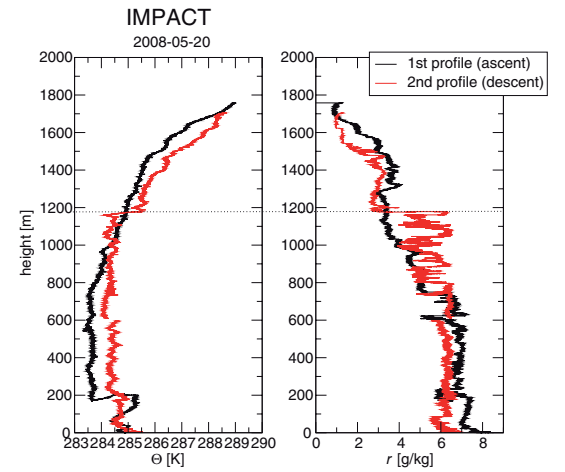

Fig. 1: *Vertical profiles of the potential temperature Θ (left panel) and the water vapor mixing ratio r (right panel). The first profile was taken directly after take-off and the second one is the final descent at the end of the flight. Within the first 200 m of the first profile, the climb rate was not monotonic due to air traffic issues; the wide span in Θ reflects the horizontal variability of the temperature field. The horizontal dotted line denotes the level of cloud formation.*

Fig. 2: *Photo of the field of freshly developed cumulus clouds taken by the on-board ACTOS camera.*

(see *Siebert et al.* [2006] for more details on the experimental setup). This sensor was carefully calibrated with a highly accurate but slow platinum resistance wire thermometer (PT-100) for which a first-order response was assumed with a time constant of 3 s. The range (peak-to-peak) of observed temperature was about +- 0.2 deg Celsius.

The next panel shows the absolute humidity *a*, which was measured with an open-path infrared absorption hygrometer (LiCor-7500). Since this device is based on differential absorption measurements, the influence of scattering and absorbing due to cloud droplets should be minimal - however, possible artifacts have to be analyzed in more detail. Next, from the temperature and the absolute humidity readings, the relative humidity is derived. Here, the longitudinal displacement of the two sensors of about one meter and a general delay of the analog output of the LiCor device was taken into account by shifting the time series. This shifting reduced extreme values at cloud edges where gradients of *T* and *e* were most pronounced. Lateral displacement is below 10 cm which is close to the spatial resolution of the measurements and a possible minor influence is therefore neglected. The absolute accuracy of derived *rH* is estimated to be on the order of a few percent due to an offset and calibration uncertainties although the amplitudes of the fluctuations are assumed to be more accurate. In order to get a qualitative feeling for the sensitivity of *rH* to the temperature measurements, *rH* was also calculated based on a low-pass filtered *T* (see dashed line in upper panel and resulting *rH* as dotted line). Note that smoothing *T* does not significantly reduce the small-scale variability of *rH*, which is in our case mainly caused by fluctuations in the water vapor field.

Therefore, even though the absolute accuracy is low, observed fluctuations in short periods with peak-to-peak values of +- 2 % are real. Furthermore, similar fluctuations of *rH* which were found inside the clouds were also observed in regions without the presence of cloud droplets but with similar thermodynamic conditions. These observations make us confident that the high fluctuations of *rH* inside the clouds are qualitatively correct.

The lowest panel shows the droplet diameters measured with the Phase-Doppler Interferometer PICT. In this analysis, the droplets are used only as a cloud indicator but it is noticeable that such young clouds already exhibits a few droplets with diameters well above 10 μm whereas the mean diameter is about 7 μm.

Discussion & Summary

A first attempt was made to measure the small-scale variability of the supersaturation field at condensation level during the development of small fair weather cumuli. Although measuring fluctuations of the (super)saturation with high absolute accuracy is still a challenge, we are confident that at cloud base fluctuations in *rH* of +- 2 % are real. The amplitude of these fluctuations are quite similar to in the well-mixed boundary layer without the presence of cloud droplets. We argue that these amplitudes can still occur at cloud base due to the large phase relaxation time order of a few seconds, the supersaturation field needs to adjust to the new conditions.

As a next step, we estimate the time scale of the humidity fluctuations and compare with the estimated phase relaxation time $\tau_p = (2\pi D d n)^{-1}$ where *D* is the water vapor diffusivity

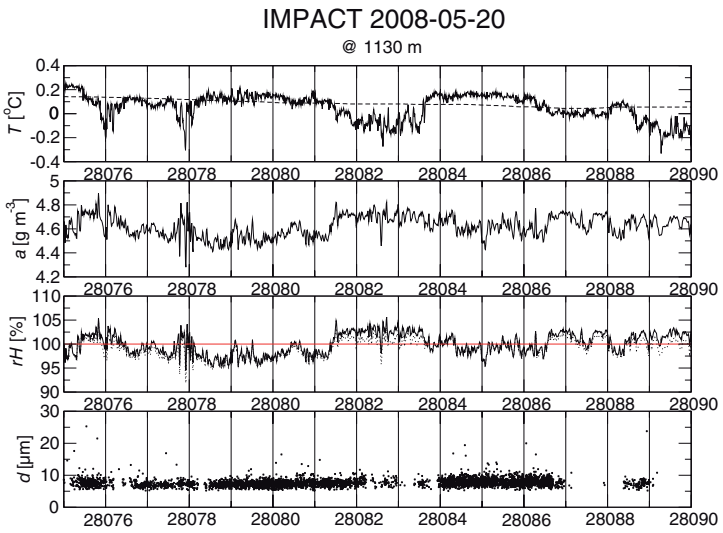

Fig. 3: *Time series of temperature T, absolute humidity a, relative humidity rH, and droplet diameter d. The data were taken at constant height in 1130 m above ground. The dashed line in the temperature plot presents a low-pass filtered temperature, the corresponding rH data are plotted with dots.*

(~ 2.2 * 10^{-5} m^2s^{-1}) and d and n are the mean droplet diameter and number concentration. With d ~ 7 µm and n ~ 100 – 500 cm^{-3} we estimate τ_p in the range of 2 – 10 s. The humidity fluctuations are sampled with a resolution of r ~ 10 cm and with the local energy dissipation rate of ε ~ 10^{-2} to 10^{-3} m^2s^{-3} we estimate the humidity fluctuation time scale $\tau_r = (r^2/\varepsilon)^{1/3}$ ~ 1 – 2 s. That is, turbulent fluctuations are likely faster than the thermodynamic response time for the droplet field and, therefore, humidity fluctuations on that small scales are not damped out due to condensation of water droplets.

Although these measurements give new insight on the small-scale structure of the humidity field at cloud base, many aspects of these observations cannot be sufficiently explained without detailed information about the history of the sampled cloud parcels. For example, it is unclear why droplets were observed in regions with comparable low saturation (e.g., the region between t = 28084 – 28087 s) but several cloud holes occur in the period between t = 28082 – 28082 s with comparable high rH. An analysis of the vertical wind velocity which is not shown here gave no convincing explanation.

The sporadically occurring high supersaturations likely have significant consequences for the activation process. These natural fluctuations might compare in importance with chemical and physical properties of cloud condensation nuclei and have to be investigated in more detail and with improved instrumentation.

Acknowledgments

We would like to acknowledge colleagues from the enviscope, rotorflug, and HeliHolland companies for their essential support during the ACTOS campaign and for preparation of the experimental setup. Furthermore, we acknowledge KNMI who hosted the IMPACT campaign.

References

Rogers, R. R. and M. R. Yau (1989): A short course in cloud physics. 3rd edition, Pergamon Press, 293 p.

Shaw, R. A. (2000): Supersaturation intermittency in turbulent clouds. *J. Atmos. Sci.*, 57, 3452-3456.

Siebert, H., et al. (2006): Probing fine-scale dynamics and microphysics of clouds with helicopter-borne measurements, *Bull. of Amer. Met. Soc.*, 87, 1727 – 1738.

Funding
- EU-Project EUCAARI

Cooperation
- Department of Physics, Michigan Technological University, Houghton, Michigan, USA
- enviscope GmbH, Frankfurt/Main, Germany
- rotorflug GmbH, Friedrichsdorf, Germany

The effect of measured surface albedo on modeled Saharan dust solar radiative forcing

Ina Tegen[1], Eike Bierwirth[2], Bernd Heinold[1], Manfred Wendisch[2]

[1]Leibniz Institute for Tropospheric Research (IfT), Leipzig, Germany
[2]Leipzig Institute for Meteorology (LIM), University of Leipzig, Germany

Der Strahlungsantrieb von Saharastaub wurde für eine Fallstudie im Rahmen des ersten SAharan Mineral dUst experiMent (SAMUM1) im Mai 2006 berechnet. Dazu wurden Staubkonzentrationen in mehreren Größenklassen mit einem regionalen Transportmodellsystem simuliert, und zusammen mit spektral aufgelösten Bodenalbedomessungen als Eingabeparameter für ein Strahlungstransfermodell genutzt. Die Bodenalbedo kann lokal einen größeren Einfluss auf den Strahlungsantrieb durch Staub am Oberrand der Atmosphäre ausüben als Variationen in den optischen Eigenschaften der Staubpartikel innerhalb ihres Unsicherheitsbereichs. Im regionalen Mittel über der Sahara führen die unterschiedlichen Annahmen zur Bodenalbedo bzw. der optischen Staubeigenschaften für die gewählte Fallstudie zu Unterschieden im Momentanwert des Strahlungsantriebs in der Größenordnung von 10 Wm^{-2}.

Introduction

The magnitude and even the sign of the solar radiative forcing by mineral dust aerosol at the top of atmosphere (TOA) are highly uncertain. The first SAharan Mineral dUst experiMent (SAMUM1) aimed at constraining Saharan dust optical properties in order to clarify the role of dust in the direct radiative forcing of the climate system (http://samum.tropos.de/). As part of SAMUM1, dust optical properties were derived from in-situ observations or laboratory measurements of collected dust samples (e.g., *Müller et al.,* [2009]). *Bierwirth et al.* [2009] made use of measurements of spectral irradiances at solar wavelengths to determine dust radiative forcing under realistic conditions along the tracks of SAMUM1 flights. *Heinold et al.* [2009] simulated dust distributions during SAMUM1 using a regional model system. Using the model results, we compute the solar part of the Saharan dust radiative forcing for May 19, 2006, when numerous different observations from the SAMUM1 field campaign are available.

Models and Measurements

Spatial and temporal dust distributions during the SAMUM1 period were computed with the mesoscale model system COSMO-MUSCAT [*Heinold et al*., 2009], consisting of the COSMO model of the Deutscher Wetterdienst as meteorological driver, and the online-coupled 3D chemistry transport model MUltiScale Chemistry Aerosol Transport Model (MUSCAT) developed at the IfT. The model computes dust emissions in the Sahara region for five size bins, at a horizontal grid resolution of 28 km.

The radiative properties of the Saharan dust are prescribed in the model. An internal mixing of the major components kaolinite (98 %) with hematite (2 %) is assumed, applying complex refractive indices by *Sokolik and Toon* [1999] ('more absorbing' dust). Alternatively, a 'less absorbing' dust with optical properties of Saharan dust is derived from sunphotometer measurements [*Dubovik et al.,* 2002]. Fields of modeled size-resolved dust distribution for May 19, 2006 12:00 UTC were used as input for the 1D radiative transfer model libRadtran [*Mayer and Kylling*, 2005] to compute dust radiative forcing within the solar wavelength range.

Surface albedo measurements used as input for libRadtran were performed as part of SAMUM1 by the Spectral Modular Airborne Radiation Measurement System (SMART)-Albedometer [*Bierwirth et al.,* 2009]. Large-scale surface albedo information is available from the MODIS satellite instrument [*Moody et al.,* 2005].

Results

Figure 1a shows the modeled dust optical thickness distribution at 550 nm on May 19, 2006, 12:00 UTC. An arc-shaped plume of dust transported toward the Moroccan coast can be identified in the northwestern part of the Sahara reaching values up to 1.

For an area between 14.5°W and 19.5°E, 15.5°N and 34.5°N the modeled profiles of dust extinction, optical properties and meteorological parameters on May 19, 2006 were re-gridded to 1° × 1° horizontal resolution. Optical properties of the dust aerosol particles were calculated from the mixtures of the individual size distributions in each layer. Each of the resulting profiles was then used as input for libRadtran to obtain a spatial distribution of dust forcing, using either the MODIS surface albedo product as input, or the generally lower surface albedo of the COSMO model.

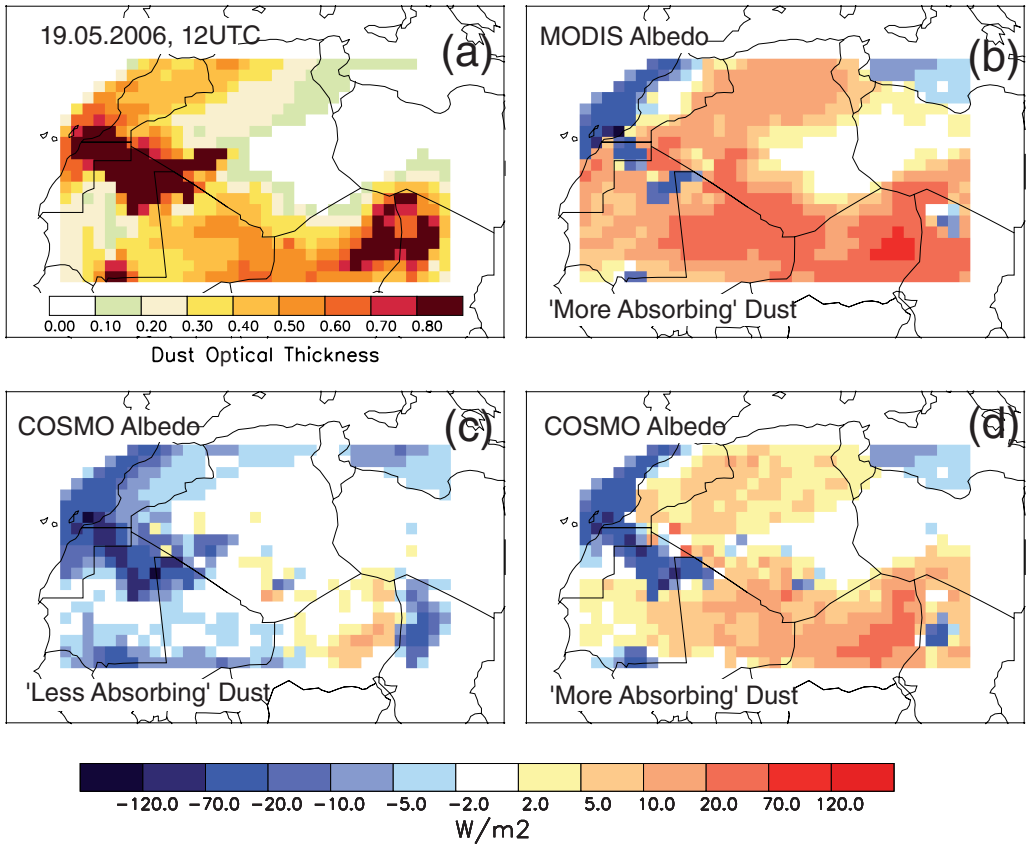

Fig. 1: *(a): Dust optical thickness (550 nm) at May 19, 2006 12:00 UTC computed with COSMO-MUSCAT [Heinold et al., 2009], regridded to 1° x 1° resolution (b)-(d): TOA forcing of modeled dust distribution computed by libRadtran. (b): MODIS surface albedo, (c) and (d): COSMO surface albedo. (c): 'less absorbing' dust, (b) and (d) 'more absorbing' dust (see text for explanation).*

The sign of the top-of-atmosphere (TOA) radiative forcing computed for the SAMUM case is influenced by both surface albedo and the optical properties of the dust (Fig. 1b-d). While dust forcing at 12:00 UTC is always positive in the regional average over the Sahara with MODIS surface albedo values, for the case of the 'less absorbing' dust and COSMO surface albedo the TOA forcing is negative at almost every location. The regional average of instantaneous TOA radiative forcing for the configurations range from +11 Wm^{-2} (for the 'more absorbing' dust and MODIS surface albedo) to -7.2 Wm^{-2} for the 'less absorbing' dust and COSMO surface albedo. When using different surface albedo fields as input, differences in instantaneous TOA forcing of up to 50 Wm^{-2} occur in areas where dust optical thickness reaches values of 1.

The modeled and measured dust optical thickness at the location Ouarzazate in Morocco is 0.4. The dependence of the computed dust solar radiative forcing at TOA in the solar wavelength range on solar zenith angle (SZA) is shown in Fig. 2. Results are shown for two surface albedo types, a dark Hamada and a bright salt-lake surface [*Bierwirth et al.*, 2009], and compared to the results obtained for a spectrally constant surface albedo of 0.2. In this case study, the TOA solar dust radiative forcing depends more strongly on variations of the surface albedo than on the optical properties for the chosen parameter range. Positive forcing at the low SZA near noontime is evident for all cases except for the 'less absorbing'

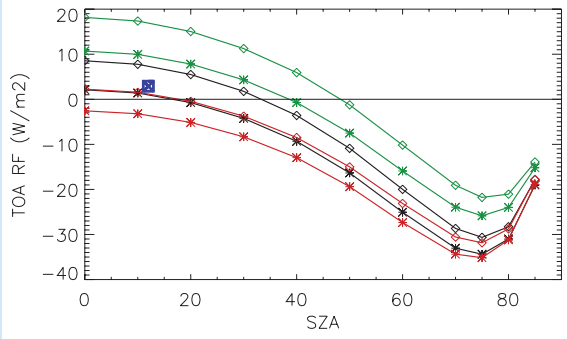

Fig. 2: *Solar dust TOA forcing (wavelength range of 320-2100 nm) in dependence on solar zenith angle (SZA) for different dust optical properties and surface albedo values, at Ouarzazate (30°56' N, 6°54' W), May 19, 2006. The color of the lines and symbols indicates the surface albedo. Red: Hamada, green: Salt-lake (both from Bierwirth et al., [2009]), black: spectrally constant surface albedo value of 0.2. Symbols: diamonds: 'more absorbing' dust, asterisks: 'less absorbing' dust. The square symbol shows the result from Bierwirth et al. [2009].*

aerosol over the darker Hamada surface, while all cases result in negative dust solar forcing at TOA at high solar zenith angles.

In the 24 hour average the results for solar TOA forcing are generally negative, ranging from -1.7 Wm^{-2} to -9.4 Wm^{-2} for the regional average, as the radiative forcing by dust is generally negative for SZA above 40°.

Conclusions

A main goal of SAMUM1 was to reduce uncertainties in dust radiative forcing by appropriate measurements. Absorption by dust particles depends in particular on the imaginary part of the refractive index of the particles. The prescribed optical properties of the 'more' and 'less' absorbing dust used in this model study correspond to imaginary parts of the complex refractive indices obtained from measurements during SAMUM1. The range of the model-prescribed values represents the range of the measurements well, reflecting the remaining uncertainty in radiative forcing by Saharan dust.

Regional variations in TOA dust forcing are strongly dependent on the spectral albedo of the underlying surface. Over the Sahara the use of surface albedo values from remote sensing provides a useful alternative to prescribing surface albedo values from soil data.

Refrences

Bierwirth, E., M. Wendisch, A. Ehrlich, B. Heese, M. Tesche, D. Althausen, A. Schladitz, D. Müller, S. Otto, T. Trautmann, T. Dinter, W. von Hoyningen-Huene, and R. Kahn (2009), Spectral surface albedo over Morocco and its impact on radiative forcing of Saharan dust, *Tellus B*, *61* (1 (Special issue on SAMUM-1)), 252-269.

Dubovik, O., B. Holben, T. F. Eck, A. Smirnov, Y. J. Kaufman, M. D. King, D. Tanré, and I. Slutsker (2002), Variability of Absorption and Optical Properties of Key Aerosol Types Observed in Worldwide Locations, *J. Atmos. Sci.*, *59*, 590-608.

Heinold, B., I. Tegen, M. Esselborn, K. Kandler, P. Knippertz, D. Müller, A. Schladitz, M. Tesche, B. Weinzierl, A. Ansmann, D. Althausen, B. Laurent, A. Massling, T. Müller, A. Petzold, K. Schepanski, and A. Wiedensohler (2009), Regional Saharan dust modelling during the SAMUM 2006 campaign, *Tellus B*, *61* (1 (Special issue on SAMUM-1)), 307-324.

Mayer, B., and A. Kylling (2005), Technical note: the libRadtran software package for radiative transfer calculations—description and examples of use, *Atmos. Chem. Phys.*, *5*, 1855-1877.

Moody, E. G., M. D. King, C. B. Schaaf, and S. Platnick (2008), MODIS-derived spatially complete surface albedo products: Spatial and temporal pixel distribution and zonal averages, *J. Appl. Met. Climatol.*, *47*, 2879-2894.

Müller, T., A. Schladitz, A. Massling, N. Kaaden, A. Wiedensohler, and K. Kandler (2009), Spectral absorption coefficients and imaginary parts of refractive indices of Saharan dust during SAMUM-1, *Tellus B*, *61* (1 (Special issue on SAMUM-1)), 79-95.

Sokolik, I. N., and O. B. Toon (1999), Incorporation of mineralogical composition into models of the radiative properties of mineral aerosol from UV to IR wavelengths, *J. Geophys. Res.*, *104*, 9423-9444.

Funding
- German Research Foundation (DFG), Bonn, Germany

Cooperation
- SAMUM consortium (http://www.tropos.de/samum/)
- Deutscher Wetterdienst, Offenbach, Germany

Meteorological processes forcing Saharan dust emission inferred from Meteosat observations

Kerstin Schepanski, Andreas Macke, Ina Tegen

Staubindexbilder abgeleitet von Messungen des Meteosat Second Generation (MSG) Satelliten im infraroten Spektralbereich wurden zur Identifizierung von Staubquellen in der Sahara genutzt. Beobachtete Staubaktivierungen wurden in Karten der Sahel und Sahara mit stündlicher (bis 12/2007 dreistündlicher) Zeitauflösung zusammengefasst. In der Sahara werden mehr als 60 % aller Staubereignisse zwischen 6:00 und 9:00 UTC initiiert. Dies deutet auf eine wichtige Rolle des Abbaus des nächtlichen Grenzschichtstrahlstroms durch einsetzende Turbulenz für die Staubmobilisierung hin. Die Ergebnisse wurden durch Modellstudien und Analysen meteorologischer Stationsdaten ergänzt.

Introduction

An adequate description of source areas and meteorological processes controlling dust emission is a prerequisite for accurate estimation of dust aerosol effects and understanding of the response of dust emission to changing climate conditions. Atmospheric processes forcing dust mobilization must generate wind speeds exceeding the local threshold velocity. Important meteorological situations that are able to provide atmospheric conditions suitable for dust mobilization include frontal passages, convective activity and the turbulent mixing of momentum from nocturnal low-level jets (LLJ), which are characterized by a horizontal wind speed maximum in the lowest few kilometers of the atmosphere. Such LLJs are most commonly observed at nighttime and may extend over hundreds of kilometers. Here, we use estimates of Saharan dust source activation (DSA) derived with high temporal and spatial resolution using measurements by infrared (IR) wavelength channels of the Meteosat Second Generation (MSG) Spinning Enhanced Visible and InfraRed Imager (SEVIRI) instrument. The data provide identification of areas that are of major importance for dust mobilization, together with the time-of-day when mobilization is initiated [*Schepanski et al.*, 2009].

Dust Source Activation from MSG-SEVIRI

For dust source area identification we use the SEVIRI instrument on-board the geostationary MSG satellite [*Schmetz et al.*, 2002]. The instrument provides narrow-band visible and IR measurements at a sampling interval of 15 minutes with a spatial resolution of up to 3 km × 3 km. A MSG dust index is calculated from differences in brightness temperatures, which are converted from measurements by SEVIRI IR channels. Individual dust plumes were identified in the MSG retrievals and tracked back to their initial location. The DSA frequencies were then binned in a gridded map at 1-hour intervals at 1° × 1° spatial resolution [*Schepanski et al.*, 2007]. It is the first available satellite-based dataset to provide information on the diurnal cycle of dust emission.

Most active dust source areas according to this dataset are located in the foothills of the Saharan mountains, and dust emissions are most frequently initiated at morning hours. Figure 1 shows the fraction of DSAs per day during 3:00-9:00 UTC representing the morning hours over the entire Saharan domain, and 12:00-0:00 UTC. More than 60 % of DSAs occur during local morning hours in the Sahara, consistent with the pronounced diurnal cycle of LLJs and near surface winds. In northern hemisphere summer, the observed frequency of morning DSA increases over the Western Sahara compared to the winter season. The fraction of DSA observed during 12:00-0:00 UTC is low compared to fractions observed during 3:00-9:00 UTC indicating the smaller role of convective events (occurring preferentially at local afternoon and evening hours) in terms of the number of dust mobilization events in most areas of the Sahara.

LLJ Occurrence and Dust Mobilization: Regional Modeling

The role of LLJs in forcing DSA is demonstrated by the regional dust emission and transport model system COSMO-MUSCAT [*Heinold et al.*, 2007]. The model system consists of the meteorological model COSMO by the Deutscher Wetterdienst, and the MUlti-Scale Chemical Aerosol Transport Model (MUSCAT). Local wind systems, clouds, precipitation, and mesoscale convection are simulated depending on topography.

Vertical distribution of horizontal wind speed, potential temperature, gradient Richardson number and surface dust emission flux resulting from COSMO-MUSCAT simulations are shown at the location of Agadez for March 19, 2006 (Fig. 2). The gradient Richardson number is used as indicator for turbulent processes. During night, the lower troposphere is stably stratified, and surface

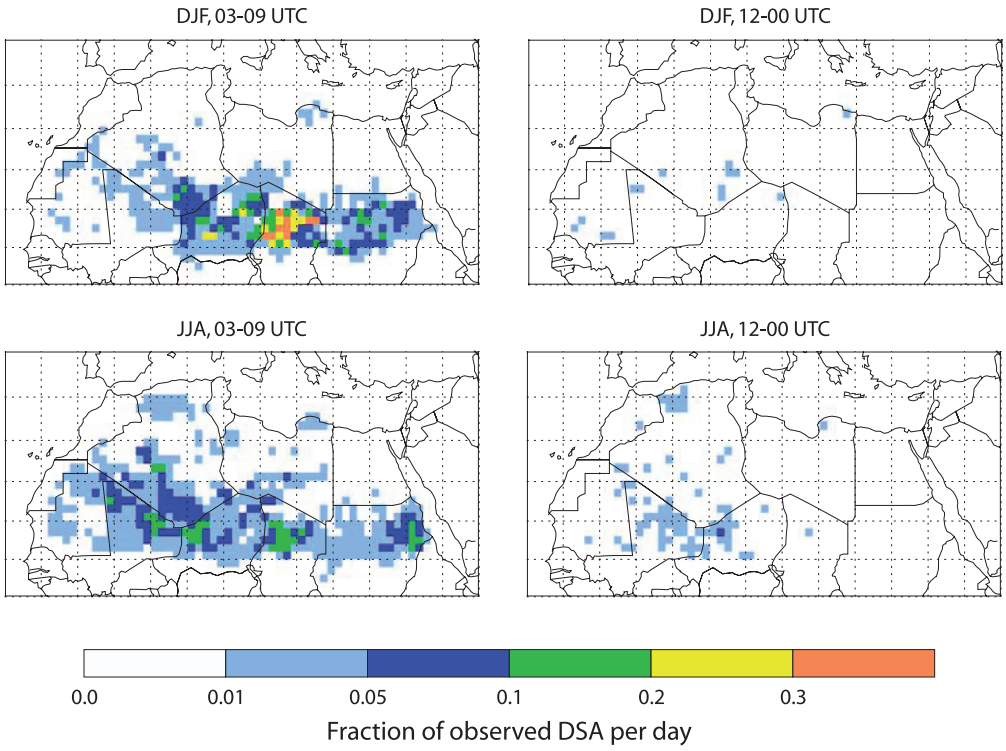

Fig. 1: *Fraction of DSA per day for summer and winter seasons observed during 3:00-9:00 UTC (comprising local morning hours over the entire Saharan domain) (left column) and seasonal fractions of dust source activations per day observed during during 12:00-0:00 UTC (right column) [Schepanski et al., 2009]. Morning time DSAs are mostly related to the break-down of the nocturnal LLJ. Afternoon to night DSAs are mostly related to convective events.*

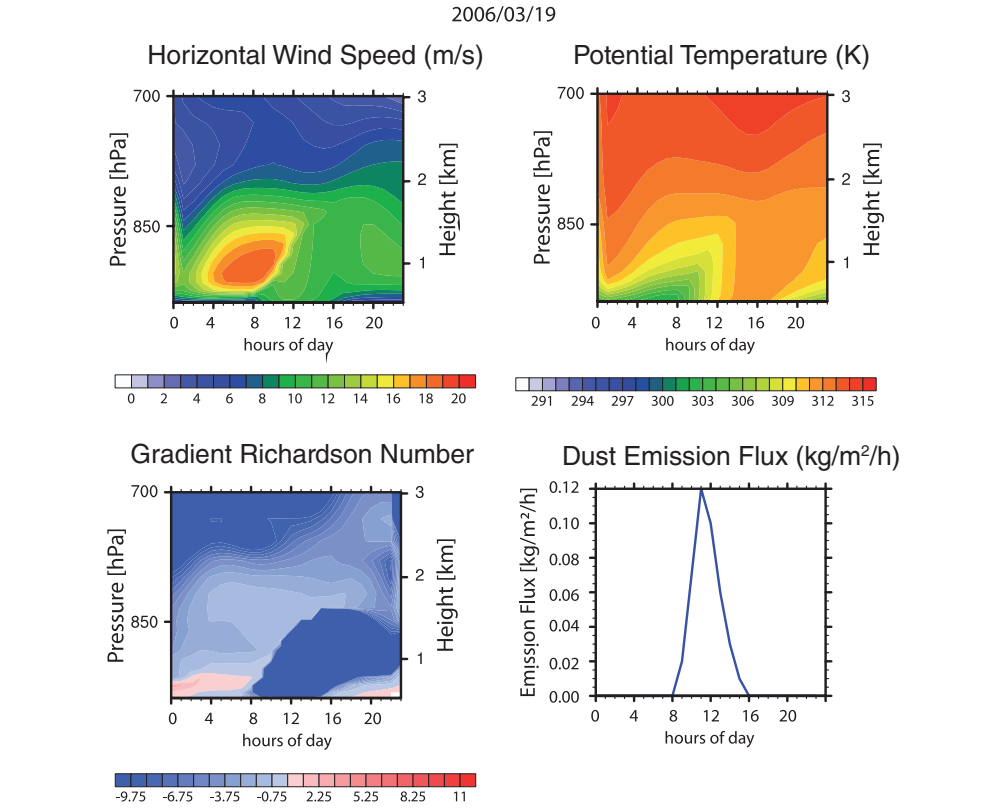

Fig. 2: *Time series of the vertical distribution of horizontal wind speed, potential temperature, Richardson number and dust emission flux at Agadez (16°58'N; 7°59'E) exemplary for the March 19, 2006. The time series are from COSMO-MUSCAT model results [Schepanski et al., 2009].*

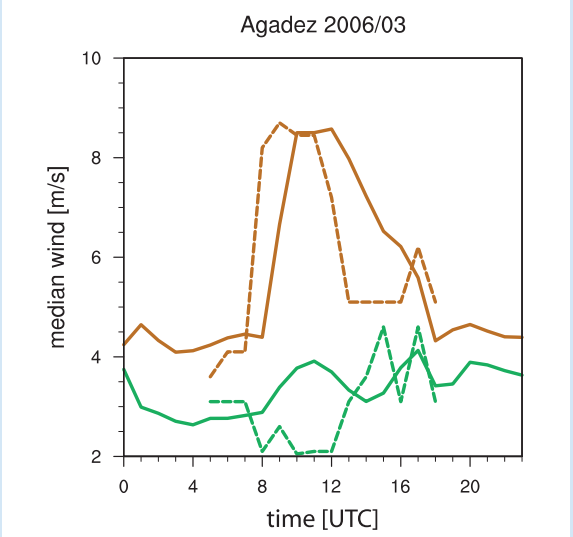

Fig. 3: *Median wind speed for March 2006 at Agadez [Schepanski et al., 2009]. Solid lines show first layer wind simulations by COSMO-MUSCAT, dashed lines synoptic observations of 10-m winds. Based on the occurrence of low-level wind speed maxima, days are separated in LLJ-days (upper pair of curves, brown) and days without LLJ development (lower pair of curves, green).*

wind speeds are too low for dust mobilization. Due to frictional decoupling of air aloft a LLJ develops, indicated by high wind speeds up to 18 ms^{-1} at about 1 km elevation. After sunrise near-surface air masses become unstable and turbulent mixing starts. The layer of unstable conditions grows with increasing surface heating. Momentum from the LLJ is mixed down leading to suddenly increasing surface wind speeds, strong enough to initiate dust emission. On days without LLJ development, both model results and observations indicate low wind speeds (Fig. 3). The distribution as well as the frequency of LLJ occurrence change with season.

Conclusion

DSA is most commonly observed close to the mountain regions of the Sahara. Model experiments confirm that the break-down of the nocturnal LLJ can lead to dust emission. The combination of the mean diurnal cycle at low levels and surface winds with the day-to-day synoptic scale variability explains much of the variability at diurnal timescales. The MSG-based analysis of DSA gives only information on the frequency of initiation of dust source activity. To clarify the role of LLJ for total dust emission fluxes, quantitative dust retrievals over desert surface are needed.

Refrences

Heinold, B., J. Helmert, O. Hellmuth, R. Wolke, A. Ansmann, B. Marticorena, B. Laurent, and I. Tegen (2007), Regional modeling of Saharan dust events using LM-MUSCAT: Model description and case studies, *J. Geophys. Res.*, *112* (D11), D11204, doi:11210.11029/12006JD007443.

Schepanski, K., I. Tegen, B. Laurent, B. Heinold, and A. Macke (2007), A new Saharan dust source activation frequency map derived from MSG-SEVIRI IR-channels, *Geophys. Res. Lett.*, *34* (18), L18803, doi:18810.11029/12007GL030168.

Schepanski, K., I. Tegen, M. C. Todd, B. Heinold, G. Bönisch, B. Laurent, and A. Macke (2009), Meteorological processes forcing Saharan dust emission inferred from MSG-SEVIRI observations of subdaily dust source activation and numerical models, *J. Geophys. Res.*, *114* (D10), D10201, doi:10210.11029/12008JD010325.

Schmetz, J., P. Pili, S. Tjemkes, D. Just, J. Kerkmann, S. Rota, and A. Ratier (2002), An introduction to Meteosat Second Generation (MSG)., *Bull. Amer. Meteor. Soc.*, *83*, 977-992.

Cooperation
- Leibniz Institute of Marine Sciences (IFM GEOMAR), Kiel, Germany

Model initialization and validation with ground- and space-based lidar measurements and sun photometer measurements

Jessica Meier, Ina Mattis, Detlef Müller, Ina Tegen

Mithilfe von Lidarmessungen, die vom Boden und vom Weltraum aus durchgeführt werden können, ist es möglich die vertikale Verteilung von Partikeln in der Atmosphäre zu bestimmen, und so eine Grundlage für die Modellierung des Partikeltransports zu schaffen. Unter Verwendung des regionalen Modells COSMO-MUSCAT wird die vertikale Verteilung des Aerosols und dessen Auswirkung auf atmosphärische Prozesse beschrieben. Vertikalprofile der Rückstreukoeffizienten, wie sie von Lidarmessungen gewonnen werden und Messungen der Aerosol-optischen Dicke dienen dabei sowohl als Eingangsinformationen für das Modell, als auch zur Validierung der vom Modell simulierten Parameter. In dieser Arbeit wurden Profile von Rückstreukoeffizienten dazu verwendet, die vertikale Verteilung der chemischen Zusammensetzung des Aerosols, speziell an den äußeren Rändern des Modellgebietes zu initialisieren.

Introduction

Large uncertainties remain in the determination of direct and indirect radiative forcing of climate by anthropogenic aerosol [*IPCC*, 2007]. Data from remote sensing, measurements of aerosol optical depth (AOD) or measurements of physiochemical aerosol properties at the surface cannot represent the large spatiotemporal variability of aerosol properties. The knowledge of the vertical distribution of atmospheric particles and their properties can help to constrain aerosol properties. The vertical aerosol distribution can be described by lidar profiling, e. g. [*Mattis et al.,* 2008]. The use of a regional model offers the possibility to characterize the aerosol and its vertical distribution on a scale that is appropriate for comparison with measurements for specific case studies.

Method

The mesoscale model system COSMO-MUSCAT (COSMO: Consortium for Small-scale Modeling; MUSCAT: MultiScale Chemistry Model) was used to perform a case study for the characterization of the European aerosol distribution. COSMO is the operational, non-hydrostatic meteorological model developed by the DWD [*Steppeler et al.*, 2003]. It is coupled online with the chemistry transport model MUSCAT [*Wolke et al.*, 2004]. The influence of the distribution pattern of chemical compounds on meteorological parameters and dynamical processes can be determined. Main focus is the validation of the vertical distribution of chemical compounds especially at the lateral model boundaries. The description of these vertical profiles was realized by lidar profiles from ground- (EARLINET: European Aerosol Research Lidar NETwork) and space-based (CALIPSO: Cloud-Aerosol Lidar and Infrared Pathfinder Satellite Observation) measurements and European sun photometer measurements (AERONET: Aerosol Robotic Network). Here, the influence of the vertical distribution at the lateral model domain is presented. The model simulations were performed for the period July 18-26, 2006. This period was characterized by an anticyclone that was situated over Europe for several days and which caused very low transport of atmospheric particles and chemical compounds from outside into the model area. To characterize the aerosol entering the model domain, three different vertical particle profiles were defined at the model boundaries:

Climatological Lidar Profile (Case 1) Based on *Wandinger et al.* [2004] a mean climatological lidar profile was used. The average backscatter profile at 355 nm, measured in Aberystwyth, Wales, was used to describe the vertical distribution of chemical compounds and aerosols. All 4 model boundaries were described by 3 layers: From bottom to 700 m height above ground, with decreasing particle load from 700 m to 2000 m and with the lowest and constant concentration from 2000 m to the model top.

Individual Lidar Profiles (Case 2) Lidar backscatter profiles, measured at EARLINET stations on July 17, 2006 (Thessaloniki (Greece), Belsk (Poland) and Minsk (Belarus)), were used as boundary information. The particle load at all four lateral model boundaries was initialized based on the shape of these backscatter profiles. In contrast to Case 1 the extension of the first aerosol layer was larger (from bottom to 2000 m). Between 2000 and 4000 m the particle load decreases and the lowest concentration occur above 4000 m.

CALIPSO Profiles (Case 3) Daily measurements by CALIPSO provide information on the vertical aerosol distribution at all four lateral model boundaries. The difference to Case 1 and Case 2 is the individual description of vertical distribution at all four sides for every day, instead of using fixed layers.

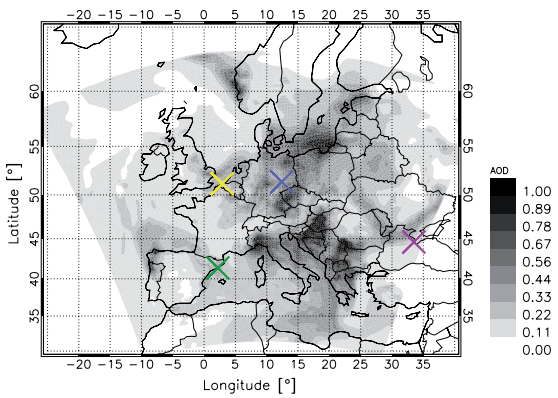

Fig. 1: AOD determined with Case 2 conditions on July 24, 2006, 12 UTC. The yellow and pink symbols show the location of the AERONET stations Oostende and Sevastopol, respectively. The EARLINET stations in Barcelona and Leipzig are illustrated with a green and a blue symbol.

From sun photometer measurements next to the lateral model boundaries, weighting factors were determined for the prescribed vertical profiles. The vertical distribution of the extinction coefficients is determined on the basis of mass extinction efficiencies and hygroscopic growth. The backscatter coefficient was calculated, using an extinction-to-backscatter (lidar) ratio of 50 sr.

Results

The horizontal distribution of AOD that follows from Case 2 conditions is shown in Fig. 1. This simulation result shows areas with very low AOD, especially at the lateral boundaries of the model domain and regions with larger values of AOD in parts of Central Europe and in the South of Europe. High values of AOD are mainly caused by the local emissions in those regions, whereas the lower values show the low transport of particles from outside the model domain. A time series of observed and simulated AOD for two AERONET stations in Europe (Oostende: 2.9°E, 51.2°N; Sevastopol: 33.5°E, 44.6°N) is shown in Fig. 2. The simulation agrees well with the observation. Case 1 mostly results in lower AOD than Case 2 and Case 3, whereas the differences between Case 2 and Case 3 are very small. In case of Sevastopol the difference between the three simulations is apparent for the entire time period with decreasing difference at the end of the period. The station in Oostende shows clear differences between the individual simulations during the first few days, but at the end of the simulation the agreement is high. Only regions close to the lateral boundaries are influenced by the different initial descriptions of the vertical distribution for chemical compounds and the results for the three different cases are similar. The agreement between the different model simulations and the measured vertical backscatter coefficient for two EARLINET stations (Barcelona: 2.2°N, 41.4°E; Leipzig: 12.4°N, 51.4°E) is shown in Fig. 3. The comparison between lidar profile and simulated profiles for the EARLINET station in Barcelona is satisfying. The general shape of the aerosol backscatter is well reproduced at all height levels. On that day a very weak dust event occurred in the region of Barcelona, which was also observed by the lidar measurements. Dust is not implemented in COSMO-MUSCAT and therefore the model underestimates aerosol

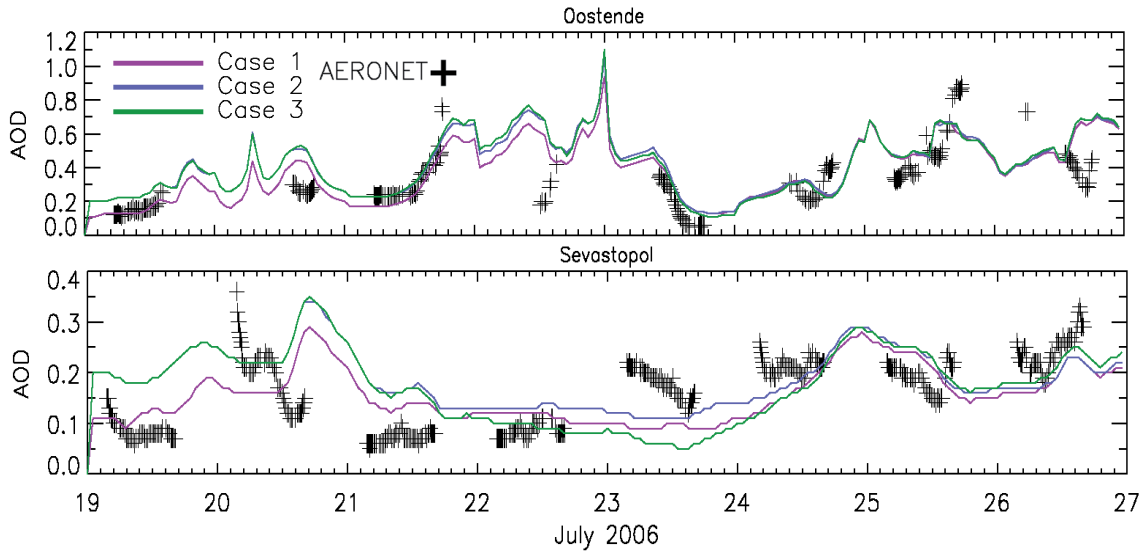

Fig. 2: Time series with simulated and observed AOD at the AERONET stations in Oostende (upper panel) and Sevastopol (lower panel).

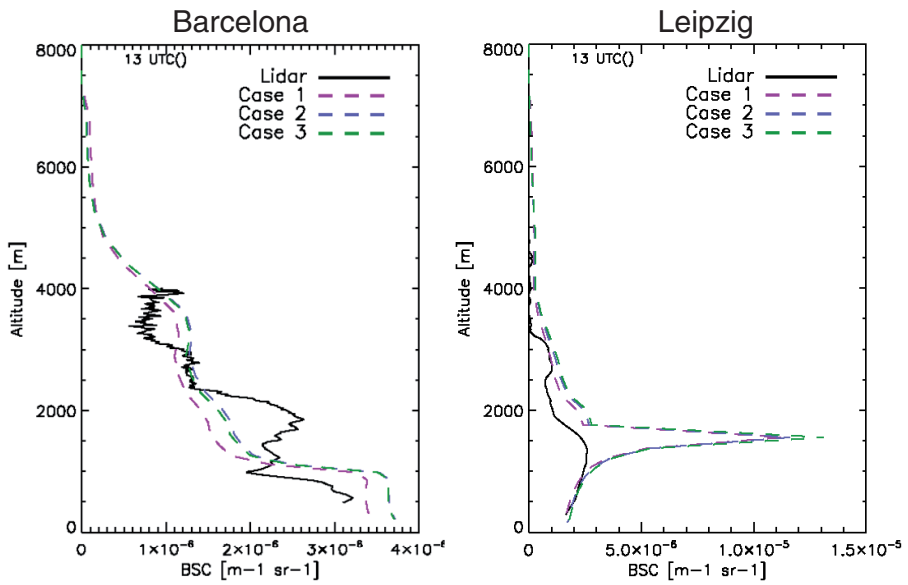

Fig. 3: *Comparisons of vertical distribution of backscatter coefficient at 532 nm, observed by lidar (black line) and obtained from three cases of model simulations (colored lines), at the EARLINET stations in Barcelona (left) and Leipzig (right) on July 24, 2006.*

backscatter between 1 and 2 km height. The agreement between model simulations and lidar observation in Leipzig is good. Between 1.5 and 2 km the profile is overestimated, because the model incorrectly simulated the presence of a (water) cloud at this location for all three cases. As for AOD, the difference between the individual cases is also not very significant regarding the vertical distribution of the backscatter coefficient. Case studies with stronger aerosol transport into the model domain will clarify the best method to prescribe aerosol profiles at the model boundaries.

Refrences

IPCC (2007), Climate Change 2007: The Physical Science Basis. Contribution of Working Group I to the Fourth Assessment Report of the Intergovernmental Panel on Climate Change, *Cambridge University Press, Cambridge, United Kingdom and New York, NY, USA*.

Mattis, I., D. Müller, A. Ansmann, U. Wandinger, J. Preißler, P. Seifert, and M. Tesche (2008), Ten Years of Multiwavelength Raman Lidar Observations of Free-Tropospheric Aerosol Layers Over Central Europe: Geometrical Properties and Annual Cycle, *J. Geophys. Res.*, *113*, 20202; doi:20210.21029/22007JD009636.

Steppeler, J., G. Doms, U. Schättler, H. W. Bitzer, A. Gassmann, U. Damrath, and G. Gregoric (2003), Meso-gamma scale forecasts using the nonhydrostatic model LM, *Meteorol. Atmos. Phys.*, *82* (1-4), 75-96.

Wandinger, U., I. Mattis, M. Tesche, A. Ansmann, J. Bösenberg, A. Chaikovski, V. Freudenthaler, L. Komguem, H. Linné, V. Matthias, J. Pelon, L. Sauvage, P. Sobolewski, G. Vaughan, and M. Wiegner (2004), Air mass modification over Europe: EARLINET aerosol observations from Wales to Belarus, *J. Geophys. Res.*, *109* (D24), 24205; doi: 24210.21029/22004JD005142.

Wolke, R., O. Hellmuth, O. Knoth, W. Schröder, B. Heinrich, and E. Renner (2004), The chemistry-transport modeling system LM-MUSCAT: Description and Citydelta applications, in *Air pollution modeling and its application XVI*, edited by C. Borrego and S. Incecik, pp. 427-439, Kluwer Academic / Plenum Publishers, New York.

COSMO-MUSCAT simulations of aerosol reduction scenarios in Germany

Detlef Hinneburg, Eberhard Renner, Ralf Wolke

Seit dem Inkrafttreten von Grenzwerten für Feinstaub (PM_{10}) und weiteren geplanten Regelungen sind praktische Maßnahmen zur Reduzierung von Emissionen unumgänglich geworden. Dabei stehen nicht nur mehr oder weniger bekannte Eingriffe in Verkehr und Industrie bevor, sondern es sind alle Bereiche und Aspekte der Wirtschaftstätigkeit und des gesellschaftlichen Lebens auf den Prüfstand zu stellen. Zu den langfristig notwendig werdenden Umstellungen gehören beispielsweise auch technologische Transformationen in der Landwirtschaft oder ökologisch und medizinisch begründete Wandlungen in der Ernährungsweise der Bevölkerung.

Alle diese primären oder sekundären, direkten oder indirekten, bewusst eingeleiteten oder natürlich ablaufenden Veränderungen wurden im Rahmen eines Verbundprojekts in die Entwicklung mehrerer Emissionsszenarien für die Jahre bis 2020 eingearbeitet, die durch diverse Atmosphärenmodelle für Ausbreitungsrechnungen auf dem Gebiet Europas verwendet werden. Die Abweichungen dieser Szenarien-Simulationen gegenüber dem Referenzzustand von 2005 liefern Aussagen zur quantitativen Wirksamkeit bestimmter emissionsreduzierender Maßnahmen. Der Anteil dieses Teilprojekts besteht in der Anwendung des Modells COSMO-MUSCAT und in seinem Beitrag zur Diversifizierung und damit Konsolidierung des kollektiven Gesamtergebnisses.

Introduction

Since Europe-wide limit values for particulate matter in ambient air (PM_{10}) were stipulated and further deadlines scheduled (for $PM_{2.5}$), many activities have been initiated to reduce the emissions. However, further practical steps are inevitable and have to be tackled in future. The problem is very complex. Simply to minimize the largest pollution sources is in general not the solution, because the greatest human exposure is not always caused by the largest emitters. The local particle concentrations depend not only on the direct particle emissions, but also on the secondary formation by precursor gases. In this case, for instance, the intended reduction of an excess reactant may be without effect on the particle formation.

There are manifold processes which affect the particles and precursor gases during their transport and dispersion. Essential influences come from (1) the irregular local distribution of the numerous emission sources including disparate chemical compositions and other characteristic properties, (2) the diurnal and annual variations of the meteorological dispersion conditions, and last but not least (3) the chemical reactions of the air constituents, which again depend on meteorology (temperature, humidity, radiation). Altogether, the interrelation between human exposure and the emissions is strongly nonlinear.

This situation is even more complicated by the political instructions to reduce the emissions, in they are in no case comprehensive, conspiring and total. In contrast, they imply or evoke very complex and partly conflicting tendencies. Moreover, the political, economical and financial scope of the arranged reduction steps is constricted and their potential can not be exploited completely (e.g., speed limit, low-emission zones, reorientation of nutrition).

A composite project under the guidance of the Federal Environment Agency has joined several groups of emission and dispersion modeling as well as in ecological research: IZT (Berlin), FAL (Braunschweig), IER (University of Stuttgart), TNO (Netherlands), TrUmF (Free University of Berlin), IfT (Leipzig), IVU (Freiburg). The members are engaged in (1) compiling all emission reduction measures possible, (2) assembling them to a set of prospective emission scenarios, (3) performing the corresponding annual atmospheric simulations, (4) ascertaining the lowering potentials of the various measures and their evaluation, and (5) identifying the optimal scenarios and the highest-possible effects. The project name is PAREST – Particle reduction strategies (http://parest.fath-berlin.de/parest_home).

General objective

The following tasks are fulfilled successively and partly by sharing the work:

(1) Development of several qualitatively differing and chronologically arranged scenarios of future emission performance and scheduled emission directives incorporating the various conceivable trends and measures;
(2) assembling of the corresponding emission data base for Europe and especially Germany, graduated according to the years 2005 (reference state), 2010, 2015, and 2020;
(3) atmospheric transport and dispersion simulations for the specified years (each

with the reference meteorology of 2005) considering all relevant gaseous and particulate pollutants;
(4) performing all simulations for the area of Europe, the territory of Germany, and certain congested sub-areas (e.g., Greater Berlin) with ascending spatial resolution;
(5) derivation of quantitative effects of the individual reduction measures from the differences between the scenario simulations, weighted with the share of concerned human population;
(6) application of different models to all cases in order to enhance the credibility of the results and to obtain a suggestion of their tolerances.

The definition and configuration of the emission reduction scenarios is of crucial importance. The scenarios have to consider not only the currently valid, the already intended, and the possible future steps of reducing the threshold values for the emissions of industrial and agricultural facilities and the traffic, but also the future trends of the demographic, cultural and economic developments in the society. These trends are more or less vague, very complex, conflicting, and have rather unpredictable side-effects. There are sparse examinations with minor reliability on this subject, thus the actual composite project will make a distinguished contribution to the problem solving.

To the more indirectly acting measures and trends with significant secondary aspects belong transformations, reorientations, and other alterations on the following fields:
(1) human nutrition (e.g., promotion of vegetarians),
(2) social behavior (restricted smoking) and habits of recreation (changed shopping and sporting activities and places),
(3) feeding stuff culture (advanced fertilizer technology),
(4) livestock farming (changes in feeding and butchering, reduced mast period),
(5) price and fiscal instruments (trends of energy costs, car tax),
(6) transport sector (speed limits, changed fuel grades, rearranged main roads, widespread low-emission zones),
(7) power industry (new power stations, reconstructions),
(8) expanded and advanced recycling techniques,
(9) heterogeneous trends in other countries.

Most of these measures or trends result in interacting, interfering, coinciding, or overlapping emission changes. So, direct interventions in the industrial livestock farming may come into conflict with trends in the feeding stuff cultivation. Consequently, to the best of our present knowledge, the final effective lowering potentials of the graduated emission scenarios will not be eminent, the more so as the national measures and the regional polluters are not all-dominant.

Special contribution

In the frame of the composite project, the IfT Leipzig adopts the part of the special model COSMO-MUSCAT consisting of two online coupled models: the prognostic meteorological model COSMO of the German Weather Service and the transport-and-chemistry model MUSCAT. The application refers to the reference year 2005 and the scenario year 2020, with rising spatial resolution for the areas of Europe (max. 0,25° / 28 km), Germany (min. 0,0625° / 7 km), and Great Berlin (0,015625° / 1 km). Due to identical emission data sets adopted by all models, the deviations among the model results trace back to formal differences between the models and mainly to the individually managed meteorology. These disturbing factors are expected to compensate to a certain degree due to the intended diversity of the models.

In principal aspects the area-nested model application resembles the studies of *Stern et al.* [2008] and *Hinneburg et al.* [2009]. The simulations for Europe are governed at the boundaries by forcing toward the re-analysis data of the global model GME (for the meteorological part) and the climatological profiles of the air ingredients (for the chemical part). In a similar way, each smaller-area simulation is controlled by adopting the isochronous values from the larger-area simulation. In addition to the customary sub-species of PM_{10}, also sea salt, elementary and organic carbon are considered.

Result

Although the completion of the collective work program is pending so far and credible results cannot be anticipated here, the special contribution of this partial project is interesting enough. Figure 1 presents the fundamental result in form of time-series of the PM_{10} concentration as obtained with the model COSMO-MUSCAT. The graphs are shown for the years 2005 and 2020 exemplarily for Berlin.

It is obvious, that the scenario of 2020 with maximum emission-lowering measures incorporated leads to a universal reduction of PM_{10}. Even though the baseline concentrations decrease by not more than about 5 µg/m^3, the important peaks of the mean daily values generally decline by 10 to 20 µg/m^3. This result is valid also for other sites in Germany and turns out not so overwhelming.

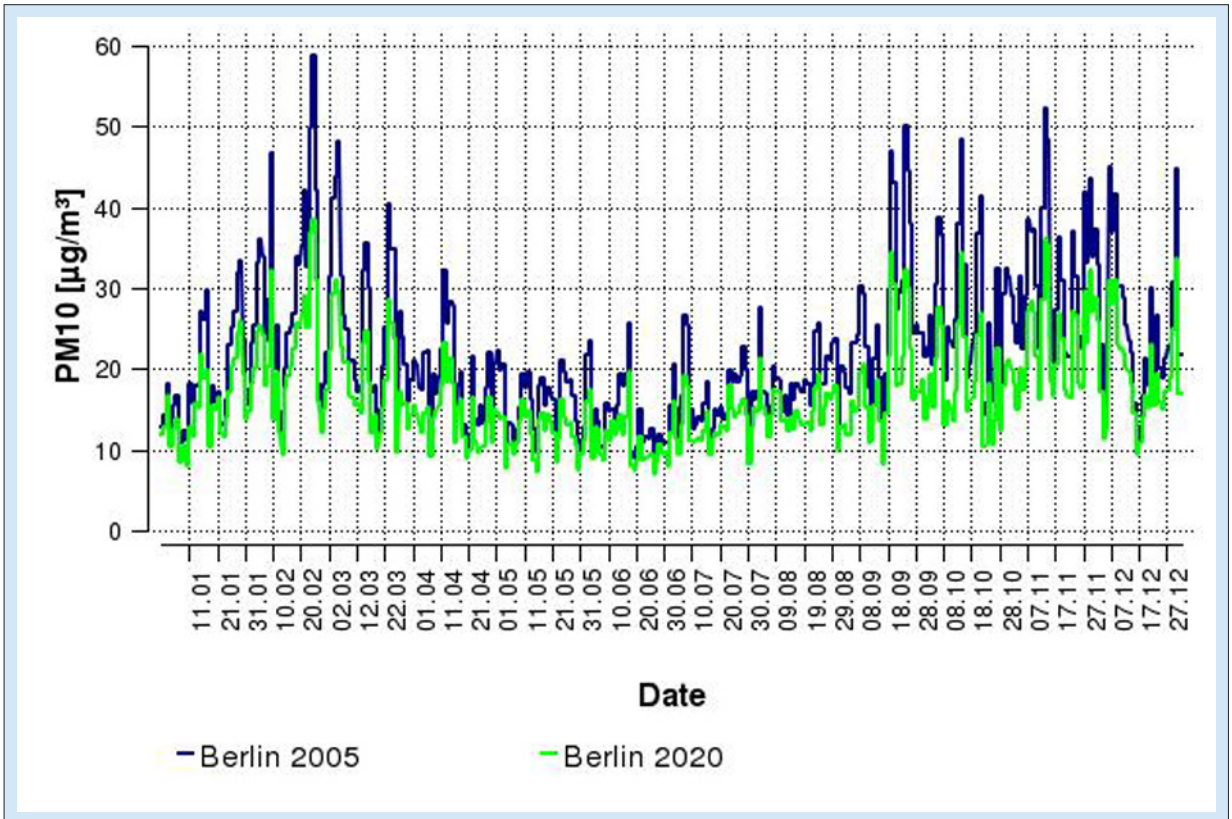

Fig. 1: *Time series of PM_{10} at Berlin for the emission scenarios of 2005 and 2020.*

References

Hinneburg, D., E. Renner, and R. Wolke (2009), Formation of secondary inorganic aerosols by power plant emissions exhausted through cooling towers in Saxony, *Environ. Sci. Pollut. Res.*, *16*, 25-35.

Stern, R., P. Builtjes, M. Schaap, R. Timmermans, R. Vautard, A. Hodzic, M. Memmesheimer, H. Feldmann, E. Renner, R. Wolke, and A. Kerschbaumer (2008), A model inter-comparison study focussing on episodes with elevated PM10 concentrations, *Atmos. Environ.*, *42*, 4567-4588.

Funding

- The Federal Environmental Agency (UBA), Dessau, Germany

LES Modeling of the moist planetary boundary layer using GPU's

Stefan Horn, Oswald Knoth

Flache Grenzschichtbewölkung in der Passatwindregion, welche einen großen Bereich der Ozeane der Erde bedeckt, stellt einen großen Unischerheitsfaktor in heutigen Klimamodellen dar. Insbesondere ihre Entwicklung unter sich ändernden atmosphärischen Bedingungen und der Übergangsbereich zwischen offenen und geschlossenen Zellstrukturen ist Gegenstand aktueller Forschung. Dieser Übergang hat einen starken Einfluss auf den Strahlungshaushalt der marinen Grenzschicht.

Large Eddy Simulationen (LES) solcher warmen Wolkenfelder, im speziellen die Untersuchung selbst organisierender Strukturen und Rückkopplungsmechanismen, erfordern große Modellgebiete und hohe räumliche und zeitliche Auflösungen. Das macht sie zu sehr rechenaufwändigen Problemstellungen. Mit der Einführung der „unified shader"-Technik in der Steuerung moderner Grafikkarten (GPUs), welche zu den effizientesten Rechengeräten unserer Zeit zählen, werden diese für den Bereich physikalischer Simulationen verfügbar. Diese „unified shader" bezeichnen kleine Programme die vom Grafikkartentreiber kompiliert werden, um dann als Kernel auf so genannten Stream-Prozessoren (SPU) zu arbeiten. Moderne Grafikkarten besitzen eine sehr große Anzahl solcher Stream-Prozessoren. Beispielsweise besteht eine ATI HD 4890 aus 800 solcher SPUs mit einer Taktfrequenz von 850 MHz und bietet damit eine Leistung von 1,2 Tflops. In dieser Arbeit wird ein neues LES-Modell vorgestellt, welches in C++ geschrieben wurde und OpenGL und die GL Shader Language verwendet, um auf die Grafikkarten zuzugreifen. Das macht es möglich, solche Simulationen sehr viel schneller als zuvor und auch auf kleineren Geräten, zum Beispiel mit ca. 500000 Zellen auf einem aktuellen Notebook, in Echtzeit, durchzuführen.

Introduction

There are various approaches to perform general purpose computation on GPUs (GPGPU). The most important are CUDA from nVidia, Brook+ from ATI and the platform independent GL Shader Language (GLSL) coming with OpenGL 2.0. To gain platform independence and to ensure future usability we chose OpenGL and GLSL to implement the LES model. It uses an explicit 2nd order three step Runge Kutta time integration scheme with time splitting methods and divergence damping after *Wicker and Skamarock* [2002] to handle the acoustic modes and fast microphysical processes. This integration scheme is also applied in the Weather Research and Forecasting Model WRF [*Skamarock et al.*, 2005] and the operational model COSMO by the DWD.

As a first step a simple one moment bulk microphysical scheme has been applied, which was extended to warm cloud parameterizations based on the work of *Seifert and Beheng* [2006] to include drizzle and rain. The model has been validated with different test cases, like a rising heat bubble in a dry environment [*Wicker and Skamarock*, 1998], a cold air bubble [*Wicker and Skamarock*, 2002], and a rising heat bubble in an moist saturated environment [*Bryan and Fritsch*, 2002]. At the moment the model is still under development and testing using warm cloud cases of the GEWEX Cloud System Study (GCSS).
Another problem in three dimensional cloud system modeling is the visualization of the produced fields. Therefore we implemented a simple ray tracing algorithm, which makes it possible to produce images at runtime as a direct feedback from the model to the modeler without the need to write large amounts of data onto a hard disk, which meanwhile becomes as time consuming as the calculation itself.

Model implementation

The implementation of such a model using GLSL is a complicated task, because the language was originally designed for graphic applications and texture operations. A texture is a two dimensional rectangular field of vectors with up to 4 components each. It can be interpreted as a picture with a red, green, blue and alpha component in every pixel. Every single information is a 32 bit floating point value.

The components of the vector of state of the atmosphere are saved in these textures. For a moist non-hydrostatic model with two-moment bulk microphysics, including water vapor, cloud water and drizzle, we need one texture with three components for the velocities and 2 textures with 4 components for the scalar variables like densities, number concentrations and temperature. Now we can apply a certain shader function to one or more textures, describing our state of the atmosphere, and calculate the needed fluxes and save them in new textures. This works by binding the shader into the render pipeline and drawing a rectangle. Finally we have to calculate the time stepping using the fluxes. The model needs different shaders for advection, pressure gradient and

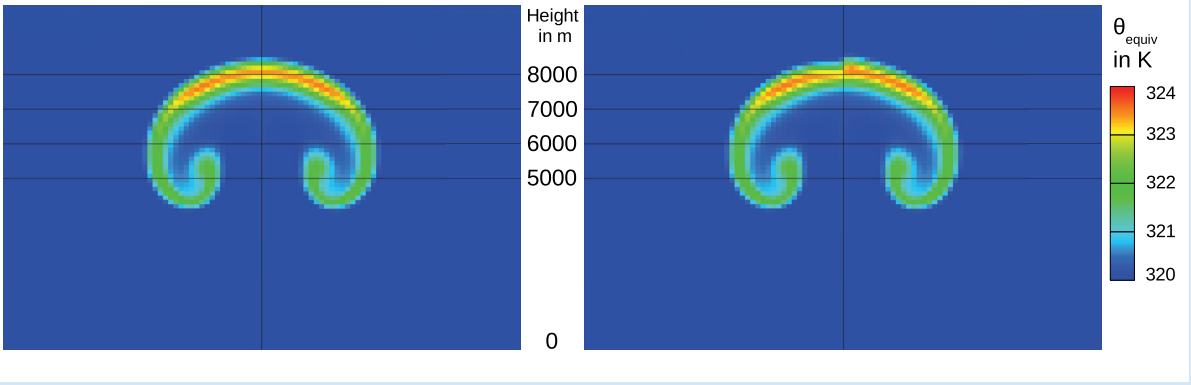

Fig. 1: *Equivalent potential temperature of rising thermal after 1000 s; left: symmetric result on ATI; right: asymmetric result on nVidia Cards.*

gravitation, divergence damping, microphysical processes, surface fluxes and time stepping.

With that approach the parallelization is completely transparent to the modeler. Although this may not be the computationally most efficient way, the effort for development is strongly reduced, and the platform dependence is minimized.

Test cases and symmetry break

From all test cases, only the heat bubble in a saturated environment and the drizzling warm cloud RICO are presented. Two results of the rising bubble test are shown in Fig. 1. The results look similar for the one moment and the 2-moment scheme without drizzle. As in the original work by *Bryan and Fritsch* [2002] the bubble rises up to about 8 km. Also the structure of the rising bubble is well reproduced. One thing to mention is that caused by the 32-bit precision a symmetry break in the divergence term during the calculation of the fast advection appeared which is caused by floating point arithmetics. On ATI Cards this could be resolved by rewriting the term in a different order but on nVidia cards it was not possible to correct for a symmetric result. One reason could be the optimizations done by the nVidia device driver during kernel compilation, so that the rewriting does not show any effect. This symmetry break through floating point arithmetic occurs on CPU's as well, but is hidden by the higher precision.

The second test is the Rain in Cumulus over the Ocean (RICO) case, which is the 9th test case of the GCSS boundary layer cloud working group. It is a more complex environment that produces a convective boundary layer with drizzling cumulus clouds. It was chosen to test the microphysical parameterizations for the processes nucleation, autoconversion, rain sedimentation and rain evaporation. A snapshot of the model visualization after 4 h model time is shown in Fig. 2, the blue fog beneath the clouds represents drizzle.

In Figure 3. Different time series for the parameters cloud top, cloud base, cloud height, cloud fraction and number concentrations for cloud droplets and rain droplets. The concentrations are mean values over cloudy grid cells. A grid cell is flagged as cloudy when the liquid water content exceeds 0.01g/kg.

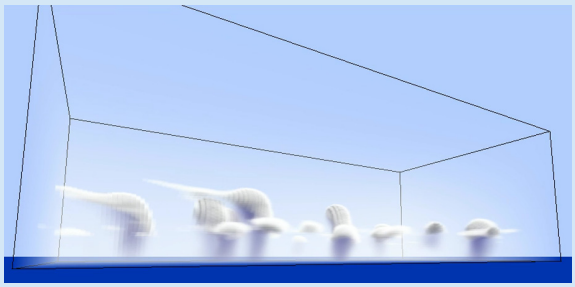

Fig. 2: *Visualization of RICO Case after 4h model time with the GPU-LES-Model (blue fog represents drizzle).*

Conclusions

The new GPU-based LES-model presented here opens the field of high resolution cloud modeling to a new community. It makes it possible to perform simulations on notebooks, but also relative huge simulations, comparable to studies done with the help of supercomputers, on ordinary cheap gaming cards. Another advantage is that the problems occurring by parallelization are completely transparent to the developer, so it is it relative easy to use and to extend the model. Because it is based on open standards, it should be possible to run this model on a variety of platforms and also for a long time in the future.

Further developments, like using several GPUs for one model run, cut cells, apply new time integration schemes, or migration to a new GLSL version are strongly recommended.

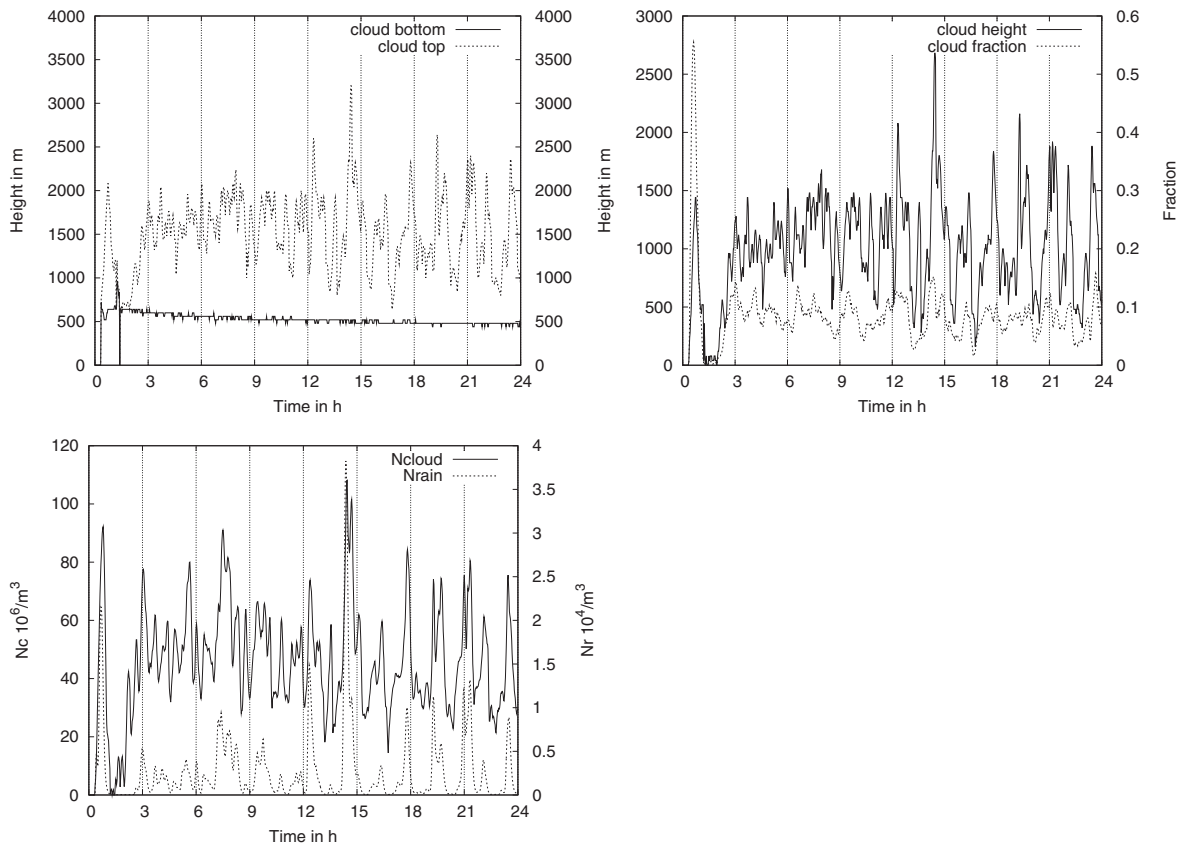

Fig. 3: *Results from the RICO test case; x-axis: time in seconds; top left: cloud-top and base; top right: cloud height and fraction; bottom left: number concentration cloud droplets and rain droplets.*

References

Bryan, G. H., and J. M. Fritsch (2002), A Benchmark Simulation for Moist Nonhydrostatic Numerical Models, *Mon. Wea. Rev.*, *130* (12), 2917-2928.

Rauber, R. M., B. Stevens, H. T. Ochs, C. Knight, B. A. Albrecht, A. M. Blyth, C. W. Fairall, J. B. Jensen, S. G. Lasher-Trapp, O. L. Mayol-Bracero, G. Vali, J. R. Anderson, B. A. Baker, A. R. Bandy, E. Burnet, J. L. Brenguier, W. A. Brewer, P. R. A. Brown, P. Chuang, W. R. Cotton, L. Di Girolamo, B. Geerts, H. Gerber, S. ke, L. Gomes, B. G. Heikes, J. G. Hudson, P. Kollias, R. P. Lawson, S. K. Krueger, D. H. Lenschow, L. Nuijens, D. W. Sullivan, R. A. Rilling, D. C. Rogers, A. P. Siebesma, E. Snodgrass, J. L. Stith, D. C. Thornton, S. Tucker, C. H. Twohy, and P. Zuidema (2007), Rain in Shallow Cumulus Over the Ocean: The RICO Campaign, *Bull. Amer. Meteor. Soc.*, *88* (12), 1912-1928.

Seifert, A., and K. D. Beheng (2006), A two-moment cloud microphysics parameterization for mixed-phase clouds. Part 2: Maritime vs. continental deep convective storms, *Meteorol. Atmos. Phys.*, *92* (1), 67-82.

Skamarock, W. C., J. Dudhia, D. Gill, D. Barker, W. Wei, and J. Powers (2005), A description of the advanced research WRF version 2 : NCAR Technical Note NCAR/TN-468+STR, 88 pp, National Center for Atmospheric Research, Boulder, CO, USA.

Wicker, L. J., and W. C. Skamarock (1998), A time-splitting scheme for the elastic equations incorporating second-order Runge-Kutta time differencing, *Mon. Wea. Rev.*, *126* (7), 1992-1999.

Wicker, L. J., and W. C. Skamarock (2002), Time-splitting methods for elastic models using forward time schemes, *Mon. Wea. Rev.*, *130* (8), 2088-2097.

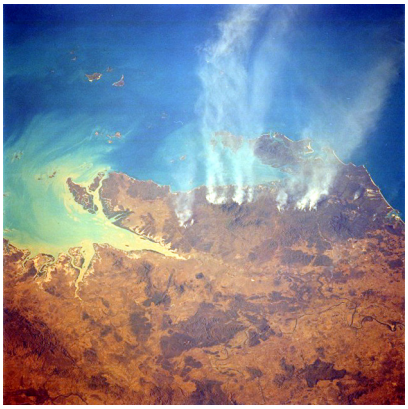

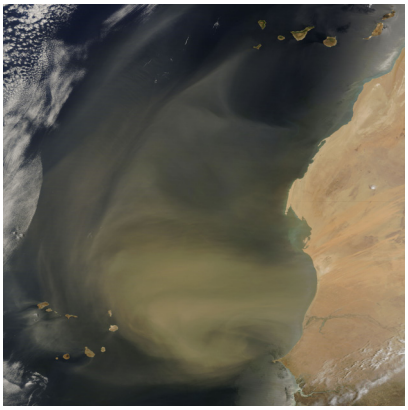

Appendices

Publication statistics

	2008	2009
Total number of publications	**205**	**263**
Books (author, editor)	0	1
Book sections	6	8
Conference proceedings	43	62
Publications, peer-reviewed	74	114
Publications, other	4	3
Lectures, invited	10	12
Lectures, other	70	57

Publications

2008

Allan, J. D., Baumgardner, D., Raga, G. B., Mayol-Bracero, O. L., Morales-García, F., García-García, F., Montero-Martínez, G., Borrmann, S., Schneider, J., Mertes, S., Walter, S., Gysel, M., Dusek, U., Frank, G. P. and Krämer, M. 2008. Clouds and aerosols in Puerto Rico - A new evaluation. Atmos. Chem. Phys., **8**, 1293-1309.

Ansmann, A., Tesche, M., Althausen, D., Müller, D., Seifert, P., Freudenthaler, V., Heese, B., Wiegner, M., Pisani, G., Knippertz, P. and Dubovik, O. 2008. Influence of Saharan dust on cloud glaciation in Southern Morocco during the Saharan Mineral Dust Experiment. J. Geophys. Res. - Atmosp., **113**, D04210, doi:10.1029/2007JD008785.

Apel, E. C., Brauers, T., Koppmann, R., Bandowe, B., Boßmeyer, J., Holzke, C., Tillmann, R., Wahner, A., Wegener, R., Brunner, A., Jocher, M., Ruuskanen, T., Spirig, C., Steigner, D., Steinbrecher, R., Gomez Alvarez, E., Müller, K., Burrows, J. P., Schade, G., Solomon, S. J., Ladstätter-Weißenmayer, A., Simmonds, P., Young, D., Hopkins, J. R., Lewis, A. C., Legreid, G., Reimann, S., Hansel, A., Wisthaler, A., Blake, R. S., Ellis, A. M., Monks, P. S. and Wyche, K. P. 2008. Intercomparison of oxygenated volatile organic compound measurements at the SAPHIR atmosphere simulation chamber. J. Geophys. Res. - Atmosp., **113**, D20307, doi:10.1029/2008JD009865.

Baars, H., Ansmann, A., Engelmann, R. and Althausen, D. 2008. Continuous monitoring of the boundary-layer top with lidar. Atmos. Chem. Phys., **8**, 7281-7296.

Berndt, T., Stratmann, F., Bräsel, S., Heintzenberg, J., Laaksonen, A. and Kulmala, L. 2008. SO_2 oxidation products other than H_2SO_4 as a trigger of new particle formation. Part 1: Laboratory investigations. Atmos. Chem. Phys., **8**, 6365-6374.

Birmili, W., Schepanski, K., Ansmann, A., Spindler, G., Tegen, I., Wehner, B., Nowak, A., Reimer, E., Mattis, I., Müller, K., Brüggemann, E., Gnauk, T., Herrmann, H., Wiedensohler, A., Althausen, D., Schladitz, A., Tuch, T. and Löschau, G. 2008. A case of extreme particulate matter concentrations over Central Europe caused by dust emitted over the southern Ukraine. Atmos. Chem. Phys., **8**, 997-1016.

Boy, M., Karl, T., Turnipseed, A., Mauldin, R. L., Kosciuch, E., Greenberg, J., Rathbone, J., Smith, J., Held, A., Barsanti, K., Wehner, B., Bauer, S., Wiedensohler, A., Bonn, B., Kulmala, M. and Guenther, A. 2008. New particle formation in the front range of the Colorado Rocky Mountains. Atmos. Chem. Phys., **8**, 1577-1590.

Bruckmann, P., Birmili, W., Straub, W., Pitz, M., Gladtke, D., Pfeffer, U., Hebbinghaus, H., Wurzler, S. and Olschewski, A. 2008. An outbreak of Saharan dust causing high PM10 levels north of the Alps (Hohe PM10-Konzentrationen nördlich der Alpen, hervorgerufen durch Ferntransport von Saharastaub). Gefahrst. Reinhalt. L., **68**, 490-498.

Charron, A., Birmili, W. and Harrison, R. M. 2008. Fingerprinting particle origins according to their size distribution at a UK rural site. J. Geophys. Res. - Atmosp., **113**, D07202, doi:10.1029/2007JD008562.

Cheng, T., Peng, Y., Feichter, J. and Tegen, I. 2008. An improvement on the dust emission scheme in the global aerosol-climate model ECHAM5-HAM. Atmos. Chem. Phys., **8**, 1105-1117.

Cheng, Y. F., Heintzenberg, J., Wehner, B., Wu, Z. J., Su, H., Hu, M. and Mao, J. T. 2008. Traffic restrictions in Beijing during the Sino-African Summit 2006: Aerosol size distribution and visibility compared to long-term in situ observations. Atmos. Chem. Phys., **8**, 7583-7594.

Cheng, Y. F., Wiedensohler, A., Eichler, H., Heintzenberg, J., Tesche, M., Ansmann, A., Wendisch, M., Su, H., Althausen, D., Herrmann, H., Gnauk, T., Brüggemann, E., Hu, M. and Zhang, Y. H. 2008. Relative humidity dependence of aerosol optical properties and direct radiative forcing in the surface boundary layer at Xinken in Pearl River Delta of China: An observation based numerical study. Atmos. Environ., **42**, 6373-6397 (doi:10.1016/j.atmosenv.2008.04.009).

Cheng, Y. F., Wiedensohler, A., Slanina, J., Heintzenberg, J., Eichler, H., Su, H., Gnauk, T., Brüggemann, E., Herrmann, H., Zeng, L. M., Tuch, T., Hu, M. and Zhang, Y. H. 2008. Aerosol optical properties and related chemical apportionment at Xinken in Pearl River Delta of China. Atmos. Environ., **42**, 6351-6372 (doi:10.1016/j.atmosenv.2008.02.034).

Cozic, J., Mertes, S., Verheggen, B., Cziczo, D. J., Gallavardin, S. J., Walter, S., Baltensperger, U. and Weingartner, E. 2008. Black carbon enrichment in atmospheric ice particle residuals observed in lower tropospheric mixed phase clouds. J. Geophys. Res. - Atmosp., **113**, D15209, doi:10.1029/2007JD009266.

Cozic, J., Verheggen, B., Weingartner, E., Crosier, J., Bower, K. N., Flynn, M., Coe, H., Henning, S., Steinbacher, M., Henne, S., Coen, M. C., Petzold, A. and Baltensperger, U. 2008. Chemical composition of free tropospheric aerosol for PM1 and coarse mode at the high alpine site Jungfraujoch. Atmos. Chem. Phys., **8**, 407-423.

Ehrlich, A., Bierwirth, E., Wendisch, M., Gayet, J.-F., Mioche, G., Lampert, A. and Heintzenberg, J. 2008. Cloud phase identification of Arctic boundary-layer clouds from airborne spectral reflection measurements: Test of three approaches. Atmos. Chem. Phys., **8**, 7493-7505.

Ehrlich, A., Wendisch, M., Bierwirth, E., Herber, A. and Schwarzenböck, A. 2008. Ice crystal shape effects on solar radiative properties of Arctic mixed-phase clouds - Dependence on microphysical properties. Atmos. Res., **88**, 266-276.

Eichler, H., Cheng, Y. F., Birmili, W., Nowak, A., Wiedensohler, A., Brüggemann, E., Gnauk, T., Herrmann, H., Althausen, D., Ansmann, A., Engelmann, R., Tesche, M., Wendisch, M., Zhang, Y. H., Hu, M., Liu, S. and Zeng, L. M. 2008. Hygroscopic properties and extinction of aerosol particles at ambient relative humidity in South-Eastern China. Atmos. Environ., **42**, 6321-6334.

Engelmann, R., Wandinger, U., Ansmann, A., Müller, D., Zeromskis, E., Althausen, D. and Wehner, B. 2008. Lidar observations of the vertical aerosol flux in the planetary boundary layer. J. Atmos. Ocean. Tech., **25**, 1296-1306.

Fan, S. J., Wang, B., Tesche, M., Engelmann, R., Althausen, D., Liu, J., Zhu, W., Fan, Q., Li, M., Ta, N., Song, L. and Leong, K. 2008. Meteorological conditions and structures of atmospheric boundary layer in October 2004 over Pearl River Delta area. Atmos. Environ., **42**, 6174-6186.

Frey, A., Rose, D., Wehner, B., Müller, T., Cheng, Y. F., Wiedensohler, A. and Virkkula, A. 2008. Application of the Volatility-TDMA technique to determine the number size distribution and mass concentration of less volatile particles. Aerosol Sci. Technol., **42**, 817-828.

Garland, R. M., Yang, H., Schmid, O., Rose, D., Nowak, A., Achtert, P., Wiedensohler, A., Takegawa, N., Kita, K., Miyazaki, Y., Kondo, Y., Hu, M., Shao, M., Zeng, L., Zhang, Y., Andreae, M. O. and Pöschl, U. 2008. Aerosol optical properties in a rural environment near the mega-city Guangzhou, China: Implications for regional air pollution and radiative forcing. Atmos. Chem. Phys., **8**, 5161-5186.

Gnauk, T., Müller, K., van Pinxteren, D., He, L.-Y., Niu, Y.-W., Hu, M. and Herrmann, H. 2008. Size-segregated particulate chemical composition in Xinken, Pearl River Delta, China: OC/EC and organic compounds. Atmos. Environ., **42**, 6296-6309.

Grützun, V., Knoth, O. and Simmel, M. 2008. Simulation of the influence of aerosol particle characteristics on clouds and precipitation with LM-SPECS: Model description and first results. Atmos. Res., **90**, 233-242.

Grzeschik, M., Bauer, H.-S., Wulfmeyer, V., Engelbart, D., Wandinger, U., Mattis, I., Althausen, D., Engelmann, R., Tesche, M. and Riede, A. 2008. Four-dimensional variational data analysis of water vapor Raman lidar data and their impact on mesoscale forecasts. J. Atmos. Ocean. Tech., **25**, 1437-1453.

Haywood, J. M., Pelon, J., Formenti, P., Bharmal, N. A., Brooks, M., Capes, G., Chazette, P., Chou, C., Christopher, S., Coe, H., Cuesta, J., Derimian, Y., Desboeufs, K., Greed, G., Harrison, M., Heese, B., Highwood, E. J., Johnson, B. T., Mallet, M., Marticorena, B., Marsham, J., Milton, S., Myhre, G., Osborne, S. R., Parker, D. J., Rajot, J.-L., Schulz, M., Slingo, A., Tanre, D. and Tulet, P. 2008. Overview of the dust and biomass-burning experiment and African monsoon multidisciplinary analysis special observing period-0. J. Geophys. Res. - Atmosp., **113**, D00C17, doi:10.1029/2008JD010077.

Heese, B. and Wiegner, M. 2008. Vertical aerosol profiles from Raman polarization lidar observations during the dry season AMMA field campaign. J. Geophys. Res. - Atmosp., **113**, doi:10.1029/2007JD009487.

Heinold, B., Tegen, I., Schepanski, K. and Hellmuth, O. 2008. Dust radiative feedback on Saharan boundary layer dynamics and dust mobilization. Geophys. Res. Lett., **35**, L09804, doi:10.1029/2008GL033654.

Heintzenberg, J., Birmili, W., Theiss, D. and Kisilyakhov, Y. 2008. The atmospheric aerosol over Siberia, as seen from the 300 meter ZOTTO tower. Tellus B, **60**, 276-285.

Hellmuth, O. 2008. *Metastable states - questions of interest from a meteorological point of view*. R. A. Nauk (Ed.), In: *Metastabil´nye sostojanija i fazovye perechody*. UrO RAN, Ekaterinburg, p. 90-116. (Sbornik nayčnych trudov ; Vypusk 9)

Hellmuth, O. 2008. *Microphysical interactions between cosmic galactic rays and clouds:"Missing Link"in the climate discussion? Hypotheses, indications and the difficulties of enquiry. Part 1: The IPCC 2007 perspective*. D. B. Herrmann (Ed.), In: *50 Jahre Weltraumforschung. Erforschung und Überwachung der Erde und des Weltraumes gestützt auf die Mittel der Raumfahrt*. trafo verlag, Berlin, p. 75-94. (Sitzungsberichte der Leibniz-Sozietät ; Band 96)

Helsper, C., Horn, H. G., Schneider, F., Wehner, B. and Wiedensohler, A. 2008. Intercomparison of five mobility size spectrometers for measuring atmospheric submicrometer aerosol particles. Gefahrst. Reinhalt. L., **68**, 475-481.

Hermann, M., Brenninkmeijer, C. A. M., Slemr, F., Heintzenberg, J., Martinsson, B. G., Schlager, H., van Velthoven, P. J., Wiedensohler, A., Zahn, A. and Ziereis, H. 2008. Submicrometer aerosol particle distributions in the upper troposphere over the mid-latitude North Atlantic - Results from the third route of "CARIBIC". Tellus B, **60**, 106-117.

Hofmann, D., Hartmann, F. and Herrmann, H. 2008. Analysis of nitrophenols in cloud water with a miniaturized light-phase rotary perforator and HPLC-MS. Anal. Bioanal. Chem., **391**, 161-169.

Hoose, C., Lohmann, U., Erdin, R. and Tegen, I. 2008. The global influence of dust mineralogical composition on heterogeneous ice nucleation in mixed-phase clouds. Environ. Res. Lett., **3**, 803-813.

Hungershöfer, K., Zeromskiene, K., Iinuma, Y., Helas, G., Trentmann, J., Trautmann, T., Parmar, R. S., Wiedensohler, A., Andreae, M. O. and Schmid, O. 2008. Modelling the optical properties of fresh biomass burning aerosol produced in a smoke chamber: results from the EFEU campaign. Atmos. Chem. Phys., **8**, 3427-3439.

Hyvarinen, A. P., Komppula, M., Engler, C., Kivekas, N., Kerminen, V. M., Dal Maso, M., Viisanen, Y. and Lihavainen, H. 2008. Atmospheric new particle formation at Uto, Baltic Sea 2003-2005. Tellus B, **60**, 345-352.

Jebens, S., Weiner, R., Podhaisky, H. and Schmitt, B. A. 2008. Explicit multi-step peer methods for special second-order differential equations. Appl. Math. Comput., **202**, 803-813.

Johnson, B. T., Heese, B., McFarlane, S. A., Chazette, P., Jones, A. and Bellouin, N. 2008. Vertical distribution and radiative effects of mineral dust and biomass burning aerosol over West Africa during DABEX. J. Geophys. Res. - Atmosp., **113**, D00C12.

Kalivitis, N., Birmili, W., Stock, M., Wehner, B., Massling, A., Wiedensohler, A., Gerasopoulos, E. and Mihalopoulos, N. 2008. Particle size distributions in the Eastern Mediterranean troposphere. Atmos. Chem. Phys., **8**, 6729-6738.

Kolgotin, A. and Müller, D. 2008. Theory of inversion with two-dimensional regularization: Profiles of microphysical particle properties derived from multiwavelength lidar measurements. Appl. Optics, **47**, 4472-4490.

Laaksonen, A., Kulmala, M., Berndt, T., Stratmann, F., Mikkonen, S., Ruuskanen, A., Lehtinen, K. E. J., Dal Maso, M., Aalto, P., Petäjä, T., Riipinen, I., Sihto, S.-L., Janson, R., Arnold, F., Hanke, M., Ücker, J., Umann, B., Sellegri, K., O´Dowd, C. D. and Viisanen, Y. 2008. SO_2 oxidation products other than H_2SO_4 as a trigger of new particle formation. Part 2: Comparison of ambient and laboratory measurements, and atmospheric implications. Atmos. Chem. Phys., **8**, 7255-7264.

Laurent, B., Heinold, B., Tegen, I., Bouet, C. and Cautenet, G. 2008. Surface wind accuracy for modeling mineral dust emissions: Comparing two regional models in a Bodélé case study. Geophys. Res. Lett., **35**, L09804, doi:10.1029/2008GL033654.

Laurent, B., Marticorena, B., Bergametti, G., Léon, J. F. and Mahowald, N. 2008. Modeling mineral dust emissions from the Sahara desert using new surface properties and soil database. J. Geophys. Res. - Atmosp., **113**, D14218, doi:10.1029/2007JD009484.

Leinert, S. and Wiedensohler, A. 2008. A DMA and APS based technique for measuring aerodynamic hygroscopic growth factors of micrometer-size aerosol particles. J. Aerosol Sci., **39**, 393-402.

Lieber, M. and Wolke, R. 2008. Optimizing the coupling in a parallel air quality model system. Environ. Modell. Softw., **23**, 235-243.

Liu, S., Hu, M., Slanina, J., He, L.-Y., Niu, Y.-W., Brüggemann, E., Gnauk, T. and Herrmann, H. 2008. Size distribution and source analysis of ionic compositions of aerosols in polluted periods at Xinken in Pearl River Delta (PRD) of China. Atmos. Environ., **42**, 6284-6295.

Liu, S., Hu, M., Wu, Z., Wehner, B., Wiedensohler, A. and Cheng, Y. F. 2008. Aerosol number size distribution and new particle formation at a rural/coastal site in Pearl River Delta (PRD) of China. Atmos. Environ., **42**, 6275-6283.

Mattis, I., Müller, D., Ansmann, A., Wandinger, U., Preißler, J., Seifert, P. and Tesche, M. 2008. Ten years of multiwavelength Raman lidar observations of free-tropospheric aerosol layers over Central Europe: Geometrical properties and annual cycle. J. Geophys. Res. - Atmosp., **113**, D20202, doi:10.1029/2007JD009636.

Morozov, I., Gligorovski, S., Barzaghi, P., Hoffmann, D., Lazarou, Y. G., Vasiliev, E. and Herrmann, H. 2008. Hydroxyl radical reactions with halogenated ethanols in aqueous solution: Kinetics and thermochemistry. Int. J. Chem. Kinet., **40**, 174-188.

Nguyen, H. N., Martinsson, B. G., Wagner, J. B., Carlemalm, E., Ebert, M., Weinbruch, S., Brenninkmeijer, C. A. M., Heintzenberg, J., Hermann, M., Schuck, T., van Velthoven, P. F. J. and Zahn, A. 2008. Chemical composition and morphology of individual aerosol particles from a CARIBIC flight at 10 km altitude between 50°N and 30°S. J. Geophys. Res. - Atmosp., **113**, D23209, doi:10.1029/2008JD009956.

Niedermeier, D., Wex, H., Voigtländer, J., Stratmann, F., Brüggemann, E., Kiselev, A., Henk, H. and Heintzenberg, J. 2008. LACIS-measurements and parameterization of sea-salt particle hygroscopic growth and activation. Atmos. Chem. Phys., **8**, 579-590.

Noh, Y. M., Kim, Y. J. and Müller, D. 2008. Seasonal characteristics of lidar ratios measured with a Raman lidar at Gwangju, Korea in spring and autumn Atmos. Environ., **42**, 2208-2224.

Papayannis, A., Amiridis, V., Mona, L., Tsaknakis, G., Balis, D., Bösenberg, J., Chaikovski, A., De Tomasi, F., Grigorov, I., Mattis, I., Mitev, V., Müller, D., Nickovic, S., Perez, C., Pietruczuk, A., Pisani, G., Ravetta, F., Rizi, V., Sicard, M., Trickl, T., Wiegner, M., Gerding, M., Mamouri, R. E., D'Amico, G. and Pappalardo, G. 2008. Systematic lidar observations of Saharan dust over Europe in the frame of EARLINET (2000-2002). J. Geophys. Res. - Atmosp., **113**, D10204, doi:10.1029/2007JD009028.

Pitz, M., Birmili, W., Schmid, O., Peters, A., Wichmann, H.-E. and Cyrys, J. 2008. Quality control and quality assurance for particle size distribution measurements at an urban monitoring station in Augsburg, Germany. J. Environ. Monitor., **10**, doi:10.1039/b807264g.

Pitz, M., Schmid, O., Heinrich, J., Birmili, W., Maguhn, J., Zimmermann, R., Wichmann, H.-E., Peters, A. and Cyrys, J. 2008. Seasonal and diurnal variation of $PM_{2.5}$ apparent particle density in urban air in Augsburg, Germany. Environ. Sci. Technol., **42**, 5087-5093.

Renner, E. and Wolke, R. 2008. *Formation of secondary inorganic aerosols by high ammonia emissions simulated by LM/MUSCAT*. C. Borrego and A. I. Miranda (Ed.), In: *Air pollution modeling and its application XIX : Proceedings of the 29th NATO/CCMS International Technical Meeting on Air Pollution and Its Application (Aveiro, Portugal, 24-28 September 2007)*. Springer, Dordrecht, p. 522-529. (NATO Science for Peace and Security Series - C : Environmental Security)

Renner, E. and Wolke, R. 2008. Simulationen zur Episode hoher Schwebstaubkonzentrationen im Januar und Februar 2006. Immissionsschutz, **13**, 13-17.

Schütze, M. and Stratmann, F. 2008. Numerical simulation of cloud droplet formation in a tank. Comput. Geosci., **34**, 1034-1043.

Spindler, G., Brüggemann, E., Gnauk, T., Grüner, A., Herrmann, H., Renner, E., Wolke, R., Koester, M., Helmholz, E. and Rienecker, H. 2008. *Photoakustische Messung der NH_3-Konzentration in Niedersachsen und Sachsen - Praktische Erfahrungen und Ergebnisse der Modellierung aus dem Projekt AMMONISAX*. KRdL (Ed.), In: *Neue Entwicklungen bei der Messung und Beurteilung der Luftqualität : Kolloquium Nürnberg, 24. und 25. Juni 2008*. VDI-Verl., Nürnberg, p. 71-88. (VDI-Berichte ; Nr. 2040)

Spracklen, D., Carslaw, K. S., Kulmala, M., Kerminen, V.-M., Sihto, S.-L., Riipinen, I., Merikanto, J., Mann, G. W., Chipperfield, M. P., Wiedensohler, A., Birmili, W. and Lihavainen, H. 2008. Contribution of particle formation to global cloud condensation nuclei concentrations. Geophys. Res. Lett., **35**, L06808, doi:10.1029/2007GL033038.

Stern, R., Builtjes, P., Schaap, M., Timmermans, R., Vautard, R., Hodzic, A., Memmesheimer, M., Feldmann, H., Renner, E., Wolke, R. and Kerschbaumer, A. 2008. A model intercomparison study focussing on episodes with elevated PM10 concentrations. Atmos. Environ., **42**, 4567-4588.

Su, H., Cheng, Y. F., Cheng, P., Zhang, Y. H., Dong, S., Zeng, L. M., Slanina, J., Shao, M. and Wiedensohler, A. 2008. Observation of night time nitrous acid (HONO) formation at a non-urban site during PRIDE-PRD2004 in China. Atmos. Environ., **42**, 6219-6232.

Su, H., Cheng, Y. F., Shao, M., Gao, D. F., Yu, Z. Y., Zeng, L. M., Slanina, J., Zhang, Y. H. and Wiedensohler, A. 2008. Nitrous acid (HONO) and its daytime sources at a rural site during the 2004 PRIDE-PRD experiment in China. J. Geophys. Res. - Atmosp., **113**, D14312, doi;10.1029/2007JD009060.

Svenningsson, B., Arneth, A., Hayward, S., Holst, T., Massling, A., Swietlicki, E., Hirsikko, A., Junninen, H., Riipinen, I., Vana, M., Dal Maso, M., Hussein, T. and Kulmala, M. 2008. Aerosol particle formation events and analysis of high growth rates observed above a subarctic wetland-forest mosaic. Tellus B, **60**, 353-365.

Swietlicki, E., Hansson, H. C., Hameri, K., Svenningsson, B., Massling, A., McFiggans, G., McMurry, P. H., Petaja, T., Tunved, P., Gysel, M., Topping, D., Weingartner, E., Baltensperger, U., Rissler, J., Wiedensohler, A. and Kulmala, M. 2008. Hygroscopic properties of submicrometer atmospheric aerosol particles measured with H-TDMA instruments in various environments - A review. Tellus B, **60**, 432-469.

Tesche, M., Müller, D., Ansmann, A., Hu, M. and Zhang, Y. H. 2008. Retrieval of microphysical properties of aerosol particles from one-wavelength Raman lidar and multiwavelength Sun photometer observations. Atmos. Environ., **42**, 6398-6404.

Thiel, S., Ammannato, L., Bais, A., Bandy, B., Blumthaler, M., Bohn, B., Engelsen, O., Gobbi, G. P., Grobner, J., Jäkel, E., Junkermann, W., Kazadzis, S., Kift, R., Kjeldstad, B., Kouremeti, N., Kylling, A., Mayer, B., Monks, P. S., Reeves, C. E., Schallhart, B., Scheirer, R., Schmidt, S., Schmitt, R., Schreder, J., Silbernagl, R., Topaloglou, C., Thorseth, T. M., Webb, A. R., Wendisch, M. and Werle, P. 2008. Influence of clouds on the spectral actinic flux density in the lower troposphere (INSPECTRO): Overview of the field campaigns. Atmos. Chem. Phys., **8**, 1789-1812.

Tilgner, A., Wolke, R. and Herrmann, H. 2008. *CAPRAM modelling of aqueous aerosol and cloud chemistry*. I. Barnes and M. Kharytonov (Ed.), In: *Simulation and assessment of chemical processes in a multiphase environment : Proceedings of the NATO Advanced Research Workshop on Simulation and Assessment of Chemical Processes in a Multiphase Environment Alushta, Ukraine 1 September 2007*. Springer, Berlin, Heidelberg, New York, p. xxv, 540. (NATO Science for Peace and Security Series C: Environmental Security)

Todd, M. C., Karam, D. B., Cavazos, C., Bouet, C., Heinold, B., Baldasano, J. M., Cautenet, G., Koren, I., Perez, C., Solmon, F., Tegen, I., Tulet, P., Washington, R. and Zakey, A. 2008. Quantifying uncertainty in estimates of mineral dust flux: An inter-comparison of model performance over the Bodélé Depression, Northern Chad. J. Geophys. Res. - Atmosp., **113**, D24107, doi:10.1029/2008JD010476.

Wehner, B., Birmili, W., Ditas, F., Wu, Z., Hu, M., Liu, X., Mao, J., Sugimoto, N. and Wiedensohler, A. 2008. Relationships between submicrometer particulate air pollution and air mass history in Beijing, China. Atmos. Chem. Phys., **8**, 6155-6168.

Wendisch, M., Hellmuth, O., Ansmann, A., Heintzenberg, J., Engelmann, R., Althausen, D., Eichler, H., Müller, D., Hu, M., Zhang, Y. and Mao, J. 2008. Radiative and dynamic effects of absorbing aerosol particles over the Pearl River Delta, China. Atmos. Environ., **42**, 6405-6416.

Wex, H., Stratmann, F., Hennig, T., Hartmann, S., Niedermeier, D., Nilsson, E., Ocskay, R., Rose, D., Salma, I. and Ziese, M. 2008. Connecting hygroscopic growth at high humidities to cloud activation for different particle types. Environ. Res. Lett., **3**, doi:10.1088/1748-9326/3/3/035004.

Wex, H., Stratmann, F., Topping, D. and McFiggans, G. 2008. The Kelvin versus the Raoult term in the Köhler equation. J. Atmos. Sci., **65**, 4004-4016, doi:4010.1175/2008JAS2720.4001.

Wisthaler, A., Apel, E. C., Bossmeyer, J., Hansel, A., Junkermann, W., Koppmann, R., Meier, R., Müller, K., Solomon, S. J., Steinbrecher, R., Tillmann, R. and Brauers, T. 2008. Technical Note: Intercomparison of formaldehyde measurements at the atmosphere simulation chamber SAPHIR. Atmos. Chem. Phys., **8**, 2189-2200.

Wolke, R., Hinneburg, D., Schröder, W. and Renner, E. 2008. *Numerical treatment of urban and regional scale interactions in chemistry-transport modelling*. C. Borrego and A. I. Miranda (Ed.), In: *Air pollution modeling and its application XIX : Proceedings of the 29th NATO/CCMS International Technical Meeting on Air Pollution and Its Application (Aveiro, Portugal, 24-28 September 2007)*. Springer, Dordrecht, p. 90-97. (NATO Science for Peace and Security Series - C : Environmental Security)

Wu, Z., Hu, M., Pen, L., Liu, S., Wehner, B. and Wiedensohler, A. 2008. Particle number size distribution in the urban atmosphere in Beijing, China. Atmos. Environ., **42**, 7967-7980.

Zhang, Y. H., Hu, M., Liu, S. C. and Wiedensohler, A. 2008. The special issue on PRIDE-PRD2004 Campaign (Editorial). Atmos. Environ., **42**, 6155-6156.

Zhang, Y. H., Hu, M., Zhong, L. J., Wiedensohler, A., Liu, S. C., Andreae, M. O., Wang, W. and Fan, S. J. 2008. Regional integrated experiments on air quality over Pearl River Delta 2004 (PRIDE-PRD2004): Overview. Atmos. Environ., **42**, 6157-6173.

Ziese, M., Wex, H., Nilsson, E. D., Salma, I., Ocskay, R., Hennig, T., Massling, A. and Stratmann, F. 2008. Hygroscopic growth and activation of HULIS particles: Experimental data and a new iterative parameterization scheme for complex aerosol particles. Atmos. Chem. Phys., **8**, 1855-1866.

2009

Achtert, P., Birmili, W., Nowak, A., Wehner, B., Wiedensohler, A., Takegawa, N., Kondo, Y., Miyazaki, Y., Hu, M. and Zhu, T. 2009. Hygroscopic growth of tropospheric particle number size distributions over the North China Plain. J. Geophys. Res. - Atmosp., **114**, D00G07, doi:10.1029/2008JD010921.

Althausen, D., Engelmann, R., Baars, H., Heese, B., Ansmann, A., Müller, D. and Komppula, M. 2009. Portable Raman Lidar Polly(XT) for automated profiling of aerosol backscatter, extinction, and depolarization. J. Atmos. Ocean. Tech., **26**, 2366-2378.

Ansmann, A., Baars, H., Tesche, M., Müller, D., Althausen, D., Engelmann, R., Pauliquevis, T. and Artaxo, P. 2009. Dust and smoke transport from Africa to South America: Lidar profiling over Cape Verde and the Amazon rainforest. Geophys. Res. Lett., **36**, L11802.

Ansmann, A., Tesche, M., Knippertz, P., Bierwirth, E., Althausen, D., Müller, D. and Schulz, O. 2009. Vertical profiling of convective dust plumes in Southern Morocco during SAMUM. Tellus B, **61**, 340-353.

Ansmann, A., Tesche, M., Seifert, P., Althausen, D., Engelmann, R., Fruntke, J., Wandinger, U., Mattis, I. and Müller, D. 2009. Evolution of the ice phase in tropical altocumulus: SAMUM lidar observations over Cape Verde. J. Geophys. Res. - Atmosp., **114**, D17208, doi:10.1029/2008JD011659.

Balis, D., Giannakaki, E., Müller, D., Amiridis, V., Kelektsoglou, K., Rapsomanikis, S. and Bais, A. 2009. Estimation of the microphysical aerosol properties over Thessaloniki, Greece, during the SCOUT-O3 campaign with the synergy of Raman lidar and sunphotometer data. J. Geophys. Res. - Atmosp., doi:10.1029/2009JD013088, in press.

Beiner, K., Plewka, A., Haferkorn, S., Iinuma, Y., Engewald, W. and Herrmann, H. 2009. Quantification of organic acids in particulate matter by coupling of thermally assisted hydrolysis and methylation with thermodesorption-gas chromatography-mass spectrometry. J. Chromatogr. A, **1216**, 6642-6650.

Berndt, T. and Bräsel, S. 2009. Epoxidation of a series of C_2-C_6 olefins in the gas phase. Chem. Eng. Technol., **32**, 1189-1194.

Bierwirth, E., Wendisch, M., Ehrlich, A., Heese, B., Tesche, M., Althausen, D., Schladitz, A., Müller, D., Otto, S., Trautmann, T., Dinter, T., von Hoyningen-Huene, W. and Kahn, R. 2009. Spectral surface albedo over Morocco and its impact on radiative forcing of Saharan dust. Tellus B, **61**, 252-269.

Birmili, W., Alaviippola, B., Hinneburg, D., Knoth, O., Tuch, T., Borken-Kleefeld, J. and Schacht, A. 2009. Dispersion of traffic-related exhaust particles near the Berlin urban motorway: Estimation of fleet emission factors. Atmos. Chem. Phys., **9**, 2355-2374.

Birmili, W., Ries, L., Sohmer, R., Anastou, A., Sonntag, A., König, K. and Levin, I. 2009. Feine und ultrafeine Aerosolpartikel an der GAW-Station Schneefernerhaus/Zugspitze. Gefahrst. Reinhalt. L., **69**, 31-35.

Birmili, W., Schwirn, K., Nowak, A., Petäjä, T., Joutsensaari, J., Rose, D., Wiedensohler, A., Hämeri, K., Aalto, P., Kulmala, M. and Boy, M. 2009. Measurements of humified particle number size distributions in a Finnish boreal forest: Derivation of hygroscopic particle growth factors. Boreal Environ. Res., **14**, 458-480.

Birmili, W., Weinhold, K., Nordmann, S., Wiedensohler, A., Spindler, G., Müller, K., Herrmann, H., Gnauk, T., Pitz, M., Cyrys, J., Flentje, H., Nickel, C., Kuhlbusch, T. A. J., Löschau, G., Haase, D., Meinhardt, F., Schwerin, A., Ries, L. and Wirtz, K. 2009. Atmospheric aerosol measurements in the German Ultrafine Aerosol Network (GUAN) - Part 1: Soot and particle number size distributions. Gefahrst. Reinhalt. L., **69**, 137-145.

Bond, T. C., Covert, D. S. and Müller, T. 2009. Truncation and angular-scattering corrections for absorbing aerosol in the TSI 3563 Nephelometer. Aerosol Sci. Technol., **43**, 866-871.

Brüggemann, E., Gerwig, H., Gnauk, T., Müller, K. and Herrmann, H. 2009. Influence of seasons, air mass origin and day of the week on size-segregated chemical composition of aerosol particles at a kerbside. Atmos. Environ., **43**, 2456-2463.

Cavazos, C., Todd, M. C. and Schepanski, K. 2009. Numerical model simulation of the Saharan dust event of 6-11 March 2006 using the Regional Climate Model version 3 (RegCM3). J. Geophys. Res. - Atmosp., **114**, D12109, doi:10.1029/2008JD011078.

Cheng, Y. F., Berghof, M., Garland, R. M., Wiedensohler, A., Müller, T., Wehner, B., Su, H., Achtert, P., Nowak, A., Pöschl, U., Zhang, Y. H., Zhu, T., Hu, M. and Zeng, L. M. 2009. Influence of soot mixing state on aerosol light absorption and single scattering albedo during air mass aging at a polluted regional site in North-Eastern China. J. Geophys. Res. - Atmosp., **114**, D00G10, doi:10.1029/2008JD010883.

Chuang, P. Y., Feingold, G., Ayers, G., Charlson, R. J., Cotton, W. R., Kreidenweis, S. M., Levin, Z., Nakajima, T., Rosenfeld, D., Schulz, M. and Siebert, H. 2009. *The extent and nature of anthropogenic perturbations of clouds*. J. Heintzenberg and R. J. Charlson (Ed.), In: *Clouds in the perturbed climate system : Their relationship to energy balance, atmospheric dynamics, and precipitation*. MIT Press, Cambridge, MA, USA, p. 433-449 (Chapter 18).

Claeys, M., Iinuma, Y., Szmigielski, R., Surratt, J. D., Blockhuys, F., Van Alsenoy, C., Böge, O., Sierau, B., Gomez-Gonzalez, Y., Vermeylen, R., Van der Veken, P., Shahgholi, M., Chan, A. W. H., Herrmann, H., Seinfeld, J. H. and Maenhaut, W. 2009. Terpenylic acid and related compounds from the oxidation of alpha-Pinene: Implications for new particle formation and growth above forests. Environ. Sci. Technol., **43**, 4976-6982.

Costabile, F., Birmili, W., Klose, S., Tuch, T., Wehner, B., Wiedensohler, A., Franck, U., König, K. and Sonntag, A. 2009. Spatio-temporal variability and principal components of the particle number size distribution in an urban atmosphere. Atmos. Chem. Phys., **9**, 3163-3195.

Cziczo, D. J., Stetzer, O., Worringen, A., Ebert, M., Kamphus, M., Curtius, J., Mertes, S., Möhler, O. and Lohmann, U. 2009. Inadvertent climate modification due to anthropogenic lead. Nat. Geosci., **2**, 333-336, doi:10.1038/ngeo499.

Dinter, T., von Hoyningen-Huene, W., Burrows, J. P., Kokhanovsky, A., Bierwirth, E., Wendisch, M., Müller, D., Kahn, R. and Diouri, M. 2009. Retrieval of aerosol optical thickness for desert conditions using MERIS observations during the SAMUM campaign. Tellus B, **61**, 229-238.

Esselborn, M., Wirth, M., Fix, A., Weinzierl, B., Rasp, K., Tesche, M. and Petzold, A. 2009. Spatial distribution and optical properties of Saharan dust observed by airborne high spectral resolution lidar during SAMUM 2006. Tellus B, **61**, 131-143.

Feingold, G. and Siebert, H. 2009. *Cloud-aerosol interactions from the micro to the cloud scale*. J. Heintzenberg and R. J. Charlson (Ed.), In: *Clouds in the perturbed climate system : Their relationship to energy balance, atmospheric dynamics, and precipitation*. MIT Press, Cambridge, MA, USA, p. 319-338 (Chapter 14).

Freudenthaler, V., Esselborn, M., Wiegner, M., Heese, B., Tesche, M., Ansmann, A., Müller, D., Althausen, D., Wirth, M., Fix, A., Ehret, G., Knippertz, P., Toledano, C., Gasteiger, J., Garhammer, M. and Seefeldner, M. 2009. Depolarization ratio profiling at several wavelengths in pure Saharan dust during SAMUM 2006. Tellus B, **61**, 165-179.

Garland, R. M., Schmid, O., Nowak, A., Achtert, P., Wiedensohler, A., Gunthe, S. S., Takegawa, N., Kita, K., Kondo, Y., Hu, M., Shao, M., Zeng, L. M., Zhu, T., Andreae, M. O. and Pöschl, U. 2009. Aerosol optical properties observed during Campaign of Air Quality Research in Beijing 2006 (CAREBeijing-2006): Characteristic differences between the inflow and outflow of Beijing city air. J. Geophys. Res. - Atmosp., **114**, D00G04, doi:10.1029/2008JD010780.

Gioda, A., Mayol-Bracero, O. L., Morales-Garcia, F., Collett, J., Decesari, S., Emblico, L., Facchini, M. C., Morales-De Jesus, R. J., Mertes, S., Borrmann, S., Walter, S. and Schneider, J. 2009. Chemical composition of cloud water in the Puerto Rican tropical trade wind cumuli. Water Air Soil Poll., **200**, 3-14 (doi:10.1007/s11270-008-9888-4).

Gligorovski, S., Rousse, D., George, C. H. and Herrmann, H. 2009. Rate constants for the OH reactions with oxygenated organic compounds in aqueous solution. Int. J. Chem. Kinet., **41**, 309-326 (doi:10.1002/kin.20405).

Hallquist, M., Wenger, J. C., Baltensperger, U., Rudich, Y., Simpson, D., Claeys, M., Dommen, J., Donahue, N. M., George, C., Goldstein, A. H., Hamilton, J. F., Herrmann, H., Hoffmann, T., Iinuma, Y., Jang, M., Jenkin, M. E., Jimenez, J. L., Kiendler-Scharr, A., Maenhaut, W., McFiggans, G., Mentel, T. F., Monod, A., Prevot, A. S. H., Seinfeld, J. H., Surratt, J. D., Szmigielski, R. and Wildt, J. 2009. The formation, properties and impact of secondary organic aerosol: Current and emerging issues. Atmos. Chem. Phys., **9**, 5155-5236.

Haustein, K., Perez, C., Baldasano, J. M., Müller, D., Tesche, M., Schladitz, A., Esselborn, M., Weinzierl, B., Kandler, K. and von Hoyningen-Huene, W. 2009. Regional dust model performance during SAMUM 2006. Geophys. Res. Lett., **36**, L03812.

Heese, B., Althausen, D., Dinter, T., Esselborn, M., Müller, T., Tesche, M. and Wiegner, M. 2009. Vertically resolved dust optical properties during SAMUM: Tinfou compared to Ouarzazate. Tellus B, **61**, 195-205.

Heinold, B., Tegen, I., Esselborn, M., Kandler, K., Knippertz, P., Müller, D., Schladitz, A., Tesche, M., Weinzierl, B., Ansmann, A., Althausen, D., Laurent, B., Massling, A., Müller, T., Petzold, A., Schepanski, K. and Wiedensohler, A. 2009. Regional Saharan dust modelling during the SAMUM 2006 campaign. Tellus B, **61**, 307-324.

Heintzenberg, J. 2009. The SAMUM-1 experiment over Southern Morocco: Overview and introduction. Tellus B, **61**, 2-11.

Heintzenberg, J. and Charlson, R. J. (Eds.) (2009), Clouds in the perturbed climate system : Their relationship to energy balance, atmospheric dynamics, and precipitation, 576 pp., 40 color illus., 71 black & white illus. pp., MIT Press, Cambridge, MA, USA.

Heintzenberg, J. and Charlson, R. J. 2009. *Introduction*. J. Heintzenberg and R. J. Charlson (Ed.), In: *Clouds in the perturbed climate system : Their relationship to energy balance, atmospheric dynamics, and precipitation*. MIT Press, Cambridge, MA, USA, p. 1-15 (Chapter 1).

Hellmuth, O., Schmelzer, J. W. P., Shchekin, A. K. and Abyzov, A. S. 2009. *Atmospheric new particle formation by heterogeneous nucleation revisited: Comments on phenomenology and genesis*. J. W. P. Schmelzer, G. Röpke, and V. B. Priezzhev (Ed.), In: *Nucleation theory and applications*. JINR, Dubna, p. 399-454.

Hinneburg, D., Renner, E. and Wolke, R. 2009. Formation of secondary inorganic aerosols by power plant emissions exhausted through cooling towers in Saxony. Environ. Sci. Pollut. Res., **16**, 25-35 (doi:10.1007/s11356-008-0081-5).

Hoffmann, D., Tilgner, A., Iinuma, Y. and Herrmann, H. 2009. Atmospheric stability of levoglucosan: A detailed laboratory and modeling study. Environ. Sci. Technol., doi: 10.1021/es902476f, in press.

Hoffmann, D., Weigert, B., Barzaghi, P. and Herrmann, H. 2009. Reactivity of poly-alcohols towards OH, NO_3 and SO_4- in aqueous solution. Phys. Chem. Chem. Phys., **11**, 9351-9363.

Iinuma, Y., Böge, O., Kahnt, A. and Herrmann, H. 2009. Laboratory chamber studies on the formation of organosulfates from reactive uptake of monoterpene oxides. Phys. Chem. Chem. Phys., **11**, 7985-7997.

Iinuma, Y., Böge, O., Keywood, M., Gnauk, T. and Herrmann, H. 2009. Diaterebic acid acetate and diaterpenylic acid acetate: Atmosperic tracers for secondary organic aerosol formation from 1,8-Cineole oxidation. Environ. Sci. Technol., **43**, 280-285.

Iinuma, Y., Engling, G., Puxbaum, H. and Herrmann, H. 2009. A highly resolved anion-exchange chromatographic method for determination of saccharidic tracers for biomass combustion and primary bio-particles in atmospheric aerosol. Atmos. Environ., **43**, 1367-1371.

Jaatinen, A., Hamed, A., Joutsensaari, J., Mikkonen, S., Birmili, W., Wehner, B., Spindler, G., Wiedensohler, A., Decesari, S., Mircea, M., Facchini, M. C., Junninen, H., Kulmala, M., Lehtinen, K. E. J. and Laaksonen, A. 2009. A comparison of new particle formation events in the boundary layer at three different sites in Europe. Boreal Environ. Res., **14**, 481-498.

Jebens, S., Knoth, O. and Weiner, R. 2009. Explicit two-step peer methods for the compressible Euler equations. Mon. Wea. Rev., **137**, 2380-2392 (doi:10.1175/2008MWR2671.1).

Jumelet, J., Bekki, S., Seifert, P., Montoux, N., Vernier, J. P. and Pelon, J. 2009. Microphysical modeling of a midlatitude "polar stratospheric cloud" event: Comparisons against multiwavelength ground-based and spaceborne lidar data. Journal of Geophysical Research-Atmospheres, **114**, D00H03.

Juranyi, Z., Gysel, M., Duplissy, J., Weingartner, E., Tritscher, T., Dommen, J., Henning, S., Ziese, M., Kiselev, A., Stratmann, F., George, I. and Baltensperger, U. 2009. Influence of gas-to-particle partitioning on the hygroscopic and droplet activation behaviour of alpha-pinene secondary organic aerosol. Phys. Chem. Chem. Phys., **11**, 8091-8097.

Kaaden, N., Massling, A., Schladitz, A., Müller, T., Kandler, K., Schütz, L., Weinzierl, B., Petzold, A., Tesche, M., Leinert, S. and Wiedensohler, A. 2009. State of mixing, shape factor, number size distribution, and hygroscopic growth of the Saharan anthropogenic and mineral dust aerosol at Tinfou, Morocco. Tellus B, **61**, 51-63.

Kahn, R., Petzold, A., Wendisch, M., Bierwirth, E., Dinter, T., Esselborn, M., Fiebig, M., Heese, B., Knippertz, P., Müller, D., Schladitz, A. and von Hoyningen-Huene, W. 2009. Desert dust aerosol air mass mapping in the Western Sahara, using particle properties derived from space-based multi-range imaging. Tellus B, **61**, 239-251.

Kandler, K., Schütz, L., Deutscher, C., Ebert, M., Hofmann, H., Jäckel, S., Jaenicke, R., Knippertz, P., Lieke, K., Massling, A., Petzold, A., Schladitz, A., Weinzierl, B., Wiedensohler, A., Zorn, S. and Weinbruch, S. 2009. Size distribution, mass concentration, chemical and mineralogical composition, and derived optical parameters of the boundary layer aerosol at Tinfou, Morocco, during SAMUM 2006. Tellus B, **61**, 32-50.

Klüser, L. and Schepanski, K. 2009. Remote sensing of mineral dust over land with MSG infrad channels: A new bitemporal mineral dust index. Remote Sens. Environ., **113**, 1853-1867, RSE-07418, doi:10.1016/j.rse.2009.04.012.

Knippertz, P., Ansmann, A., Althausen, D., Müller, D., Tesche, M., Bierwirth, E., Dinter, T., Müller, T., Hoyningen-Huene, W. v., Schepanski, K., Wendisch, M., Heinold, B., Kandler, K., Petzold, A., Schütz, L. and Tegen, I. 2009. Dust mobilization and transport in the Northern Sahara during SAMUM 2006 - A meteorological overview. Tellus B, **61**, 12-31.

Köppe, M., Hermann, M., Brenninkmeijer, C. A. M., Heintzenberg, J., Schlager, H., Schuck, T., Slemr, F., Sprung, D., van Velthoven, P. F. J., Wiedensohler, A., Zahn, A. and Ziereis, H. 2009. Origin of aerosol particles in the mid-latitude and subtropical upper troposphere and lowermost stratosphere from cluster analysis of CARIBIC data. Atmos. Chem. Phys., **9**, 8413-8430.

Kulmala, M., Asmi, A., Lappalainen, H. K., Carslaw, K. S., Pöschl, U., Baltensperger, U., Hov, O., Brenguier, J. L., Pandis, S. N., Facchini, M. C., Hansson, H. C., Wiedensohler, A. and O'Dowd, C. D. 2009. Introduction: European Integrated Project on Aerosol Cloud Climate and Air Quality interactions (EUCAARI) - integrating aerosol research from nano to global scales (vol 9, pg 2825, 2009). Atmos. Chem. Phys., **9**, 3443-3444.

Kulmala, M., Asmi, A., Lappalainen, H. K., Carslaw, K. S., Pöschl, U., Baltensperger, U., Hov, O., Brenquier, J. L., Pandis, S. N., Facchini, M. C., Hansson, H. C., Wiedensohler, A. and O'Dowd, C. D. 2009. Introduction: European Integrated Project on Aerosol Cloud Climate and Air Quality interactions (EUCAARI) - integrating aerosol research from nano to global scales. Atmos. Chem. Phys., **9**, 2825-2841.

Kurtén, T., Berndt, T. and Stratmann, F. 2009. Hydration increases the lifetime of HSO_5 and enhances its ability to act as a nucleation precursor - A computational study. Atmos. Chem. Phys., **9**, 3357-3369.

Laj, P., Klausen, J., Bilde, M., Plass-Dülmer, C., Pappalardo, G., Cierbaux, C., Baltensperger, U., Hjorth, J., Simpson, D., Reimann, S., Coheur, P.-F., Richter, A., De Maziere, M., Rudich, Y., McFiggans, G., Torseth, K., Wiedensohler, A., Morin, S., Schulz, M., Allan, J., Attie, J.-L., Barnes, I., Birmili, W., Cammas, P., Dommen, J., Dorn, H.-P., Fowler, D., Fuzzi, J.-S., Glasius, M., Granier, C., Hermann, M., Isaksen, I., Kinne, S., Koren, I., Madonna, F., Maione, M., Massling, A., Möhler, O., Mona, L., Monks, P., Müller, D., Müller, T., Orphal, J., Peuch, V.-H., Stratmann, F., Tanre, D., Tyndall, G., Riziq, A. A., Van Roozendael, M., Villani, P., Wehner, B., Wex, H. and Zardini, A. A. 2009. Measuring atmospheric composition change. Atmos. Environ., **43**, 5351-5414.

Laurent, B., Marticorena, B., Bergametti, G., Tegen, I., Schepanski, K. and Heinold, B. 2009. Modelling mineral dust emissions. IOP Conf. Ser.: Earth Environ. Sci., **7**, 012006, doi:10.1088/1755-1307/7/1/012006 (10 pp).

Lehmann, K., Siebert, H. and Shaw, R. A. 2009. Homogeneous and inhomogeneous mixing in cumulus clouds: Dependence on local turbulence structure. J. Atmos. Sci., **66**, 3641-3659.

Liu, S., Hu, M., Slanina, S., He, L.-Y., Niu, Y.-W., Brüggemann, E., Gnauk, T. and Herrmann, H. 2009. Size distribution and source analysis of ionic compositions of aerosols in polluted periods at Xinken in Pearl River Delta (PRD) of China. Atmos. Environ., **42**, 6284-6295.

Martet, M., Peuch, V. H., Laurent, B., Marticorena, B. and Bergametti, G. 2009. Evaluation of long-range transport and deposition of desert dust with the CTM MOCAGE. Tellus B, **61**, 449-463.

Martinsson, B. G., Brenninkmeijer, C. A. M., Carn, S. A., Hermann, M., Heue, K.-P., van Velthoven, P. F. J. and Zahn, A. 2009. Influence of the 2008 Kasatochi volcanic eruption on sulfurous and carbonaceous aerosol constituents in the lower stratosphere. Geophys. Res. Lett., **36**, L12813, doi:10.1029/2009GL038735.

Massling, A., Stock, M., Tuch, T., Wehner, B., Wu, Z. and Hu, M. 2009. Size-segregated determination of differently hygroscopic paticle fractions and soluble volume size distributions of the urban submicrometer Beijing aerosol. Atmos. Environ., **43**, 1589-1590.

Massling, A., Stock, M., Wehner, B., Wu, Z., Hu, M., Brüggemann, E., Gnauk, T., Herrmann, H. and Wiedensohler, A. 2009. Size segregated water uptake and total soluble volume of the urban submicrometer aerosol in Beijing. Atmos. Environ., **43**, 1578-1589.

Mattis, I., Tesche, M., Grein, M., Freudenthaler, V. and Müller, D. 2009. Systematic error of lidar profiles caused by a polarization-dependent receiver transmission: Quantification and error correction scheme. Appl. Optics, **48**, 2742-2751.

Meier, J., Wehner, B., Massling, A., Birmili, W., Nowak, A., Gnauk, T., Brüggemann, E., Herrmann, H., Min, H. and Wiedensohler, A. 2009. Hygroscopic growth of urban aerosol particles in Beijing (China) during wintertime: A comparison of three experimental methods. Atmos. Chem. Phys., **9**, 6865-6880.

Mildenberger, K., Beiderwieden, E., Hsia, Y. J. and Klemm, O. 2009. CO2 and water vapor fluxes above a subtropical mountain cloud forest-The effect of light conditions and fog. Agric. For. Meteor., **149**, 1730-1736.

Müller, C., Iinuma, Y., Karstensen, J., van Pinxteren, D., Lehmann, S., Gnauk, T. and Herrmann, H. 2009. Seasonal variation of aliphatic amines in marine sub-micrometer particles at the Cape Verde Islands. Atmos. Chem. Phys., **9**, 9587-9897.

Müller, D., Ansmann, A., Freudenthaler, V., Kandler, K., Toledano, C., Hiebsch, A., Gasteiger, G., Esselborn, M., Tesche, M., Heese, B., Althausen, D., Weinzierl, B., Petzold, A. and von Hoyningen-Huene, W. 2009. Mineral dust observed with AERONET sun photometer, Raman lidar, and in-situ instruments during SAMUM 2006: Shape-dependent particle properties. J. Geophys. Res. - Atmosp., doi:10.1029/2009JD012523, in press.

Müller, D., Heinold, B., Tesche, M., Tegen, I., Althausen, D., Alados Arboledas, L., Amiridis, V., Amodeo, A., Ansmann, A., Balis, D., Comeron, A., D´Amico, G., Gerasopoulos, E., Guerrero-Rascado, J. L., Freudenthaler, V., Giannakaki, E., Heese, B., Iarlori, M., Knippertz, P., Mamouri, R. E., Mona, L., Papayannis, A., Pappalardo, G., Perrone, R.-M., Pisani, G., Rizi, V., Sicard, M., Spinelli, N., Tafuro, A. and Wiegner, M. 2009. EARLINET observations of the 14-22-May longe-range dust transport event during SAMUM 2006: Validation of results from dust transport modelling. Tellus B, **61**, 325-339.

Müller, D., Weinzierl, B., Petzold, A., Kandler, K., Ansmann, A., Müller, T., Tesche, M., Freudenthaler, V., Esselborn, M., Heese, B., Althausen, D., Schladitz, A., Otto, S. and Knippertz, P. 2009. Mineral dust observed with AERONET sun photometer, Raman lidar, and in situ instruments during SAMUM 2006: Shape-independent particle properties. J. Geophys. Res. - Atmosp., doi:10.1029/2009JD012520, in press.

Müller, T., Nowak, A., Wiedensohler, A., Sheridan, P., Laborde, M., Covert, D. S., Marinoni, A., Imre, K., Henzing, B., Roger, J. C., dos Santos, S. M., Wilhelm, R., Wang, Y. Q. and de Leeuw, G. 2009. Angular illumination and truncation of three different integrating nephelometers: Implications for empirical, size-based corrections. Aerosol Sci. Technol., **43**, 581-586.

Müller, T., Schladitz, A., Massling, A., Kaaden, N., Wiedensohler, A. and Kandler, K. 2009. Spectral absorption coefficients and imaginary parts of refractive indices of Saharan dust during SAMUM-1. Tellus B, **61**, 79-95.

Naoe, H., Hasegawa, S., Heintzenberg, J., Okada, K., Uchiyama, A., Zaizen, Y., Kobayashi, E. and Yamazaki, A. 2009. State of mixture of atmospheric submicrometer black carbon particles and its effect on particulate light absorption. Atmos. Environ., **43**, 1296-1301.

Nordmann, S., Birmili, W., Weinhold, K., Wiedensohler, A., Mertes, S., Müller, K., Gnauk, T., Herrmann, H., Pitz, M., Cyrys, J., Flentje, H., Ries, L. and Wirtz, K. 2009. Atmospheric aerosol measurements in the German Ultrafine Aerosol Network (GUAN) - Part 2: Comparison of measurements techniques for graphitic, light-absorbing, and elemental carbon, and the non-volatile particle volume under field conditions. Gefahrst. Reinhalt. L., **69**,

Otto, S., Bierwirth, E., Weinzierl, B., Kandler, K., Esselborn, M., Tesche, M., Schladitz, A., Wendisch, M. and Trautmann, T. 2009. Solar radiative effects of a Saharan dust plume observed during SAMUM assuming spheroidal model particles. Tellus B, **61**, 270-296.

Paasonen, P., Sihto, S.-L., Nieminen, T., Vuollekoski, H., Riipinen, I., Plass-Dülmer, C., Berresheim, H., Birmili, W. and Kulmala, M. 2009. Connection between new particle formation and sulphuric acid at Hohenpeissenberg (Germany) including the influence of organic compounds. Boreal Environ. Res., **14**, 616-629.

Papayannis, A., Amiridis, V., Mona, L., Mamouri, R. E., Apituley, A., Alados-Arboledas, L., Balis, D., Chaikovski, A., De Tomasi, F., Grigorov, I., Gustafsson, O., Linnè, H., Mattis, I., Mitev, V., Molero, F., Müller, D., Nicolae , D., Pérez, C., Pietruczuk, A., Putaud, J. P., Ravetta, F., Rizi, V., Schnell, F., Sicard, M., Simeonov, V., Stebel, K., Trickl, T., D´Amico, G., Pappalardo, G. and Wang, X. 2009. Coordinated lidar observations of Saharan dust over Europe in the frame of EARLINET-ASOS project during CALIPSO overpasses: A strong dust case study analysis with modeling support. Proc. SPIE, **7479**, 74790C (10 pp).

Pappalardo, G., Mona, L., Wandinger, U., Mattis, I., Amodeo, A., Ansmann, A., Apituley, A., Alados-Arboledas, L., Balis, D., Chaikovsky, A., Comeron, A., D´Amico, G., Freudenthaler, V., Giunta, A., Grigorov, I., Hiebsch, A., Linnè, H., Madonna, F., Papayannis, A., Perrone, M. R., Pietruczuk, A., Pujadas, M., Rizi, V., Spinelli, N. and Wiegner, M. 2009. Analysis of the EARLINET correlative measurements for CALIPSO. Proc. SPIE, **7479**, 74790B (10 pp).

Pappalardo, G., Papayannis, A., Bösenberg, J., Ansmann, A., Apituley, A., Alados Arboledas, L., Balis, D., Böckmann, C., Chaikovsky, A., Comeron, A., Gustafsson, O., Hansen, G., Mitev, V., Mona, L., Nicolae , D., Perrone, M. R., Pietruczuk, A., Pujadas, M., Putaud, J.-P., Ravetta, F., Rizi, V., Simeonov, V., Spinelli, N., Stoyanov, D., Trickl, T. and Wiegner, M. 2009. EARLINET coordinated lidar observations of Saharan dust events on continental scale. IOP Conf. Ser.: Earth Environ. Sci., **7**, 012002, doi:10.1088/1755-1307/7/1/012002, (6 pp).

Pappalardo, G., Wandinger, U., Mona, L., Hiebsch, A., Mattis, I., Amodeo, A., Ansmann, A., Seifert, P., Linné, H., Apituley, A., Alados Arboledas, L., Balis, D., Chaikovsky, A., D´Amico, G., De Tomasi, F., Freudenthaler, V., Giannakaki, E., Giunta, A., Grigorov, I., Iarlori, M., Madonna, F., Mamouri, R.-E., Nasti, L., Papayannis, A., Pietruczuk, A., Pujadas, M., Rizi, V., Rocadenbosch, F., Russo, F., Schnell, F., Spinelli, N., Wang, X. and Wiegner, M. 2009. EARLINET correlative measurements for CALIPSO: First intercomparison results. J. Geophys. Res. - Atmosp., doi:10.1029/2009JD012147, in press.

Petters, M. D., Wex, H., Carrico, C. M., Hallbauer, E., Massling, A., McMeeking, G. R., Poulain, L., Wu, Z., Kreidenweis, S. M. and Stratmann, F. 2009. Towards closing the gap between hygroscopic growth and activation for secondary organic aerosol: Part 2: Theoretical approaches. Atmos. Chem. Phys., **9**, 3999-4009.

Philippin, S., Laj, P., Putaud, J.-P., Wiedensohler, A., Leeuw, G., Fjaeraa, A. M., Platt, U., Baltensperger, U. and Fiebig, M. 2009. EUSAAR – An unprecedented network of aerosol observations in Europe. Earozoru Kenkyu (Jap. J. Aerosol Res.), **24**, 78-83.

Reinfried, F., Tegen, I., Heinold, B., Hellmuth, O., Schepanski, K., Cubasch, U., Hübener, H. and Knippertz, P. 2009. Simulations of convectively-driven density currents in the Atlas Region using a reginal model: Impacts on dust emission and sensitivity to horizontal resolution and convection schemes. J. Geophys. Res. - Atmosp., **114**, D08127, doi:10.1029/2008JD010844.

Reutter, P., Su, H., Trentmann, J., Simmel, M., Rose, D., Gunthe, S. S., Wernli, H., Andreae, M. O. and Pöschl, U. 2009. Aerosol- and updraft-limited regimes of cloud droplet formation: Influence of particle number, size and hygroscopicity on the activation of cloud condensation nuclei (CCN). Atmos. Chem. Phys., **9**, 7067-7080.

Rusumdar, A. J., Abuthalib, A., Mohan, V. M., Kumar, C. S., Sujatha, V. and Prasad, P. R. 2009. Hydrodynamics and energy consumption studies in a three-phase liquid circulating three-phase fluid bed contactor. Exp. Therm. Fluid Sci., **33**, 791-796.

Salonen, M., Kurtén, T., Vehkamäki, H., Berndt, T. and Kulmala, L. 2009. Computational investigation of the possible role of some intermediate products of SO_2 oxidation in sulfuric acid-water nucleation. Atmos. Res., **91**, 47-52.

Schepanski, K., Tegen, I. and Macke, A. 2009. Saharan dust transport and deposition towards the tropical northern Atlantic. Atmos. Chem. Phys., **9**, 1173-1189.

Schepanski, K., Tegen, I., Todd, M. C., Heinold, B., Bönisch, G., Laurent, B. and Macke, A. 2009. Meteorological processes forcing Saharan dust emission inferred from MSG-SEVIRI observations of subdaily dust source activation and numerical models. J. Geophys. Res. - Atmosp., **114**, D10201, doi:10.1029/2008JD010325.

Schladitz, A., Müller, T., Massling, A., Kaaden, N., Kandler, K. and Wiedensohler, A. 2009. In situ measurements of optical properties at Tinfou (Morocco) during the Saharan Mineral Dust Experiment SAMUM 2006. Tellus B, **61**, 64-78.

Schlegel, M., Knoth, O., Arnold, M. and Wolke, R. 2009. Multirate Runge-Kutta schemes for advection equations. J. Comput. Appl. Math., **226**, 345-357.

Schmitt, B. A., Weiner, R. and Jebens, S. 2009. Parameter optimization for explicit parallel peer two-step methods. Appl. Numer. Math., **59**, 769-782.

Siebesma, A. P., Brenguier, J.-L., Bretherton, C. S., Grabowski, W. W., Heintzenberg, J., Kärcher, B., Lehmann, K., Petch, J. C., Spichtinger, P., Stevens, B. and Stratmann, F. 2009. *Cloud-controlling factors*. J. Heintzenberg and R. J. Charlson (Ed.), In: *Clouds in the perturbed climate system : Their relationship to energy balance, atmospheric dynamics, and precipitation*. MIT Press, Cambridge, MA, USA, p. 269-290 (Chapter 12).

Slemr, F., Ebinghaus, R., Brenninkmeijer, C. A. M., Hermann, M., Kock, H. H., Martinsson, B. G., Schuck, T., Sprung, D., van Velthoven, P., Zahn, A. and Ziereis, H. 2009. Gaseous mercury distribution in the upper troposphere and lower stratosphere observed onboard the CARIBIC passenger aircraft. Atmos. Chem. Phys., **9**, 1957-1969.

Spindler, G., Brüggemann, E., Gnauk, T., Müller, K. and Herrmann, H. 2009. A four-year size-segregated characterization study of particles PM10, PM2.5 and PM1 depending on air mass origin at Melpitz. Atmos. Environ., doi:10.1016/j.atmosenv.2009.10.015, in press.

Stratmann, F., Möhler, O., Shaw, R. and Wex, H. 2009. *Laboratory cloud simulation: Capabilities and future directions*. J. Heintzenberg and R. J. Charlson (Ed.), In: *Clouds in the perturbed climate system : Their relationship to energy balance, atmospheric dynamics, and precipitation*. MIT Press, Cambridge, MA, USA, p. 149-172 (Chapter 7).

Takegawa, N., Miyakawa, T., Kuwata, M., Kondo, Y., Zhao, Y., Han, S., Kita, K., Miyazaki, Y., Deng, Z., Xiao, R., Hu, M., van Pinxteren, D., Herrmann, H., Hofzumahaus, A., Holland, F., Wahner, A., Blake, D. R., Sugimoto, N. and Zhu, T. 2009. Variability of submicron aerosol observed at a rural site in Beijing in the summer of 2006. J. Geophys. Res. - Atmosp., **114**, D00G05, doi:10.1029/2008JD010857.

Takegawa, N., Miyakawa, T., Watanabe, M., Kondo, Y., Miyazaki, Y., Han, S., Zhao, Y., van Pinxteren, D., Brüggemann, E., Gnauk, T., Herrmann, H., Xiao, R., Deng, Z., Hu, M., Zhu, T. and Zhang, Y. 2009. Performance of an aerodyne aerosol mass spectrometer (AMS) during intensive campaigns in China in the summer of 2006. Aerosol Sci. Technol., **43**, 189-204.

Tegen, I. 2009. *Aerosol (Mineral)*. V. Gornitz (Ed.), In: *Encyclopedia of paleoclimatology and ancient environments*. Springer, Dordrecht, p. 1-2. (Encyclopedia of earth sciences series ; XXVIII)

Tegen, I. 2009. *Dust transport, quarternary*. V. Gornitz (Ed.), In: *Encyclopedia of paleoclimatology and ancient environments*. Springer, Dordrecht, p. 286-290. (Encyclopedia of earth sciences series ; XXVIII)

Tegen, I. and Schepanski, K. 2009. The global distribution of mineral dust. IOP Conf. Ser.: Earth Environ. Sci., **7**, 012001, doi:10.1088/1755-1307/7/1/012001, (6 pp).

Tesche, M., Ansmann, A., Müller, D., Althausen, D., Engelmann, R., Freudenthaler, V. and Groß, S. 2009. Vertically resolved separation of dust and smoke over Cape Verde by using multiwavelength Raman and polarization lidars during Saharan Mineral Dust Experiment 2008. J. Geophys. Res. - Atmosp., **114**, D13202, doi:10.1029/2009JD011862.

Tesche, M., Ansmann, A., Müller, D., Althausen, D., Mattis, I., Heese, B., Freudenthaler, V., Wiegner, M., Esselborn, M., Pisani, G. and Knippertz, P. 2009. Vertical profiling of Saharan dust with Raman lidar and airborne HSRL in Southern Morocco during SAMUM. Tellus B, **61**, 144-164.

Toledano, C., Wiegner, M., Garhammer, M., Seefeldner, M., Gasteiger, J., Müller, D. and Koepke, P. 2009. Spectral aerosol optical depth characterization of desert dust during SAMUM 2006. Tellus B, **61**, 216-228.

Tuch, T. M., Haudek, A., Müller, T., Nowak, A., Wex, H. and Wiedensohler, A. 2009. Design and performance of an automatic regenerating adsorption aerosol dryer for continuous operation at monitoring sites. Atmos. Meas. Tech. (AMT), **2**, 1-6.

van Pinxteren, D., Brüggemann, E., Gnauk, T., Iinuma, Y., Müller, K., Nowak, A., Achtert, P., Wiedensohler, A. and Herrmann, H. 2009. Size- and time-resolved chemical particle characterization during CAREBeijing-2006: Different pollution regimes and diurnal profiles. J. Geophys. Res. - Atmosp., **114**, D00G09, doi:10.1029/2008JD010890.

von Hoyningen-Huene, W., Dinter, T., Kokhanovsky, A. A., Burrows, J. P., Wendisch, M., Bierwirth, E., Müller, D. and Diouri, M. 2009. Measurements of desert dust optical characteristics at Porte au Sahara during SAMUM. Tellus B, **61**, 206-215.

Wagner, F., Bortoli, D., Pereira, S., Costa, M. J., Silva, A. M., Weinzierl, B., Esselborn, M., Petzold, A., Rasp, K., Heinold, B. and Tegen, I. 2009. Properties of dust aerosol particles transported to Portugal from the Sahara desert. Tellus B, **61**, 297-306.

Washington, R., Bouet, C., Cautenet, G., Mackenzie, E., Ashpole, I., Engelstaedter, S., Lizcano, G., Henderson, G., Schepanski, K. and Tegen, I. 2009. Dust as a tipping element: The Bodélé depression, Chad. Proc. Nat. Acad. Sci., doi:10.1073/pnas.0711850106.

Wehner, B., Berghof, M., Cheng, Y. F., Achtert, P., Birmili, W., Nowak, A., Wiedensohler, A., Garland, R. M., Pöschl, U., Hu, M. and Zhu, T. 2009. Mixing state of non-volatile aerosol particle fractions and comparison with light absorption in the polluted Beijing-region. J. Geophys. Res. - Atmosp., **114**, D00G17, doi:10.1029/2008JD010923.

Wehner, B., Uhrner, U., von Löwis, S., Zallinger, M. and Wiedensohler, A. 2009. Aerosol number size distributions within the exhaust plume of a diesel and a gasoline passenger car under on-road conditions and determination of emission factors. Atmos. Environ., **43**, 1235-1245.

Weigel, R., Hermann, M., Curtius, J., Voigt, C., Walter, S., Böttger, T., Lepukhov, B., Belyaev, G. and Borrmann, S. 2009. Experimental characterization of the condensation particle counting system for high altitude aircraft-borne application. Atmos. Meas. Tech. (AMT), **2**, 243-258.

Weigelt, A., Hermann, M., van Velthoven, P. F. J., Brenninkmeijer, C. A. M., Schlaf, G., Zahn, A. and Wiedensohler, A. 2009. Influence of clouds on aerosol particle number concentrations in the upper troposphere. J. Geophys. Res. - Atmosp., **114**, D01204, doi:10.1029/2008JD009805.

Weiner, R., Schmitt, B. A., Podhaisky, H. and Jebens, S. 2009. Superconvergent explicit two-step peer methods. J. Comput. Appl. Math., **223**, 753-764.

Wensch, J., Knoth, O. and Galant, A. 2009. Multirate infinitesimal step methods for atmospheric flow simulation. BIT Numer. Math., **49**, 449-473.

Wessels, A., Birmili, B., Hellack, B., Jermann, E., Wick, G., Albrecht, C., Harrison, R. and Schins, R. P. F. 2009. Electron paramagnetic resonance spectrometry as a tool to estimate the biological activity of size-fractionated atmospheric particles. N.-S. Arch. Pharmacol., **379**, 427.

Wex, H., Niedermeier, D. and Hartmann, S. 2009. FROST - FReezing Of duST. Geochim. Cosmochim. Acta, **73**, A1432-A1432.

Wex, H., Petters, M. D., Carrico, C. M., Hallbauer, E., Massling, A., McMeeking, G. R., Poulain, L., Wu, Z., Kreidenweis, S. M. and Stratmann, F. 2009. Towards closing the gap between hygroscopic growth and activation for secondary organic aerosol: Part 1: Evidence from measurements. Atmos. Chem. Phys., **9**, 3987-3997.

Wiedensohler, A., Cheng, Y. F., Nowak, A., Wehner, B., Achtert, P., Berghof, M., Birmili, W., Wu, Z. J., Hu, M., Zhu, T., Takegawa, N., Kita, K., Kondo, Y., Lou, S. R., Hofzumahaus, A., Holland, F., Wahner, A., Gunthe, S. S., Rose, D. and Pöschl, U. 2009. Rapid aerosol particle growth and increase of Cloud Condensation Nucleus (CCN) activity by secondary aerosol formation and condensation: A case study for regional air pollution in North-Eastern China. J. Geophys. Res. - Atmosp., **114**, D00G08, doi:10.1029/2008JD010884.

Wiegner, M., Gasteiger, J., Kandler, K., Weinzierl, B., Rasp, K., Esselborn, M., Freudenthaler, V., Heese, B., Toledano, C., Tesche, M. and Althausen, D. 2009. Numerical simulations of optical properties of Saharan dust aerosols with emphasis on lidar applications. Tellus B, **61**, 180-194.

Wu, Z. J., Cheng, Y. F., Hu, M., Wehner, B., Sugimoto, N. and Wiedensohler, A. 2009. Dust events in Beijing, China (2004-2006): Comparison of ground based measurements with columnar integrated observations. Atmos. Chem. Phys., **9**, 6915-6932.

Wu, Z. J., Poulain, L., Wehner, B., Wiedensohler, A. and Herrmann, H. 2009. Characterization of the volatile fraction of laboratory-generated aerosol particles by Thermodenuder-Aerosol Mass Spectrometer coupling experiments. J. Aerosol Sci., **40**, 603-612.

Yue, D. L., Hu, M., Wu, Z. J., Wang, Z., Guo, S., Wehner, B., Nowak, A., Achtert, P., Wiedensohler, A., Jung, J., Kim, Y. J. and Liu, S. C. 2009. Characteristics of aerosol size distributions and new particle formation in summer of mega-city Beijing, China. J. Geophys. Res. - Atmosp., **114**, doi:10.1029/2008JD010894, in press.

Zhu, T., Liu, S., Hu, M., Shao, M., Kondo, Y., Wahner, A., Wiedensohler, A., Pöschl, U., Li, X. and Tang, X. Y. 2009. Overview of 2006-CAREBEIJING: Campaigns of air quality research in Beijing and surrounding region. J. Geophys. Res. - Atmosp., **114**, Foreword.

Awards

Publication award of the Leibniz Institute for Tropospheric Research 2008

Berndt, T., et al. (2008), SO_2 oxidation products other than H_2SO_4 as a trigger of new particle formation. Part 1: Laboratory investigations, *Atmos. Chem. Phys.*, *8*, 6365-6374.

Publication award of the Leibniz Institute for Tropospheric Research 2009

Jebens, S., O. Knoth, and R. Weiner (2009), Explicit two-step peer methods for the compressible Euler equations, *Mon. Wea. Rev.*, *137*, 2380-2392 (doi:2310.1175/2008MWR2671.2381).

Cross-departmental publication award in 2009

van Pinxteren, D., E. Brüggemann, T. Gnauk, Y. Iinuma, K. Müller, A. Nowak, P. Achtert, A. Wiedensohler, and H. Herrmann (2009), Size- and time-resolved chemical particle characterization during CAREBeijing-2006: Different pollution regimes and diurnal profiles, *J. Geophys. Res. - Atmos.*, *114* (Campaigns of Air Quality Research in Beijing and Surrounding Region: 2006 (Special Issue CAREBeijing-2006)), D00G09, doi:10.1029/2008JD010890.

Birmili, W., B. Alaviippola, D. Hinneburg, O. Knoth, T. Tuch, J. Borken-Kleefeld, and A. Schacht (2009), Dispersion of traffic-related exhaust particles near the Berlin urban motorway: Estimation of fleet emission factors, *Atmos. Chem. Phys.*, *9*, 2355-2374.

University courses

Lecturer	Course	WS 2007/ 2008	SS 2008	WS 2008/ 2009	SS 2009	WS 2009/ 2010
Ansmann, A. Müller, D. Wandinger, U.	Active remote sensing (LIDAR) in environmental and atmospheric research and passive aerosol remote sensing		x		x	
Heintzenberg, J. Stratmann, F. Wiedensohler, A.	Atmospheric Aerosols I Lab	x		x		x[2)]
Heintzenberg, J. Tegen, I. Wiedensohler, A.	Atmospheric Aerosols II		x			
Heintzenberg, J. Dubois, R. Klugmann, D. Siebert, H. Spindler, G.	Modern Meteorological Instruments I		x			
Heintzenberg, J.	Modern Meteorological Instruments II	x		x		
Heintzenberg, J.	Frontlines of Atmospheric Research	x		x		
Heintzenberg, J.	Guest lecture: 125th public experimental lecture, topic: "Cloud research in Leipzig", University of Leipzig, Faculty of Physics and Earth Science			x		
Heintzenberg, J.	Guest lecture: "Atmospheric Chemistry and Radiation in the Atmosphere", Stockholm University, Department of Meteorology, Sweden			x		
Hellmuth, O.	Guest lecture: "Weather Prognosis (NWP)" within the series of lectures "Sources, Pathways and Receptors of Extreme Floods" (FLOODmaster Programme (Integrated Flood Risk, Management of Extreme Events)), Technische Universität Dresden		x		x	
Hermann, M.	Guest lecture: two lectures in the course of the EUFAR Summer School for Airborne Cloud and Aerosol Science, Utrecht, The Netherlands		x			
Herrmann, H.	Atmospheric Chemistry I Atmospheric Chemistry Seminar Atmospheric Chemistry Lab	x		x[1)]		x
Herrmann, H.	Atmospheric Chemistry II Practice Atmospheric Chemistry Seminar		x		x	
Kahnt, A.	Practices in general and anorganic chemistry			x		

Lecturer	Course	WS 2007/ 2008	SS 2008	WS 2008/ 2009	SS 2009	WS 2009/ 2010
Müller, D.	Guest lecture: bloc lecture “Remote Sensing Techniques and Data Analysis”, Universidad de Granada, Department of Applied Physics, Spain		x			
Müller, D.	Guest lecture: “Remote Sensing of Aerosols”, Gwangju Institute of Science and Technology, Department of Environmental Science and Engineering, Republic of Korea			x		
Renner, E. Knoth, O. Wolke, R. Hellmuth, O. Tegen, I. Grützun, V.	Mesoscale Meteorological Modeling/ Regional Climate Modeling		x		x	
Renner, E.	Modeling of Transport and Chemical Transformation of Air Pollutants	x		x		x
Tegen, I.	General Circulation G2					x[3)]
Wandinger, U.	Atmospheric Optics	x		x		
Ziemann, A. (University Leipzig) Heintzenberg, J. Herrmann, H.	Fundamentals of Cloud Physics	x				

[1)] Only “Atmospheric Chemistry Seminar”
[2)] Lecture was held by A. Wiedensohler and F. Stratmann
[3)] Lecture was held by I. Tegen (substitute for Prof. Metz, Leipzig Insitute of Meteorology)

Habilitation, Doctoral theses, Diploma, Master of Science and Bachelor of Science

Degree*)	Name	Title	Year	Faculty
Habil.	Tegen, I.	Soil dust aerosol and climate	2008	University of Leipzig, Faculty of Physics and Earth Science
Ph. D.	Grützun, V.	Influence of aerosol particles on deep convective clouds: Investigations with the new model LM-SPECS	2009	University of Leipzig, Faculty of Physics and Earth Science
Ph. D.	Heinold, B.	Regional modeling of Saharan dust in the framework of the SAMUM (SAharan Mineral dUst experiMent) field project	2008	University of Leipzig, Faculty of Physics and Earth Science
Ph. D.	Schepanski, K.	Characterising Saharan dust sources and export using remote sensing and regional modelling	2009	University of Kiel, Faculty of Mathematics and Natural Sciences
Ph. D.	Tilgner, A.	Modelling of the physico-chemical multiphase processing of tropospheric aerosols	2009	University of Leipzig, Faculty of Physics and Earth Science
Dipl.	Achtert, P.	Klassifizierung der hygroskopischen Wachstumsfaktoren von atmosphärischen Aerosolen in der nordchinesischen Tiefebene	2008	University of Leipzig, Faculty of Physics and Earth Science
Dipl.	Berghof, M.	Variation des Mischungszustandes nicht flüchtiger Aerosolbestandteile in stark verschmutzten Regionen in China	2008	University of Leipzig, Faculty of Physics and Earth Science
Dipl.	Bräuer, P.	Mechanismusentwicklung zur troposphärischen Halogenchemie	2009	University of Leipzig, Faculty of Physics and Earth Science
Dipl.	Ditas, F.	Aerosol number-size distributions inside and outside clouds: Characterisation of a new measurement system and first results	2009	University of Leipzig, Faculty of Physics and Earth Science
Dipl.	Fruntke, J.	Charakterisierung der Grenzschicht anhand von Vertikalwindmessungen mit einem Doppler-Lidar	2009	University of Leipzig, Faculty of Physics and Earth Science
Dipl.	Hartmann, S.	First experimental and theoretical studies concerning heterogeneous ice nucleation at the Leipzig Aerosol Cloud Interaction Simulator	2009	University of Leipzig, Faculty of Physics and Earth Science
Dipl.	Herold, C.	Wasserdampf- und Temperaturmessung mittels Lidar während COPS und SAMUM	2009	University of Leipzig, Faculty of Physics and Earth Science
Dipl.	Katzwinkel, J.	Investigation of the thermodynamics of deliquescence / efflorescence induced hysteresis in hygroscopic growth of soluble particles	2009	University of Leipzig, Faculty of Physics and Earth Science

Degree*)	Name	Title	Year	Faculty
Dipl.	Kopka, K.	Variabilität des Aerosols und Partikelneubildung in und an Wolken	2008	University of Leipzig, Faculty of Physics and Earth Science
Dipl.	Köppe, M.	Charakterisierung der Submikrometer-Aerosolpartikel in der oberen Troposphäre und unteren Stratosphäre	2008	University of Leipzig, Faculty of Physics and Earth Science
Dipl.	Kunze, T.	Einfluss der Rand- und Anfangsbedingungen sowie der Eisnukleation auf die Starkregenvorhersage des COSMO-DE am Beispiel des Elbehochwassers 2002	2009	University of Leipzig, Faculty of Physics and Earth Science
Dipl.	Preißler, J.	Geometrische und optische Eigenschaften von Aerosolschichten aus verschiedenen Quellregionen Europas	2008	University of Leipzig, Faculty of Physics and Earth Science
Dipl.	Schmidt, J.	Aufbau und Test von Mehrfachstreudetektionskanälen zur Messung der Wolkentröpfchengröße mit einem Ramanlidar	2009	University of Leipzig, Faculty of Physics and Earth Science
Dipl.	Schrödner, R.	Aerosolkammeruntersuchungen und CE/ESI-MS Analyse partikulärer Produkte der Ozonolyse von Alkenen	2009	University of Leipzig, Faculty of Physics and Earth Science
Dipl.	Walter, J.	Charakterisierung einer kleinen Nebelkammer	2008	University of Leipzig, Faculty of Physics and Earth Science
Dipl.	Weber, S.	Aufbau und Charakterisierung einer Apparatur zur zeitaufgelösten breitbandigen UV-VIS-Untersuchung chemischer Reaktionen in einer optischen Faser	2009	University of Applied Sciences Jena, SciTec Department
M.Sc.	Meusinger, C.	Calibration of a spectral particle absorption photometer for determination of atmospheric mineral dust concentrations and measurements on Cape Verde Islands	2009	University of Leipzig, Faculty of Physics and Earth Science
B.Sc.	Höpner, F.	Einfluss von Wolken auf die Aerosolpartikelkonzentrationen in der oberen Troposphäre	2009	University of Leipzig, Faculty of Physics and Earth Science

*) Habil.: Habilitation, Ph. D.: Doctoral theses, Dipl.: Diploma, M.Sc.: Master of Science, B.Sc.: Bachelor of Science

Guest scientists

Name	Period of stay	Institution
Shaw, R.	01.01. - 31.07.08	Michigan Technological University, Atmospheric Physics, Houghton, Michigan, USA
Maßling, A.	04. - 25.01.08	National Environmental Research Institute, Roskilde, Denmark
Frey, A.	16. - 30.01.08	Finnish Meteorological Institute, Helsinki, Finland
Costabile, F.	12.02. - 12.08.08	Italian National Research Council - Institute for Atmospheric Pollution (CNR-IIA), Rom, Italy
Covert, D.	17.03. - 25.04.08	University of Washington, Department of Atmospheric Sciences, Washington, USA
Burkart, J.	31.03. - 18.04.08	University of Vienna, Austria
Schneider, J.	31.03. - 18.04.08	Max Planck Institute for Chemistry, Mainz, Germany
Schmale, J.	31.03. - 18.04.08	Max Planck Institute for Chemistry, Mainz, Germany
Reitz, P.	31.03. - 18.04.08	Max Planck Institute for Chemistry, Mainz, Germany
Mentel, Th.	31.03. - 18.04.08	Forschungszentrum Jülich, Germany
Spindler, Ch.	31.03. - 18.04.08	Forschungszentrum Jülich, Germany
Martinez, A.	01.04. - 30.09.08	Universidad de Valencia, Burjassot, Spain
Kolgotin, A.	01. - 18.05.08	Physics Instrumentation Center of General Physics Institute, Troitsk, Moscow region, Russia
Perez, D.	03.08. - 24.10.08	Universidad de Granada, Centro Andaluz de Medio Ambiente (CEAMA), Grupo de Física de la Atmósfera, Granada, Spain
Chuang, P.	10.09. - 01.10.08	University of California, Santa Cruz, California, USA
Ruehl, Ch.	10.09. - 01.10.08	University of California, Santa Cruz, California, USA
Sipilä, M.	02. - 07.10.08	University of Helsinki, Finland
Guzman, F. N.	03. - 19.10.08	Universidad de Granada, Centro Andaluz de Medio Ambiente (CEAMA), Grupo de Física de la Atmósfera, Granada, Spain
Mamouri, R.-E.	06. - 23.10.08	Physics Department, Technical University of Athens, Greece
Deng, Z.	08.11. - 06.12.08	Peking University, China
Liu, P.	08.11 - 06.12.08	Peking University, China
Malinka, A.	20. - 27.11.08	B. I. Stepanov Institute of Physics, National Academy of Sciences of Belarus, Minsk, Republic of Belarus
Noh, Y.	01. - 31.12.08	Gwangju Institute of Science and Technology (GIST), Republic of Korea
Shaw, R.	08. - 20.12.08	Michigan Technological University, Atmospheric Physics, Houghton, USA
Morozov, I.	09. - 19.12.08	Russian Academy of Sciences, Institute for Chemical Physics, Moscow, Russia
Shen, X.	03.01. - 03.02.09	Chinese Academy of Meteorological Sciences, Beijing, China
Rizzo, L.	02.02. - 11.02.09	University of São Paulo, Brazil

Name	Period of stay	Institution
Reitz, P.	19.03. - 10.04.09	Max Planck Institute, Mainz, Germany
Kessel, S.	19.03. - 10.04.09	Max Planck Institute, Mainz, Germany
Petters, M.	19.03. - 10.04.09	Colorado State University, Fort Collins, Colorado, USA
Reimann, B.	19.03. - 10.04.09	Goethe University Frankfurt, Germany
Buchholz, A.	19.03. - 10.04.09	Forschungszentrum Jülich, Germany
Sierau, B.	20.03. - 03.04.09	Swiss Federal Institute of Technology Zurich, Switzerland
Stetzer, O.	20.03. - 08.04.09	Swiss Federal Institute of Technology Zurich, Switzerland
Sullivan, R.	26.03. - 09.04.09	Colorado State University, Fort Collins, Colorado, USA
Aiken, A.	01.04. - 08.04.09	Swiss Federal Institute of Technology Zurich, Switzerland
Ma, N.	01.05. - 29.05.09	Peking University, China
Liu, P.	01.05. - 29.05.09	Peking University, China
Deng, Z.	01.05. - 29.05.09	Peking University, China
Slesar, A.	02.05. - 31.05.09	National Academy of Sciences of Belarus, Minsk, Republic of Belarus
Karol, M.	02.05. - 05.06.09	National Academy of Sciences of Belarus, Minsk, Republic of Belarus
Lopatsin, A.	02.05. - 05.06.09	National Academy of Sciences of Belarus, Minsk, Republic of Belarus
Asipenka, F.	02.05. - 05.06.09	National Academy of Sciences of Belarus, Minsk , Republic of Belarus
Pavlovich, A.	02.05. - 05.06.09	National Academy of Sciences of Belarus, Minsk , Republic of Belarus
Shin, D.-H.	04. - 30.05.09	Gwangju Institute of Science and Technology (GIST), Republik of Korea
Shchekin, A.	11. - 18.05.09	St. Petersburg State University, Russia
Filep, A.	22.06. - 10.07.09	University of Szeged, Hungary
Lopez, E. F.	07. - 18.07.09	The University of Manchester, United Kingdom
Jagodnicka, K.	04. - 31.08.09	University of Warsaw, Poland
Zhang, Q.	14. - 20.09.09	University at Albany, State University of New York, Albany, USA
Morozov, I.	21.09. - 16.11.09	Russian Academy of Sciences, Institute for Chemical Physics, Moscow, Russia
Deguillaune, L.	26. - 30.10.09	Le laboratoire de Météorologie Physique, Département de l‘ Atmosphère, Aubière Cedex, France
Laborde, M.	17. - 27.11.09	Paul Scherer Institute, Villingen, Switzerland
Villano, P.	30.11. - 04.12.09	University Joseph Fourier, Grenoble, France

Visits of IfT scientists at other research institutions

Name	Period of stay	Institution
Müller, D.	01. - 13.03.08	National Technical University of Athens, Physics Department, Zografou, Greece
Müller, D.	30.03. - 13.04.08	Universidad de Granada, Centro Andaluz de Medio Ambiente (CEAMA), Grupo de Física de la Atmósfera, Granada, Spain
Hellmuth, O.	11. - 19.04.09	Joint Institute for Nuclear Research (JINR) Dubna, Russia
Hellmuth, O.	12. - 26.04.08	Joint Institute for Nuclear Research (JINR) Dubna, Russia
Müller, Th.	18.04. - 16.05.08	National Oceanic and Atmospheric Administration (NOAA), Boulder, Colorado, USA
Heintzenberg, J.	23. - 30.04.08	University of California, Berkeley, California, USA
Heintzenberg, J.	21. - 25.05.08	Stockholm University, Department of Meteorology, Sweden
Seifert, P.	30.06. - 04.07.08	National Center for Atmospheric Research (NCAR), Boulder, Colorado, USA
Heintzenberg, J.	11.10. - 02.11.08	Stockholm University, Department of Meteorology, Sweden
Mattis, I.	21.11. - 20.12.08	Gwangju Institute of Science and Technology (GIST), Department of Environmental Science and Engineering, Atmospheric Remote Sensing Laboratory, Republic of Korea
Müller, D.	30.04. - 09.05.09	Universidad de Granada, Centro Andaluz de Medio Ambiente (CEAMA), Grupo de Física de la Atmósfera, Granada, Spain
Müller, D.	28.09. - 03.10.09	Institute of Methodologies for Environmental Analysis (CNR-IMAA), Potenza, Italy
Seifert, P.	27.11. - 12.12.09	Gwangju Institute of Science and Technology (GIST), Department of Environmental Science and Engineering, Atmospheric Remote Sensing Laboratory, Republic of Korea

Meetings

Meeting	Date	national/ international	Number of participants
Calibration workshop for particle size spectrometers, Leipzig	25. - 29.02.08	international	22
2nd meeting on the measurement of ultra fine respirable dust in the atmosphere, Leipzig	27.06.08	national	22
3rd International Workshop on Mineral Dust, Leipzig	15. - 17.09.08	international	145
SAMUM Workshop, Leipzig	18./19.09.08	international	35
1st IfT meeting, Kloster Nimbschen, Grimma	01. - 04.12.08	national	80
EARLI09 measuring campaign, Leipzig	04. - 31.05.09	international	25
3rd NA3 S/DMPS Intercomparision Workshop, Leipzig	15. - 24.06.09	international	20
2nd NA4 Absorption Photometer Workshop, Leipzig	29.06. - 10.07.09	international	20
IfT summer school, Rabenberg	16. - 28.08.09	international	31
HALO/ACRIDICON Workshop, Leipzig	04. - 06.10.09	international	22

International and national field campaigns

Field Campaign	Project partner
AIDA Campaign ACI 02 Karlsruhe, Germany IfT: Physics Dept.	Germany, Switzerland, United Kingdom
AIDA Campaign ACI 03 Karlsruhe, Germany IfT: Physics Dept.	Germany, United Kingdom, USA, Switzerland
ALPACA *Aerosol Lidar measurements at Punta Arenas in the frame of Chilean - German cooperation* Punta Arenas, Chile IfT: Physics Dept.	Universidad de Magallanes, Punta Arenas, Chile
AMAZE 2008	AMAZE Consortium
EARLI09 *EArlinet Reference Lidar Intercomparison 2009* Leipzig, Germany IfT: Physics Dept.	EARLINET Consortium; University of Leipzig, Germany; Jenoptik, Germany; Leosphere, France
EARLINET (permanent experiment) *European Aerosol Research Lidar Network* Leipzig, Germany IfT: Physics Dept.	EARLINET Consortium
EUCAARI *European Integrated Project on Aerosol, Cloud, Climate and Air Quality Interactions* Brazil, China and South Africa IfT: Physics Dept.	EUCAARI Consortium
EUCAARI *European Integrated Project on Aerosol, Cloud, Climate and Air Quality Interactions* Forschungszentrum Jülich, Germany IfT: Physics Dept.	EUCAARI Consortium
EUCAARI *European Integrated Project on Aerosol, Cloud, Climate and Air Quality Interactions* Melpitz, Germany IfT: Physics and Chemistry Depts.	Finland, France, Germany, Switzerland, The Netherlands, United Kingdom, Sweden, Hungary, Norway, Greece
EUSAAR *European Super-Sites for Atmospheric Research* IfT: Physics and Chemistry Depts.	EUSAAR Consortium: Czech Republik, South Africa, India, Denmark, UAE, Brazil, Israel, Poland, Portugal, Estonia, China
Examination of the Hygroscopicity of Algaae-Exudates IfT: Physics Dept.	University of Manchester, United Kingdom
Feinstaubbelastung in städtischen Ballungsgebieten am Beispiel von Dresden und Leipzig IfT: Physics Dept.	Dresden University of Technology, Institute for traffic planning and road traffic, Dresden, Germany; Federal Environment Agency, Berlin-Dahlen, Germany; Humboldt University Berlin, Department of Geography, Berlin, Germany

Field Campaign	Project partner
FROST-II - Freezing of Dust IfT: Physics and Chemistry Depts.	Colorado State University, Fort Collins, Colorado, USA; Swiss Federal Institute of Technology Zurich, Switzerland; Johannes Gutenberg University Mainz, Germany; Goethe University Frankfurt, Germany; Forschungszentrum Jülich, Germany
GUAN *German Ultrafine Aerosol Network* IfT: Physics and Chemistry Depts.	Umweltbundesamt Langen, Germany; German Research Center for Environmental Health, Munich, Germany; Saxon State Ministry of the Environment and Agriculture, Dresden, Germany; Institute of Energy and Environmental Technology e.V. (IUTA), Duisburg, Germany; DWD Hohenpeißenberg, Germany
HaChi *Haze in China* IfT: Physics and Chemistry Depts.	Peking University, China; China Meteorological Administration, Beijing, China
IMPACT IfT: Physics Dept.	The Netherlands
Influence of small wood firings on the immission situation - part immission measurement IfT: Physics and Chemistry Depts.	Saxon State Ministry of the Environment and Agriculture, Dresden, Germany
LACIS Campaign FROST-I LACIS, IfT Leipzig, Germany IfT: Physics Dept.	University of Vienna, Austria; Forschungszentrum Jülich, Germany; Johannes Gutenberg University Mainz, Germany; Michigan Technology University, Houghton, Michigan, USA; University of Washington, Seattle, Washington, USA
LACIS Campaign phase Doppler interferometer LACIS, IfT Leipzig, Germany IfT: Physics Dept.	University of California, Santa Cruz, California, USA
Lagrangian Turbulence of Cloud Droplets Umweltforschungsstation Zugspitze, Germany IfT: Physics Dept.	Michigan Technology University, Houghton, Michigan, USA; Max Planck Institute for Dynamics and Self-Organization, Göttingen, Germany
MEGACITIES Zhongshan, China IfT: Physics Dept.	University of Leipzig, Germany; Peking University, China; Anhui Institute of Optics and Fine Mechanics, Chinese Academy of Sciences, Hefei, China
MEGAPOLI *Megacities: Emissions, urban, regional and global atmospheric pollution and climate effects, and integrated tools for assessment and mitigation* Paris, France IfT: Physics Dept.	MEGAPOLI Consortium

Field Campaign	Project partner
Melpitz EMEP *Co-operative Program for Monitoring and Evaluation of the Long-range Transmission of Air pollutants in Europe* IfT: Physics and Chemistry Depts.	Switzerland, Czech Republic, Denmark, Spain, Ireland, Italy, The Netherlands, Norway, United Kingdom
OCEANET *Autonome Messplattformen zur Bestimmung des Stoff- und Energieaustauschs zwischen Ozean und Atmosphäre* IFM-GEOMAR: Polarstern and IfT: Physics Dept.	Leibniz-Institut für Meereswissenschaften IFM-GEOMAR, Kiel, Germany; GKSS-Forschungszentrum, Geesthacht, Germany; Alfred-Wegener-Institut für Polar- und Meeresforschung AWI, Potsdam, Germany; Universität Bremen, Germany
SAMUM-II *Saharan Mineral Dust Experiment* Cape Verde IfT: Physics Dept.	SAMUM-II Consortium
SOPRAN *Surface Ocean Processes in the Anthropocene* Cape Verde IfT: Physics, Chemistry and Modeling Depts.	Germany, United Kingdom, Cape Verde

Reviews

Reviews	Number	
	2008	***2009***
Journals	115	140
Projects	18	27
Others	77	6
Total	**210**	**173**

Memberships

Name	Board	Year
Birmili, W.	Editorial Board Member "Atmospheric Chemistry and Physics"	2008
	Member of the advisory board of "Boreal Environmental Research"	2008
Gnauk, T.	VDI/DIN KRdL-AG Messen von Partikeln in der Außenluft	2009
Heintzenberg, J.	DFG-Fachkollegium „Ozeanographie und Atmosphärenforschung"	2008/2009
	Ordentliches Mitglied der Sächsischen Akademie der Wissenschaften	2008/2009
	Außerordentliches Mitglied der Berlin-Brandenburgischen Akademie der Wissenschaften	2008/2009
	Stellvertretender Sprecher der Sektion E der Wissenschaftsgemeinschaft „Gottfried Wilhelm Leibniz"	2008/2009
	Editorial Board "Tellus B"	2008/2009
	Editorial Board "Atmospheric Research"	2008/2009
	Permanent Scientific Advisory Committee of the Centro de Geofísica de Évora, Portugal	2008/2009
	Advisory Board of the Indian Institute of Technology (IIT) in Roorkee, India for the Max-Planck-Partner Group IIT	2008/2009
	Mitglied des Wissenschaftlichen Lenkungsausschusses für HALO	2008/2009
Herrmann, H.	Vorsitz des Arbeitskreises „Atmosphärenchemie" in der GDCh-Fachgruppe „Umweltchemie und Ökotoxikologie (AKAC)"	2008/2009
	DECHEMA/GDCh/Bunsengesellschaft; Gemeinschaftsausschuss „Chemie der Atmosphäre"	2008/2009
	DECHEMA/GDCh/KRdL Expertengruppe Feinstaub - Mitglied der Lenkungsgruppe	2008/2009
	Mitglied des wissenschaftlichen Beirats der „Kommission zur Reinhaltung der Luft" (KRdL) des Vereins Deutscher Ingenieure (VDI)	2008/2009
	Fellow of International Union of Pure and Applied Chemistry	2008/2009
Mertes, S.	Assoziiertes Mitglied des DFG-Sonderforschungsbereichs 641 „Die troposphärische Eisphase"	2008/2009
Renner, E.	DECHEMA/GVC-Arbeitsausschuss „Schadstoffausbreitung"	2008/2009
	Scientific Committee of the NATO/CCMS ITM conference series, German member	2008/2009
Siebert, H.	WG4 leader and Management Comity in "COST ACTION MP0806-Particles in Turbulence"	2009
Stratmann, F.	Member of the committee of the International Conference on Nucleation & Atmospheric Aerosols	2008/2009
	Member of the committee of the International Conference on Cloud and Precipitation	2008/2009
	Work Package (WP) Leader EU-Projekt EUROCHAMP 2	2009

Name	Board	Year
Stratmann, F.	Member of the EUROCHAMP 2 User Selection Panel (USP)	2009
Tegen, I.	GESAMP (Group of Experts on the Scientific Aspects of Marine Environmental Protection), Member of Working Group 38, The Atmospheric Input of Chemicals to the Ocean	2008/2009
	ISAR (International Society for Aeolian Research), Board Member	2008/2009
	SDS-WAS (WMO Sand and Dust Storm Warning Advisory and Assessment System), Member of Steering Committee	2008/2009
	ADOM (Atmospheric Dynamics during the last glacial cycle: Observation and Modeling) Co-Chair Eolian Records – Atmospheric Dynamics Working Group of PAGES (Past Global Changes, IGBP)	2008/2009
	Guest Editor "Annales Geophysicae", Special Issue 'From Deserts to Monsoons', 2009	2009
Wandinger, U.	Topical Editor "Applied Optics"	2008/2009
	Member of the ESA-JAXA EarthCARE Joint Mission Advisory Group	2008/2009
	Member of the EARLINET Council	2008/2009
Wehner, B.	Mitglied des GAeF-Vorstands (Gesellschaft für Aerosolforschung)	2008/2009
	Co-Chair der Working Group "Atmospheric Aerosols" within the EAA (European Aerosol Assembly)	2008/2009
Wiedensohler, A.	"Scientific Advisory Group" for aerosols within the "Global Atmosphere Watch"-program of the World Meteorological Organization	2008/2009
	Editorial Board Member "Atmosphere, Water, Air and Soil Pollution"	2008/2009
	VDI-Ausschuss „Partikelzählung in der Atmosphäre"	2008/2009
	Member Scientific Steering Committee (SSC) and Work Package (WP) Leader EU-Projekt ACCENT	2008/2009
	Member SSC EU-Projekt EUSAAR	2008/2009
	Guest Professor "Peking University", Department of Environmental Science, China	2008/2009
	Leiter Weltkalibrierzentrum für Aerosolphysik im Rahmen von WMO-GAW	2008/2009
	Editorial Board Member "Atmospheric Chemistry and Physics"	2008/2009
	Editorial Board Member "Atmospheric Measurement Techniques"	2009
Wolke, R.	European Geoscience Union (EGU)	2008

Cooperations

International Cooperations

Research project	Cooperation partners
ACCENT *Atmospheric Composition Change: A European Network*	Italy, France, United Kingdom, Finland, Norway, The Netherlands, Greece, Greenland, Denmark, Czech Republic, Switzerland, Hungary, Ireland, Surinam, Portugal, Lithuania, Latvia, Belgium, Austria, Spain, Bulgaria, Poland
ACTOS *Airborne Cloud Turbulence Observation System - Interaction between turbulent mixing processes and cloud micro-physical characteristics in stratiform boundary layer clouds*	Michigan Technological University, Department of Physics, Houghton, Michigan, USA
AERONET *Aerosol Robotic Network*	National Aeronautics and Space Administration (NASA), USA
AIE *Atmospheric Environmental Impacts of Aerosol in East Asia*	30 partners
ALPACA *Aerosol Lidar measurements at Punta Arenas in the frame of Chilean - German cooperation*	Universidad de Magallanes, Punta Arenas, Chile
Anthropogenic influence of Asian aerosol on tropical cirrus clouds	National Center for Atmospheric Research (NCAR), Boulder, Colorado, USA
AQMEII *Air Quality Model Evaluation International Initiative*	Austria, Australia, Belgium, Canada, Switzerland, Cyprus, Germany, Denmark, Finland, France, Greece, Italy, Luxembourg, Malta, The Netherlands, Norway, Poland, Portugal, Sweden, United Kingdom, USA
Atmospheric Nucleation	Universities of Helsinki and Kuopio, Finland
BodEx *Quantification of near source dust emission and dust properties in the Bodele Depression*	University Oxford, United Kingdom; University College London, United Kingdom; NASA Goddard Space Flight Center, USA; Cornell University, Ithaca, New York, USA
CARIBIC *Civil Aircraft for Remote Sensing and In situ measurement in Tropospheric and Lower Stratosphere based on the Instrumentation Container Concept*	Germany, United Kingdom, France, The Netherlands, Switzerland, Sweden
CLACE *Cloud and Aerosol Characterization Experiment in the free Troposphere*	Switzerland, United Kingdom, Finland, Denmark, Germany
CLOUD – ITN *Cosmics leaving OUtdoor Droplets - International Training Network*	Germany, Switzerland, Finland, Austria, United Kingdom

Research project	Cooperation partners
CLOUD *Cosmics Leaving OUtdoor Droplets*	Germany, Switzerland, Finland, Austria, Portugal, Russia, United Kingdom, Bulgaria
Comparison of regional dust modells	France, United Kingdom, Spain, Israel, Italy
Cooperation partners involved in research projects at the IfT Research Station Melpitz	Norway, United Kingdom, Italy, Switzerland, Czech Republic, Hungary, Ireland, Finland, Austria, Sweden, Bulgaria, Belgium, France, Greece, The Netherlands, Spain, Denmark, Latvia, Poland, Portugal
COST *Chemistry transport model intercomparison*	Germany, The Netherlands, Finland, France
Development and evaluation of methods for the quantification of trace compounds produced by biomass burning	Academy of Science of Taipei, Taiwan
DFG-COPS *Convective and Orographically-induced Precipitation Study*	Germany, France, The Netherlands, United Kingdom, Italy, Switzerland, USA
EARLINET *European Aerosol Research Network*	Germany, Italy, Greece, Switzerland, Sweden, Spain, Portugal, Poland, Republic of Belarus, United Kingdom, France, Bulgaria
EARLINET-ASOS *European Aerosol Research Network-ASOS*	Italy, Germany, Spain, Greece, Switzerland, Sweden, Poland, Republic of Belarus, France, Bulgaria, Romania, Norway, The Netherlands
ESA-ADM *European Space Agency, Atmospheric Dynamics Mission*	European Space Research and Technology Center (ESTEC), The Netherlands
ESA-CALIPSO *EARLINET's Spaceborne-lidar-related Activity During the CALIPSO Mission*	European Space Research and Technology Center (ESTEC), The Netherlands; EARLINET Consortium
ESA-EarthCARE *European Space Agency, Earth Clouds, Aerosol and Radiation Explorer*	European Space Research and Technology Center (ESTEC), The Netherlands; Japan Aerospace Exploration Agency
EUCAARI *European Integrated Project on Aerosol, Cloud, Climate and Air Quality Interactions*	Norway, Germany, Finland, France, Switzerland, The Netherlands, United Kingdom, Italy, Sweden, Hungary, Ireland, Greece, Czech Republic, Denmark, India, Brazil, South Africa, India, Estonia, Austria, Poland, Portugal, China
EUFAR *European Fleet for Airborne Research in the Field of Environment and Geo Science*	Germany, United Kingdom, France, Ireland, Sweden

Research project	Cooperation partners
EUROCHAMP *Integration of European Simulation Chambers for Investigating Atmospheric Processes*	Germany, Italy, Spain, United Kingdom, Ireland, France, Switzerland, Sweden
EUROCHAMP-II *Integration of European Simulation Chambers for Investigating Atmospheric Processes*	Denmark, Germany, Italy, Spain, United Kingdom, Ireland, France, Switzerland, Sweden
EUSAAR *European Supersites for Atmospheric Aerosol Research*	United Kingdom, The Netherlands, Finland, Switzerland, Norway, France, Greece, Spain, Bulgaria, Ireland, Lithuania, Germany, Italy, Sweden, Czech Republic
HaChi *The regional aerosol in eastern China and its cloud microphysical and optical properties at high relative humidities*	China, Germany
IAGOS *Integration of routine Aircraft measurements into a Global Observing System*	Germany, United Kingdom, France
ICAROHS *Observational Requirements for Multi-wavelength HSRL Systems*	European Space Research and Technology Center (ESTEC), The Netherlands; Deutsches Zentrum für Luft- und Raumfahrt (DLR), Oberpfaffenhofen, Germany; Royal Netherlands Meteorological Institute (KNMI), de Bilt, The Netherlands; Meteorologisches Institut der Ludwig-Maximilians-Universität, München, Germany; DEIMOS Space S.L., Madrid, Spain
Inter-comparison of dust regional models	LISA - Laboratoire Interuniversitaire des Systèmes Atmosphériques, Université Paris, France; LaMP - Laboratoire de Météorologie Physique, Université Blaise Pascal Clermont-Ferrand, France
IRMA *Imager Retrieval Methods and ATLID synergy*	European Space Research and Technology Center (ESTEC), The Netherlands; BMT ARGOSS, The Netherlands; University of Bremen, Germany; German Meteorological Service, Richard Aßmann Observatory, Lindenberg, Germany
Laboratory investigations in the field of liquid phase chemistry	National Institute of Chemistry Ljubljana, Slovenia; Université de Lyon, France; Université de Marseilles, France; Semenov Institute of Chemical Physics, Moskow, Russia

Research project	Cooperation partners
LACIS *Leipzig Aerosol Cloud Interaction Simulator*	USA, United Kingdom, Russia, Denmark, Germany, Finland
Lidar development, Measurement of Asian Aerosols	Gwangju Institute of Science and Technology (GIST), Republic of Korea
MEGACITIES *Satellite-Based Aerosol Mapping over Megacities: Development of Methodology and Application in Health and Climate Related Studie*	University of Leipzig, Germany; University of Bielefeld, Germany; Peking University, China; Anhui Institute of Optics and Fine Mechanics, Chinese Academy of Sciences, Hefei, China
MEGAPOLI *Megacities: Emissions, urban, regional and Global Atmospheric Pollution and climate effects, and Integrated tools for assessment and mitigation*	MEGAPOLI-Consortium
Multiple scattering in Raman lidar signals	National Academy of Science of Belarus, Institute of Physics, Minsk, Republic of Belarus
NASA-CALIPSO *Cloud-Aerosol Lidar and Infrared Pathfinder Satellite Observations* (Lidar ground truth, EARLINET)	National Aeronautics and Space Administration (NASA), USA
PAREST *PArtikel-REduktions-STrategien*	Germany, The Netherlands
Polar stratospheric clouds	Service d'Aéronomie CNRS/IPSL UPMC, Paris, France
Polly XT (Compact Lidar Development)	Listar GmbH Leipzig, Germany
Polly-Measurements in Brazil	INPA - Instituto Nacional de Pesquisa da Amazônia, Manaus, Brazil
Relations between directly emitted wood burning emissions and ambient particle concentration in the Melbourne region	Commonwealth Scientific and Industrial Research Organization (CSIRO), Melbourne, Australia
Secondary new particle formation in Europe	Universities Helsinki and Kuopio, Finland
Twinning Partnership with GAW-Stations	Korean Meteorological Service; Global Atmosphere Watch (GAW), Anmyeon, Republic of Korea; Malaysian Meteorological Service, Danum Valley, Malaysia; Bulgarian Academy of Sciences, BEO-Moussala, Bulgaria
UFIPOLNET *Ultrafine particle size distributions in air pollution monitoring networks*	Germany, Italy, Sweden, Czech Republic
ZOTTO *Zotino Tall Tower Facility (sources and budgets of tropospheric aerosols over Siberia)*	Max Planck Institute for Biogeochemistry, Jena, Germany; Max Planck Institute for Chemistry, Mainz, Germany; IFOR-RASS, Krasnojarsk, Russia

National Cooperations

Research project	Cooperation partners
AirShield (BMBF-Verbundprojekt) *Airborne remote sensing for hazard inspection by network enabled lightweight drones*	8 Projektpartner
Anzahl ultrafeiner Partikel in der städtischen Außenluft (Vergleichsmessungen im Prüflabor)	Sächsisches Landesamt für Umwelt, Landwirtschaft und Geologie, Dresden; TOPAS GmbH
BMU Feinstaub-II *Wärme aus Holz-Feinstaubemissionen: Brennstoffeinfluss, Nutzer, Feuerungswettbewerb, Sekundärmaßnahmen, Charakterisierung, Toxizität*	Deutsches BiomasseForschungsZentrum, Leipzig; TU Hamburg-Harburg; Universität Konstanz; Technologie- und Föderzentrum im Kompetenzzentrum für Nachwachsende Rohstoffe, Straubing
DFG-Forschergruppe SAMUM *Saharan Mineral Dust Experiment*	9 Projektpartner
DFG-SPP HALO	
Mission: ML-CIRRUS	12 Projektpartner
Mission: ACRIDICON	16 Projektpartner
Mission: NARVAL	11 Projektpartner
Konzeption der HALO-Datenbank und eines HALO-Missionsplanungswerkeugs	World Data Center for Climate; Max-Placnk-Institut für Meteorologie, Hamburg; Deutsches Zentrum für Luft- und Raumfahrt (DLR), Oberpfaffenhofen
DFG-SPP MetStröm *Skalenübergreifende Modellierung in der Strömungsmechanik und Meteorologie* Gebietszerlegungsverfahren für positiv definite Helmholtz-Gleichungen	Potsdam-Institut für Klimafolgenforschung, Potsdam; Max-Planck-Institut für Meteorologie, Hamburg; Universität Bonn; Technische Universität Dresden
DFG-SPP Niederschlagsvorhersage *Spektrale Mikrophysik in Vorhersagemodellen unter besonderer Berücksichtigung der Tropfennukleation*	21 Projektpartner
DWD-Raman-Lidar	Kayser-Threde GmbH, München; DWD Offenbach; Meteorologisches Observatorium, Lindenberg; inqbus it-consulting, Leipzig; Loritus GmbH, München
Entwicklung eines mobilen Aerosol-Standards	Sächsisches Landesamt für Umwelt, Landwirtschaft und Geologie, Dresden
Feinstaubbelastung in städtischen Ballungsgebieten am Beispiel von Dresden und Leipzig	Technische Universität Dresden (Verkehrswesen); TU Freiberg, Interdisziplinäres Ökologisches Zentrum; Umweltbundesamt Berlin

Research project	Cooperation partners
Hochauflösende Modellierung von Wolken und Schwerewellen: Skalenanalyse, Numerik, Validierung (Leibniz-Pakt-Verfahren)	Leibniz-Institut für Atmosphärenphysik, Rostock; Potsdam-Institut für Klimafolgenforschung, Potsdam
Influence of domestic wood stoves on particulate concentrations in rural areas of Saxony	Sächsisches Landesamt für Umwelt, Landwirtschaft und Geologie, Dresden
MARGA *Physikalisch-chemische Charakterisierung des dynamischen Verhaltens von Ammoniumsalzen im Feinstaub-Aerosol - Erprobung eines neuen zeitlich hochauflösenden Messverfahrens an der EMEP-Level 3-Station Melpitz*	Umweltbundesamt, Dessau-Roßlau
Non-volatile components of particulate air pollution in Augsburg	Technische Bergakademie Freiberg; GSF-Forschungszentrum für Umwelt und Gesundheit GmbH, Neuherberg
OCEANET *Autonome Messplattformen zur Bestimmung des Stoff- und Energieaustauschs zwischen Ozean und Atmosphäre*	Leibniz-Institut für Meereswissenschaften IFM-GEOMAR, Kiel; GKSS-Forschungszentrum, Geesthacht; Alfred-Wegener-Institut für Polar- und Meeresforschung AWI, Potsdam; Universität Bremen
Paralleles Kopplungs-Framework und moderne Zeitintegrationsverfahren für detaillierte Wolkenprozesse in atmosphärischen Modellen	Technische Universität Dresden, Zentrum für Informationsdienste und Hochleistungsrechnen; Martin-Luther-Universität Halle-Wittenberg
Physikalisch-chemische Charakterisierung des Aerosols an der Messstelle Melpitz als deutscher Beitrag zur EMEP-Intensivmessphase 2008	Umweltbundesamt, Berlin
Physikalische und chemische Charakterisierung von Fein- und Ultrafeinstaubpartikeln in der Außenluft	Umweltbundesamt, Dessau-Roßlau, Langen, Schneefernerhaus (Zugspitze), Schauinsland (Oberried/ Hofsgrund); Deutscher Wetterdienst, Hohenpeißenberg; IUTA Duisburg e. V., Duisburg; Helmholtz-Zentrum, München; Universität Augsburg
Quality assurance and evaluation of particle size distribution measurements from the UBA network	Umweltbundesamt, Dessau-Roßlau
REGKLAM (BMBF-Verbundprojekt) *Entwicklung und Erprobung eines integrierten regionalen Klimaanpassungsprogramms für die Modellregion Dresden*	6 Projektpartner
Short-term Health Effects of Fine and Ultra-fine Particle Pollution in Beijing, China	Institut für Epidemiologie, GSF-Forschungszentrum für Umwelt und Gesundheit GmbH, Neuherberg; Helmholtz-Zentrum für Umweltforschung UFZ, Abteilung Expositionsforschung und Epidemiologie, Leipzig

Research project	Cooperation partners
SOPRAN (BMBF) *Surface Ocean Processes in the Anthropocene*	8 Projektpartner
Strahlungseigenschaften von stratiformen Wolken	Johannes-Gutenberg-Universität, Mainz
TRACES (WGL-Pakt) *Ocean-Atmosphere-Land Impacts on Tropical Atlantic Ecosystems* Unterprojekt: Transport- und Umwandlungsprozesse in der Atmosphäre des tropischen Atlantiks	Leibniz-Institut für Meereswissenschaften IFM-GEOMAR, Kiel; Leibniz-Institut für Ostseeforschung, Warnemünde; Potsdam Institut für Klimafolgenforschung
TROPEIS *Sammlung und physiko-chemische Charakterisierung troposphärischer Eiskeime in Zusammenarbeit mit dem DFG-Sonderforschungsbereich 641*	Max-Planck-Institut für Chemie, Mainz; Universität Mainz; Universität Frankfurt; Technische Universität Darmstadt
UFOPLAN Umweltforschungsplan	GSF-Forschungszentrum für Umwelt und Gesundheit GmbH, Neuherberg; Deutscher Wetterdienst Offenbach; Institut für Energie- und Umwelttechnik e. V., Duisburg
Vergleich von Mobilitätsspektrometern des Typs UFP	Sächsisches Landesamt für Umwelt, Landwirtschaft und Geologie, Dresden; TSI GmbH Aachen; Topas GmbH Dresden; Gewerbeaufsichtsamt Hildesheim; Helmholtz-Zentrum München
Vergleichsmessung von Mobilitätsspektrometern verschiedener Bauart	Sächsisches Landesamt für Umwelt, Landwirtschaft und Geologie, Dresden
Verkehrsinduzierte Partikel am Schlesischen Platz in Dresden	Sächsisches Landesamt für Umwelt, Landwirtschaft und Geologie, Dresden

Boards

Scientific advisory board

Name	Institution
Prof.Dr. Th. Benter (Chair)	Bergische Universität Wuppertal, Physikalische Chemie, FB C - Mathematik und Naturwissenschaften
PD Mag. Dr. F. H. Berger	Deutscher Wetterdienst, Richard-Aßmann- Observatorium, Tauche/ Lindenberg
Prof. Dr. A. Bott	Meteorologisches Institut, Universität Bonn
Prof.Dr. P. Builtjes	TNO Environment and Geosciences, Department of Air Quality and Climate, The Netherlands
Ms. Prof.Dr. S. Crewell	Universität Köln, Institut für Geophysik und Meteorologie
Dr. Gerhard Ehret	Deutsches Zentrum für Luft- und Raumfahrt (DLR), Institut für Physik der Atmosphäre, Abteilung LIDAR
Ms. Prof.Dr. A. Flossmann	Observatoire de Physique du Globe de Clermont-Ferrand, Université Blaise Pascal, Aubière, France
Prof. Dr. Johannes Orphal	Forschungszentrum Karlsruhe GmbH, Institut für Meteorologie und Klimaforschung (IMK)
Prof. Dr. Manfred Wendisch	Institut für Meteorologie der Universität Leipzig
Prof. Dr. Andreas Wahner	Forschungszentrum Jülich GmbH ,Institut für Chemie und Dynamik der Geosphäre, ICG-2: Troposphäre

Boards of trustees

Name	Institution
MinR´in Dr. P. Karl	Sächsisches Staatsministerium für Wissenschaft und Kunst, Dresden
RD'in Dr. G. Helbig	Bundesministerium für Bildung und Forschung, Bonn
Prof. Dr. C. Simmer	Rheinische Friedrich-Wilhelms-Universität, Meteorologisches Institut, Bonn

Member of the IfT-Association

Name	Institution
MinR´in Dr. P. Karl	Sächsisches Staatsministerium für Wissenschaft und Kunst, Dresden
RD'in Dr. G. Helbig	Bundesministerium für Bildung und Forschung, Bonn
Prof. Dr. P. Warneck	Mainz
Prof. Dr. B. Brümmer	Universität Hamburg, Meteorologisches Institut
Prof. Dr. W. Engewald **(Chair)**	Universität Leipzig, Fakultät für Chemie und Mineralogie

Leibniz-Institut für Troposphärenforschung e.V.

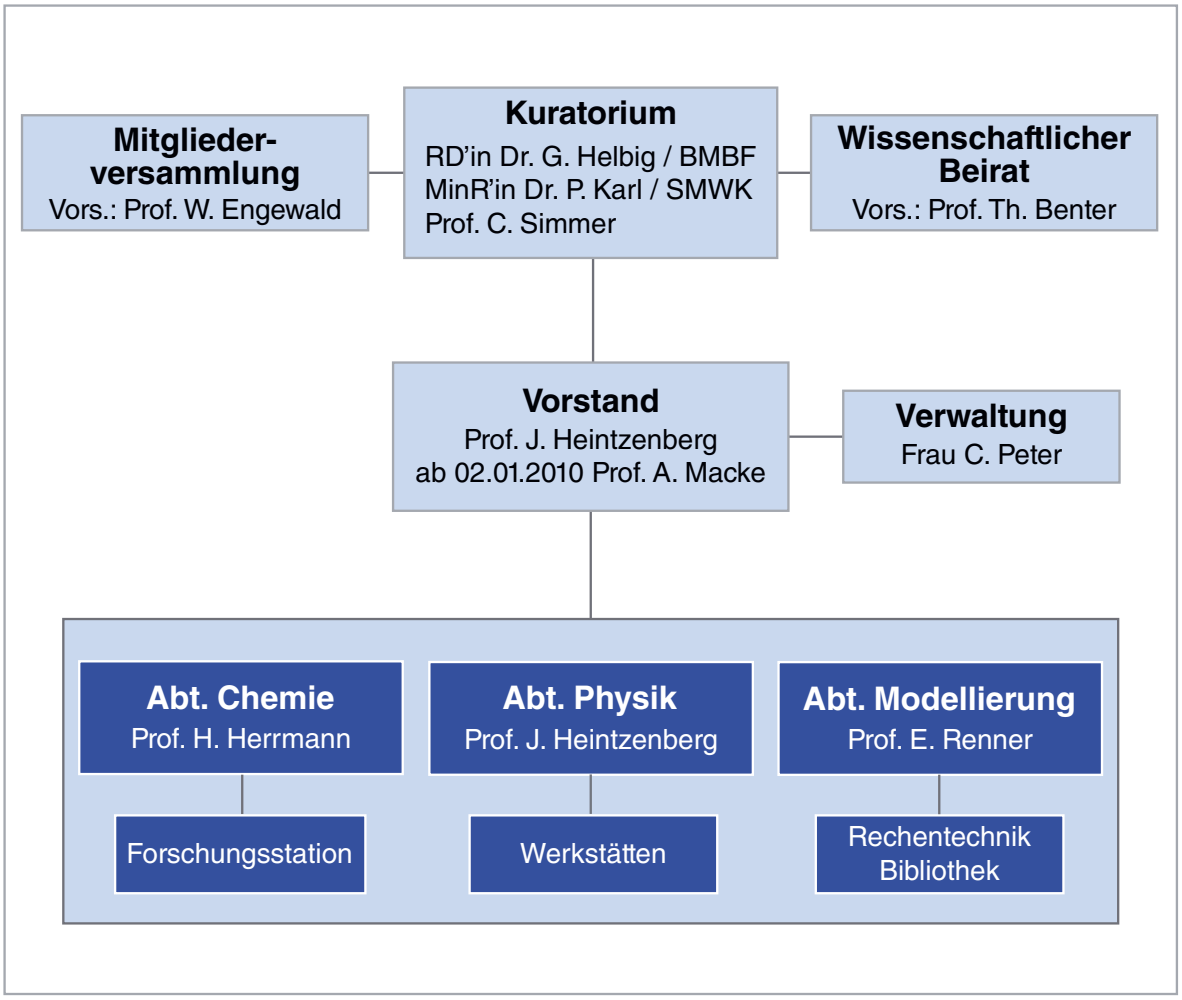

Leibniz Institute for Tropospheric Research & Research Park Leipzig Permoserstrasse